



저작자표시-비영리-변경금지 2.0 대한민국

이용자는 아래의 조건을 따르는 경우에 한하여 자유롭게

- 이 저작물을 복제, 배포, 전송, 전시, 공연 및 방송할 수 있습니다.

다음과 같은 조건을 따라야 합니다:



저작자표시. 귀하는 원저작자를 표시하여야 합니다.



비영리. 귀하는 이 저작물을 영리 목적으로 이용할 수 없습니다.



변경금지. 귀하는 이 저작물을 개작, 변형 또는 가공할 수 없습니다.

- 귀하는, 이 저작물의 재이용이나 배포의 경우, 이 저작물에 적용된 이용허락조건을 명확하게 나타내어야 합니다.
- 저작권자로부터 별도의 허가를 받으면 이러한 조건들은 적용되지 않습니다.

저작권법에 따른 이용자의 권리는 위의 내용에 의하여 영향을 받지 않습니다.

이것은 [이용허락규약\(Legal Code\)](#)을 이해하기 쉽게 요약한 것입니다.

[Disclaimer](#)

이학박사학위논문

Multi-scale modeling of biological systems

생물계의 여러 눈금 모형화

2020년 7월

서울대학교 대학원
물리천문학부
김 순 호

이학박사학위논문

Multi-scale modeling of biological systems

생물계의 여러 눈금 모형화

2020년 7월

서울대학교 대학원
물리천문학부
김 순 호

Abstract

Biological systems are the quintessential complex systems of nature, with emergent phenomena at multiple length scales. While the theoretical physicist's ultimate goal would be to understand the complexities of life under a unified framework, there is still much work to be done in understanding the rules that dictate the rich emergent phenomenon at each scale. Many fields of biology are in need of mathematical models that can explain the vast amount of experimental data regarding their specific target phenomena.

In this dissertation, five biological phenomena are studied with the aid of mathematical models and methods from statistical physics: autophagy dynamics and its effect on amyloid- β peptide levels; aggregation of amyloid- β in Alzheimer's disease; entrainment of the circadian system and recovery by light treatment; energy expenditure during gradient walking; and the behavioral dynamics of interceptive walking. For each topic, we provide background information on the topic at hand, discuss a model developed to understand the system, report the results of the model, and discuss the meaning of the results.

keywords: mathematical model, complex systems, biological systems, emergence, autophagy, amyloid-beta, Alzheimer's disease, size distribution, growth model, sleep-wake switch, circadian rhythm, orexin, entrainment, energy expenditure, gradient walking, behavioral dynamics, pedestrian, Lagrangian mechanics, principle of least effort

student number: 2013-22982

Contents

Abstract	i
Contents	ii
List of Tables	iv
List of Figures	v
1 Introduction	1
2 Autophagy and its effect on amyloid-β peptide levels	5
2.1 Background	5
2.2 Mathematical model	7
2.3 Model dynamics	15
2.4 Discussion of the autophagy model	23
3 Aggregation of amyloid-β peptides in Alzheimer's disease	28
3.1 Background	28
3.2 Merging model	30
3.3 Toxicity of aggregate size distributions	31
3.4 Size distribution of plaques	32
3.5 Discussion: Towards a multi-scale model of Alzheimer's disease	35

4	Disruption of the circadian rhythm and recovery via light treatment	36
4.1	Background	36
4.2	Model of the sleep-wake system coupled with the circadian oscillator	38
4.3	Period Locking Zone	45
4.4	Diseased States and Light Treatment	48
4.5	Discussion	54
5	Predicting expenditure during gradient walking	57
5.1	Background	57
5.2	Data collection	59
5.3	Model construction	62
5.4	Fitting results	67
5.5	Discussion	69
6	Behavioral dynamics of interceptive walking	71
6.1	Background	71
6.2	Model based on a least action principle	73
6.3	Recasting the model to describe bearing angle and affordance	85
6.4	Fitting results	89
6.5	Discussion	96
	국문 초록	117
	감사의 글	118

List of Tables

2.1	Nominal parameters for the autophagy model describing the essential autophagy dynamics of a neuron.	14
3.1	Table of $A\beta$ aggregation model parameters.	31
4.1	Nominal parameter values of the sleep-wake model.	43
5.1	Coefficients for the full model reported with the RMSD on comparison with data.	67
6.1	Fitting parameters v_m , t_a , and τ for the averaged data, together with Lagrangian constant a_m , using each model and fit to each age group. .	82
6.2	Table summarizing age groups and experimental parameters.	84
6.3	Proportion of successful crossings to all crossing attempts for several values of y_0 and l_g , when $v_c = 30$ km/h and vehicle type is sedan. . .	89
6.4	Proportion of two-step crossings to all successful crossings for several values of y_0 and l_g , when $v_c = 30$ km/h and vehicle type is sedan.. . .	90

List of Figures

2.1	Schematic diagram of the model system. The rounded rectangles with white borders illustrate the four compartments of the model: intracellular protein, autophagosome, autolysosome, and extracellular A β peptide.	7
2.2	The basal steady-state A β concentrations and fluxes.	16
2.3	Intracellular A β concentrations under normal and pathological conditions. The intracellular A β concentration C_{S3} displays oscillatory behaviors depending on the parameters.	17
2.4	Extracellular A β concentrations under normal and pathological conditions. The extracellular A β concentration C_{ES3} displays oscillatory behaviors depending on the parameters.	18
2.5	A β secretion and clearance fluxes in normal and pathological conditions. F_{sec} and F_{clr} denote the A β secretion flux (from the intracellular to the extracellular space) and A β clearance flux in the extracellular space, respectively. The results in the second column have been obtained under 20-fold increase in the autophagosome formation rate constant, with other parameters kept unchanged.	19

2.6	<p>$A\beta$ concentrations depending upon activities of three autophagy steps. The surfaces specify time-averaged intracellular $A\beta$ concentration $\langle C_{S3} \rangle$ (first row) and extracellular $A\beta$ concentration $\langle C_{ES3} \rangle$ (second row) for basal parameter values; regions above and below the surfaces correspond to $A\beta$ concentrations lower and higher than the basal values. The first and the second columns correspond to $\beta/\beta^{(0)} = 10$ and $\beta/\beta^{(0)} = 100$, respectively. Computations were performed with $r_{l3}/r_{l3}^{(0)}$ and $r_{h3}/r_{h3}^{(0)}$ varied in increments and the mixed cubic and quintic spline interpolation applied. On the surfaces in purple the $A\beta$ concentrations display oscillations while oscillations are absent on the green surfaces.</p>	22
2.7	<p>Log-normal relations between average $A\beta$ concentrations and $r_{g3}/r_{g3}^{(0)}$. Log-log plots of $\langle C_{S3} \rangle$ (top) and $\langle C_{ES3} \rangle$ (bottom) versus $r_{g3}/r_{g3}^{(0)}$ for $r_{l3}/r_{l3}^{(0)} = r_{h3}/r_{h3}^{(0)} = 1$ (left column) and 0.1 (right column). Data were obtained at $\beta/\beta^{(0)} = 10$. Squares indicate average values obtained via simulations and lines depict the least square fit of the log-normal relation.</p>	23
2.8	<p>Effects of r_{l3} and r_{h3} on $A\beta$ concentrations. Average intracellular $A\beta$ concentration $\langle C_{S3} \rangle$ (first and third rows) and extracellular $A\beta$ concentration $\langle C_{ES3} \rangle$ (second and fourth rows) at $\beta/\beta^{(0)} = 10$ (upper two rows) and $\beta/\beta^{(0)} = 100$ (lower two rows), depending upon changes of $r_{l3}/r_{l3}^{(0)}$ (first column), $r_{h3}/r_{h3}^{(0)}$ (second column), and $r_{l3}/r_{l3}^{(0)}$ and $r_{h3}/r_{h3}^{(0)}$ together (third column). At data points in purple, oscillations of $A\beta$ concentrations are observed; at green data points, concentrations are stationary.</p>	24
3.1	<p>Numerical solution of model in equations 1 and 2, along with Weibull and log-normal curve fits (left). Data curves of solutions at times $t = 10, 50, 100$ hs (right).</p>	32

3.2	Size distribution of a monomer population after ten years in basal, early AD, and late AD conditions.	33
3.3	Autophagy shifts the distribution away from the toxic species.	33
3.4	Effect of higher $A\beta$ production on size distribution of aggregates after ten years. Magenta indicates the normal rate, while green indicates AD. The size is in arbitrary units.	34
4.1	Schematic diagram of the connections between components of the model. Pointed-ends represent excitatory connections, while flat-ends represent inhibitory connections.	42
4.2	Limit-cycle dynamics of the model for nominal parameters, plotted for 48 h. Entrainment due to the light input I (in units of lux) is exhibited as seen in the period-locked oscillations of cell potentials V_v , V_m , and V_o (in units of mV) as well as the seven dynamical variables n , x , x_c , and H (unitless).	44
4.3	(a) Δ (average shift of the CBT minimum) obtained via simulations with $T_d = 11$ h, in the ν_{mo} - I_d parameter space. (b) Period-locking zone boundaries for $T_d = 9$ h and 11 h. Circle indicates the point representing normal conditions, square indicates seasonal disorder, and triangle indicates non-seasonal disorder. The arrows indicate shifts from the normal state to the disordered states. Note that in simulations the shift to seasonal disorder (leftward arrow) is accompanied by a change in T_d from 11 h to 9 h. The area enclosed in the the dotted box is enlarged in the inset.	47

4.4	Simulations of non-seasonal affective disorder: black lines indicate daily sleep times and colored dots indicate CBT minima. On day 7, ORX is increased, as indicated by an arrow, causing instability. Morning light treatment of 10,000 lux for 1.5 hour daily is administered starting on day 14, also indicated by an arrow. Periods of light treatment are labeled yellow. Note the gradual return to normal phase. . . .	48
4.5	(a) Recovery time t_r (in days) verses treatment timing t_0 . t_r indicates the number of days of treatment required for recovery from the circadian instability caused by orexinergic imbalance. Plotted for two values of ν_{mo} . Interpolation has been used to produce a smooth curve. (b) I_{tr} - ν_{mo} phase diagram for morning treatment ($t_0 = 7$ am) and afternoon treatment ($t_0 = 3$ pm). Recover occurs above the curves. . . .	51
4.6	(a) Core body temperature minimum time $t_{CBT,i}$ versus noise level D , obtained from simulations. The averages and standard deviations are plotted for the 90th, 110th, and 130th days (blue, green, orange) for $D = 0.01$ mV to 0.25 mV. (b) Light treatment simulations for $\nu_{mo} = 0.33$ mV s, treatment time $t_0 = 7:00$, and $I_{tr} = 10,000$ lux, in the presence of noise $D = 0.1$ mV. As in the case without noise, recovery to the normal phase is observed.	53
5.1	A sample of 4 seconds of raw data from the pressure sensors. The vertical position of each number of the array indicates the time, ordered from top to bottom at an increment of 0.1 seconds. Each column denotes a sensor, with left foot and right foot separated. The colored portions indicate when our algorithm decided the foot was off the ground.	61
5.2	Graph of total pressure from the left foot sole over an interval of 10 seconds obtained from the foot monitoring system from the same data as presented in Fig. 5.1. The two dashed lines indicate the upper and lower thresholds used to calculate the step frequency.	62

5.3	Three-dimensional scatterplot of data (dots) and model prediction (lines) of P versus P_U and P_K for (a) women and (b) men.	65
5.4	Boxplots of the percent errors of predictions made by the model and Fitbit Surge. Errors have been estimated via Eq. 5.9.	66
5.5	Step frequency f multiplied by height h plotted against average walking speed v . Least squares fit line $fh = 0.52v + 1.02$ (m/s) is also shown.	66
6.1	(a) Dependence of the Lagrangian L on the speed v (in the absence of acceleration, $a = 0$). (b) Dependence of L on a (for $v = 0$) for the quadratic form (blue) and the logarithmic form (red).	76
6.2	Top-down diagram of the crossing environment at time $t = 0$. The two boxes on the road depict two vehicles facing the right, which move forward at a constant speed. The circle depicts the pedestrian, who begins at rest and is facing in the direction the arrow. Labeled are experimental parameters l_g , y_0 , and the bearing angle to the crossing point θ_c	77
6.3	Fitting results and data for (a) adults and (b) children, displaying the position y (in meters) versus time t (in seconds). Circles and error bars indicate averages and standard deviations of positions, respectively. Blue and red lines correspond to the quadratic and logarithmic models fitted to the averaged data, respectively. The blue and red lines overlap significantly. Individual data time series are plotted in grey and rectangles represent vehicles.	81

6.4	Pedestrian position-time plots illustrating typical crossing patterns. Black traces indicate example data; red traces indicate the corresponding model fits. Left and right boxes indicate the temporal and spatial area that the leading and the trailing vehicles occupy, respectively. Intersecting one of the box lines would indicate a collision. In both examples, the conditions are described by $y_0 = -3.5$ m, $t_g = 3.0$ s, and $v_c = 30$ km/h, with the vehicle type set to be a sedan. (a) an example of the simple cross with a single acceleration event followed by constant speed walking; (b) an example of the two-step cross with two acceleration events.	87
6.5	Distributions of parameter t_a for varying y_0 and l_g . Here, $v_c = 30$ km/h and vehicle type is sedan. Columns indicate the average values of t_a in the data for given experimental conditions while error bars represent standard deviations. Pairs of samples, marked with asterisks, are presumed to belong to different distributions ($p < 0.05$) according to the Mann-Whitney U test. (Note here that not all such pairs are marked.)	92
6.6	Distributions of parameters t_a (left) and t_d (right) for varying vehicle speeds v_c and for two vehicle types. Other parameters are set to $t_g = 3$ s and $y_0 = -3.5$ m. Columns indicate the average values in the data for given experimental conditions while error bars represent standard deviations. Pairs of samples, marked with asterisks, are presumed to belong to different distributions ($p < 0.05$) according to the Mann-Whitney U test.	93

- 6.7 Data plotted with boundaries representing the affordance of the gap. (a) data plotted with surfaces in the three-dimensional parameter space (τ, v_{\max}, t_a) defined by Equation 6.20. Data points for $l_g = 25$ m and $y_0 = -3.5$ m are plotted for all age groups; dots represent simple crossings and crosses represent two-step crossings; (b) data plotted with boundaries on the two-dimensional plane (v_{\max}, t_a) defined by Equation 6.21. To illustrate the effects of a shift in affordance, data and boundaries for $l_g = 25$ m and $y_0 = -3.5$ m (black) are plotted with those for l_g changed to 33.3 m and for y_0 changed to -6.5 m are shown in red and in blue, respectively. Triangles indicate average parameter values. 95
- 6.8 Time evolution of the bearing angle θ_c , defined by Equation 6.23. The gap length is $l_g = 25$ m and the initial position is $y_0 = -3.5$ m and -6.5 m for red and cyan lines, respectively. Colored lines are computed from data, while black lines show the analytical results using average parameter values. The time axis is given in terms of time before crossing $t - t^*$, so that the zero point is equal to the intersection time of the run (i.e., the time at which $y(t) = 0$). 97

Chapter 1

Introduction

Biological systems are nature's quintessential complex systems. Complexity emerges at all length and time scales, from the scale of the molecular building blocks of life (e.g. the fractal nature of DNA packing) to the scale of organisms (e.g. language and movement) and further on into collective systems. More than any other type of system observed, countless emergent phenomena arise. To understand these systems with a unified framework may be one of the great tasks of theoretical physics. In order to reach this lofty goal, however, more work needs to be done to elucidate the workings of the large variety of systems within even a single organism.

This dissertation presents four chapters each detailing a modeling study of a specific biological phenomena. Chapters 2, 4, 5, and half of chapter 6 are reprints of publications by the author with a few modifications [1, 2, 3, 4]. These are all studies of human biology, although some of the results are general across a range of species. They are presented in terms of increasing length scale, ranging from the cellular scale to the behavioral scale.

We begin with a study of the effects of autophagy on amyloid- β ($A\beta$) monomer concentration and aggregation in the brain [1]. Autophagy (from the Greek, autos, or "self", and phagein, "to eat") is an evolutionarily conserved catabolic pathway whose primary function is to degrade cytoplasmic constituents such as proteins and organelles

in the lysosome and recycle them for energy [5, 6, 7]. However, it is becoming increasingly clear that autophagy interacts with various processes in complex ways, playing a role in regulating protein quality, energy balance, metabolic homeostasis, and even cell death and survival [6, 7, 12, 8]. Adenosine triphosphate (ATP) and amino acids are produced by the recycling process, which in turn regulate the consecutive steps of the autophagy process, i.e., sequestration (or autophagosome formation), autophagosome maturation (autolysosome formation), and intralysosomal hydrolysis, via mammalian target of rapamycin (mTOR) (for amino acids) and AMP-activated protein kinase (AMPK) pathways (for ATP) [9, 10, 11, 76]. Neurons are especially vulnerable to autophagy dysfunction because they rely heavily upon autophagy for preventing the accumulation of toxic substances such as damaged proteins and protein aggregates [13, 14, 15]. For this, the brain is considered to be the most severely affected organ by the autophagy dysfunction [14, 15]: It is particularly related to the development of neurodegenerative disorders such as Alzheimer's disease (AD) and Parkinson's disease (PD) [13, 14, 16, 17, 18, 19, 20].

In chapter 3, we model the aggregation of $A\beta$ peptides into polymers, which is a key process implicated in Alzheimer's disease (AD). The amyloid hypothesis posits that amyloid aggregation plays a causal role in the disease [21, 22]. While the hypothesis is under debate, there is no doubt that understanding the mechanics behind the formation of $A\beta$ monomers into oligomers and fibrils and further into plaques is key to gaining a full understanding of the pathology of AD. We build a model for the aggregation of $A\beta$ by building a model based on key *in vitro* observations, in particular the existence of a critical aggregation concentration and a skewed size distribution [24]. Hence, we develop a model that pays special attention to the size distribution of the aggregates, based on the growth model from statistical physics [25].

In chapter 4, we move to a macroscopic description of the brain in order to study the entrainment of the circadian system, its disruption under abnormal circumstances, and its subsequent recovery via light treatment [2]. The suprachiasmatic nucleus (SCN),

located in the hypothalamus, plays the role of a central pacemaker in the brain [26]. Under normal circumstances, the SCN is entrained to the light-dark cycle of the environment via photic and non-photoc influences. However, under pathological conditions it may fail to be entrained to the environment. This often coincides with sleep disorders [27] as well as psychiatric disorders such as depression [28] and bipolar disorder [29], as well as neurodegenerative disorders such as Alzheimer's disease [30]. In all of these cases, the causal relation is not clear. Here, we study the potential effects of the neurotransmitter orexin on circadian treatment, and the prospect for recovery via light treatment.

In the chapter 5, we examine a whole-body phenomenon: the energy expenditure during walking on gradient surfaces [3]. Physical inactivity, despite its well-known health risks [31, 32], continues to be a serious public health issue [33]. Recently, various wearable devices, including wristbands and mobile phones, have offered a way to track physical activity throughout the day. Such devices can be used in ambulatory conditions by individuals or in clinical settings to monitor patients' physical activity. Many of these devices use an accelerometer-based method to predict energy expenditure [34, 35, 36]. However, these methods are limited in precision [37]. In order to begin addressing this, we propose a model based on simple physical arguments, and the model parameters are fit to data from a treadmill experiment.

Finally, we explore the behavioral dynamics of interceptive walking [4, 38]. In particular, we use the model to examine the behaviors of pedestrians crossing a road between moving vehicles. This problem is one of public health interest, as pedestrian accidents take up a large proportion of traffic-related accidents, particularly in areas of high population density [39, 40]. A quantitative study of the behavioral dynamics of road crossing may help develop strategies to prevent accidents [40, 41, 42]. A model for simple interceptive walking is proposed based on the principle of least action from Lagrangian mechanics. The model is used to extract statistical information from the data, and implications for pedestrian safety are discussed.

Biological systems are inherently unpredictable and contain a high degree of randomness. Order that does emerge can be described by mathematical models that ignore irrelevant details. Such models inherently have high uncertainty, but they are valuable in that they can capture the essential features of a phenomena.

The five topics under study all ask vastly different questions, and the models are tailored to describe specific phenomena at different scales. However, we observe some connections between the studies. The behavioral study of interceptive walking (chapter 6) assumes that effort is proportional to the metabolic energy consumption. The predictive model of energy consumption during walking in chapter 5 tells us that the metabolic energy consumption is proportional to v^2 , where v is the walking speed. This suggests that the effort function might change when the walking surface has a slope, and this connection can guide generalizations of the behavioral model. In chapter 4, we explore macroscopic oscillations of the brain that lead to the 24 hour sleep-wake cycle. The autophagy model of chapter 2 also exhibits intracellular oscillations modulated by up- and down-regulation of autophagy depending on stress levels. In real systems, these oscillations are linked and interacting. As both autophagy and sleep is linked to a myriad of diseases, a study of their interactions may provide hints towards understanding each. In particular, sleep disorders have also been linked to neurodegenerative disease such as AD.

The connections between the models studied reflect the flow of information between multiple scales in biological systems. When a renormalization group is applied to a model, information about relevant parameters is preserved while those about irrelevant parameters are lost [43]. A unified understanding of biology requires an understanding of how information flows not only from one component of the system to another, but also how it flows through a wide range of spatial and temporal scales.

Chapter 2

Autophagy and its effect on amyloid- β peptide levels

2.1 Background

In this chapter, we explore the effect of autophagy on amyloid- β ($A\beta$) levels in the extracellular fluid of the brain. Autophagy efficiently delivers toxic substances along the unusually large architectures of axons and dendrites to lysosomes, which are concentrated in the cell body, while old (deteriorated) neurons have reduced autophagic degradation efficacy. It is becoming increasingly evident that the autophagic degradations of aggregate-prone proteins in neurons are highly substrate-selective [44]. This specificity seems to rely on the specific interactions between substrates and autophagy receptors/adaptors to sequester certain substrates within autophagosomes, and then the substrates proceed to the same degradation machinery as non-selective (bulk) autophagy [45, 46, 47, 48]. The modulation of substrate–receptor/adaptor interactions has been suggested as a new therapeutic strategy for neurodegenerative disorders [44].

Alzheimer’s disease (AD) is the most common form of dementia, and it is expected to become for prevalent with the aging population [49, 50]. The neuropathological hallmarks include deposition of extracellular plaques and formation of intracellular neurofibrillary tangles (NFTs), which predominantly consist of amyloid- β peptides ($A\beta$) and tau proteins, respectively [51]. According to the amyloid hypothesis, an

accumulation of $A\beta$ is the primary factor for the onset and progression of AD and the rest of the process including the NFT formation is the secondary effects of the $A\beta$ toxicity [22, 52, 53]. Increased intracellular $A\beta$ level is observed prior to the onset of extracellular plaque formation.

$A\beta$ consists of 36 to 43 amino acids and is intracellularly generated by specific proteolytic cleavage of the amyloid precursor protein (APP), an integral membrane protein which is concentrated in the synapses of neurons. An altered balance between generation, degradation, secretion (from the intra to the extracellular space of a neuron), and clearance (from the extracellular space) of $A\beta$ is responsible for the intracellular accumulation and extracellular plaque formation. It has been reported that the $A\beta$ generation rate is abnormally high in the early and late stages of AD [54]. $A\beta$ is degraded preferentially via autophagy; yet during late stages of AD autophagosomes fail to fuse with lysosomes [54]. In addition, the $A\beta$ secretion rate depends on the autophagy activity [55, 56, 57]: the secretion rate is reduced in mice lacking autophagy-related gene 7 (Atg7) [56]. On the other hand, the autophagic activity is influenced by the intracellular $A\beta$ concentration [54, 59, 60, 61]. The $A\beta$ clearance rate in the extracellular space varies with the $A\beta$ concentration in a biphasic manner [62]. The AD patient is associated with a decrease in clearance by roughly 30%, which may lead to toxic levels of $A\beta$ accumulation in the extracellular space over about 10 years [63].

Although many individual mechanisms have been studied for decades, the association of $A\beta$ kinetics with autophagy activity and the roles of autophagy in the pathogenesis of AD remain elusive. In this study, we develop a mathematical model for autophagy with respect to $A\beta$ kinetics, integrating various individual molecular and cellular data sets, in hope of providing a unified framework for understanding the complex dynamics between autophagy and $A\beta$ pathways. Simulations are performed to identify the quantitative relationship between autophagy activity and $A\beta$ kinetics, including the intra and extracellular levels, secretion, clearance, and autophagic degradation. This may provide a starting point for understanding the effects of autophagy

on the pathogenesis of AD and implications of pharmacological autophagy modulation for AD therapy and prevention.

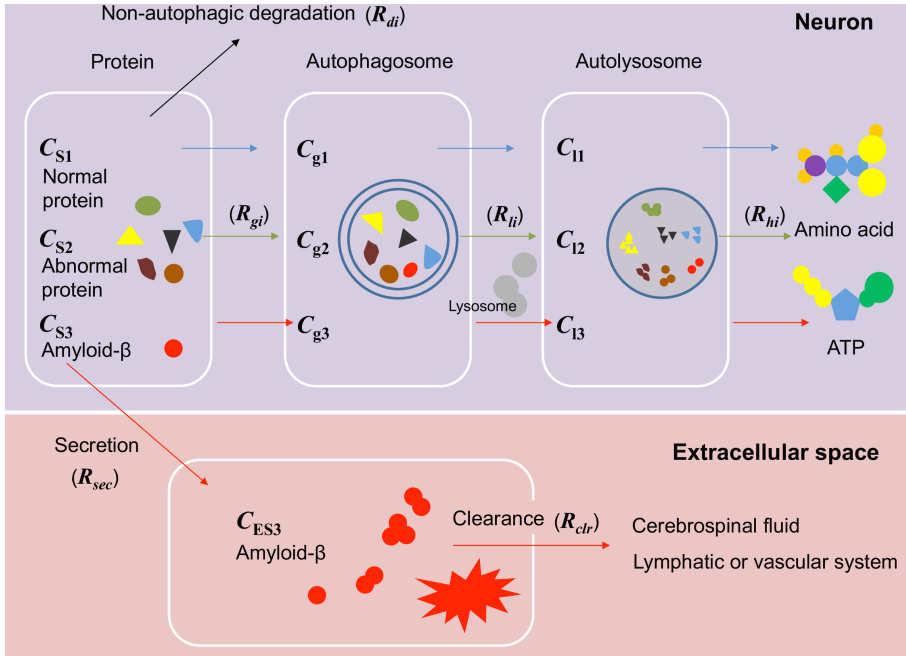


Figure 2.1: Schematic diagram of the model system. The rounded rectangles with white borders illustrate the four compartments of the model: intracellular protein, autophagosome, autolysosome, and extracellular A β peptide.

2.2 Mathematical model

The model assumes a four-compartment description of the autophagy process, including 1) intracellular protein (including normal/abnormal protein and intracellular A β), 2) autophagosome, 3) autolysosome, and 4) extracellular A β compartments (Fig. 2.1).

The model includes a nonlinear relationship between autophagy activity and intracellular and extracellular A β levels. Autophagy degrades intracellular A β and influences the A β secretion from the inside to the outside of the neuron (i.e., extracellu-

lar space) and the concentration-dependent biphasic $A\beta$ clearance in the extracellular space. Conversely, the intracellular $A\beta$ level regulates the autophagy induction step (i.e., autophagosome formation or protein sequestration). The dynamics of these relations are described by twelve coupled differential equations which are solved via the 5th order Runge-Kutta method for very high precision.

Dynamic equations Intracellular proteins are classified as resident proteins S_1 which conduct normal functions in a cell, abnormal proteins S_2 including damaged proteins and those abnormally transcribed or translated, and $A\beta$ peptide S_3 . We write the equations for the dynamics of their respective concentrations C_{S1} , C_{S2} , and C_{S3} as follows:

$$\frac{dC_{S1}}{dt} = (1 - \alpha)R_S - \sigma C_{S1} - R_{g1}C_{S1} - R_{d1} - \beta C_{S1}, \quad (2.1)$$

$$\frac{dC_{S2}}{dt} = \alpha R_S + \sigma C_{S1} - R_{g2}C_{S2} - R_{d2}, \quad (2.2)$$

$$\frac{dC_{S3}}{dt} = \beta C_{S1} - R_{g3}C_{S3} - R_{d3} - R_{sec}C_{S3}, \quad (2.3)$$

where R_S represents the (total) protein synthesis rate (from DNA) and α is the fraction of S_2 , namely, S_1 and S_2 are produced at the rates of $(1-\alpha)R_S$ and αR_S , respectively. σ is the rate constant for deterioration of S_1 (i.e., transformation from S_1 to S_2). R_{gi} and R_{di} represent the specific rates of autophagosome formation and the non-autophagic degradation of S_i (for $i = 1, 2$, and 3), respectively. β denotes the rate constant for $A\beta$ generation and R_{sec} is the $A\beta$ secretion specific rate from the intra to the extracellular space. The dynamics of the $A\beta$ concentration in the extracellular space C_{ES3} reads:

$$\frac{C_{ES3}}{dt} = R_{sec}C_{S3} - R_{clr}C_{ES3}, \quad (2.4)$$

where R_{clr} denotes the specific clearance rate for $A\beta$ in the extracellular space. Variations of the intracellular autophagosome concentration with time are determined by the difference between the autophagosome formation specific rate R_{gi} and the autolysosome formation specific rate R_{li} ($i = 1, 2$, and 3 for S_1, S_2 , and S_3 , respectively).

With C_{gi} denoting the concentration of autophagosome originating from S_i ($i = 1, 2,$ and 3), the dynamics of the concentration is governed by the following equation:

$$\frac{dC_{gi}}{dt} = R_{gi}C_{Si} - R_{li}C_{gi}. \quad (2.5)$$

The intracellular concentration C_{li} of autolysosomes originating from S_i ($i = 1, 2,$ and 3) is determined by the difference between R_{li} and the intralysosomal hydrolysis specific rate R_{hi} ($i = 1, 2,$ and 3). The equation governing the dynamics takes the form:

$$\frac{dC_{li}}{dt} = R_{li}(t - \tau)C_{gi}(t - \tau) - R_{hi}C_{li}. \quad (2.6)$$

Note that the autolysosome concentration at time t is affected by the autophagosome concentration at time $t - \tau$, earlier by the delay time τ , which is taken to be eight minutes ($\tau = 480$ s) [64, 65, 66].

The dynamics of intracellular amino acids, the concentration of which is denoted by C_a reads:

$$\frac{dC_a}{dt} = \mu_a R_{hi} \sum_{i=1}^3 C_{li} + \mu_d \sum_{i=1}^3 R_{di} + R_a - \mu_s R_S. \quad (2.7)$$

The first and second terms on the right-hand side correspond to the supply of amino acids due to the autophagic intralysosomal hydrolysis and non-autophagic protein degradation, respectively, with appropriate constants μ_a and μ_d describing the average numbers of amino acids produced from autophagic and non-autophagic degradation, respectively. The third term represents the rate of amino acid supply from extracellular fluid into cells that is assumed to be proportional to the metabolic demand (i.e., protein synthesis rate R_S) and the loss of protein (i.e., secretion rate of $A\beta$, given by $R_{sec}C_{S3}$) such that $R_a = \mu_c R_S + \mu_\beta R_{sec}C_{S3}$ with appropriate constants μ_c and μ_β . The last term describes the reduction of amino acids due to protein synthesis with the constant μ_s , the average number of amino acids in a protein molecule.

The dynamic equation for intracellular ATP concentration C_A reads:

$$\frac{C_A}{dt} = \nu_a R_{hi} \sum_{i=1}^3 C_{li} + \nu_d \sum_{i=1}^3 R_{di} + R_A - \nu_s R_S. \quad (2.8)$$

where ν_a and ν_d are the average numbers of ATP molecules produced from autophagic degradation and from non-autophagic degradation, respectively. The net intracellular ATP generation rate R_A is assumed to be $R_A = \nu_c R_S + \nu_\beta R_{sec} C_{S3}$ that is associated with the metabolic demand and the loss of protein, with appropriate constants ν_c and ν_β . The last term corresponds to the reduction of ATP due to protein synthesis, where μ_s gives the average number of ATP molecules in a protein.

An average protein molecule in a cell is assumed to be composed of 500 amino acid residues; in other words, 500 amino acids are consumed in unit protein synthesis (i.e., $\mu_s = 500$). Considering that elongation of one amino acid during translation requires approximately four ATP molecules, we have assumed that 2000 ATP molecules are required for the synthesis of a protein ($\nu_s = 2000$). However, the numbers of amino acids and ATP molecules per degradation of one protein via autophagic or non-autophagic protein degradation have been set to be less than those required in the protein synthesis, because the efficacy of protein recycling is expected to be less than 100%; this yields $\mu_a = \mu_d = \mu_\beta = \nu_a = \nu_d = \nu_\beta = 300$, $\mu_c = 200$, and $\nu_c = 1700$.

Details of the autophagy-related rates in Eqs. (2.1) to (2.8) are given in the following subsections. The parameters are summarized in Table 1.

Autophagosome formation

We take the autophagosome formation specific rates R_{gi} from S_i (for $i = 1, 2$, and 3), which depend on the intracellular concentrations C_{S3} of A β [54, 59, 60, 61], C_A of

ATP [67, 62], and C_a of amino acids [69] as follows:

$$R_{g1}(C_{S3}, C_a, C_A) = r_{g1}(\omega_g C_{S3}^{\zeta_g} + \psi_g C_{S3} + 1) \frac{C_A^4}{C_a^4 + k_g^4} \frac{p_g^1 2}{C_A^1 2 + p_g^1 2} \frac{a_g^8}{C_a^8 + a_g^8} \left(1 + \gamma_g e^{-\xi C_a}\right), \quad (2.9)$$

$$R_{g2}(C_{S3}, C_a, C_A) = r_{g2}(\omega_g C_{S3}^{\zeta_g} + \psi_g C_{S3} + 1) \frac{C_A^4}{C_a^4 + k_g^4} \frac{p_g^1 2}{C_A^1 2 + p_g^1 2} \left(1 + \gamma_g e^{-\xi C_a}\right), \quad (2.10)$$

$$R_{g3}(C_{S3}, C_a, C_A) = r_{g3}(\omega_g C_{S3}^{\zeta_g} + \psi_g C_{S3} + 1) \frac{C_A^4}{C_a^4 + k_g^4} \frac{p_g^1 2}{C_A^1 2 + p_g^1 2} \left(1 + \gamma_g e^{-\xi C_a}\right), \quad (2.11)$$

where r_{gi} is the rate constant for autophagosome formation from S_i (for $i = 1, 2$, and 3), with appropriate constants $\omega_g, \zeta_g, \psi_g$ (for $A\beta$), k_g, p_g (ATP), a_g, γ_g , and ξ_g (amino acids). Intracellular $A\beta$ affects the mTOR signaling, which negatively regulates autophagy induction, exhibiting a nonlinear relationship: The mTOR activity increases (i.e., suppressing autophagosome formation) with the $A\beta$ level until reaching a certain threshold ($0.5 \mu M$) and then the activity gradually decreases (restoring autophagosome formation) above the threshold concentration [54, 59, 60, 61]. This nonlinear relationship has been included in Eqs. (2.9) to (2.11) as a simple algebraic equation in the form of $\omega_g C_{S3}^{\zeta_g} + \psi_g C_{S3} + 1$.

The remaining part of the right-hand side contains the ATP and amino acid dependency of the autophagosome formation step. Under normal conditions, it appears that S_2 and S_3 , abnormal proteins and $A\beta$, are preferentially degraded by autophagy. However, as the intracellular energy/nutrient reduces due to, e.g., starvation or increased metabolic demand, all the proteins (S_1, S_2 and S_3) are degraded non-selectively for the rapid supply of essential energy molecules (e.g., ATP) and metabolic building blocks (i.e., amino acids) [48, 47, 70, 71]. Therefore, it is assumed in this model that the autophagosome formation rate from resident proteins S_1 , which is lower than that from abnormal proteins and $A\beta$ (S_2 and S_3) under normal conditions, becomes gradually equal to those of S_2 and S_3 as the amino acid concentration is decreased [72, 73, 74,

75].

Autolysosome formation and intralysosomal hydrolysis

The autolysosome formation specific rate R_{li} reads ($i = 1, 2,$ and 3 for $S_1, S_2,$ and S_3)

$$R_{li}(C_A) = r_{li} \frac{C_A^4}{C_A^4 + k_l^4} \frac{p_l^2}{C_A^2 + p_l^2}, \quad (2.12)$$

where r_{li} denotes the rate constant for autolysosome formation from S_i with appropriate constants k_l and p_l for ATP, based on biological experiments [67, 68].

The intralysosomal hydrolysis specific rate R_{hi} is taken as a function of the intracellular ATP concentration ($i = 1, 2,$ and 3):

$$R_{hi}(C_A) = r_{hi} \frac{C_A^{\delta_h}}{C_A^{\delta_h} + k_l^{\delta_h}}, \quad (2.13)$$

with appropriate exponent δ_h and constant k_h for ATP, where r_{hi} is the rate constant for intralysosomal hydrolysis [67, 68]. Further details of the equations for autolysosome formation and intralysosomal hydrolysis can be found in literature [12, 76, 77, 78].

Secretion and clearance of amyloid- β

Considering that $A\beta$ secretion from the intra to extra cellular space of a neuron is positively correlated with the autophagy induction level [55, 56, 57], we assume the $A\beta$ secretion specific rate R_{sec} to be proportional to the degree of amino acid- and ATP-dependent autophagosome induction, as defined in Eqs. (9)-(11), with an appropriate constant r_{sec} :

$$R_{sec}(C_a, C_A) = r_{sec} \frac{C_A^4}{C_a^4 + k_g^4} \frac{p_g^2}{C_A^2 + p_g^2} \left(1 + \gamma_g e^{-\xi C_a}\right). \quad (2.14)$$

The concentration-dependent biphasic $A\beta$ clearance rate R_{clr} in the extracellular space is assumed, on the basis of biological experiments [62, 63, 79], to take the form:

$$R_{clr}(C_{ES3}) = r_{clr}(C_{ES3} + \omega_{ext}), \quad (2.15)$$

where r_{clr} denotes the rate constant for $A\beta$ clearance, with an appropriate constant ω_{ext} . The rate of $A\beta$ clearance varies with the concentration according to the measurement on Alzheimer's mouse model [62]: While the half-life is very short at high concentrations of extracellular $A\beta$, it grows longer as the concentration decreases. Equation (15) captures qualitatively this biphasic nature of $A\beta$ clearance and its value lies within a reasonable range consistent with the state-of-the-art measurements [63, 79].

Protein synthesis and non-autophagic degradation

The (total) protein synthesis rate R_S which depends on intracellular concentrations C_a of amino acids and C_A of ATP reads [80]

$$R_S(C_a, C_A) = \begin{cases} r_s \frac{C_a}{C_a + k_s} \frac{\exp[C_A] - 1}{\exp[C_A^{(m)}] - 1} & \text{for } C_A < C_A^{(m)} \\ r_s \frac{C_a}{C_a + k_s} & \text{for } C_A > C_A^{(m)} \end{cases} \quad (2.16)$$

th appropriate constant k_s for amino acid, where $C_A^{(m)}$ is the ATP concentration corresponding to the maximal protein synthesis rate and r_s denotes the rate constant for the protein synthesis. Further details of the protein synthesis can be found in literature [12, 76, 77, 78].

The non-autophagic protein degradation machinery such as the ubiquitin-proteasome system has been considered in the model. We assume that the amount of protein degradation by autophagy constitutes 80% of the total amount of protein degradation and the non-autophagic protein degradation machinery is responsible for the remaining 20% [81]. Accordingly, we take the rate of non-autophagic degradation R_{di} ($i = 1, 2,$ and 3) to be 25% of autophagic degradation:

$$R_{di} = \frac{1}{4} R_{hi} C_{li}. \quad (2.17)$$

Parameter	Value	Unit	Description
$r_{gi}^{(0)}$	1.12×10^{-5}	s^{-1}	Rate constant for autophagosome formation of Si ($i = 1, 2, 3$) (normal value)
α	1.00×10^{-2}	1	Fraction of S2 in protein synthesis rate R_S
$\beta^{(0)}$	5.56×10^{-10}	s^{-1}	Rate constant for A β generation (normal value)
σ	4.00×10^{-7}	s^{-1}	Rate constant for deterioration of S1
ω_g	-9.43×10^{-1}	$mM^{-0.1}$	Constant for autophagosome formation (A β dependency)
ζ_g	1.00×10^{-1}	1	Constant for autophagosome formation (A β dependency)
ψ_g	1.01×10^2	mM^{-1}	Constant for autophagosome formation (A β dependency)
k_g	2.83	mM	Constant for autophagosome formation (ATP dependency)
p_g	3.00	mM	Constant for autophagosome formation (ATP dependency)
a_g	4.50	mM	Constant for autophagosome formation (amino acids dependency)
a_g	4.50	mM	Constant for autophagosome formation (amino acids dependency)
ξ_g	7.49×10^{-2}	mM^{-1}	Constant for autophagosome formation (amino acids dependency)
$r_{li}^{(0)}$	2.47×10^{-5}	s^{-1}	Rate constant for autolysosome formation of Si ($i = 1, 2, 3$) (normal value)
k_l	2.43	mM	Constant for autolysosome formation (ATP dependency)
p_l	3.00	mM	Constant for autolysosome formation (ATP dependency)
$r_{hi}^{(0)}$	1.39×10^{-5}	s^{-1}	Rate constant for intralysosomal hydrolysis of Si ($i = 1, 2, 3$) (normal value)
δ	7.24×10^{-1}	1	Exponent for intralysosomal hydrolysis (ATP dependency)
k_h	2.99	mM	Constant for intralysosomal hydrolysis (ATP dependency)
r_s	1.48×10^{-5}	$mM \cdot s^{-1}$	Rate constant for protein/organelle synthesis
k_s	1.77×10^1	mM	Constant for protein/organelle synthesis (amino acids dependency)
$C_A^{(m)}$	2.00	mM	ATP concentration corresponding to maximal protein/organelle synthesis rate
r_{sec}	4.67×10^{-9}	s^{-1}	Rate constant for A β secretion
r_{clr}	2.23×10^{-1}	$mM^{-1} \cdot s^{-1}$	Rate constant for A β clearance
ω_{ext}	6.34×10^{-5}	mM	Rate constant for A β clearance

Table 2.1: Nominal parameters for the autophagy model describing the essential autophagy dynamics of a neuron.

2.3 Model dynamics

A β kinetics under normal and pathological conditions

In Fig. 2.2, the relation of intracellular (C_{S3}) and extracellular (C_{ES3}) A β levels with the respective A β fluxes under normal conditions (i.e., for basal parameter values) are shown, providing kinetic and dynamic insights into the A β regulation. As illustrated in Fig. 2.1, C_{S3} (the second row of the first column) is determined by the difference between influx (i.e., A β generation flux, denoted by F_{gen} , the concentration of A β generated per unit time given in units of mM/s) and efflux rates such as autophagic sequestration F_{seq} (the concentration of intracellular A β sequestered into autophagosomes per unit time, i.e., $F_{seq} = R_{g3}C_{S3}$), non-autophagic degradation F_{nap} (the concentration of intracellular A β degraded via the non-autophagic mechanism per unit time, i.e., $F_{nap} = R_{d3}$), and secretion F_{sec} (the concentration of intracellular A β secreted from the inside to outside of a neuron per unit time, i.e., $F_{sec} = R_{sec}C_{S3}$). C_{ES3} (the third row of the second column) is governed by F_{sec} and the clearance flux F_{clr} (the concentration of A β removed from the extracellular space per unit time, i.e., $F_{clr} = R_{clr}C_{ES3}$).

Figs. 2.3 and 2.4 compare values of C_{S3} and C_{ES3} , respectively, under the normal, early stage (i.e., abnormal increase in A β generation), and late stage AD (i.e., increased A β generation together with decreased autophagic lysosomal degradation) conditions [54]. The simulations have been performed with the basal value $\beta^{(0)}$ of the A β generation rate constant, i.e., $\beta = \beta^{(0)}$, for the normal condition, while data for the early and late stage AD conditions have been obtained at an extremely high A β generation rate, $\beta = 100 \times \beta^{(0)}$. Further, in the late stage case, the specific rate constants of autolysosome formation and intralysosomal hydrolysis have been set to be 10% of the basal values.

It is observed that C_{S3} and C_{ES3} are significantly higher in AD conditions than in the basal condition— C_{S3} is higher at the early stage than at the late stage AD (Fig.

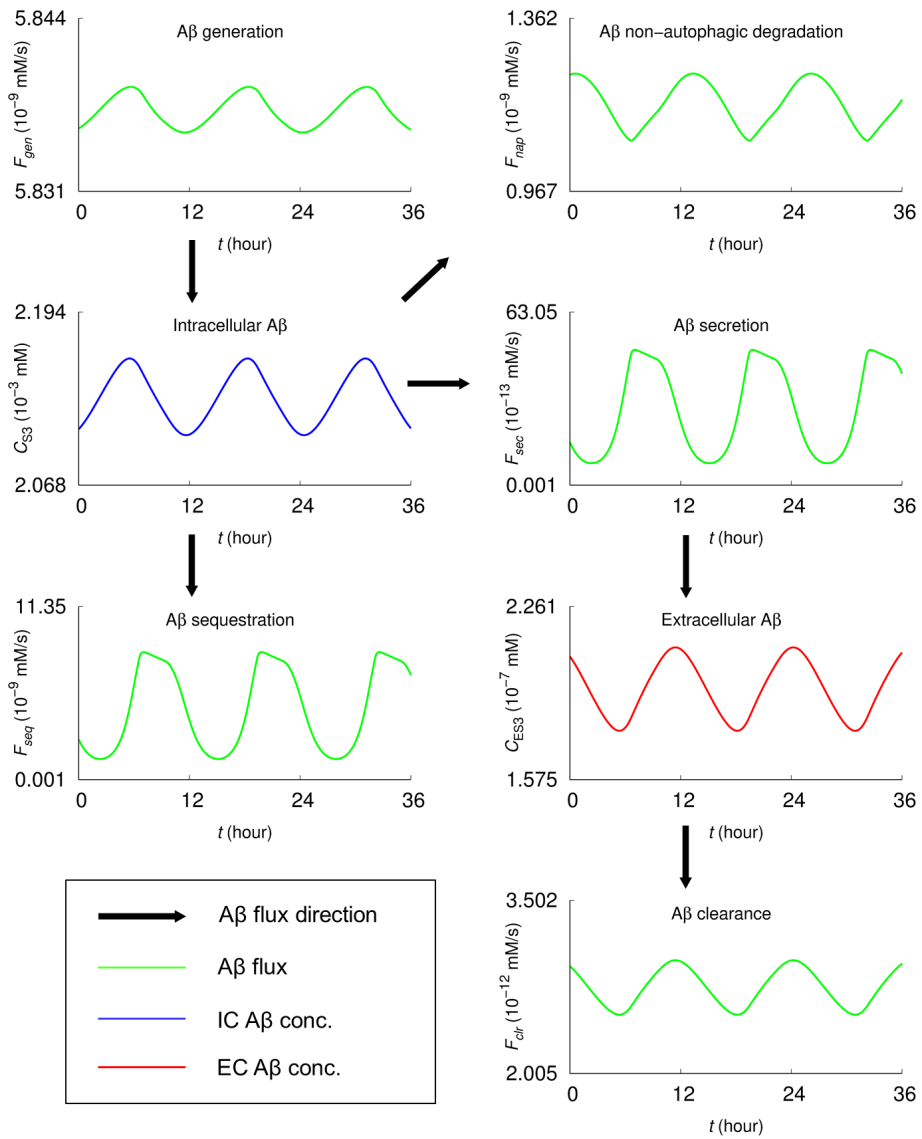


Figure 2.2: The basal steady-state Aβ concentrations and fluxes.

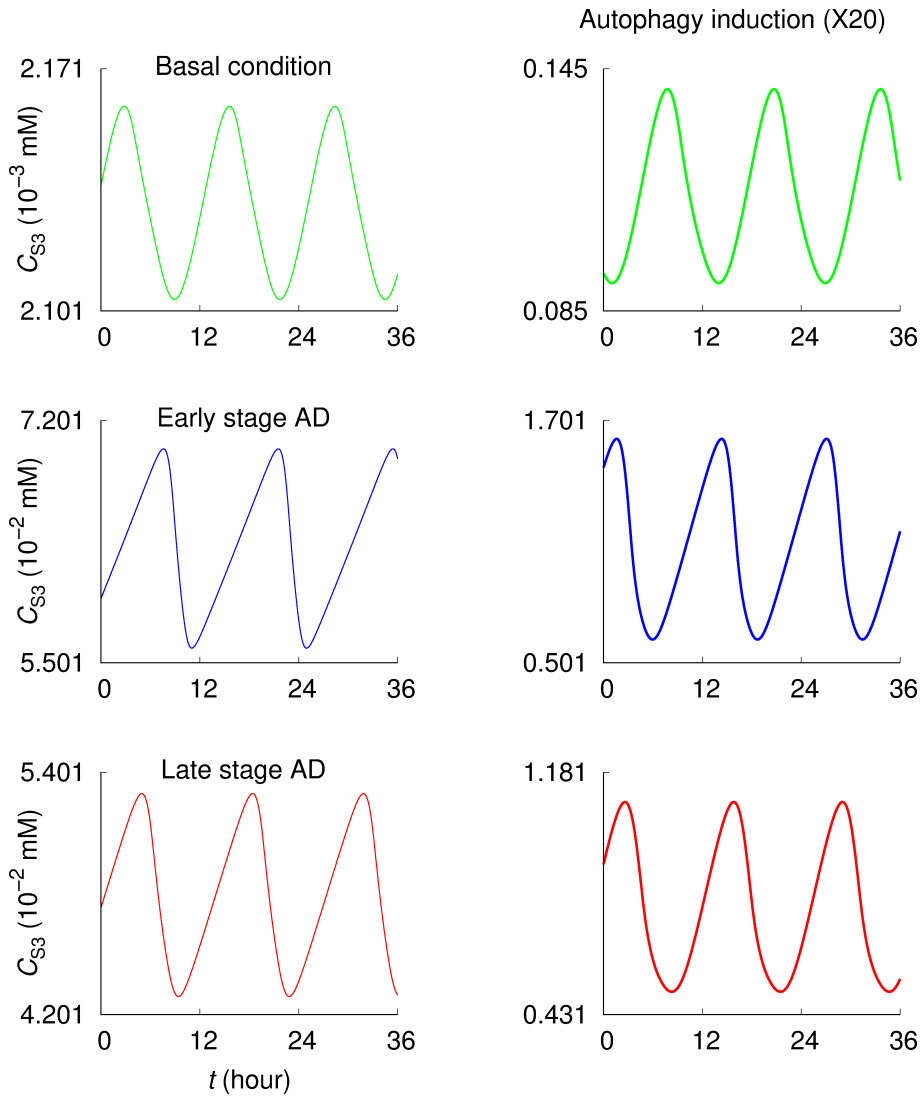


Figure 2.3: Intracellular $A\beta$ concentrations under normal and pathological conditions. The intracellular $A\beta$ concentration C_{S3} displays oscillatory behaviors depending on the parameters.

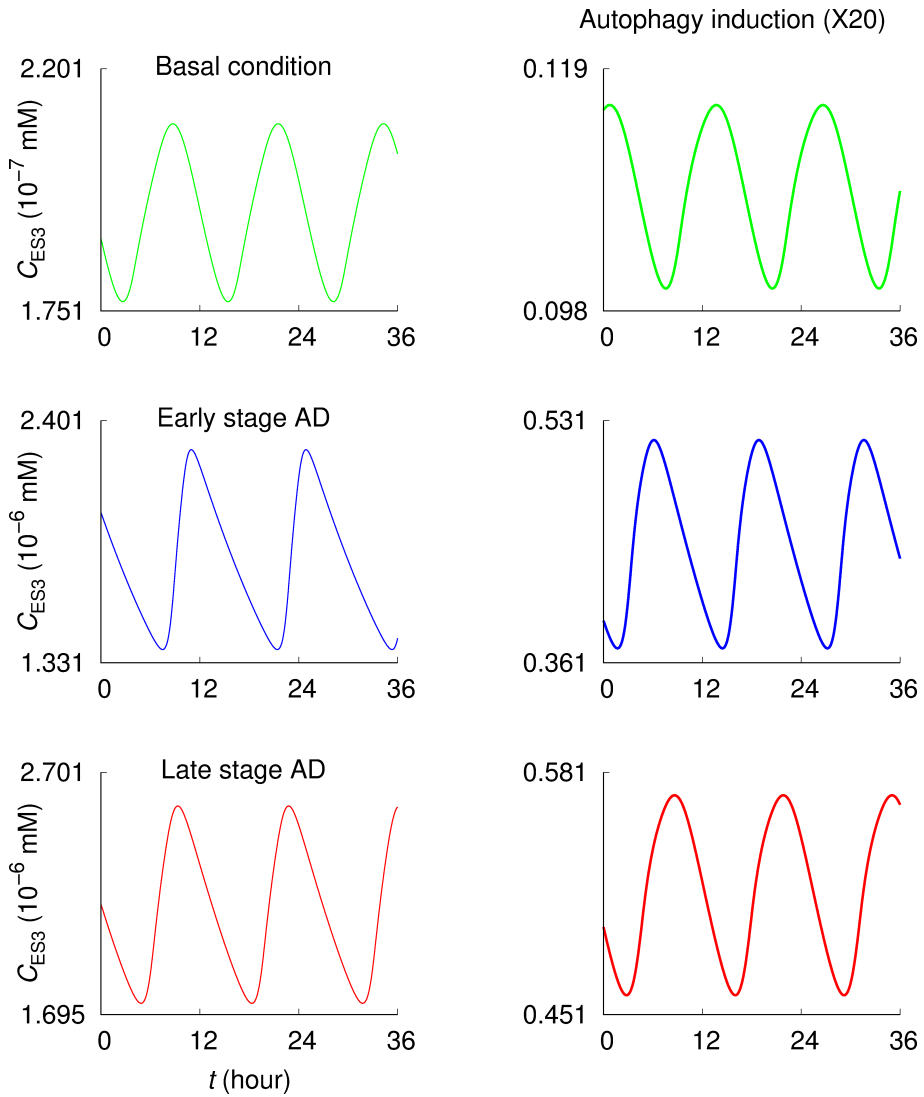


Figure 2.4: Extracellular $A\beta$ concentrations under normal and pathological conditions. The extracellular $A\beta$ concentration C_{ES3} displays oscillatory behaviors depending on the parameters.

2.3) while C_{ES3} is higher at the late stage AD (Fig. 2.4). In both pathological conditions, autophagy induction (i.e., a 20-fold increase in the autophagosome formation rate constant: $r_{g3} = 20 \times r_{g3}$) significantly reduces C_{S3} and C_{ES3} . In addition, the early and late stage AD exhibit asymmetric oscillating patterns. C_{S3} increases gradually and then drops rapidly; conversely, C_{ES3} increases rapidly and drops gradually. Under the basal condition they exhibit relatively symmetrical oscillation patterns.

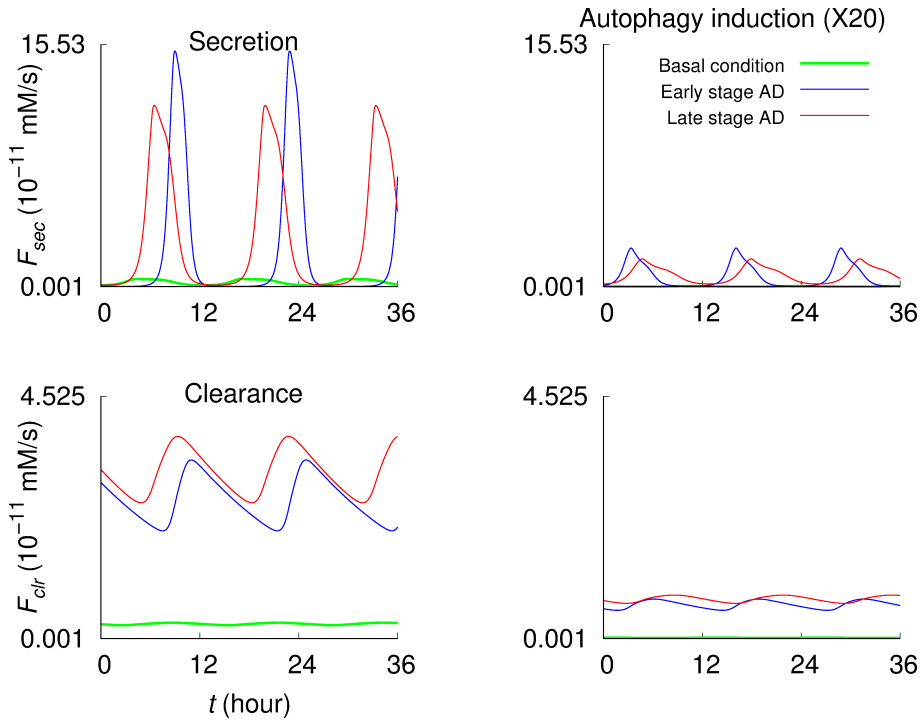


Figure 2.5: $A\beta$ secretion and clearance fluxes in normal and pathological conditions. F_{sec} and F_{clr} denote the $A\beta$ secretion flux (from the intracellular to the extracellular space) and $A\beta$ clearance flux in the extracellular space, respectively. The results in the second column have been obtained under 20-fold increase in the autophagosome formation rate constant, with other parameters kept unchanged.

Both $A\beta$ secretion flux F_{sec} and clearance flux F_{clr} are significantly promoted in the early and late stage AD cases compared to those in the basal condition (the first

column of Fig. 2.5). The peaks of F_{sec} in early AD are sharper and higher but stay at the near-zero rate for a longer period than in late AD. In contrast, F_{clr} exhibits higher peaks in late AD than in early AD. Autophagy induction (i.e., $r_{g3} = 20 \times r_{g3}$) significantly reduces those fluxes, close to the basal levels. In what follows, autophagy dynamics corresponding to the normal and AD conditions are presented, including steady-state concentrations of autophagosome, autolysosome, and autophagic fluxes.

Dynamics of autophagy and implications in the $A\beta$ regulations

Protein sequestration (i.e., autophagosome formation) flux F_{seq} , autophagosome maturation (i.e., autolysosome formation) flux F_{mat} , and intralysosomal hydrolysis flux F_{hyd} in both early and late stage AD are significantly increased compared with those on the basal condition (the first, third, and fifth rows of Fig. 2.6). The peaks of F_{seq} and F_{mat} in early stage AD are sharper and higher than those in the late stage. The steady-state concentrations of autophagosomes and autolysosomes, C_{g3} and C_{l3} , in the AD cases are greater than those in the basal condition case: the values at the late stage of AD are about ten times greater than those at the early stage (the second and fourth rows of Fig. 2.6).

In the cases of early and late stage AD, autophagy induction significantly decreases F_{seq} and F_{mat} , while it increases F_{hyd} (Fig. 2.6). The steady-state autophagosome concentration C_{g3} is decreased while the autolysosome concentration C_{l3} is increased upon autophagy induction (the second and fourth rows of the second and third columns of Fig. 2.6). Under the basal condition, the oscillatory patterns of autophagic fluxes and steady-state concentrations of autophagosomes and autolysosomes are not significantly affected by the autophagy induction, compared to the AD cases.

As shown above, autophagy induction (i.e., $r_{g3} = 20 \times r_{g3}$) significantly reduces C_{S3} and C_{ES3} . Increasing r_{g3} beyond this rate further reduces the $A\beta$ levels until they reach basal levels. However, the required value of r_{g3} to bring the basal levels may vary depending on the stage of AD and the activities of the other autophagic steps.

Fig. 2.7 presents a three-dimensional surface plot, exhibiting step-specific and combined effects of the autophagy pathway on $A\beta$ levels for a moderately high $A\beta$ formation rate $\beta/\beta^{(0)} = 10$ (first column) and an extremely high formation rate $\beta/\beta^{(0)} = 100$ (the second column). The vertical axis measures the autophagosome formation rate relative to its normal value (i.e., $r_{g3}/r_{g3}^{(0)}$) and the two horizontally placed axes represent the autolysosome formation and the intralysosomal hydrolysis rates relative to the normal values, spanning the range from highly induced activity ($r_{l3}/r_{l3}^{(0)} = r_{h3}/r_{h3}^{(0)} = 30$) to normal ($r_{l3}/r_{l3}^{(0)} = r_{h3}/r_{h3}^{(0)} = 1$) and extremely reduced activity ($r_{l3}/r_{l3}^{(0)} = r_{h3}/r_{h3}^{(0)} = 0.1$). The surfaces designate time-averaged intracellular $A\beta$ concentration $\langle C_{S3} \rangle$ (top) and extracellular $A\beta$ concentration $\langle C_{ES3} \rangle$ (bottom) for basal parameter values (i.e., under normal conditions); regions above and below the surface correspond to $A\beta$ concentrations lower and higher than the basal values, respectively.

For both $A\beta$ synthesis rates ($\beta/\beta^{(0)} = 10$ and 100), $\langle C_{S3} \rangle$ and $\langle C_{ES3} \rangle$ decrease with r_{g3} in a log-normal manner,

$$\langle C \rangle (r_{g3}/r_{g3}^{(0)} = x) = (\gamma / (x\sigma\sqrt{2\pi})) \exp a[-(\log x\mu)^2 / 2\sigma^2], \quad (2.18)$$

where $\langle C \rangle$ denotes $\langle C_{ES3} \rangle$ or $\langle C_{S3} \rangle$ and γ , σ , and μ are adjustable parameters (Fig. 2.8). When r_{l3} is decreased from 1 to 0.1, $\langle C_{S3} \rangle$ decreases while $\langle C_{ES3} \rangle$ increases. In contrast, when $r_{l3} > 1$, the concentrations are relatively independent of r_{l3} . The effects of r_{h3} generally follow the trend.

The surface shape of Fig. 2.7 reflects the combined effects of the three-autophagy steps. A greater value of r_{g3} is required to return to basal values in the case $\beta/\beta^{(0)} = 100$ compared with the case $\beta/\beta^{(0)} = 10$. At $r_{l3}/r_{l3}^{(0)} < 1$ and $r_{h3}/r_{h3}^{(0)} < 1$ both concentrations change greatly compared with the case $r_{l3}/r_{l3}^{(0)} > 1$ and $r_{h3}/r_{h3}^{(0)} > 1$, indicating that reduction of autolysosome formation and/or intralysosomal hydrolysis has greater impact on the $A\beta$ concentrations than promotion of these steps. Above $r_{h3}/r_{h3}^{(0)} = 45.21$ (for $\beta/\beta^{(0)} = 10$) and $r_{h3}/r_{h3}^{(0)} = 11.1$ (for $\beta/\beta^{(0)} = 100$), the oscillations of proteins (C_{S1} , C_{S2} , C_{S3} , C_{ES3}), ATP (C_A), and amino acids (C_a)

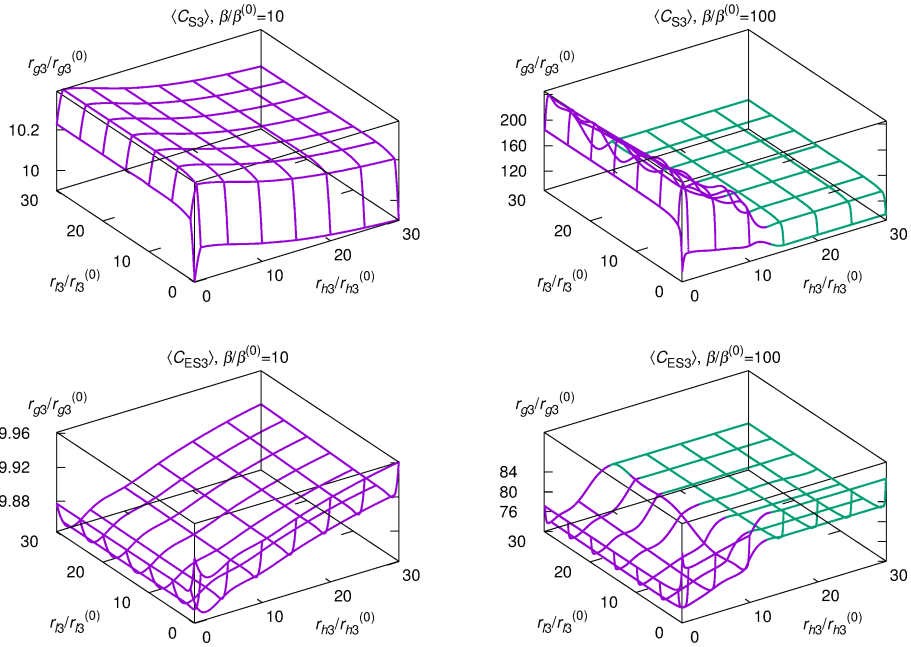


Figure 2.6: $A\beta$ concentrations depending upon activities of three autophagy steps. The surfaces specify time-averaged intracellular $A\beta$ concentration $\langle C_{S3} \rangle$ (first row) and extracellular $A\beta$ concentration $\langle C_{ES3} \rangle$ (second row) for basal parameter values; regions above and below the surfaces correspond to $A\beta$ concentrations lower and higher than the basal values. The first and the second columns correspond to $\beta/\beta^{(0)} = 10$ and $\beta/\beta^{(0)} = 100$, respectively. Computations were performed with $r_{l3}/r_{l3}^{(0)}$ and $r_{h3}/r_{h3}^{(0)}$ varied in increments and the mixed cubic and quintic spline interpolation applied. On the surfaces in purple the $A\beta$ concentrations display oscillations while oscillations are absent on the green surfaces.

disappear, converging to stationary values (green surfaces in Figs. 2.7 and 2.9). In the stationary region, the effects of $r_{l3}/r_{l3}^{(0)}$ and $r_{h3}/r_{h3}^{(0)}$ are minimal, as manifested by the flatness of the green surface.

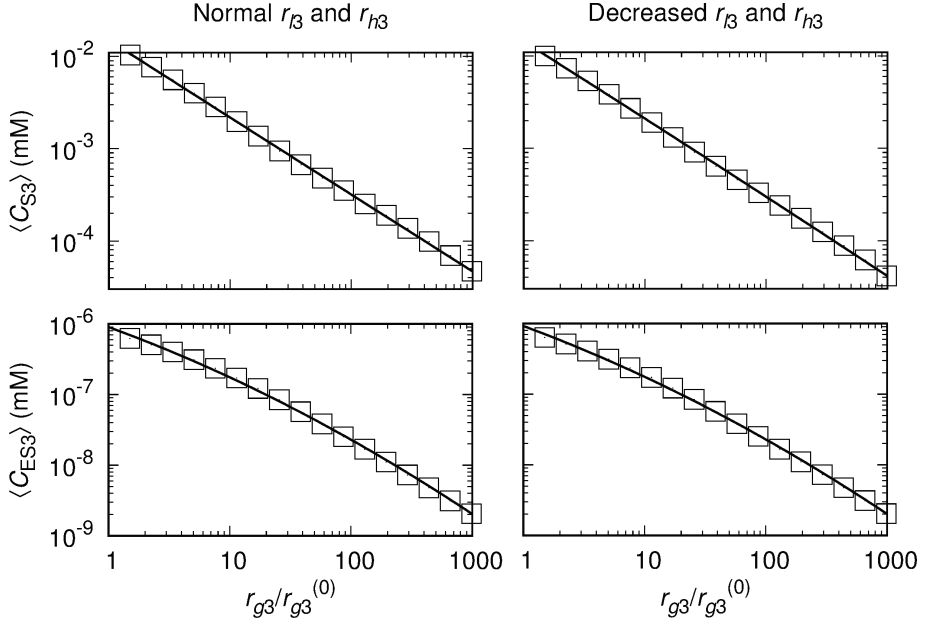


Figure 2.7: Log-normal relations between average A β concentrations and $r_{g3}/r_{g3}^{(0)}$. Log-log plots of $\langle C_{S3} \rangle$ (top) and $\langle C_{ES3} \rangle$ (bottom) versus $r_{g3}/r_{g3}^{(0)}$ for $r_{l3}/r_{l3}^{(0)} = r_{h3}/r_{h3}^{(0)} = 1$ (left column) and 0.1 (right column). Data were obtained at $\beta/\beta^{(0)} = 10$. Squares indicate average values obtained via simulations and lines depict the least square fit of the log-normal relation.

2.4 Discussion of the autophagy model

In this chapter we have investigated via modeling and simulations how autophagy activity affects A β kinetics such as the intra and extracellular levels, secretion, clearance, and autophagic degradation. The mathematical model is extended from the multi-compartment autophagy model originally developed by Han and Choi [12, 76, 77, 78]

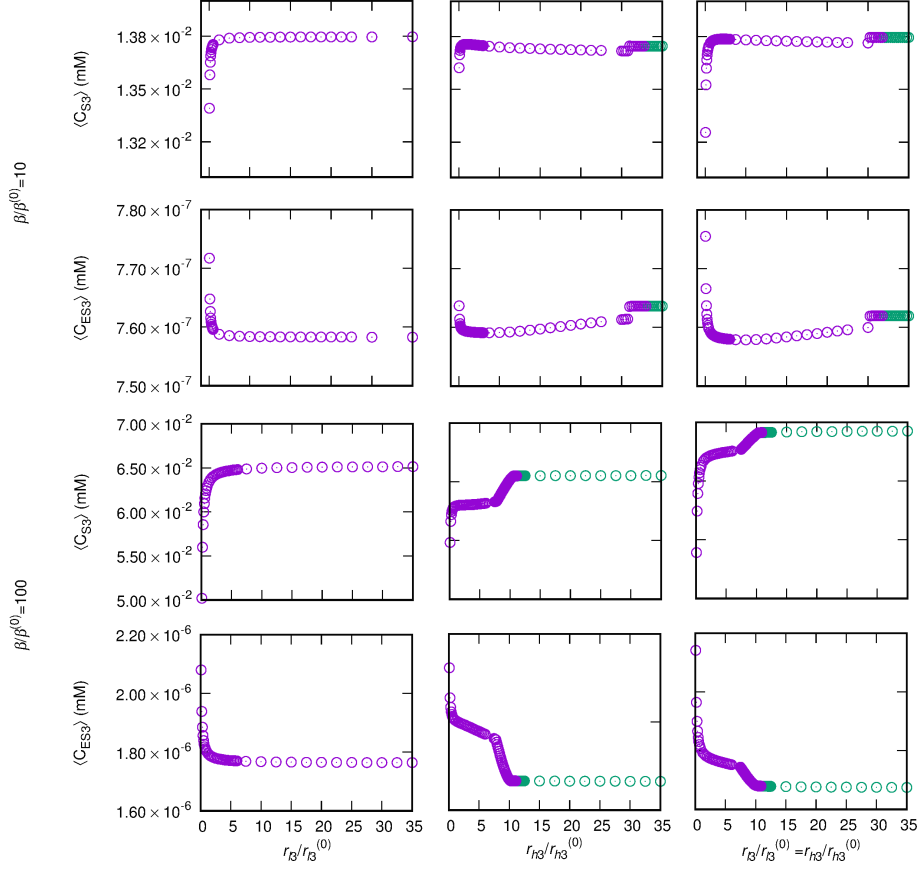


Figure 2.8: Effects of r_{l3} and r_{h3} on A β concentrations. Average intracellular A β concentration $\langle C_{S3} \rangle$ (first and third rows) and extracellular A β concentration $\langle C_{ES3} \rangle$ (second and fourth rows) at $\beta/\beta^{(0)} = 10$ (upper two rows) and $\beta/\beta^{(0)} = 100$ (lower two rows), depending upon changes of $r_{l3}/r_{l3}^{(0)}$ (first column), $r_{h3}/r_{h3}^{(0)}$ (second column), and $r_{l3}/r_{l3}^{(0)}$ and $r_{h3}/r_{h3}^{(0)}$ together (third column). At data points in purple, oscillations of A β concentrations are observed; at green data points, concentrations are stationary.

to incorporate $A\beta$ kinetics, accommodating the current working hypothesis and the experimental mechanistic studies on the relationship between autophagy activity and $A\beta$ kinetics. Such multi-compartment frameworks are especially useful for testing biological hypotheses regarding the selective autophagy including Aggrephagy (i.e., autophagic degradation of protein aggregates), Mitophagy (for mitochondria), and Xenophagy (for microbes) [82] because the model can be easily modified to incorporate new substrates for selective degradation in each compartment. This approach can be further improved by including detailed mathematical descriptions of autophagy-related cellular signaling pathways, which have been extensively explored in recent years [84, 84, 85, 86, 87].

In the examination of autophagy dynamics under normal and pathological conditions (Fig. 2.6), the autophagic fluxes and the concentrations of autophagosome and autolysosome in both early and late stage AD are significantly increased than in the basal condition. C_{g3} and C_{l3} are about ten times greater in late stage AD than in early stage AD. This implies that at the late stage AD the increased concentrations due to reduced maturation and intralysosomal hydrolysis may clog neurons, which would further reduce the autophagic $A\beta$ degradation efficacy. Under normal conditions the basal autophagy level is sufficient for removing intracellular $A\beta$ as the mTOR activity is tightly regulated. However, during early and late stage of AD, an increase in soluble $A\beta$ levels leads to mTOR hyperactivity, which should in turn suppress autophagosome formation (i.e., reduced $A\beta$ sequestration) (for details see Autophagosome formation in Mathematical model). Reduced autophagosome formation would increase further the $A\beta$ levels, creating a vicious cycle.

The influence of each autophagic step on the intracellular and the extracellular $A\beta$ concentrations (C_{S3} and C_{ES3}) was examined, providing insight into disease and potential effects of drugs targeting specific steps in the autophagic pathway. The autophagosome formation activity plays a significant role in regulating average values of C_{S3} and C_{ES3} via a log-normal relation: promoting the autophagosome formation

step decreases both $A\beta$ levels. As the autolysosome formation and intralysosomal hydrolysis rates are decreased, as expected in late stage AD, C_{S3} decreases but C_{ES3} increases. It is thus disclosed that the progress from early to late stage AD leads to higher C_{ES3} levels, which could contribute to the deposition of extracellular plaques. On the other hand, C_{S3} decreases along the pathway to late stage AD (i.e., autophagic $A\beta$ degradation is defective in addition to the increased $A\beta$ generation).

The model successfully reproduced the oscillatory behavior of autophagy activity concerning the autophagy-related fluxes and the concentrations of $A\beta$, autophagosome, and autolysosome (Figs. 2.2-6). Such simulated “autophagy oscillations” are qualitatively similar to those observed via biological experiments [88, 89, 90, 91, 94, 93, 94, 95, 96, 97]. However, mechanisms underlying the phenomena have only begun to be explored [96, 97, 98]; the oscillations may be tightly controlled via the autophagy-related signaling pathways to keep the autophagy activity within physiological levels that is important for cellular homeostasis. The simulations presented here exhibit two interesting features: 1) In the early and late-stage AD asymmetric oscillating patterns of C_{S3} and C_{ES3} are exhibited, while symmetrical patterns were seen under the basal condition. 2) Above certain activity levels of autolysosome formation (r_{l3}) and intralysosomal hydrolysis (r_{h3}) for $A\beta$, the oscillations of proteins (C_{S1} , C_{S2} , C_{S3} , and C_{ES3}), ATP (C_A), and amino acids (C_a) disappear.

These findings are expected to be useful for the design of future studies and may give insight to maintaining physiological regulation of the $A\beta$ levels. Defects arising in different steps of the autophagy process would influence in a different way the $A\beta$ kinetics, which will give rise to distinct AD pathology. This suggests that pharmacological modulations of the different autophagy steps may have different implications for AD therapy and prevention.

There is much room for refinement of the model. While the current model describes autophagy in the general neuron, for a more complete picture of the role of autophagy in neurodegenerative disorders, cell type-specific modeling must be done.

Different types of neurons may respond differently to stress. Moreover, non-neuronal cells such as microglia cells and astrocytes may have drastically different autophagic responses to stress compared to neurons, and they may play a crucial role in pathology [99]. Microglia in particular can contribute to A β clearance by digesting extracellular A β via endocytosis, and an impaired microglial response may be a factor in AD [100]. A complete picture of the effects of autophagy on A β levels will thus include such factors. We leave this to a future study.

Chapter 3

Aggregation of amyloid- β peptides in Alzheimer's disease

3.1 Background

Although Alzheimer's disease (AD) has many contributing factors, the amyloid hypothesis currently stands as the dominant model of AD pathogenesis [101, 102, 21, 22, 23]. According to this model, the key initiating event in AD is the aggregation of the amyloid- β peptide ($A\beta$), a naturally occurring peptide consisting of 36 to 43 amino acids generated from proteolytic cleavage of the amyloid precursor protein (APP). AD-causing mutations in APP and in presenilins 1 and 2 alter the active cleavage sites of APP, elevating the relative levels of the more aggregate-prone species $A\beta_{42}$ [103, 104, 105]. The apolipoprotein E (ApoE) $\epsilon 4$ allele, the strongest known genetic risk factor for AD [106], exhibits an increase in amyloid plaques and deposits [107, 108], likely due to chronically impaired $A\beta$ clearance [109]. ABCA7, a more recently found risk factor [110], has also been shown to be involved in $A\beta$ clearance [111]. $A\beta$ dyshomeostasis and its subsequent aggregation is thus a central process in AD, and understanding the precise aggregation features of $A\beta$ is important in identifying therapeutic targets.

A large part of the difficulty in studying the precise pathological mechanisms of $A\beta$ is its diverse structure [112]. The AD-relevant $A\beta_{42}$ is more hydrophobic and aggregate prone compared to $A\beta_{40}$ and forms soluble oligomers through a distinct pathway [113]. While the highly ordered fibrillar structures were thought to be necessary for amyloid toxicity, mounting evidence points towards soluble oligomers as the primary toxic species [114, 53]. $A\beta_{42}$ oligomers can lead to a decrease in synapse density and cause memory loss [115, 116]. Plaque cores isolated from AD brains and washed do not impair long term potentiation, but the diffusible $A\beta_{42}$ oligomers that are released from them do [117]. A separate study has also shown that plaques have a penumbra of soluble $A\beta$ oligomers in which the synaptic density is low [118]. While the plaque sizes do not seem to change over time [119], plaque-associated toxicity has also been shown to increase over time [120]. A recent study of the nanoscale structure of amyloid plaques also found a higher concentration of soluble oligomers around plaques of autosomal dominant AD patients [121].

In systems containing elements across multiple length scales, size distributions contain information about the underlying formation process [122, 25]. *In vitro* studies of oligomer size distributions have reported skewed distributions, sometimes fit to log-normal curves [113, 24]. Interestingly, skewed size distributions in large plaques in post mortem brains also exhibit a skewed distribution [123, 119]. Mouse models also exhibit skewed plaque size distributions [124].

The previous chapter examined the relation between the autophagy process of a generic neuron and the secretion of $A\beta$ into the extracellular space. This chapter seeks to characterize the aggregation of $A\beta$ into oligomers by modeling the size distribution of aggregates.

3.2 Merging model

We define the size distribution function $f(x, t)$, defined as the concentration of oligomers of size x at time t . The time evolution of $f(x, t)$ is given by

$$\begin{aligned} \frac{df(x; t)}{dt} = & [R_{sec}(g(t))g(t) - R_{clr}(f(1; t))f(1; t)]\delta(x - 1) \\ & + \sum_{\alpha} \left[-\lambda(\alpha, x)f(x; t) - \frac{\lambda(\alpha, x)}{\alpha - 1} f\left(\frac{x}{\alpha - 1}; t\right) + \frac{\lambda(\alpha, x/\alpha)}{\alpha} f\left(\frac{x}{\alpha}; t\right) \right] \\ & + \sum_{\beta} \left[-r(\beta, x)f(x; t) + \frac{r(\beta, x/(\beta - 1))}{\beta - 1} f\left(\frac{x}{\beta - 1}; t\right) + \frac{r(\beta, x/\beta)}{\beta} f\left(\frac{x}{\beta}; t\right) \right] \end{aligned} \quad (3.1)$$

Here R_{sec} is the secretion rate of $A\beta$ into the extracellular space, R_{clr} is the clearance from the extracellular space, $\lambda(\alpha, x)$ is the merging rate of polymers of size x with those of size $(\alpha - 1)x$. The summation is over all α such that αx spans all positive integers (in numerical integrations, up to some maximum size N_{max}). $r(\beta, x)$ is the disassociation rate from polymers of sizes x to sizes of βx and $(1 - \beta)x$.

$$\begin{aligned} \lambda(\alpha, x) &= \lambda_0 e^{-(\alpha-1)x/A} \\ r &= r_0 e^{B(\beta-1)} \end{aligned} \quad (3.2)$$

We first consider the case in which we begin with a solution of only monomers, and observe their aggregation. We assume negligible disassociation rate $r(\beta, x) = 0$ and no secretion or clearance, hence having

$$\frac{df(x; t)}{dt} = \sum_{\alpha} \left[-\lambda(\alpha, x)f(x; t) - \frac{\lambda(\alpha, x)}{\alpha - 1} f\left(\frac{x}{\alpha - 1}; t\right) + \frac{\lambda(\alpha, x/\alpha)}{\alpha} f\left(\frac{x}{\alpha}; t\right) \right]$$

With initial condition $f(x, t = 0) = c\delta(x - 1)$. The rate constants are set to $\lambda_0 = 0.01$ mM/h, $r_0 = 0.1$ mM/h, $A = 20.0$ mM, $B = 20.0$ (Table 3.1). This results in the distribution described in Figure 1.

The figure also shows fits of the Weibull and lognormal distributions to the numerical solution. The log-normal fit parameters are $\mu = 4.4662 \pm 0.0002$, $\sigma =$

Parameter	Description	Value
λ_0	rate of association	0.01 nM/h
A	exponential factor of association	0.01 nM/h
r_0	rate of disassociation	0.0 nM/h
B	exponential factor of disassociation	0.0 nM/h
x_n	fibril nucleus size	6
c_n	”critical concentration”	90nM

Table 3.1: Table of A β aggregation model parameters.

0.5026 ± 0.0002 . The log-normal distribution is given by

$$f(x) = \frac{A}{x\sigma\sqrt{2\pi}} e^{-(\log x - \mu)^2/\sigma^2} \quad (3.3)$$

We find that the merging/disassociation model gives rise to a distribution very close to a log-normal distribution, as found in [24]. This model is structurally similar to the binary fission model [25], which in the simplest case results in a Weibull distribution. Interestingly, the addition of multiple ratios b and β , along with the exponential forms in Eq. 3.2, result in a distribution closer to the log-normal distribution. The log-normal distribution also emerges from a self-replicating growth process.

3.3 Toxicity of aggregate size distributions

Recent studies suggest that the toxic amyloid species are middle-sized oligomers. Figure 3.2 shows the resulting distribution after 10 years of monomers secreted by a neuronal cell as established in chapter 2. The magenta points indicate basal autophagy rates. The red points indicate early AD, while the blue indicate late AD. We observe a slight shift towards larger oligomers in late AD compared to early AD, and a significant shift towards larger species for both early and late AD when compared with the basal levels.

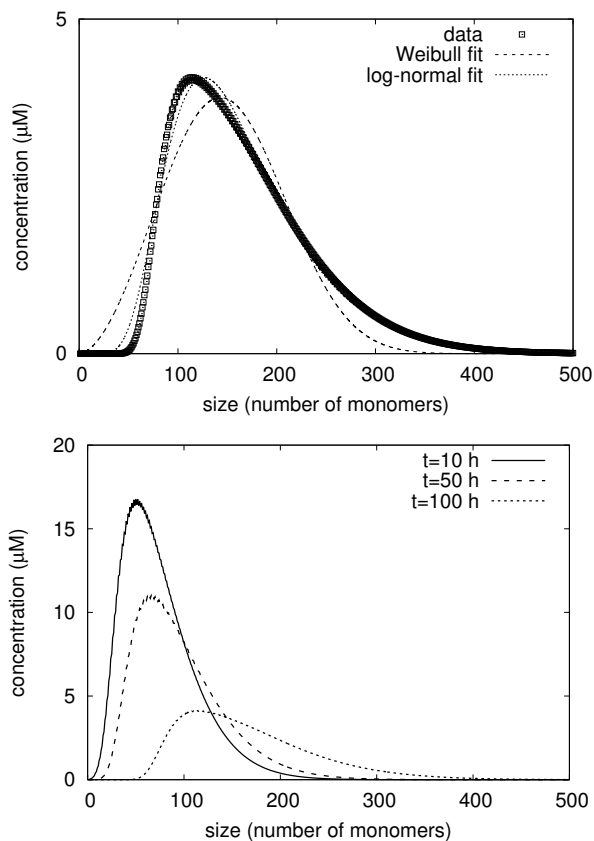


Figure 3.1: Numerical solution of model in equations 1 and 2, along with Weibull and log-normal curve fits (left). Data curves of solutions at times $t = 10, 50, 100$ hs (right).

When autophagy is induced during this time, we have the distribution plotted in green Figure 3.3. This exhibits a significant shift towards small, non-toxic oligomeric species. This indicates the potential clinical effects of autophagy induction in reducing $A\beta_{42}$ buildup.

3.4 Size distribution of plaques

The merging model was fit to *in vitro* data and describes oligomer formation. This resulted in a log-normal distribution, as found in experiments. $A\beta$ oligomers and fibrils

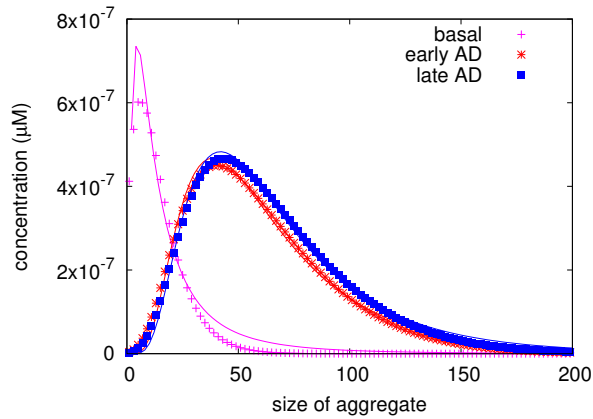


Figure 3.2: Size distribution of a monomer population after ten years in basal, early AD, and late AD conditions.

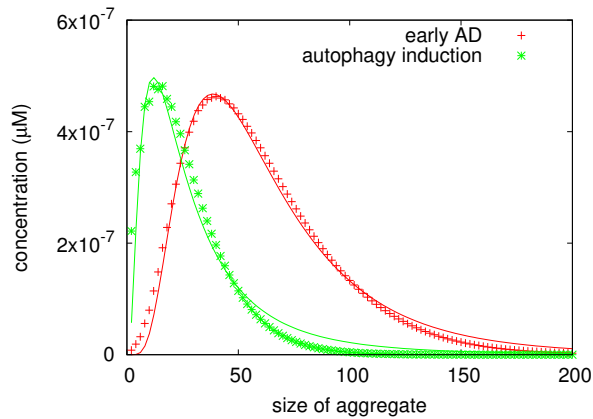


Figure 3.3: Autophagy shifts the distribution away from the toxic species.

further aggregate into plaques, dense macroscopic structures composed of entangled fibrils and oligomers.

Here we use Equation (3.1) to mimic an *in vivo* situation in which there is $A\beta$ secretion and clearance. The delta function in the first line of Eq. (3.1) indicates that only monomers are subject to secretion and clearance. It should be noted that in reality, oligomers up to a certain size can be subject to clearance by proteolysis or microglial

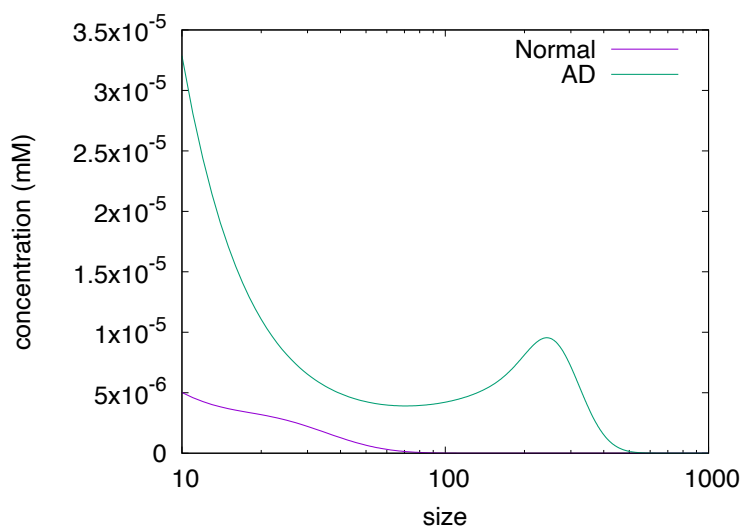


Figure 3.4: Effect of higher $A\beta$ production on size distribution of aggregates after ten years. Magenta indicates the normal rate, while green indicates AD. The size is in arbitrary units.

endocytosis. However, aggregates beyond a certain size are no longer able to be removed. The current model serves as a first approximation of such a situation.

We assume that $A\beta$ secretion and clearance levels are such that $f(1, t)$ is constant, with the value 0.00019 mM in the basal case and 0.0022 mM in AD with higher $A\beta$ production, according to the results of the previous chapter. The results are shown in Figure (3.4). Here we see a log-normal-like peak in the higher sizes superposed with decaying curve starting from the monomer population.

3.5 Discussion: Towards a multi-scale model of Alzheimer's disease

Despite great efforts to treat Alzheimer's disease by targeting $A\beta$ aggregation, such therapeutic methods have seen limited efficacy [129]. This has led to some researchers to turn to other targets. While it is important to explore other avenues treatment, our understanding of the effects of $A\beta$ is incomplete, and gaining a better understanding of $A\beta$ aggregation could lead to new ways to target aggregation.

While preliminary, the results of this chapter provides a starting point to quantitatively model the aggregation of $A\beta$ into oligomers and further on into plaques. The form of Figure (3.4) represents a complete size distribution including oligomers and larger aggregates, albeit with a simplified model. Future studies should used data from *in vivo* samples that analyze the size distribution more completely than found in previous studies, which focus either on oligomers or plaques and rarely both.

Future work will also seek to perform Monte Carlo simulations of aggregation. While the current merging model can compute size distributions, it does not contain information about aggregate morphology. Simulations can reveal how microscopic aggregation mechanics lead to the range of structures seen in postmortem histology data (e.g. diffuse plaques, dense core plaques, etc.).

Chapter 4

Disruption of the circadian rhythm and recovery via light treatment

4.1 Background

As a result of the 24 hour light-dark cycle of the earth, organisms have evolved to have biological oscillations that are collectively termed circadian rhythms [130]. In the case of mammals, the suprachiasmatic nucleus (SCN), located in the hypothalamus, orchestrates these circadian rhythms, playing the role of a central pacemaker [26]. The SCN has an intrinsic cycle of near-24 hours with some individual variation. It gives various cues throughout the brain, acting as a master clock.

The evolutionary advantage of the circadian pacemaker is its ability to allow the body to anticipate periodic events of the environment. While period of the SCN is not exactly 24 hours, it adjusts its phase in response to the environment, becoming entrained to the daily cycle in normal circumstances. While entrainment can be due to multiple environmental cues, one of the most significant ones is the light-dark cycle. Information on light intensity is transmitted via the retinohypothalamic tract to the SCN [132, 133]. With a strong enough light-dark cycle, the SCN is locked to the 24-h cycle of the environment, ensuring that we are active during the day and at rest during

the night [134, 135]. One of the most significant ways in which the SCN regulates the body is surely its influence on the sleep-wake cycle. The SCN applies increasing sleep pressure as the clock approaches subjective night [131]. The monoamine nucleus (MA), ventrolateral preoptic nucleus (VLPO), homeostatic (H) regulators including adenosine, and orexergic (ORX) neurons along with the SCN interact to consolidate a stable 24-hour sleep-wake cycle [136, 137, 138, 139, 131].

The SCN may, however, fail to be entrained to the environment. This often coincides with sleep disorders [27]. When the SCN is desynchronized with the environment, one may experience drowsiness during the day and sleeplessness during the night. These sleep disorders are associated with psychiatric disorders such as depression [28] and bipolar disorder [29], as well as neurodegenerative disorders such as Alzheimer's disease [30]. In all of these cases, the causal relation is not clear. In order to model the phenomenon of circadian entrainment and how it may fail, we model the brain at a macroscopic scale. We consider the essential regions of the brain involved in the regulation of the sleep-wake cycle and circadian rhythm, and quantitatively model their interactions with physiological evidence. Indeed, for centuries such mathematical models for sleep-wake dynamics have accompanied experimental discoveries [140, 141, 142]. For our purposes, we borrow the framework of the Phillips-Robinson (PR) model [143, 144], which models the sleep-wake system as a flip-flop switch between mutually inhibiting neuronal populations [138]. The PR model has been used to successfully describe the main features of sleep, and can be fit to quantitative observations. Previous studies have examined responses of the model to external impulses [145] and noise [146]. The model has been extended to study specific phenomena including sleep deprivation [147], caffeine [148], narcolepsy [149], and shift work [150].

In this chapter, we extend the PR model to incorporate the effects of both orexin and a circadian oscillator. We show the interdependent effects of both an imbalanced orexin level and insufficient light on the stability of the 24-h period lock. This pro-

vides a way to examine the effects of orexin and light on the circadian system together, whereas previous research has focused on the effects of just one or the other. The effects of orexin on sleep stability was examined by a previous study [149] but did not explore the question of entrainment. A circadian oscillator model was developed to study circadian dysregulation in a shift work setting, but physiological factors such as orexin were not considered [150]. This combined model allows us to examine the effects of orexin, a neurotransmitter implicated in many of the aforementioned disorders, together in and conjunction with light. We also simulate light treatment, and seek to offer a more complete picture of the efficacy of such procedures, providing insight into optimal treatment.

4.2 Model of the sleep-wake system coupled with the circadian oscillator

We base our model on the PR model [143]. At the center of the model is the flip-flop switch consisting of two mutually inhibiting neuronal populations, the VLPO and the MA. The dynamical variables V_v and V_m of the model represent the average cell body potentials of the VLPO and MA, respectively. In addition, ORX neurons are incorporated with cell potential V_o , following the previous model of narcolepsy [149]. The MA represents the ascending arousal system; when it is activated, it sustains the wake state. The VLPO's role is to measure sleep pressure and, when it is high enough, inhibit the MA, thereby causing sleep. The ORX plays a role in stabilizing the wake state by exciting the MA neurons during wake, preventing random fluctuations causing a transition into sleep. The following coupled differential equations describe their time

evolution:

$$\begin{aligned}
\tau_v \frac{dV_v}{dt} &= -V_v + \nu_{vm}Q_m + \nu_{vh}H + \nu_{vc}C + A_v \\
\tau_m \frac{dV_m}{dt} &= -V_m + \nu_{mv}Q_v + \nu_{mo}Q_o + A_m \\
\tau_o \frac{dV_o}{dt} &= -V_o + \nu_{ov}Q_v + \nu_{oc}C + A_o
\end{aligned} \tag{4.1}$$

Here, τ_j is the characteristic time of population j ($= v, m, o$) and ν_{ij} (for $i, j = v, m, o, c, h$) total strength of the connection between j to i , with its sign indicating whether it is an excitatory or inhibitory connection [151]. ν_{ij} is hence proportional to the average number of synapses from neurons of region j to neurons of region i [152]. In particular, ν_{mo} is positive; this reflects the stabilizing effect of orexin by exciting the MA, thus promoting wake. ν_{mo} , dubbed the orexin level, is interpreted to be the amount of orexin neurotransmitters in the brain.

The firing rate Q_j of population j has the form

$$Q_j = \frac{Q_{\max}}{1 + \exp[(\Theta - V_j)/\sigma]}, \tag{4.2}$$

where Q_{\max} is the maximum firing rate, Θ the mean firing threshold, and $(\pi/\sqrt{3})\sigma$ the standard deviation of the firing threshold. In Eq. (4.1), A_v , A_m , and A_o are constants while H and C denote the homeostatic sleep drive and the circadian sleep drive, respectively.

The homeostatic sleep drive H is described by

$$\chi \frac{dH}{dt} = -H + \mu_m \frac{Q_m^2}{\eta_h + Q_m^2} \tag{4.3}$$

where χ is the characteristic time of its decay. Hence, H increases during wake (when Q_m large) and decreases during sleep (when Q_m is close to zero). The second term on the right-hand side describes the saturation behavior of H for larger values of Q_m , with appropriate constants μ_m and η_h [149].

The sleep-wake switch is coupled with the SCN, which has previously been modeled with a modified van der Pol oscillator subject to photic and non-photoc influences [153]. A previous work combined this with the PR model to study adaptation to

shift work [150]. The equations for the circadian oscillator are

$$\begin{aligned}\frac{1}{\Omega} \frac{dx}{dt} &= x_c + \gamma \left(\frac{1}{3}x + \frac{4}{3}x^3 - \frac{256}{105}x^7 \right) + B + N_s \\ \frac{1}{\Omega} \frac{dx_c}{dt} &= qBx_c - x (\delta^2 + kB),\end{aligned}\quad (4.4)$$

which can be derived via the Liénard transformation of the Van der Pol equation [153]. Here x is the component directly related to the circadian sleep drive while x_c is a complementary variable. Their ratio gives the circadian phase ϕ_x according to the formula $\tan \phi_x = x/x_c$. Ω , the characteristic frequency, scales the equation to the 24-hour period. γ is the oscillator's stiffness constant while q and k are constants modulating the strength of the effect of light via B . Finally, δ represents the intrinsic period of the oscillator relative to 24 hours. We here set the intrinsic circadian period to 24.2 h [154], or $\delta = (24 \times 3600)/(24.2 \times 3600 \times 0.997) = 0.994$, where the correction factor 0.997 accounts for the nonlinearity of the oscillator.

The sleep drive C is defined simply to be $C = x$ while the photic and non-photoc influences B and N_s on the circadian oscillator are

$$\begin{aligned}B &= G\alpha(1-n)(1-\epsilon x)(1-\epsilon x_c) \\ N_s &= \rho \left(\frac{1}{3} - s \right) [1 - \tanh(rx)].\end{aligned}\quad (4.5)$$

Here G , ϵ , and r are constants and dynamical variable n is the fraction of photoreceptor cells that are activated. The first equation in Eq. 4.5 characterizes the varying sensitivity of the circadian oscillator to light throughout a day. Here ρ is the rate constant while s is a binary state variable indicating wake ($s = 1$) or sleep ($s = 0$). Hence $s = \theta(V_m - V_m^{th})$, where θ is the Heavyside step function and $V_m^{th} = -2$ mV is the threshold mean potential above which the system is defined to be in the waking state.

The rate of conversion of the photoreceptors from the ready to the activated state is given by

$$\frac{dn}{dt} = \alpha(1-n) - \beta n \quad (4.6)$$

where I is the light intensity and

$$\alpha = \alpha_0 \left(\frac{I}{I_0} \right)^p \frac{I}{I + I_1}, \quad (4.7)$$

where β is the rate of conversion from the activated state to the ready state. The form of α and constants α_0 , I_0 , I_1 , and p are borrowed from [153], in which they were calibrated to fit the intensity response curve in a wide range of intensities. At low intensities, α increases with the light intensity in proportion to $I^{3/2}$, and at intensities much higher than I_1 it does in proportion to $I^{1/2}$. The light intensity $I(t)$ affecting the photoreceptor cells is a function of the environmental light $\tilde{I}(t)$ along with the gating effect:

$$I(t) = s\tilde{I}(t). \quad (4.8)$$

The photic driving force is thus gated by the sleep-wake state. The tilde sign on \tilde{I} will henceforth be omitted for simplicity.

It should be noted that Eqs. (4.4) to (4.8) are not present in Ref. [149], which assumed a fixed sinusoidal sleep drive C . This is reasonable when modeling narcolepsy, a state of unstable sleep-wake patterns. The purpose of the current model is to probe the effects of orexin on a different kind of instability, circadian disruption, and hence the addition of a circadian oscillator is necessary. The oscillator model adopted accurately describes the human phase-response curve to light [153], and we have found that the phase-response curve remains nearly unchanged in the integrated model. The above model is illustrated schematically in Fig. 4.1, which exhibits the components of the model and interconnections between them.

Nominal Parameters and Light Input

Table 1 displays the nominal parameters of the model. We have taken parameters involving the sleep-wake switch and homeostatic sleep drive from Ref. [149] and those involving the circadian oscillator from Ref. [150], with a few adjustments, e.g. $\chi = 40$ h to produce a stable 8-hour daily sleep bout with the 24-hour period.

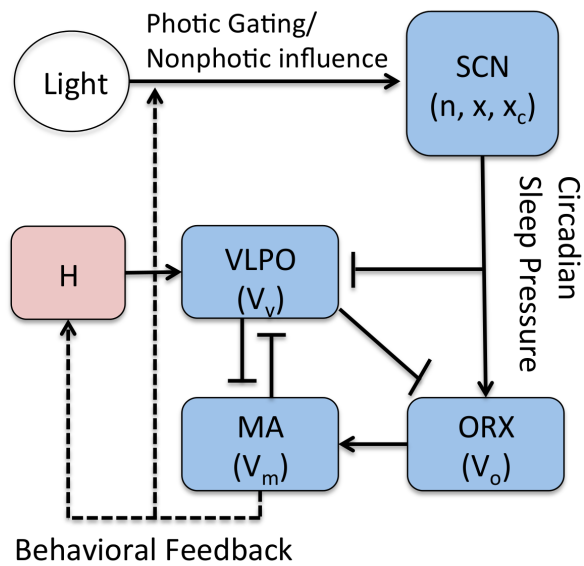


Figure 4.1: Schematic diagram of the connections between components of the model. Pointed-ends represent excitatory connections, while flat-ends represent inhibitory connections.

Sleep-Wake Switch			Circadian Pacemaker		
Parameters	Values	Units	Parameters	Values	Units
Q_{max}	100.00	s^{-1}	Ω	7.2722×10^{-5}	s^{-1}
Θ	10.000	mV	γ	0.13000	—
σ	3.000	mV	q	0.60000	—
ν_{vm}	-2.1000	mVs	k	0.51000	—
ν_{mv}	-1.8000	mVs	δ	0.9944	—
ν_{vc}	-0.3000	mV	β	0.0070000	s^{-1}
ν_{vh}	1.0000	mV	α_0	0.100000	s^{-1}
ν_{oc}	1.0000	mV	p	0.5	—
ν_{mo}	0.30000	mVs	I_0	9500	lux
ν_{ov}	-1.0000	mVs	I_1	100	lux
τ_v, τ_m	10	s	G	2220.0	s
τ_o	120	s	ρ	0.032000	—
χ	40.000	h	ϵ	0.40000	—
μ_m	17.000	—	r	10.000	—
η_h	2.3000	s^{-2}	I_d	600	lux
A_v	-8.5000	mV	I_n	150	lux
A_m	0.52000	mV	T_d	11.000	h
A_o	1.0000	mV			

Table 4.1: Nominal parameter values of the sleep-wake model.

The environmental light is described by a simple square wave,

$$I(t) = \begin{cases} I_d & \text{for } 12 \text{ h} - T_d/2 \leq t^* < 12 \text{ h} + T_d/2 \\ I_n & \text{otherwise,} \end{cases} \quad (4.9)$$

where t^* is defined to be t modulo 24 h and corresponds to the day time. $I(t)$ is given by a 24 h-periodic square function with T_d hours of daylight of intensity I_d and $24 - T_d$ hours of dim light of intensity I_n . The dynamical equations then exhibit periodic oscillations, corresponding to the 24-hour day-night cycle. For our nominal parameter set, we select $I_d = 600$ lux, $I_n = 150$ lux, and $T_d = 11$ h (see Table 4.1).

Figure 4.2 exhibits the resulting oscillations of the seven dynamical variables: the fraction n of activated photoreceptor cells, circadian oscillator variables x and x_c ,

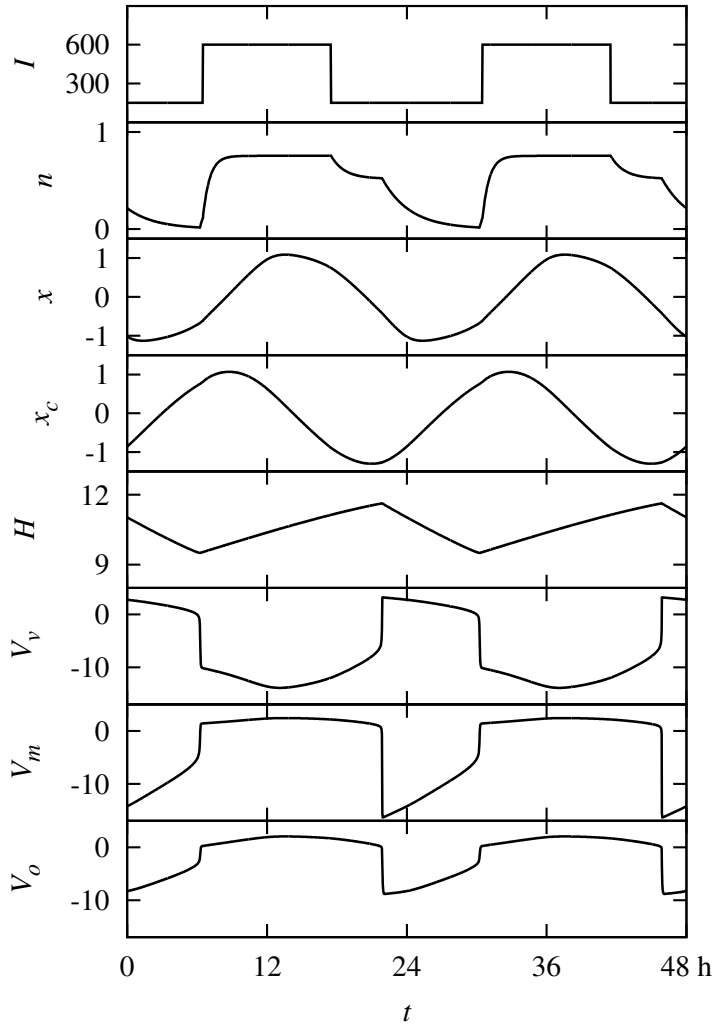


Figure 4.2: Limit-cycle dynamics of the model for nominal parameters, plotted for 48 h. Entrainment due to the light input I (in units of lux) is exhibited as seen in the period-locked oscillations of cell potentials V_v , V_m , and V_o (in units of mV) as well as the seven dynamical variables n , x , x_c , and H (unitless).

sleep drive H , and cell potentials V_v , V_m , and V_o of VLPO, MA, and ORX neurons, respectively, are plotted, together with the input light intensity I .

The circadian phase is related to the core body temperature (CBT) minimum via [153]

$$t_{\text{CBT},i} = t_{\phi,i} + t_d, \quad (4.10)$$

where $t_{\text{CBT},i}$ is the time of the CBT minimum on the i th day and $t_{\phi,i}$ is the time at which the circadian phase takes the value $\phi_x = -170.7^\circ$ on the same day i . The time lag between the two is given by $t_d = 0.97$ h. We then define the average phase shift between CBT minima of successive days to be

$$\Delta \equiv \frac{1}{N-1} \sum_{i=1}^{N-1} [t_{\text{CBT},i+1} - t_{\text{CBT},i}], \quad (4.11)$$

where N is the number of days under calculation.

4.3 Period Locking Zone

We now study the dynamics of the model by means of simulations, employing the 4th-order Runge-Kutta method. Numerical integration of the equations describing the model with the nominal parameters in Table 1 results in a stable 24-hour limit cycle, which is interpreted as successful light entrainment: The circadian oscillator is coupled well to the light Zeitgeber, via the term B in Eq. (4.4), and the circadian oscillator in turn fixes the sleep-wake cycle [Eq. (1)], so that sleep occurs during the dark phase and wake occurs during the light phase.

Performing simulations in the absence of light ($I_d = I_n = 0$), we find that the system exhibits a limit cycle with a period of 24 hours and 22 minutes. Hence if the strength of light is weakened, the intrinsic period of the system will overcome the effects of light and there will be a constant phase delay. The critical daylight intensity at which the stable state disappears corresponds to the period-locking bifurcation point.

On the other hand, when the orexin level ν_{mo} is varied, this intrinsic period is altered by the change in the phase and length of the non-photoc influence N_s : A higher

values of ν_{mo} leads to a longer period. This is an alternate way in which stability can disappear.

We carry out simulations of the model using a range of values of ν_{mo} and I_d . To be specific, we sweep the ν_{mo} - I_d parameter space, and take values of ν_{mo} ranging from 0.2 mV s to 0.35 mV s with increments of 0.0002 mV s and of I_d from 150 to 16,000 lux with increments of 10 lux. For each pair of parameters, simulations have been performed for the duration of 60 weeks, of which the data for the first 20 weeks are discarded for equilibration. Accordingly, the average phase shift Δ in Eq. (4.11) is obtained via averaging over the last 40 weeks (i.e., $N = 280$ days). The resulting heatmap plot of the phase shift Δ is given in Fig. 4.3a. The red region indicates the period-locked zone, where no phase shift arises ($\Delta = 0$).

The boundaries of this zone are depicted in Fig. 4.3(b) for two different values of daytime duration T_d . When the total exposure to bright light is low as in winter ($T_d = 9$ h), the stability region is observed to be reduced appreciably. On the other hand, extended duration of daytime ($T_d = 11$ h) tends to widen the stable region.

Figure 4.3 manifests that there are three routes to the loss of the 24-h period: (1) by decreasing the daytime duration T_d , which shrinks the area of the period-locked zone; (2) by lowering the daylight intensity I_d , which amounts to moving left on the ν_{mo} - I_d parameter plane; and (3) by changing ν_{mo} , which corresponds to moving up or down on the parameter plane.

The sleep-wake system maintains a stable 24-hour cycle by means of its phase-resetting response to light. When daylight is insufficient, the photic driving force is not enough for entrainment to occur. This is the case in routes (1) and (2) above. However, route (3) shows that an imbalance in orexinergic neurons can cause circadian disruption even when daylight is typically sufficient. The mechanism by which this occurs is due to the wake-promoting nature of ORX. When ν_{mo} is increased, sleep and wake onset times are delayed with respect to the phase of the circadian oscillator. Due to the gating effects present in the photic drive B , this causes more light to enter

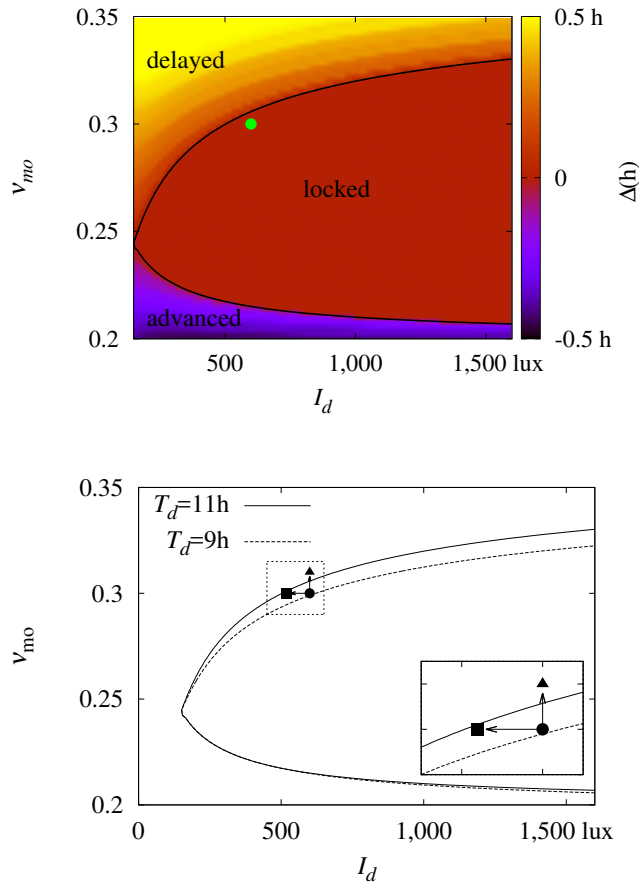


Figure 4.3: (a) Δ (average shift of the CBT minimum) obtained via simulations with $T_d = 11$ h, in the ν_{mo} - I_d parameter space. (b) Period-locking zone boundaries for $T_d = 9$ h and 11 h. Circle indicates the point representing normal conditions, square indicates seasonal disorder, and triangle indicates non-seasonal disorder. The arrows indicate shifts from the normal state to the disordered states. Note that in simulations the shift to seasonal disorder (leftward arrow) is accompanied by a change in T_d from 11 h to 9 h. The area enclosed in the the dotted box is enlarged in the inset.

the system at subjective night and less to enter in the subjective morning. The human phase response curve is such that morning light causes phase advance and evening light causes delay. In consequence the increase in ORX causes phase delay. Similar effects are observed when a constant excitatory stimulation term is added to ORX; this may be achieved simply by increasing the constant A_o .

4.4 Diseased States and Light Treatment

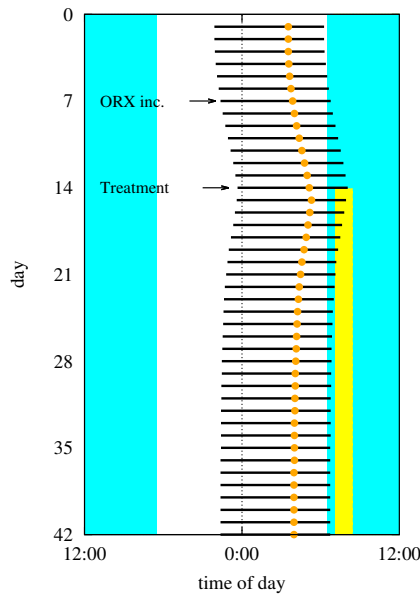


Figure 4.4: Simulations of non-seasonal affective disorder: black lines indicate daily sleep times and colored dots indicate CBT minima. On day 7, ORX is increased, as indicated by an arrow, causing instability. Morning light treatment of 10,000 lux for 1.5 hour daily is administered starting on day 14, also indicated by an arrow. Periods of light treatment are labeled yellow. Note the gradual return to normal phase.

The above results show that both lack of daylight and high orexin levels can cause destabilization in the timing of the onset of sleep. The former is thought to be the case

in seasonal affective disorder while the latter is regarded as a possible mechanism for non-seasonal affective disorder. Here we examine the effects of light treatment on such diseased states.

We first simulate bright light treatment in the case of insufficient light, which consists in artificial exposure to strong white light for a short time (e.g., 1.5 h). Simulations begin in the limit cycle of the model with nominal parameters; then the daylight length T_d and intensity I_d are reduced linearly, from 11 to 9 hours and from 600 to 520 lux, respectively. This is intended to simulate a rapid change into winter light conditions, inducing circadian phase shifts to become increasingly misaligned with the light input.

We then consider the treatment by applying light of intensity I_{tr} in addition to the underlying (environmental) light in Eq. (4.9). During four days into full winter, light treatment is applied daily by taking $I_{tr} = 10,000$ lux for an hour and half each day. Light treatment protocols vary across studies; here the intensity and duration of light has been adopted from the study of light treatment as an antidepressant [155]. Treatment begins at time t_0 of each day, which we set to 7 am unless stated otherwise. If the time t_{CBT} of the CBT minimum drifts towards a stable time within an hour from its initial value, we consider the system to be recovered.

In winter simulations, the wake onset time is retarded under the winter conditions and becomes desynchronized with light in the absence of light treatment. When light treatment is applied, the wake onset is advanced from the delayed phase and settles into the value near its initial phase of 10 pm, indicating recovery.

Next, we simulate a diseased state under normal light circumstances, where the instability is caused by an abnormal value of ν_{mo} . We see in Fig. 4.3 that there are two ways in which this can happen: one by a large value of ν_{mo} , where sleep timing is constantly delayed, and the other by a low value of ν_{mo} , where sleep is advanced. Here we illustrate the former case only.

Figure 4.4 presents the result of the non-seasonal case. Starting on day 10, we raise ν_{mo} from 0.3 to 0.31 mV s, which lies above the stable zone in Fig. 4.3(a), while keep-

ing I_d and T_d in their nominal values. As in the seasonal case, stability is restored when light treatment is applied and the system returns to a normal sleep-wake cycle. Thus the model shows that light treatment has stabilizing effects even when the instability does not arise from the lack of environmental light.

Optimal Light Treatment Times

We now explore how the efficacy of bright light treatment depends on the timing of treatment. Figure 4.5(a) demonstrates the sensitive dependence of the recovery time t_r , i.e., the time duration of treatment required for a return to the initial phase, on the beginning time t_0 of light treatment in the case of non-seasonal depression, for two values of ν_{mo} . Note that in the case of $\nu_{mo} = 0.31$ mV s, recovery occurs in the two limits of the treatment timing: one in the morning and the other in the afternoon. When $\nu_{mo} = 0.315$ mV s, the recovery time for morning recovery is increased while afternoon recovery ceases to work.

It is suggested in Fig. 4.5(a) that in the case of phase-delay instability, both morning and evening bright light treatments are effective although morning treatment will be efficacious in a larger range of parameters. To make clear the difference in the efficacy between morning and afternoon treatments, we select two representative values of t_0 corresponding to morning ($t_0 = 7:00$) and afternoon ($t_0 = 15:00$) treatments. For each treatment time, we calculate the light treatment intensity I_{tr} at which recovery occurs for varying orexin levels.

This leads to a phase diagram on the $I_{tr}-\nu_{mo}$ plane, which is shown in Fig. 4.5(b). It is observed that for all values of ν_{mo} , the required treatment intensity is much larger for afternoon treatment. It is also observed that the required treatment intensity I_{tr} grows rapidly with ν_{mo} . Specifically, at $\nu_{mo} = 0.32$ mV s, the intensity I_{tr} becomes unrealistically large, indicating that only morning treatment is feasible. As ν_{mo} is increased further, e.g., to $\nu_{mo} = 0.34$ mV s, this light treatment scheme becomes unfeasible at any intensity.

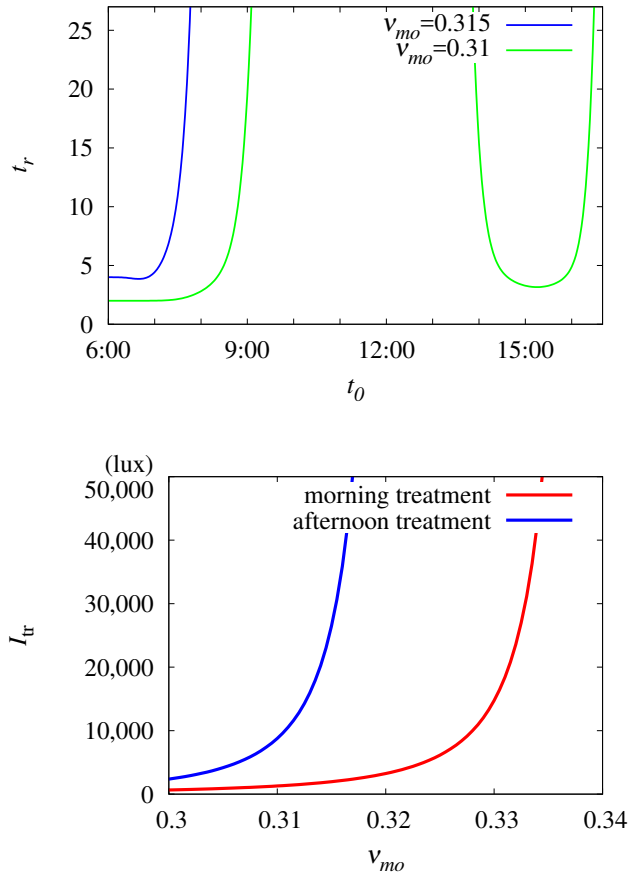


Figure 4.5: (a) Recovery time t_r (in days) versus treatment timing t_0 . t_r indicates the number of days of treatment required for recovery from the circadian instability caused by orexinergic imbalance. Plotted for two values of ν_{mo} . Interpolation has been used to produce a smooth curve. (b) I_{tr} - ν_{mo} phase diagram for morning treatment ($t_0 = 7$ am) and afternoon treatment ($t_0 = 3$ pm). Recover occurs above the curves.

Effects of Noise

Noise is an important aspect of a realistic biological system. Here we consider the effects of noise by modifying the VLPO and MA equations of Eq. (4.1) in the following way:

$$\begin{aligned}\tau_v \frac{dV_v}{dt} &= -V_v + \nu_{vm}Q_m + \nu_{vh}H + \nu_{vc}C + A_v + D\xi_v(t), \\ \tau_m \frac{dV_m}{dt} &= -V_m + \nu_{mv}Q_v + \nu_{mo}Q_o + A_m + D\xi_m(t),\end{aligned}\quad (4.12)$$

where the added terms ξ_j ($j = v, m$) are Gaussian white noise characterized by $\langle \xi_j(t) \rangle = 0$ and $\langle \xi_j(t)\xi_j(t') \rangle = \delta(t - t')$ with noise strength D . Following existing studies [149, 156], we choose not to add noise to the ORX equation; we expect that doing so would bring additional noise in the MA neurons and not affect significantly the results.

Starting from the periodic solution, we perform simulations for 90 days, so as for the circadian system to settle possibly into its new equilibrium. We then simulate additional 40 days and observe whether circadian phase shifts occur. This process is repeated 50 times with new random seeds. Initially, the noise level is taken to be $D = 0.01$ mV, and the entire process is repeated with D increased in increments of 0.01 mV.

Figure 4.6(a) shows the distribution of the CBT minimum time $t_{\text{CBT},i}$ over the last 40 days of simulations for the range of D considered. It is observed that the circadian phase shifts to earlier timings as the noise level is increased. Moreover, noise tends to provoke the CBT timing (specified by $t_{\text{CBT},i}$) to spread: For instance, the standard deviation of $t_{\text{CBT},i}$ takes the value of about 7 minutes at $D = 0.1$ mV. When the noise level is low ($D < 0.21$ mV), the system settles into a new equilibrium within 90 days and the distribution of $t_{\text{CBT},i}$ does not change significantly over the next 40 days. In other words, periodicity, albeit fluctuating, is preserved. At $D = 0.21$ mV, however, there appears a slight advance, which, for $D > 0.21$ mV, increases substantially; this indicates that circadian disruption occurs at $D = 0.21 \pm 0.01$ mV. When D is increased

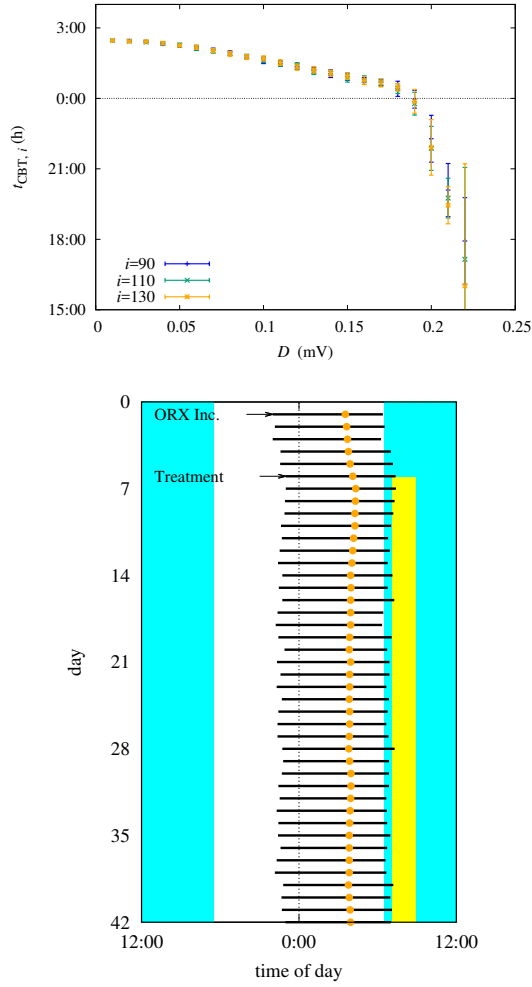


Figure 4.6: (a) Core body temperature minimum time $t_{CBT,i}$ versus noise level D , obtained from simulations. The averages and standard deviations are plotted for the 90th, 110th, and 130th days (blue, green, orange) for $D = 0.01$ mV to 0.25 mV. (b) Light treatment simulations for $\nu_{mo} = 0.33$ mV s, treatment time $t_0 = 7:00$, and $I_{tr} = 10,000$ lux, in the presence of noise $D = 0.1$ mV. As in the case without noise, recovery to the normal phase is observed.

further to the order of 1 mV, noise dominates the sleep-wake switch and drives the system to switch erratically between sleep and wake.

Due to the phase advance effect described above, we expect the stability landscape of Fig. 4.6(a) to change with the introduction of noise. Setting $D = 0.1$ mV, we perform simulations with ν_{mo} varied about its nominal value in increments of 0.001 mV s, and find that circadian entrainment occurs in the range $0.244 \text{ mV s} \leq \nu_{mo} \leq 0.321 \text{ mV s}$, below/above which continuous phase advance/delay is observed. This range is to be compared with that in the absence of noise ($D = 0$ mV), namely, $0.229 \text{ mV s} \leq \nu_{mo} \leq 0.305 \text{ mV s}$. Such a shift of the stability region toward higher orexin levels indicates that the addition of noise offsets some of the phase-delaying effects of orexin. Finally, we simulate morning bright light treatment with $D = 0.1$ mV, $\nu_{mo} = 0.33 \text{ mV s}$, $t_0 = 7:00$, and $I_{tr} = 10,000$ lux, to find that the system undergoes recovery to the normal phase [see Fig. 4.6(b)].

4.5 Discussion

The results of the integrated sleep-wake model provides a mathematical basis for many results established as to circadian entrainment. For example, many blind individuals experience a cyclic sleep disorder: They experience normal sleep-wake behavior for days to weeks at one time, followed by difficulty in sleeping at night and staying awake during the day for a period of time. Observation of such patients discloses that they experience continuous phase delay [157, 158]. Such patients are not entrained to light because they lack stimulation via the retinohypothalamic tract. Assuming nominal parameters otherwise, we should expect behavior corresponding to the upper left-most region in Fig. 4.3(a), which does indicate continuous phase delay.

In sighted individuals, failure of entrainment results in non-24-h sleep-wake syndrome, similar to the above case. On the other hand, there are cases where the circadian phase is period-locked but at an abnormal time. This is the case in delayed sleep

phase syndrome or advanced sleep phase syndrome, where the patient has a 24-hour circadian rhythm but with a phase significantly late or early relative to the socially acceptable time. Namely, the system locates on the right of the curves in Fig. 4.3, but has a late or early phase due to an abnormal orexin level or inadequate exposure to light. Previous studies reported that delayed sleep phase syndrome arises in both circadian and sleep homeostatic systems [159]; our model offers a way to examine the interplay of those contributions, and although this issue is not explicitly explored in this study, it should be explored in the future.

Circadian rhythm disruption is known to be important in seasonal affective disorder, where change in the intensity and duration of light exposure is involved [160, 28]. In our model, we have seen that this corresponds to moving to the left on the parameter plane of Fig. 4.3(b) and shrinking the period-locking curve. The restoration of entrainment via bright light treatment as seen in our model is a possible mechanism behind the reported efficacy of bright light treatment as an antidepressant in seasonal affective disorder [160, 161]. Note here that lack of light exposure is not the only cause of circadian instability and that there is also evidence for the effectiveness of the bright light therapy in treatment of nonseasonal mood disorders [162, 163]. Relatedly, ORX neurons are implicated both in sleep disorders and in mood disorders [164]; our model study has shown that circadian disruption is a channel through which these effects may occur.

Our results thus demonstrate two different channels through which circadian disruption can occur: lack of light and orexin imbalance. Moreover, it shows that bright light treatment can be effective in restoring a normal circadian rhythm in both cases. In the case of orexin imbalance, Fig. 4.4 shows that there are two time windows during which bright light treatment is effective, with morning treatment being effective for a wider range of circumstances. This result is consistent with the fact that morning bright light treatment is generally more effective than evening treatment in clinical studies. For example, Ref. [165] studied changes in the Hamilton Rating Scale for De-

pression (HRSD) scores after bright light treatment in winter depression, and found that morning treatment resulted in significantly higher remission rates compared with evening treatment. With refinement, our approach can be used to predict the efficacy of bright light treatment in specific circumstances and to guide practical applications. In that regard, it would be desirable to have more rigorous fitting to experimental results, based on, e.g., systematic investigation of the noise effects on entrainment conditions and the efficacy of bright light treatment.

Chapter 5

Predicting expenditure during gradient walking

5.1 Background

Physical inactivity, despite its well-known health risks [31, 32], continues to be a serious public health issue [33]. Recently, various wearable devices, including wristbands and mobile phones, have offered a way to track physical activity throughout the day. Such devices can be used in ambulatory conditions by individuals or in clinical settings to monitor patients' physical activity. Many of these devices use an accelerometer-based method to predict energy expenditure [34, 35, 36]. However, these methods are limited in precision [37]. A basic, common assumption used is that the calorie consumption rate is proportional to the walking velocity. A GPS tracker can then be used to measure the walking distance and then compute the total energy consumption. However, this method is limited in accuracy and may not be feasible indoors.

The energetics of human locomotion has been closely studied for decades. Early studies focused on energy expenditure during walking [166, 167, 168, 169, 170] and running [171, 172, 173, 174], and made comparisons with the energy expenditures of other animals [175]. Most relevantly, studies on walking energetics found a proportional relationship between energy expenditure and the square of the velocity. These early studies showed that reasonable accuracy can be attained with simple relations,

despite the complexity of the act of walking. More recently, detailed models of walking dynamics have been presented that examine more closely the mechanics of walking [18-24][176, 177, 178, 179, 180, ?, 182]. These biomechanical models aim to explain human gait patterns via energy minimization. Also studied have been movements of the arm [183, 184] and the head and trunk [185], as well as gait patterns in special groups of interest [186, 187]. Such models have also been used in the field of robotics in developing walking robots [188]. Previous studies were primarily of academic interest, although inexpensive commercial devices have recently been made available for personal or clinical use. Such devices offer noninvasive ways to measure daily caloric consumption, and they have been assessed by numerous validation studies in the literature [189, 190, 191, 192, 193, 194]. The most common types of commercially available products include the wrist-worn accelerometer and devices based on heart rate monitors. Although these devices are good predictors of the number of steps and heart rate, accurate prediction of energy expenditure is yet to be achieved [195]. These validation studies test for various settings; however, they usually lack a discussion of the model or algorithm used in their predictions.

This study proposes a model of walking energetics applicable to a range of slopes. The model is based on a simple equation and uses data from a wearable device. The method uses a foot monitoring system that can sense footsteps, which allows for direct measurement of step frequency. We found that a high-accuracy model can be developed for a range of upward and downward slopes. The fact that it is based on a direct measurement of footsteps allows the device to be versatile and applicable to diverse walking situations. The ability to track expenditure while walking on sloped surfaces is helpful for sloped outdoor ground and also indoor use of stairs or sloped treadmills.

5.2 Data collection

For model development and validation, an experiment was devised in which 73 healthy participants (34 female, 39 male) walked on a treadmill. The participants had a mean age of 43.6 (SD 15.0) years, mean height of 168.3 (SD 10.5) cm, and mean weight of 68.1 (SD 12.1) kg. Participants were selected from healthy volunteers (age 20 to 60 years) who registered in the department of Sport Science, Pusan National University, Busan, Korea. We excluded participants who had cardiovascular, musculoskeletal, or neurological disorders to avoid any confounding factors or biases. The participants were asked to walk on a treadmill at various values of the incline angle, θ , and speed, v . Specifically, the angle was taken to be 0° (indicating no incline); 4° , 9° , and 14° (uphill); and -4° , -9° , and -14° (downhill). It was observed that calorie consumption took approximately 30 seconds to stabilize to a linear rate while walking. Each walking measurement lasted approximately 5 minutes to ensure a sufficiently long sample.

Calorie consumption was measured with a COSMED K4b2 portable gas analyzer system. This indirect calorimetry, based on the gas analyzer system, measures oxygen consumption, from which energy expenditure is computed. This method has been validated as an accurate measure through numerous comparative studies [196, 197, 198] and is used as a criterion measure in many validation studies [189, 190, 191, 193, 194, 195]. The gas analyzer was worn during the treadmill experiment, and it recorded a time series of cumulative calorie consumption. To eliminate noise associated with the beginning and end of the experiment, we discarded data for the first 50 seconds and the final 10 seconds before computing the energy consumption rate. Then the basal metabolic rate [199] was subtracted to obtain the energy expenditure associated with walking, which is denoted by P .

Each participant also wore a foot monitoring system, consisting of shoe insoles equipped with eight pressure sensors. The insole used was a prototype developed by 3L Labs (Seoul, Korea), and provided to us for research purposes. A Fitbit Surge, a wrist-worn accelerometer device, was also worn by each participant to compare the accuracy

of its caloric consumption prediction. This study was approved by the Institutional Review Board of Pusan National University, Busan, Korea. All participants provided written informed consent (PNU IRB/2015_33_HR).

A value of 0, 1, or 2 indicated the pressure on each of the pressure sensors and was recorded with a frequency of 10 Hz, which resulted in an array of 16 integers for each time step of 0.1 s. A snippet from example data is shown in Fig. 5.1. From the pressure sensor data, we were able to extract the step frequency, f . We performed this by examining the sum of the pressure sensor values at each time step. An example is shown in Fig. 5.2.

Although it is natural to consider the foot to be off the ground when this sum is 0, this can result in erroneous results if one or more of the pressure sensors remain at a value above 0 throughout the entire step cycle, either due to a faulty sensor or residual pressure. We found that better accuracy was achieved when high and low thresholds were used. This was done by first assigning the on-ground status to the first-time step, and then sequentially assigning either the on-ground or off-ground status to each following time step. If the previous time step was on-ground and the pressure sum was below the lower threshold, we assigned the off-ground status to that time step; if the threshold was not crossed, the time step was left in on-ground status. If the previous status was off-ground, the on-ground status was assigned if the pressure sum was above the upper threshold, and the off-ground status was assigned otherwise. Threshold values between 1 and 10 were tested and compared with manually assigned steps. Lower and upper threshold values of 2 and 5, shown in Fig. 2., were found to produce accurate results.

After assigning a status to each time step, we counted the number of transitions from the on-ground to off-ground status and divided it by the time interval to obtain the frequency. As with the gas analyzer data, we omitted data for the first 50 s and the final 10 s. Only one shoe insole is required to calculate the step frequency; however, we used the average of both sides in this study.

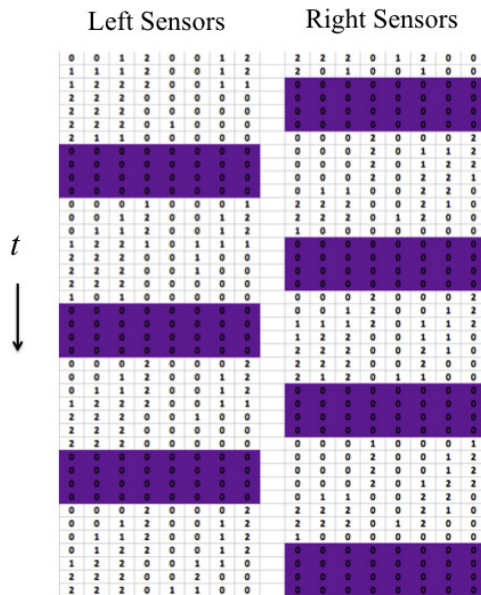


Figure 5.1: A sample of 4 seconds of raw data from the pressure sensors. The vertical position of each number of the array indicates the time, ordered from top to bottom at an increment of 0.1 seconds. Each column denotes a sensor, with left foot and right foot separated. The colored portions indicate when our algorithm decided the foot was off the ground.

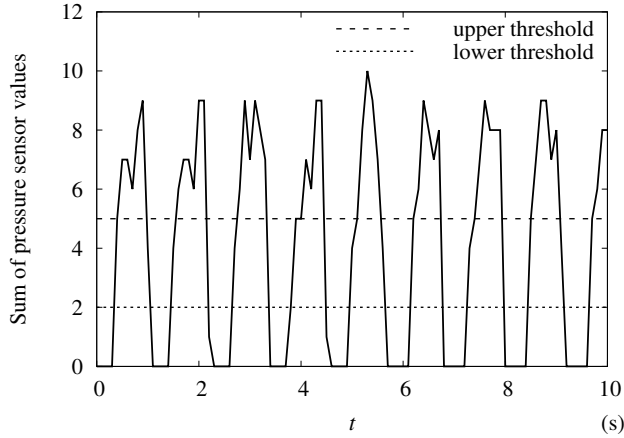


Figure 5.2: Graph of total pressure from the left foot sole over an interval of 10 seconds obtained from the foot monitoring system from the same data as presented in Fig. 5.1. The two dashed lines indicate the upper and lower thresholds used to calculate the step frequency.

5.3 Model construction

Our model was constructed from considering the energy changes involved in walking. Suppose a participant with body mass M is walking with average speed v on a surface inclined by θ from the horizontal. The participant is swinging their legs with frequency f . The energy consumption rate, P , is given by

$$P = \begin{cases} \gamma P_K + b_0 P_U + P_0 & \text{if } \theta \geq 0 \\ \gamma P_K + b_0 P_U + b_1 P_0^{-1} P_U^2 + P_0 & \text{if } \theta < 0 \end{cases} \quad (5.1)$$

Here positive and negative values of the slope, θ , of the walking surface correspond to walking uphill and downhill, respectively. P_K and P_U are rates of changes in the kinetic energy and in the potential energy, respectively, whereas coefficients γ , b_0 , b_1 , and P_0 are parameters to be determined empirically from the data. The energy change

rates for P_K and P_U are given by

$$P_K = 2Mv^2f, \quad (5.2)$$

$$P_U = Mgv \sin \theta \quad (5.3)$$

In the following, we give an explanation of each term in consideration of energy.

Kinetic energy component

We first consider walking on a horizontal surface (ie, $\theta = 0$). When walking on a treadmill, the upper body moves in a relatively constant velocity, with the moving legs supporting this movement. The legs swing back and forth relative to the upper body's position, undergoing an acceleration-deceleration cycle. We postulated that the energy expenditure was proportional to the kinetic energy change of the legs. The work done on the legs during each walking cycle is given by

$$W = 4 \times \frac{1}{2}mv_0^2 \quad (5.4)$$

Here m is the mass of each leg, v_0 is the maximum speed of each leg's center of mass, and the factor of 4 accounts for the two legs each undergoing acceleration and then deceleration. This differs from the assumption that the legs swing like a pendulum, in which case gravity would do the work.

Since we usually have no way to easily measure leg mass or leg velocity, we defined two ratios: (1) the ratio α of the leg mass, m , to the body mass, M ; and (2) the ratio β of the maximum velocity, v_0 , of the leg to the average walking speed, v , as follows:

$$\alpha \equiv \frac{m}{M}, \beta \equiv \frac{v_0}{v} \quad (5.5)$$

This allowed us to rewrite Eq. 5.3 as $W = 2\alpha\beta M^2v^2$, giving an expression for the work done per cycle. Assuming that the human body converts chemical energy into kinetic energy with efficiency η_K , the energy consumption rate due to the kinetic

energy is given by

$$\frac{1}{\eta_K} W f = 2\gamma M v^2 f = \gamma P_K. \quad (5.6)$$

In writing the right-hand side of Eq. 5.5, the measurable terms are grouped into P_K as in Eq. 5.2, whereas the rest are grouped into dimensionless coefficient γ , given by

$$\gamma \equiv \frac{\alpha\beta^2}{\eta_K} \quad (5.7)$$

Potential energy component

When walking on a horizontal surface perpendicular to the direction of gravity, there is no net change in potential energy. It changes when the subject is walking up or down a slope. We first considered upward inclines. When one walks up a slope of angle θ at speed v parallel to the surface, their potential energy, U , changes at a rate $\frac{dU}{dt} = P_U$, given by Eq. 5.2. For simplicity, we further assumed that when walking up a slope, additional energy proportional to this term is required. Accordingly, the energy expenditure rate associated with the changing potential energy is given by $b_0 P_U$, where b_0 is the inverse of the efficiency, η_U , (Eq. 5.7) with which the body converts stored energy to potential energy.

One might consider simply using the same formula for downhill inclines, in which case the term $b_0 P_U = b_0 M g v \sin \theta$ becomes negative. This would imply that when walking downslope, the change in potential energy can be converted into kinetic energy, thereby subtracting from the total energy cost. However, this leads to a nonsensical result for higher slopes, as it can lead to negative energy consumption. When a downhill slope is steeper than a certain angle, the subject would need to exert a frictional force to prevent from falling forward or walking too fast. Therefore, $b_0 P_U$ does not provide an adequate description of the energy expenditure in this case.

Figs. 5.3 present scatterplots of the data in the three-dimensional space (P_K , P_U , P) for women and men, respectively. This visualization shows that P first decreases then increases as P_U is decreased from zero. Such a parabolic shape indicates the

presence of a quadratic term; thus, we added to P a term proportional to P_U^2 . The energy expenditure associated with potential energy in the case of downhill walking is given by Eq. 5.8. The second term is multiplied by P_0^{-1} so that the coefficient b_1 is kept dimensionless. In other words, b_1 is the coefficient of the quadratic term in the case of downhill walking in units of P_0 . This leads to the full model, described by Eq. 5.1.

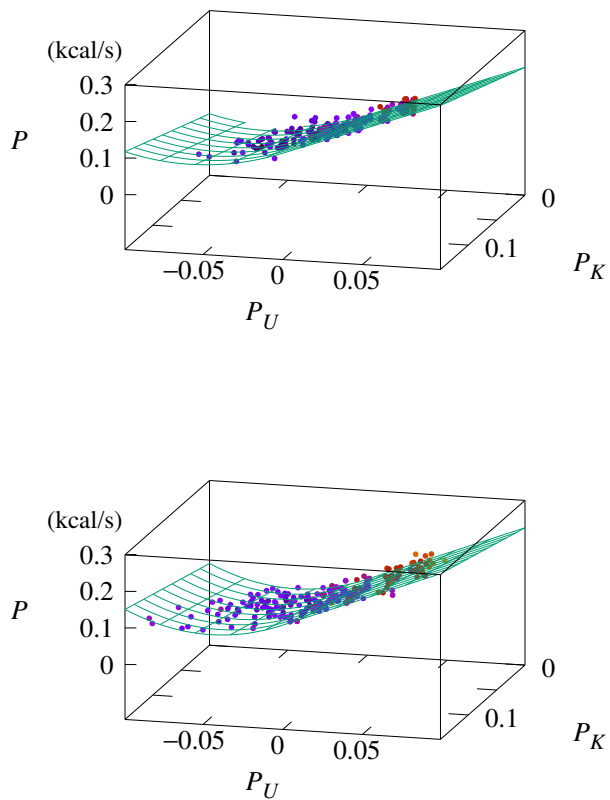


Figure 5.3: Three-dimensional scatterplot of data (dots) and model prediction (lines) of P versus P_U and P_K for (a) women and (b) men.

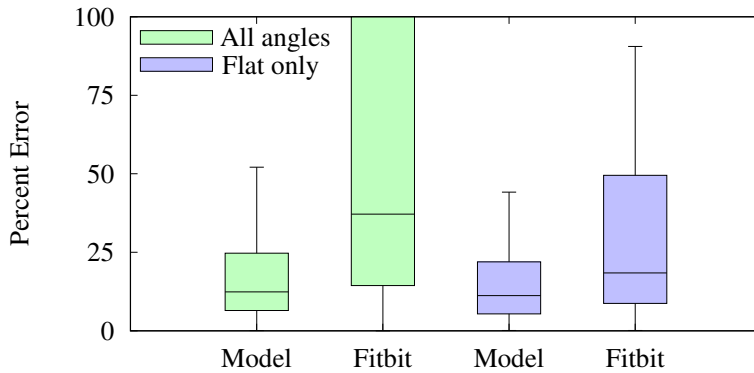


Figure 5.4: Boxplots of the percent errors of predictions made by the model and Fitbit Surge. Errors have been estimated via Eq. 5.9.

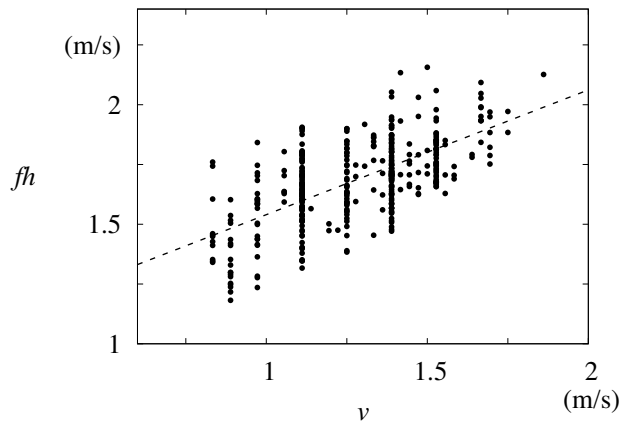


Figure 5.5: Step frequency f multiplied by height h plotted against average walking speed v . Least squares fit line $fh = 0.52v + 1.02$ (m/s) is also shown.

Coefficient	Units	Women	Men
γ	1	0.662	0.517
b_0	1	1.591	1.694
b_1	1	0.575	1.086
P_0	kcal/s	0.0042	0.058
RMSD	kcal/s (kcal/min)	0.016 (0.96)	0.016 (0.96)

Table 5.1: Coefficients for the full model reported with the RMSD on comparison with data.

Linear Regression

The preceding model described leaves parameters γ , b_0 , b_1 , and P_0 to be determined. We obtained these parameters by first taking data for flat and uphill surfaces ($\theta \geq 0$) and performing multiple linear regression through the use of the first equation in Eq. 5.1 with γ , b_0 , and P_0 as fitting parameters. The adjusted R^2 value for the fits of both women and men was .83. Then b_1 was obtained via fitting the second equation of Eq. 5.1 to flat and downslope data ($\theta \leq 0$). During this secondary fit, γ , b_0 , and P_0 were set constant at the values obtained earlier.

5.4 Fitting results

The full set of coefficients, obtained through linear regression, is given in Table 5.1. The dependency of P on P_K and P_U is represented by the surfaces in Fig. 5.3. Due to the piecewise functional form of the model (Eq. 5.1), the prediction plane has no curvature for $P_U > 0$ but does in the region $P_U < 0$.

in a root-mean-square deviation (RMSD) of 0.96 kcal/min for both women and men. A boxplot of the percentage errors of all trials is given in Fig. 5.4, in which the errors have been calculated according to Eq. 5.9. Here P is the prediction by the

method whereas P' is the standard given by the gas analyzer. The median errors were 16.9% for women, 11.2% for men, and 12.4% for both groups. These errors are substantially lower than those found in a validation study for multiple commercial devices, which yielded median accuracies of 28.6% to 35.0% across devices for walking [195].

The predictions made by Fitbit Surge had an RMSD of 2.58 kcal/min (2.7 times that of the model) and a median percent error of 37.3% (3 times that of the model). However, this high error was mostly due to inaccuracies in sloped walking. When restricted to flat surfaces, the Fitbit Surge's accuracy increased dramatically, whereas the model's accuracy increased moderately. The Fitbit Surge's RMSD on flat surfaces was 1.82 kcal/min (2.3 times that of the model, 0.79 kcal/min), and the median percent error was 18.4% (1.6 times that of the model, 11.2%). Distributions of percent errors are portrayed with boxplots in Fig. 5.4.

Before discussing the implications of these results, we note that the variables v and f are not independent. If l is the average length of a step, then $v = fl$. Assuming the approximate relation $h \approx l$, where h is the subject's height, we obtain

$$v \sim fh. \quad (5.8)$$

This relation was observed in the data, as shown in Fig. 5.5.

Equation 5.7 implies that $\eta_U = 0.547$ for women and 0.596 for men. In principle, γ depends on α , β , and η_K . We assumed the average value of $\alpha = 0.185$ for women and 0.165 for men, obtained from an anatomical reference [200], and that $\eta_K = \eta_U$. Taking these values and the fitting result for γ , we obtained from Eq. 5.6 the ratio β with values 1.47 for women and 1.36 for men. This difference in the average may reflect the difference in the average height between women and men. Specifically, Eqs. 5.4 and 5.10 imply $\beta = v_0/v \sim v_0/fh$. The ratio of the value of β for women to that for men equaled 1.08, whereas the ratio of the average height of men to that of women equaled 1.11.

5.5 Discussion

We developed a model based on rates of change in kinetic and potential energies. In general, it predicts linear dependence of the energy consumption on these rates; in particular, it predicts quadratic dependence of the energy consumption on the potential energy change in the case of downhill walking. The method, used in conjunction with a foot monitoring system, predicts energy expenditure with an RMSD of 0.98 kcal/min and a median percent error of 12.4%, lower than those of wrist-worn commercial devices in predicting energy expenditure for walking. With one simple piecewise function, the model adequately predicts energy expenditure for walking in a wide range of the gradient. Notice the differences in parameter values between women and men. The appreciable difference in the value of b_1 between men and women may result from the difference in walking posture; this is beyond the scope of this work and left for future study. In principle, the parameters are fit for each individual and should vary by subject. Thus, Table 1 presents average values of the coefficients within each gender. Even so, it is remarkable that a high degree of accuracy is observed.

Although the model accounts for varying body mass and step frequency (cadence), this does not account for additional individual variations in parameter values due to walking gait and body dimensions. There may be ways to account for such variations without complicating the model. In addition, because the treadmill incline lies between 14° uphill and 14° downhill, we are not able to validate the model for more extreme slopes [201]. In addition, the method has not been tested and calibrated for outdoor walking or variable temperatures and altitudes. However, we believe that our pilot study provides a groundwork for follow-up studies under more ambulatory conditions.

Prior studies have noted the strong correlations between P and v^2 for level walking [168]. The authors have also similarly considered additional energy expenditure when walking uphill, attributing it to vertical lift work. In contrast, our study proposes a simple formula that predicts energy consumption reasonably well for horizontal, uphill, and downhill surfaces within a unified framework. In addition, Ref. [167] made

use of individual measurements, including resting metabolic rate and leg length. Our model shows that high accuracy can be achieved via reasonable assumptions used in conjunction with a wearable, mobile device.

Other existing studies have studied energy expenditure during uphill and downhill walking [201, 202]. The authors reported a minimum energy cost when walking 10° downhill, which is consistent with our results. These studies did not incorporate varying walking speed and body weight, and relied on regression analysis with those variables kept constant. Our study offers a simple formula that applies to various walking speeds and subjects, while also accounting for the surface gradient.

Our method fits separately for women and men. Prior validation studies have found differences in the accuracy of devices between the two genders. A comparative validation study found that gender was one of the strongest predictors for accuracy, with a rate significantly higher for men than for women [195]. Our results suggest that similar error rates for both genders can be achieved.

In conclusion, we have developed a model that predicts energy expenditure during walking on a gradient surface between 14° uphill and 14° downhill, with an RMSD of 0.98 kcal/min. The model has been used in conjunction with a wearable device, the foot monitoring system, which directly measures footsteps. Thus, it offers an accessible method of measuring energy expenditure in realistic walking settings, where gradient walking is common. Future work may test Eq. 5.1 in a wider range of values in the P_K – P_U space. Testing the method on outdoor walking is also desirable for further validation. Although not yet explored, the device could also be used in conjunction with other activity monitoring devices, such as wrist-worn ones, to produce more accurate measures of energy expenditure.

Chapter 6

Behavioral dynamics of interceptive walking

6.1 Background

In this chapter, we explore the walking trajectories of pedestrians crossing a road between vehicles. When pedestrians cross a road with moving vehicles, a situation that can commonly arise in countries where traffic laws are not strictly obeyed, they are intercepting a gap between the cars. Thus we may formulate the problem as one of interceptive walking. This problem is one of public health interest, as pedestrian accidents take up a large proportion of traffic-related accidents, particularly in areas of high population density [39, 40]. A quantitative study of the behavioral dynamics of road crossing may help develop strategies to prevent accidents [40, 41, 42].

The crossing task involved an act of avoidance [41, 204] as well as interception [205, 206, 207]. One possible strategy that people employ to intercept moving objects is the constant bearing angle strategy [205, 206, 207], connected to how walking is visually controlled [214, 208, 209, 210]. In addition, the concept of affordance has also been utilized in the study of such tasks, where affordance is the range of possibilities for action constrained by the environment and physical conditions of the actor [211, 212, 213]. Other studies have provided statistical analyses of pedestrian inter-vehicle gap acceptance rates, which were shown to be related with the pedestri-

ans' perception of affordance [215]. However, these studies do not provide a dynamic model of interceptive walking. We thus need an approach that describes the essential components of walking. To do this, we look for inspiration in the principle of least effort, a widely used idea in studies of human activity. It was first used to explain the rank-frequency distributions of words in the English language[216], and subsequently a diverse range of phenomena such as crowd behavior [217], and even mental effort [218]. These studies have found predictable patterns within the unpredictability of human behavior. The principle of least effort has precedence in the principle of least action in classical mechanics, and other such principles in theories of physics (e.g. in quantum mechanics [219] and general relativity [220]). The interceptive walking task considered here, while not without variability, is simple enough to reveal regularly chosen crossing trajectories that can be modeled quantitatively. We may thus take the approach of Lagrangian mechanics and perhaps model the individual trajectories of pedestrians.

In the following section, we develop such a model by following the procedure of Lagrangian mechanics. We define a Lagrangian and solve the resulting Euler-Lagrange equation, which yields the path of stationary action. We postulate that the Lagrangian is a function of effort (taking inspiration from the principle of least effort) as well as a quantity we call security. Two specific forms of the Lagrangian are proposed and their equations of motion are derived. We verify the model by fitting them to positional time series data from a virtual reality crossing experiment. The experiment simulates a road crossing situation in which a pedestrian crosses a road between two moving vehicles [221, 42, 203]. We find that both forms of the model describe the data accurately.

In the next section, we take one of the models and apply it to data from a wide range of experimental parameters. The best fit parameters contain information about the essential characteristics of each crossing event. We examine the dependence of the average value of each parameter on the crossing conditions. We examine the effects

of the gap size and the initial distance as well as the pedestrian's age, vehicle speed, and vehicle type. We also derive an inequality among the parameters that must be satisfied for successful crossing to occur, hence describing the affordance [212, 213], and also discuss the bearing angle hypothesis within the context of the model.

6.2 Model based on a least action principle

We take inspiration from Lagrangian mechanics, where the Lagrangian is defined as $L = T - U$ with kinetic energy T and potential energy U . Here, we consider a Lagrangian of the form

$$L = E - S, \quad (6.1)$$

where E denotes the *effort* and S the *security*. It is well established that the energy expenditure during walking is proportional to the square of the walking speed [167, 217, 3]. We thus assume that the effort for walking is proportional to v^2 , and write, up to multiplicative and additive constants,

$$E = \left(\frac{v}{v_m} \right)^2, \quad (6.2)$$

where v_m is a scaling constant, making E dimensionless. It will be seen that it is the maximum walking speed.

We reason that security is related to the motivation of the pedestrian to reach a goal while avoiding danger, depends on the walking speed and acceleration. The pedestrian should feel safe when she or he can quickly crosses the gap. Measuring the speed in units of v_m , we thus assume that the drive to move forward is described by $v/v_m (< 1)$, neglecting higher-order terms. We also assume a biomechanically preferred degree of acceleration. The pedestrian thus feels unsafe at low accelerations and prefers either to keep a constant speed or to accelerate quickly. This effect is taken into account by a function $g(a)$ (again up to multiplicative and additive constants), which we presume to be a function with zeros at $a = 0$ and a_m which is convex in between so that $g(a) < 0$

when $0 < a < a_m$, thus preferring either zero or high accelerations. This results in

$$S = \frac{v}{v_m} + g(a). \quad (6.3)$$

We discuss two different forms of $g(a)$ below. The Lagrangian is then given by the difference between Eq. (6.2) and Eq. (6.3).

The Lagrangian is naturally independent of the position y and depends only on the speed $\dot{y} \equiv v$, and of the acceleration $\ddot{y} \equiv a$. We may assume $v > 0$ without loss of generality by choosing a reference frame in which the pedestrian is moving forward. Further, we suppose that the pedestrian does not decelerate until crossing, which implies $a \geq 0$.

We now derive a form of the Euler-Lagrange equation that will simplify the calculations of each specific Lagrangian form. The stationary path for a Lagrangian of the form $L = L(y, v, a)$ obeys the Euler-Lagrange equation

$$\frac{\partial L}{\partial y} - \frac{d}{dt} \frac{\partial L}{\partial v} + \frac{d^2}{dt^2} \frac{\partial L}{\partial a} = 0. \quad (6.4)$$

We use the fact that $\partial L / \partial y = 0$ and integrate with respect to time t , reducing Eq. (6.4) to

$$\frac{\partial L}{\partial v} - \frac{d}{dt} \frac{\partial L}{\partial a} + c_1 = 0 \quad (6.5)$$

with an integration constant c_1 . The chain rule, together with the fact $\partial L / \partial t = \partial L / \partial y = 0$, yields $dL/dt = \partial L / \partial t + v \partial L / \partial y + a \partial L / \partial v + \dot{a} \partial L / \partial a = a \partial L / \partial v + \dot{a} \partial L / \partial a$, which we substitute into Eq. (6.5) to obtain

$$\frac{dL}{dt} - \dot{a} \frac{\partial L}{\partial a} - a \frac{d}{dt} \frac{\partial L}{\partial a} + c_1 a = \frac{d}{dt} \left[L - \left(a \frac{\partial L}{\partial a} \right) + c_1 v \right] = 0 \quad (6.6)$$

Integrating Eq. (6.6), we have

$$L - a \frac{\partial L}{\partial a} + c_1 v - c_2 = 0, \quad (6.7)$$

where integration constants c_2 and c_1 may respectively be absorbed into L as an overall additive constant and as a multiplicative coefficient of the linear velocity term in

Eq. (6.3). We may therefore set $c_1 = c_2 = 0$, which gives us

$$L - a \frac{\partial L}{\partial a} = 0. \quad (6.8)$$

We next discuss two forms of $g(a)$ and solve the resulting Euler-Lagrange equations.

Case 1: Quadratic form

We first consider a quadratic equation $g(a) = (a/a_m)(1 - a/a_m)$, resulting in the Lagrangian

$$L = \left(\frac{v}{v_m}\right)^2 - \frac{v}{v_m} + \frac{a}{4a_m} \left(1 - \frac{a}{a_m}\right), \quad (6.9)$$

where we have included a factor $1/4$ on the second term. Substituting Eq. (6.9) into Eq. (6.8) results in

$$\frac{dv}{dt} = 2a_m \sqrt{\frac{v}{v_m} \left(1 - \frac{v}{v_m}\right)}. \quad (6.10)$$

Eq. (6.10) has fixed points at $v = 0$ and v_m which are unstable. In the range $0 \leq v \leq v_m$, we have the solution

$$v(t) = v_m \cos^2 \left(\frac{t}{4\tau} - \frac{\pi}{4} \right), \quad (6.11)$$

where $\tau \equiv v_m/4a_m$. Eq. (6.11) oscillates between the fixed points and τ corresponds to the duration of each acceleration and deceleration region. With boundary conditions such that the pedestrian begins at rest and intercepts a target at constant speed, the least action path can be constructed as a piecewise functions with the two fixed points and Eq. (6.11) during a time interval centered at time $t = t_a$, resulting in:

$$v(t) = \begin{cases} 0, & t - t_a \leq -\pi\tau \\ v_m \cos^2((t - t_a)/4\tau - \pi/4), & -\pi\tau < t - t_a < \pi\tau \\ v_m, & t - t_a \geq \pi\tau \end{cases} \quad (6.12)$$

Integrating Eq. (6.12) gives us

$$y(t) = \begin{cases} y_0, & t - t_a \leq -\pi\tau \\ y_0 + \frac{\tau v_m}{2} \left(\pi + \frac{t-t_a}{\tau} - 2 \cos \left[\frac{t-t_a}{2\tau} \right] \right), & -\pi\tau < t - t_a < \pi\tau \\ y_0 + v_m(t - t_a), & t - t_a \geq \pi\tau \end{cases} \quad (6.13)$$

Eq. (6.12) and Eq. (6.13) obey the Euler-Lagrange equation at all points. However, they exhibit singularities in the higher derivatives at times $t = t_a \pm \pi\tau$.

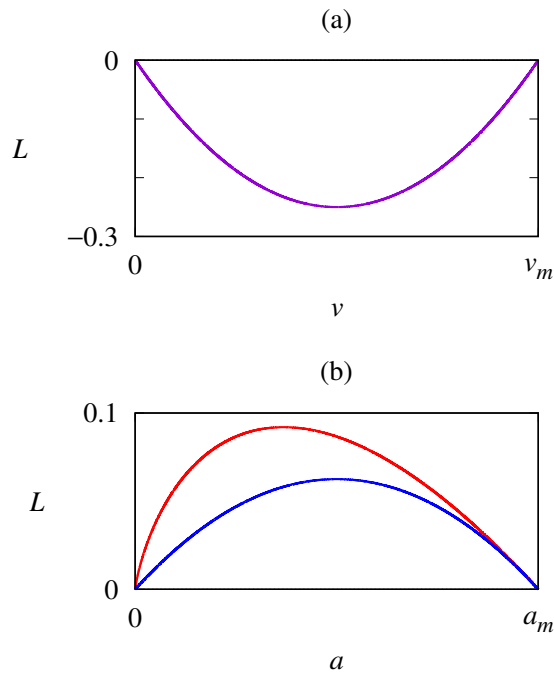


Figure 6.1: (a) Dependence of the Lagrangian L on the speed v (in the absence of acceleration, $a = 0$). (b) Dependence of L on a (for $v = 0$) for the quadratic form (blue) and the logarithmic form (red).

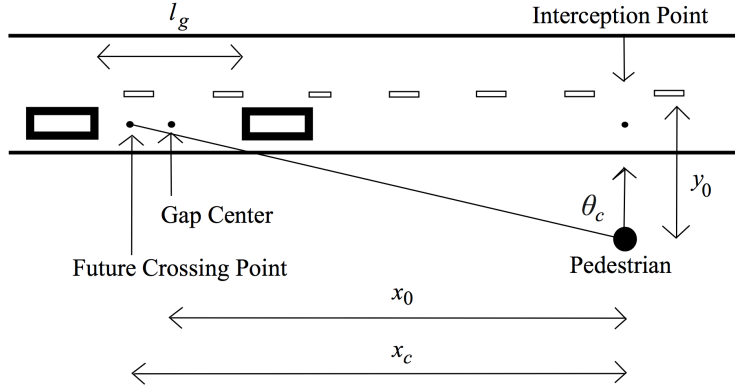


Figure 6.2: Top-down diagram of the crossing environment at time $t = 0$. The two boxes on the road depict two vehicles facing the right, which move forward at a constant speed. The circle depicts the pedestrian, who begins at rest and is facing in the direction the arrow. Labeled are experimental parameters l_g , y_0 , and the bearing angle to the crossing point θ_c .

Case 2: Logarithmic form

As a second case, we take $g(a) = (a/a_m) \log(a/a_m)$, giving us

$$L = \left(\frac{v}{v_m}\right)^2 - \frac{v}{v_m} - \frac{a}{4a_m} \log\left(\frac{a}{a_m}\right), \quad (6.14)$$

again with a factor of $1/4$. Unlike the quadratic equation, this form of $g(a)$ is asymmetrical and steeper on the left side. Plugging into Eq. (6.8) results in the logistic equation

$$\frac{dv}{dt} = \frac{4a_m v}{v_m} \left(1 - \frac{v}{v_m}\right), \quad (6.15)$$

which carries the solution for the speed:

$$v(t) = \frac{v_m}{2} \left[\tanh\left(\frac{t - t_a}{2\tau}\right) + 1 \right], \quad (6.16)$$

where τ is defined the same way as above and again measures the duration of acceleration, and the integration constant t_a determines the timing of acceleration. Note in

Eq. (6.16) that v_m indeed corresponds to the maximum walking speed; further, differentiation of Eq. (6.16) with respect to t manifests that the maximum acceleration is given by a_m . Integrating Eq. (6.16) also gives the position as a function of time:

$$y(t) = y_0 + v_m \tau \log \left[1 + \exp \left(\frac{t - t_a}{\tau} \right) \right]. \quad (6.17)$$

Unlike Eq. (6.13), Eq. (6.17) is free singularities. But the velocity never reaches exactly 0 or v_m , and so has the disadvantage of being an approximation (albeit with an error that decays exponentially).

Hamiltonian formulation

The definition of a Lagrangian immediately suggests that a Hamiltonian can also be constructed. The proposed Lagrangian differs from those typical in classical mechanics in that it contains a derivative of order higher than one. Lagrangians of such form have been studied, and instabilities that arise from unavoidable linear terms in their Hamiltonian functions have been cited as reasons that nature is not described by higher-order Lagrangians in fundamental theory[223, 224]. We appeal to the phenomenological nature of the model and ignore these instabilities here. We construct a Hamiltonian by using Ostrogradsky's construction for third order Lagrangians:[222]

$$\begin{aligned} Q_1 &\equiv x \\ Q_2 &\equiv \dot{x} \\ P_1 &\equiv \frac{\partial L}{\partial \dot{x}} - \frac{d}{dt} \frac{\partial L}{\partial \ddot{x}} \\ P_2 &\equiv \frac{\partial L}{\partial \ddot{x}}. \end{aligned} \quad (A1)$$

Then the Hamiltonian is obtained by performing the Legendre transform,

$$H(Q_1, Q_2, P_1, P_2) = P_1 Q_2 + P_2 A(Q_1, Q_2, P_2) - L(Q_1, Q_2, A), \quad (A2)$$

where A is the acceleration function written in terms of the canonical coordinates.

In the quadratic case, this results in a Hamiltonian of the form

$$H = \frac{Q_2}{v_m} - \frac{Q_2^2}{v_m^2} + Q_2 P_1 - \frac{a_m}{2} P_2 - a_m^2 P_2^2 + \frac{3}{16}, \quad (\text{A3})$$

while in the logarithmic case, we have

$$H = \frac{Q_2^2}{v_m^2} - \frac{1}{4} e^{-4a_m P_2 - 1} + Q_2 P_1 - \frac{2Q_2^2}{v_m^2} - \frac{1}{v_m}. \quad (\text{A5})$$

The Hamiltonians obtained are indeed conserved quantities.

Data Collection

To verify the validity of each case of the model, we make a comparison with the data obtained from a virtual reality road-crossing experiment. In this experiment, human participants walked on a customized treadmill (of dimensions 0.67 m wide, 1.26 m long, and 1.10 m high) with four magnetic counters that track movements. A Velcro belt connected to the treadmill was worn for suppression of vertical and lateral movements, and a handrail was placed for safety. Each participant wore a commercial virtual reality headset connected to a standard desktop PC. The headset portrayed a realistic view of a typical crosswalk in Korea in 1280×800 resolution stereoscopic visual images which shift in real time according to the participant's steps and head turns. Sixteen children (of age 12.2 ± 0.8 yrs, i.e., mean age 12.2 years and standard deviation 0.8 years) and sixteen adults (of age 22.8 ± 2.6 yrs) with normal or corrected-to-normal vision were recruited for this experiment. Informed written consent was obtained from every individual participant. The protocol was approved by the Kunsan National University Research Board. Details of the experiment can be found in Chung *et al.* [203]

Fig. 6.2 presents a schematic diagram of the crossing simulations viewed from above. While the two parallel vehicles are moving at equal constant speed $v_c = 30$ km/h, the pedestrian attempts to cross the road in the perpendicular direction. The paths of the pedestrian and of vehicles intersect at the crossing point. The pedestrian is instructed to cross between the two vehicles if possible. The empty space between

the two vehicles, called the gap, is set to be $l_g = 25$ m in length. The distance between the midpoint of the gap and the intersection point, denoted by x_g , has the initial value 33.3 m, so that the gap center reaches the crossing point in 4 s. The position of the pedestrian is measured by the distance y from the crossing point taken as the origin, and is recorded to generate positional time series. The initial position y_0 is set to be -4.5 m.

Fitting Results

Eq. (6.13) and Eq. (6.17) were fit to the data, making use of v_m , τ , and t_a as fitting parameters. When Eq. (6.13) was fit to the data, the root-mean-square deviation (RMSD) turned out to be 0.052 m on average, with the standard deviation 0.022 m and the maximum RMSD of 0.10 m. Meanwhile, when Eq. (6.17) was fit to the data, the RMSD was 0.056 m on average, with the standard deviation 0.024 m and the maximum RMSD of 0.12 m. It was thus concluded that each model function makes a description of each individual crossing with high accuracy, and no significant difference between the two was found. All time series are plotted in Fig. 6.4, which manifests that overall, data (thin gray lines) fit closely to the model.

There were individual variations in the slope v_m and the acceleration timing t_a , resulting in a spread of the data as seen in Fig. 6.4. Taking the average of the position data in 0.25 s increments, we obtain the average behavior of each collective group, and plot the averages and standard deviations also in Fig. 6.4. The thick red and blue lines depict Eq. (6.13) and (6.17) fitted to the averaged position data, with the fitting parameters given in Table 6.3. Note first that the averaged data also display a good fit to both cases of the model. By plotting the two age groups separately, we observe a difference in the slope. Accordingly, v_m takes different fitting values: The adult group has a higher value by 0.24 m/s (see Table 6.3). Other parameters do not differ significantly.

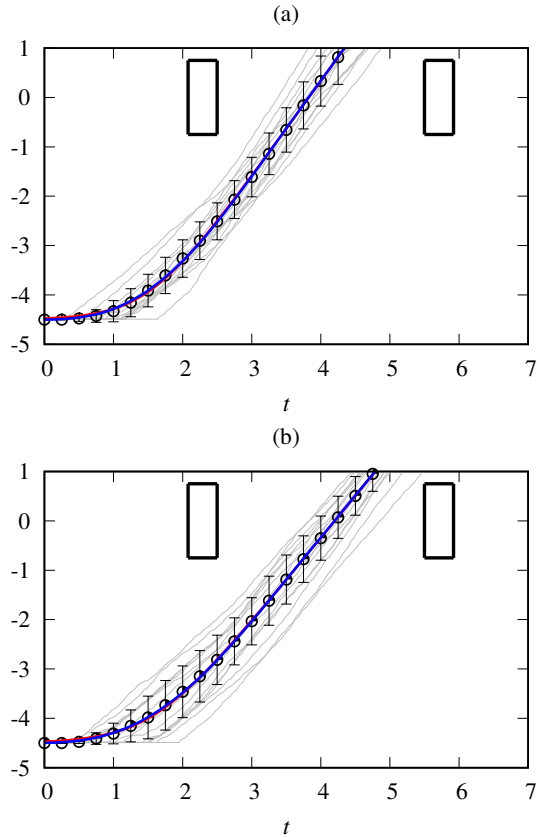


Figure 6.3: Fitting results and data for (a) adults and (b) children, displaying the position y (in meters) versus time t (in seconds). Circles and error bars indicate averages and standard deviations of positions, respectively. Blue and red lines correspond to the quadratic and logarithmic models fitted to the averaged data, respectively. The blue and red lines overlap significantly. Individual data time series are plotted in grey and rectangles represent vehicles.

Model	Age group	v_m (m/s)	τ (s)	t_a (s)	a_m (m/s ²)
quadratic	adults	1.94	0.54	1.50	0.90
	children	1.70	0.59	1.55	0.72
logarithmic	adults	1.94	0.43	1.51	0.32
	children	1.70	0.47	1.57	0.27

Table 6.1: Fitting parameters v_m , t_a , and τ for the averaged data, together with Lagrangian constant a_m , using each model and fit to each age group.

Discussion of the model

We have presented a model for goal-directed human walking behavior, based on a principle of least action. The approach can be considered as generalization of the principle of least effort, incorporating another term called security. Walking behavior results from the assumption of three simple terms making up effort and security. The resulting equations have been found to fit experimental data from a virtual reality road-crossing experiments.

It is not conceivable that our simple model captures the full complexity of the complex biomechanics and psychology involved in walking. The model treats the walker as a self-propelling particle and thus provides rather a coarse approach compared with biomechanical studies [225]. However, we presume that the form of Eq. (6.1) should contain all the essential features of goal-directed walking, including psychological factors. This approach may thus be useful in the study of pedestrian trajectories.

In validating the model, an experimental setup was employed which imposed a gap interception task on the participant. The results show that the participant choose the path of least action as defined by the model. However, while the initial conditions are constrained, the experiments force the participants not into a single point but into a spatiotemporal range (the gap). Accordingly, there are individual variations in the

end point the participant chooses. In addition, we expect that physiological differences lead to differences in constants v_m and a_m , which could result in variations in the least-action path even with the same boundaries. This is made apparent in the difference in v_m between the age groups, which is manifested by different values of v_m and a_m in the Lagrangian.

One may note the limitations of using a treadmill, which may change walking behavior and also constrains the participant to walk in a straight line. Additional walking simulations have been done in which the participants walk freely in a room, with sensors used to detect their positions. The results were again consistent with the model (data not shown). However, an additional dimension is added due to the freedom in the walking direction. There were no interesting features in the dynamics of the angle, which was generally held constant. The choice of the angle exhibits also individual variations; this is beyond the scope of the current model.

The model has been also limited to the case of positive acceleration ($a > 0$). The quadratic Lagrangian (Eq. (6.9)) can already describe negative accelerations, as a piecewise function can be constructed with a deceleration event from velocity v_m to 0 due to the oscillatory form of Eq. (6.11). For the logarithmic Lagrangian of Eq. (6.14), if negative acceleration ($a < 0$) is allowed, we may assume that the security feeling of the pedestrian should depend only on the magnitude (regardless of the sign), and put the absolute value $|a|$ in place of a in equation (6.3). This time-reverses the solution: The speed begins at v_m , then decreases to zero. These solutions describe the deceleration event after the pedestrian has reached a destination. Under some experimental conditions not shown here, the participant walked forward, stopped, and then accelerated again to cross the gap. The stopping behavior between walking can be seen as a deceleration event described by the model with $a < 0$. For simplicity, this is treated in a later section.

We note that the present model has similarity with other models of pedestrian behavior, e.g., in Guy *et al.*, [217], which also defines effort as the metabolic energy

Participant group	Number of participant
Children	16
Young adults	16
Elderly	14
Experimental parameter	Values used
y_0 (initial distance)	-3.5, -4.5, -5.5, -6.5 m
t_g (gap time)	2.5, 3, 4 s
v_c (vehicle speed)	30, 60 km/h
vehicle type	sedan, bus
total configurations	48

Table 6.2: Table summarizing age groups and experimental parameters.

consumption. Our model differs from those previous models in that it includes additional terms (security) affecting the trajectory and also in that it produces an analytical solution for the entire walking trajectory, which is possible due to the simplicity of the walking task. Guy *et al* instead simulate collision avoidance in crowds by restricting the direction of movement based on the environment at each simulation step.

There is much room for refinement of the present model. For instance, the model may be extended further to include a second dimension and/or interactions with other pedestrians. This is left for future study. A detailed examination of the effects of various other crossing conditions (e.g. the initial position of the pedestrian, the gap length, and the vehicle speed) on fitting parameters using one of the models developed here is given next.

6.3 Recasting the model to describe bearing angle and affordance

The position and velocity data from the logarithmic form are here called the simple crossing model. We use this to analyze the crossing data. The velocity is reproduced below,

$$v(t) = v_{\max} \frac{\exp[(t - t_a)/\tau]}{1 + \exp[(t - t_a)/\tau]}, \quad (6.18)$$

which, upon integration, results in the position as a function of time:

$$y(t) = y_0 + v_{\max} \tau \log\{1 + \exp[(t - t_a)/\tau]\}. \quad (6.19)$$

Equation (6.19) is plotted in Figure 6.4a (red line). Constants t_a , τ , v_{\max} are fitting parameters whose meanings can be understood as follows: The measurement begins at time $t = 0$. Assuming $t_a - 2\tau > 0$, we have the initial position and velocity of the pedestrian, $y(t=0) \approx y_0 (< 0)$ and $v(t=0) \approx 0$, respectively. Then, the pedestrian accelerates smoothly until the maximum velocity v_{\max} is reached. The parameter τ then serves as a measure for the duration of this acceleration, the midpoint between which is given by t_a . Note that, at time $t = t_a - 2\tau$, the velocity in Equation (6.18) becomes $v(t = t_a - 2\tau) = v_{\max} e^{-2}/(1 + e^{-2}) \approx 0.1 v_{\max}$. While Equation (6.18) never gives $v = 0$ exactly, in practice, we may define $t_d \equiv t_a - 2\tau$ to be the time at which the pedestrian begins to accelerate forward. If preferable, one may take alternatively $t_d \equiv t_a - 3\tau$, which corresponds to $v(t = t_d) \approx 0.01 v_{\max}$.

A second model, called the two-step crossing model, is used to analyze crossings that have more than one acceleration event and thus do not fit the simple crossing model (Figure 6.4b). The two-step crossing model is discussed in the Appendix.

Each piece of data classified as a simple crossing is fit to Equation (6.19) by minimizing RMSD with respect to the fitting parameters. We probe the effects of gap characteristics by examining how the distributions of parameters change with the variation of certain features of the gap, and discuss the results in Section 6.4. Those data

displaying the two-step pattern are fitted separately to the extended model, and the results are discussed in the Appendix.

Affordance

Affordance stands for the range of possible actions that the environment offers to the acting agent. In the crossing task, the affordance is determined by how long the gap overlaps with the participant's walking trajectory. Assuming the simple crossing model (i.e., Equations (6.18) and 6.19), the affordance of the gap is described by the inequality

$$\begin{aligned} t_f - \tau \log[e^{(-y_0 - w/2)/v_{\max}\tau} - 1] &< t_a \\ &< t_b - \tau \log[e^{(-y_0 + w/2)/v_{\max}\tau} - 1]. \end{aligned} \quad (6.20)$$

Here, $t_f \equiv |x_0 + l_g/2|v_c^{-1}$ corresponds to the time at which the back bumper of the leading vehicle passes the intersection point and $t_b \equiv |x_0 - l_g/2|v_c^{-1}$ corresponds to the time at which the front bumper of the trailing vehicle passes the point, while w denotes the width of the vehicles and equals 1.5 m in our experiment. t_f is hence manifested in Figure 6.4a by the time coordinate of the right side of the box to the left (2.5 s), while t_b is by that of the left side of the box to the right (5.5 s). Equation (6.20) thus describes the condition under which the pedestrian's trajectory passes between the two boxes in Figure 6.4a.

In general typical values of τ are smaller than the time scale of crossing, e.g., compared with $(-y_0 \pm w/2)/v_{\max}$. (Note that $y_0 < 0$ in our coordinate system.) Accordingly, we may take the limit $\tau \rightarrow 0$, and reduce Equation (6.20) to

$$t_f - \frac{1}{v_{\max}} \left(-y_0 - \frac{w}{2} \right) < t_a < t_b - \frac{1}{v_{\max}} \left(-y_0 + \frac{w}{2} \right). \quad (6.21)$$

This provides a simpler inequality involving two fitting parameters.

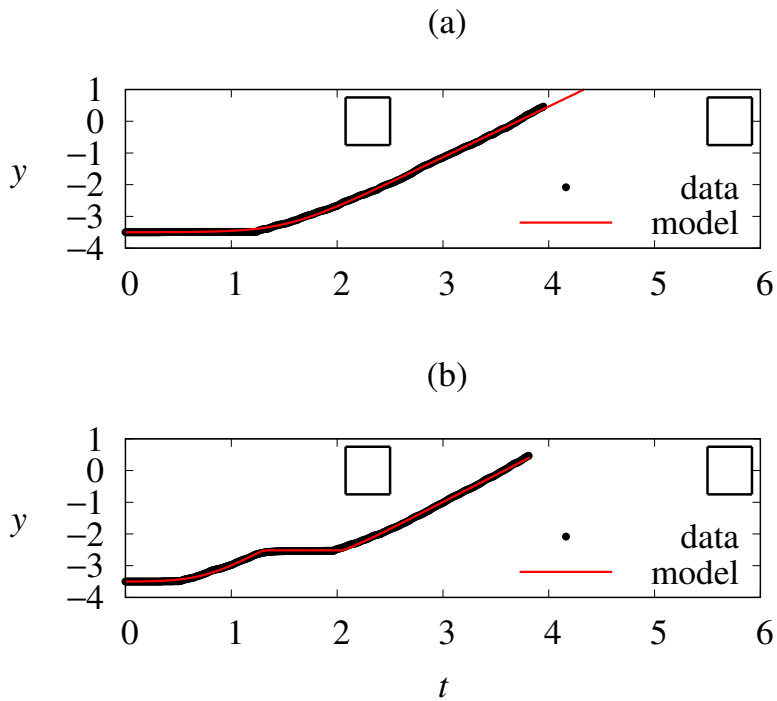


Figure 6.4: Pedestrian position-time plots illustrating typical crossing patterns. Black traces indicate example data; red traces indicate the corresponding model fits. Left and right boxes indicate the temporal and spatial area that the leading and the trailing vehicles occupy, respectively. Intersecting one of the box lines would indicate a collision. In both examples, the conditions are described by $y_0 = -3.5$ m, $t_g = 3.0$ s, and $v_c = 30$ km/h, with the vehicle type set to be a sedan. **(a)** an example of the simple cross with a single acceleration event followed by constant speed walking; **(b)** an example of the two-step cross with two acceleration events.

Bearing Angle

Dynamics of interceptive movement are often described in terms of the bearing angle [206, 207], which refers to the angle between the velocity vector of the human subject and the line of sight between the subject and the object she/he hopes to intercept. In brief, this model asserts that people intercept a moving object by choosing such a trajectory that the bearing angle is kept constant.

Our case of crossing a road may be cast into an interception task: The pedestrian must “intercept” the empty gap between the vehicles [221]. We may hence apply the bearing angle approach to our crossing experiment and model. One difficulty with this approach is that the gap is not a point but a moving area. As an obvious choice, we may simply use the gap center $x_g(t)$, with respect to which the bearing angle is $\theta_g(t) = \arctan [x_g(t)/y(t)]$. However, the pedestrian may not cross the gap center; it is thus more appropriate to examine the bearing angle with respect to the point within the moving gap that the pedestrian actually crosses. With t^* denoting the crossing time, we have $y(t^*) = 0$ and let the position of the gap center at the crossing time be Δx , i.e., $x_g(t^*) = \Delta x$. We then define the crossing point,

$$x_c(t) = x_g(t) - \Delta x = x_0 - \Delta x + v_c t = v_c(t - t^*), \quad (6.22)$$

and consider the angle with respect to x_c :

$$\theta_c(t) = \arctan \left[\frac{x_c(t)}{y(t)} \right]. \quad (6.23)$$

Taking the time derivative of Equation (6.23) results in

$$\dot{\theta}_c = \frac{x_c y}{x_c^2 + y^2} \left(\frac{\dot{x}_c}{x_c} - \frac{\dot{y}}{y} \right). \quad (6.24)$$

Assuming that y follows the simple crossing model (i.e., Equation (6.19)), $|y|$ is small when $t < t_a$. Considering the signs of variables (especially, $x_c < 0$ and $\dot{x}_c > 0$), we thus have that $\dot{\theta}_c < 0$, indicating a decreasing bearing angle. When $t > t_a + 2\tau$, the speed approaches the maximum: $\dot{y} \approx v_{\max}$, so that we have

$$\frac{\dot{x}_c}{x_c} - \frac{\dot{y}}{y} \approx \frac{v_c}{v_c(t - t^*)} - \frac{v_{\max}}{v_{\max}(t - t^*)} = 0, \quad (6.25)$$

which, upon substituting into Equation (6.24), yields $\dot{\theta}_c = 0$ or a constant bearing angle. The model thus predicts that the bearing angle should decrease at the first stage of crossing and remain constant thereafter. The constant value θ_c^* that the bearing angle approaches can be estimated by

$$\begin{aligned} \lim_{\Delta t \rightarrow 0} \theta_c(t^* - \Delta t) &= \lim_{\Delta t \rightarrow 0} \arctan \left(\frac{v_c \Delta t}{v_{\max} \Delta t} \right) \\ &= \arctan \left(\frac{v_c}{v_{\max}} \right). \end{aligned} \quad (6.26)$$

6.4 Fitting results

Data Analysis

Tables 6.3 and 6.4 show the percentage of successful crossings in this group and the proportions of two-step crossings to the total successful crossings. The success rate drops significantly when the gap length is made small at 20.8 m but still stays above 80%. The highest proportion of two-step crossings occurs when the gap is the shortest and the walking distance is the furthest.

Successful Crossings			
l_g (m) \diagdown y_0 (m)	20.8	25	33.3
-3.5	88 %	100 %	100 %
-4.5	100 %	100 %	100 %
-5.5	100 %	94 %	100 %
-6.5	82 %	94 %	100 %

Table 6.3: Proportion of successful crossings to all crossing attempts for several values of y_0 and l_g , when $v_c = 30$ km/h and vehicle type is sedan.

Equation (6.19) was fit to simple crossings with an average RMSD of 0.068 m.

Two-Step Crossings			
l_g (m) \ y_0 (m)	20.8	25	33.3
-3.5	42 %	25 %	6 %
-4.5	31 %	0 %	0 %
-5.5	0 %	26 %	0 %
-6.5	15 %	6 %	0 %

Table 6.4: Proportion of two-step crossings to all successful crossings for several values of y_0 and l_g , when $v_c = 30$ km/h and vehicle type is sedan..

The low RMSD values indicate that the model accurately describes the majority of crossings. Two-step crossings were also found to be accurate, and are discussed in the Appendix. Examples of the model equations fit to simple and two-step crossing time series are given in Figure 6.4a,b, respectively.

Behavioral Response to Gap Features

Restricting the analysis to simple crossings, we consider the variations of the parameters to changing crossing conditions. Experimental parameters y_0 and l_g affect directly the affordance of the gap by changing the temporal window of the gap or the distance the pedestrian needs to traverse to reach the gap. Effects of the experimental parameters on the three fitting parameters v_{\max} , t_a , and τ have been examined; only t_a has turned out to respond significantly. Figure 6.5 shows the distribution of t_a obtained for several values of y_0 and l_g . It is observed that t_a generally increases as y_0 approaches zero. This can be understood intuitively as follows: Recall that y_0 denotes the distance the pedestrian must traverse to reach the gap. The larger the distance, the earlier they must begin walking. However, when the initial position is farther, namely, when y_0

is made larger, this trend disappears and t_a tends to stay at slightly over one second ($t_a \gtrsim 1$ s). This is likely to result from the minimum response time. Namely, the pedestrian may not cross earlier than the earliest timing at which they can reasonably begin to walk. On the other hand, an increase in the gap size appears to lower t_a . This indicates that, when the gap is accessible earlier, the pedestrian tends to cross earlier. The distributions of the other two parameters v_{\max} and τ have also been examined. While the average value of v_{\max} tends generally to increase with y_0 , the trend is not statistically significant. No significant trends have been observed for τ .

Contrary to y_0 and l_g , the vehicle speed v_c and the vehicle type are manipulated without changing the gap affordance. These experimental parameters affect the visual perception of the gap without changing its temporal window of availability. Figure 6.6 displays the effects of the vehicle speed and type on t_a when the gap time t_g is set to be 3 s and y_0 to be -3.5 m. Doubling the vehicle speed results in a significant increase in t_a . Moreover, in several cases, buses resulted in a greater value of t_a than sedans did.

On the other hand, when the same comparison is made for data with $y_0 < -3.5$ m, there arises no significant shift in t_a or t_d upon changing the vehicle type. For $y_0 < -4.5$ m, no significant shift is observed upon changing the vehicle speed as well. This suggests that, when the initial distance is sufficiently far, pedestrian's judgement of the gap is hardly affected by the vehicle type or speed.

Finally, we examine differences among age groups. According to the Mann–Whitney U test, the difference in the distribution of v_{\max} is found to be significant ($p < 0.05$) when either the young adult group or the elderly group is compared with the child group. Both the young adult and elderly groups consistently have higher average values of v_{\max} across all crossing conditions, by about 0.3 m/s. While children have generally slightly lower values of t_a , perhaps a sign of earlier start up times to compensate for their lower speeds, the differences are not found to be statistically significant. The young adult and elderly groups do not show significant differences.

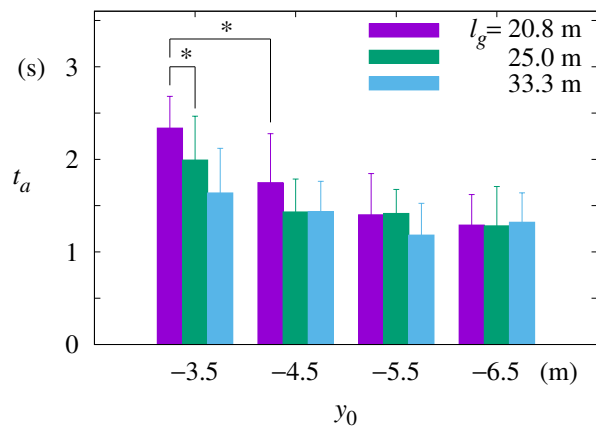


Figure 6.5: Distributions of parameter t_a for varying y_0 and l_g . Here, $v_c = 30$ km/h and vehicle type is sedan. Columns indicate the average values of t_a in the data for given experimental conditions while error bars represent standard deviations. Pairs of samples, marked with asterisks, are presumed to belong to different distributions ($p < 0.05$) according to the Mann-Whitney U test. (Note here that not all such pairs are marked.)

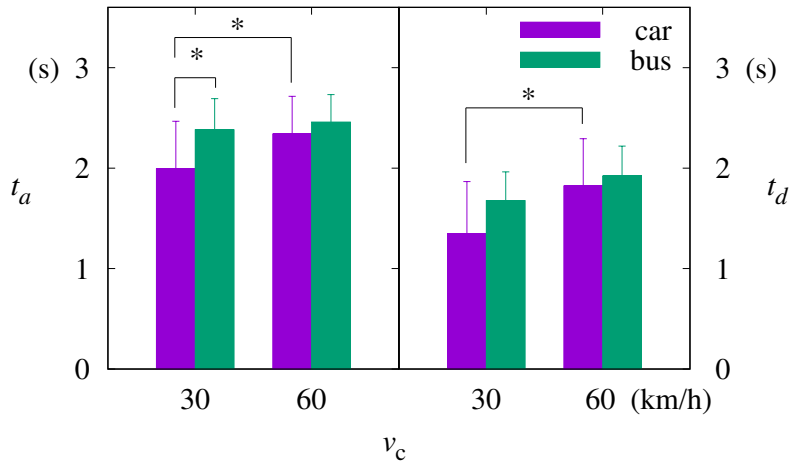


Figure 6.6: Distributions of parameters t_a (left) and t_d (right) for varying vehicle speeds v_c and for two vehicle types. Other parameters are set to $t_g = 3$ s and $y_0 = -3.5$ m. Columns indicate the average values in the data for given experimental conditions while error bars represent standard deviations. Pairs of samples, marked with asterisks, are presumed to belong to different distributions ($p < 0.05$) according to the Mann–Whitney U test.

Parameters Fall within Affordance

Due to the accuracy of the simple crossing model, we expect Equations (6.20) and (6.21) to hold for the fitting parameters derived from the data. Figure 6.7a presents the affordance boundaries in the 3D parameter space. The curved surfaces depict the boundaries specified by Equation (6.20), and each data point plots the parameters corresponding to a single crossing. For comparison, data for two-step crossings (crosses) as well as simple crossings (circles) are displayed. It is observed that the circles, corresponding to simple crossings indeed lie within the volume between the boundaries. In contrast, most of the crosses are located outside, above the higher surface. This indicates that the subject is on route to collide with the leading vehicle and therefore deceleration is necessary.

Plotting Equation (6.21) on the 2D parameter plane (v_{\max}, t_a) corresponds to the projection of the 3D plot in Figure 6.7a onto the plane defined by $\tau = 0$. This results in Figure 6.7b, where two more cases have been included in addition to the case of the gap length $l_g = 25$ m and the initial position $y_0 = -3.5$ m presented in Figure 6.7a. Namely, to probe how the distribution of parameter values shifts with l_g and y_0 , we consider the data for a larger gap $l_g = 33.3$ m and for a farther initial position $y_0 = -6.5$ m. Accordingly, Figure 6.7b presents data for three sets of the gap length and initial position together with the corresponding boundaries (lines instead of surfaces in Figure 6.7a) determined by Equation (6.21). Specifically, the cases of $(l_g = 33.3$ m, $y_0 = -3.5$ m) and $(l_g = 25$ m, $y_0 = -6.5$ m) are plotted in red and in blue, respectively, as well as the case of $(l_g = 25$ m, $y_0 = -3.5$ m) plotted in black. It is observed that, as the gap is widened, the average behavior (designated by red triangles) shifts toward smaller t_a and larger v_{\max} . This reflects the tendency of the pedestrian to cross early before the gap center when possible. On the other hand, in the case that the initial position becomes farther from the intersection point, the pedestrian must compensate by either beginning to walk earlier or walking faster. Data in blue indeed exhibit on average a decrease in t_a and a slight increase in v_{\max} (which is,

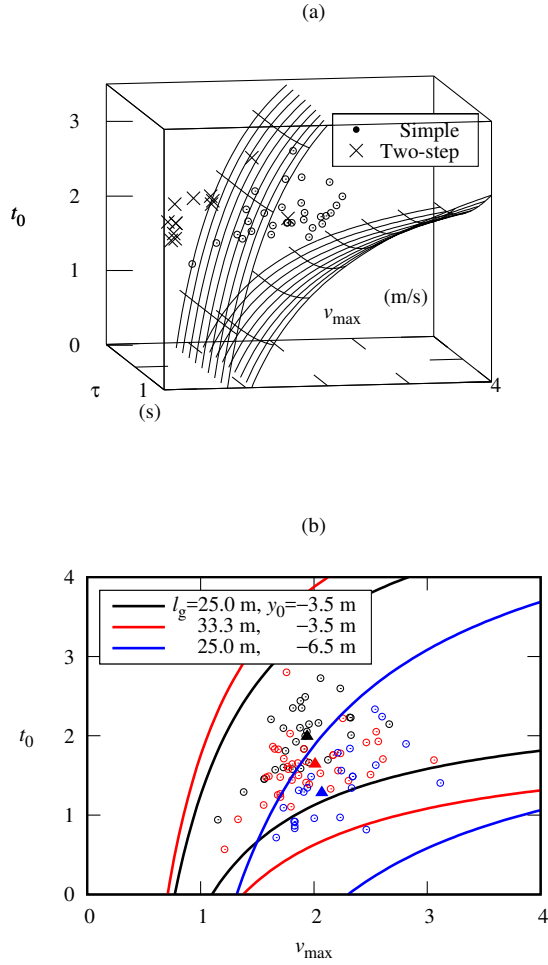


Figure 6.7: Data plotted with boundaries representing the affordance of the gap. **(a)** data plotted with surfaces in the three-dimensional parameter space (τ, v_{\max}, t_a) defined by Equation 6.20. Data points for $l_g = 25$ m and $y_0 = -3.5$ m are plotted for all age groups; dots represent simple crossings and crosses represent two-step crossings; **(b)** data plotted with boundaries on the two-dimensional plane (v_{\max}, t_a) defined by Equation 6.21. To illustrate the effects of a shift in affordance, data and boundaries for $l_g = 25$ m and $y_0 = -3.5$ m (black) are plotted with those for l_g changed to 33.3 m and for y_0 changed to -6.5 m are shown in red and in blue, respectively. Triangles indicate average parameter values.

however, not statistically significant). We remark that Figure 6.7b corresponds directly to Figures 3C and 3D of [213] while Figure 6.7a is a generalization.

Bearing Angle Analysis

Finally, we examine the bearing angle of the data and compare it with the model predictions. Figure 6.8 shows the bearing angle as a function of time for two sets of data (colored lines). The bearing angle tends to decrease in the first few seconds of crossing and to remain constant thereafter, as predicted by Equation (6.26). In addition, the analytical results given by Equation (6.23) are plotted with the average parameter values (black line). Both the theory (analytical result from the model) and the experiment (result computed from data) show that a constant bearing angle is held once the pedestrian starts moving at a nearly constant speed. It is shown in Figure 6.8 that the time interval during which the constant angle is observed is significantly shorter for $y_0 = -3.5$ m (red) than for $y_0 = -6.5$ m (cyan). This reflects the smaller value of t_a in the latter case, when the initial position is farther from the interception point.

We note that the fluctuations of the data in Figure 6.8 are due to measurement error, which is magnified immediately before the pedestrian meets the crossing point. This can be seen in Equation (6.22) by considering that $y(t) \rightarrow 0$ as $t \rightarrow t^*$, causing the error in the argument of the arctan function to become magnified.

6.5 Discussion

In this study, we have proposed a model for pedestrian crossing and utilized it to extract information from experimental data. The model fit the data with high accuracy, allowing for applications of different methods. In particular, the model allows us to visualize the affordance of each gap and see whether the data lies within it. The model also predicts a constant bearing angle, which has been observed in the data.

The fitting parameters of the model, t_a , v_{\max} and τ , provide a physically intuitive

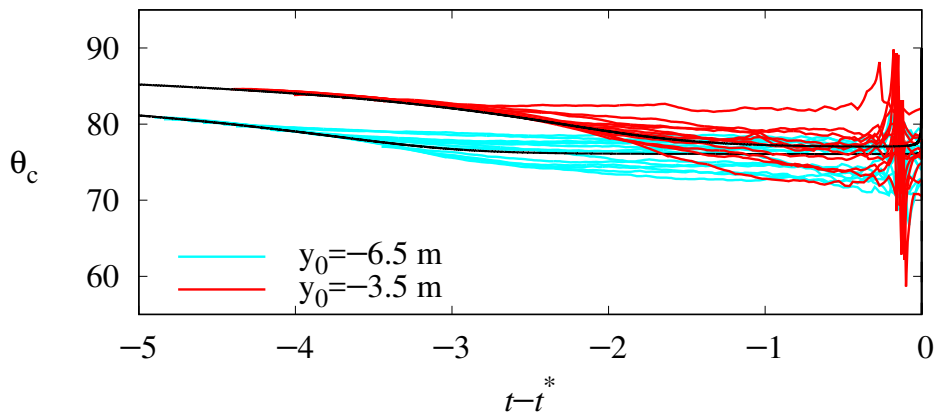


Figure 6.8: Time evolution of the bearing angle θ_c , defined by Equation 6.23. The gap length is $l_g = 25$ m and the initial position is $y_0 = -3.5$ m and -6.5 m for red and cyan lines, respectively. Colored lines are computed from data, while black lines show the analytical results using average parameter values. The time axis is given in terms of time before crossing $t - t^*$, so that the zero point is equal to the intersection time of the run (i.e., the time at which $y(t) = 0$).

interpretation of the data. Analysis has revealed that pedestrians respond to shifting gap affordances primarily by timing their accelerations, rather than changing their walking speeds, as shown by the distributions of t_a . Moreover, shifts in t_a have been observed in response to the speed of the gap and the size of the surrounding vehicles, even if the gap affordance remains the same, indicating that these environmental factors can change the visual perception of the gap. However, this trend disappeared when the initial distance was greater, suggesting that a greater distance from the road tends to offer a more accurate visual perception of the gap. It has also been observed that children's lower walking velocities indirectly shrank the affordances of the gaps and in certain situations failed to compensate.

Due to the simplicity of the equations, this methodology offers a versatile method to analyze pedestrian behavior. While the velocity equation does not necessarily need to follow a logistic function in particular, the high accuracy with which the equation fits the data and its ease of manipulation makes it an ideal tool for such an analysis.

It should be noted that the accuracy of affordance judgments in virtual environments has been questioned in previous studies [226]. In addition, it is not straightforward to measure walking speeds on treadmills, and a different method was proposed [227]. These factors should be considered when interpreting the results, but we expect them to affect neither qualitative results nor the efficacy of the model. Moreover, it would be desirable to include more general walking scenarios where the pedestrian is not constrained to walk in a straight line. This is left for future study.

Analysis of two-step crossings

In order to model two-step crossings in which there are two acceleration events (Figure 6.4b), we extend the model in the following way: We first take the acceleration equation

$$\ddot{y} = \frac{\dot{y}}{\tau} \left(1 - \frac{\dot{y}}{v_{\max}} \right), \quad (\text{A1})$$

which is equivalent to Equations 1 and 2 with appropriate initial conditions. In the two-step crossing, after acceleration (i.e., at time $t > t_a + 2\tau$), the pedestrian will decelerate at a point y_s and stop until she/he accelerates again at time t_s . This behavior may be described by adding two terms in Equation A1, which leads to

$$\ddot{y} = \frac{\dot{y}}{\tau} \left(1 - \frac{\dot{y}}{v_{\max}} \right) - r_s \dot{y} \exp \left[-\frac{(y - y_s)^2}{\sigma_s^2} \right] \theta(t_s - t) + v_s \delta(t - t_s), \quad (\text{A2})$$

where the second and the third terms of the right-hand side represent repulsion and impulse force, respectively. The repulsion is centered at position y_s with range σ_s ; y_s may be interpreted as the point beyond which the pedestrian perceives to be unsafe, due to the incoming traffic. Accordingly, y_s is the position of the flat region of the curve in Figure 6.4b, i.e., $y_s = -2.3$ m in this example. The Heaviside step function $\theta(t_s - t)$ effectively "turns off" the repulsion force at time t_s , thus removing the potential for collision after the vehicle has passed. The parameter r_s adjusts the overall strength of the repulsion. The impulse term is necessary for the model to undergo sharp acceleration from rest, so that the pedestrian starts to walk again at time t_s . In the example of Figure 6.4b, the time at which the subject begins the second acceleration is given by $t_s = 2.0$ s. The magnitude v_s of the impulse is a fraction of v_{\max} , and determines how quickly the model regains the maximum velocity.

We fit Equation A2 to the data for the case $y_0 = -3.5$ m and $l_g = 25$ m, yielding $y_s = -2.29 \pm 0.22$ m. This implies that participants who performed two-step crossings walked forward about 1.2 m before stopping, which amounts to about 1.5 m from the path of the vehicles. We also have the impulse magnitude $v_s/v_{\max} = 0.67 \pm 0.22$ and time $t_s = 2.41 \pm 0.26$ s, which corresponds to the time for the pedestrian to start walking again. This range includes the time (about 2.5 s) at which the leading vehicle passes the interception point. Other parameters, repulsion strength r_s and range σ_s , which suffer from large fluctuations due to the very limited sample number, are obtained as $r_s = 520 \pm 480 \text{ s}^{-1}$ and $\sigma_s = 0.26 \pm 0.24$ m. However, the sample size of

two-step crossings was insufficient to derive statistically meaningful results. A possible behavioral interpretation of this type of crossing is as exchanging the additional energy required for deceleration and acceleration in favor of more safety or security.

Bibliography

- [1] K. Han, S. H. Kim and M.Y. Choi. *Theor. Biol. Med. Model*, **17**, 2 (2020).
- [2] S. H. Kim, S. Goh, K. Han, J. W. Kim and M.Y. Choi. *Theor. Biol. Med. Model*. **15**, 5 (2018).
- [3] S. H. Kim, J. W. Kim, J. J. Park, M. J. Shin and M. Y. Choi. *JMIR MHealth UHealth* **7**, e12335 (2019).
- [4] S. H. Kim, J. W. Kim, H. C. Chung, G. Choi and M. Y. Choi. *Appl. Sci.* **10**, 859 (2020).
- [5] A.V.S. De Reuck and M. P. Cameron, eds. *Ciba Foundation Symposium on Lysosomes* (London: J.A. Churchill Ltd; 1963).
- [6] N. Mizushima and M. Komatsu. *Cell* **147**, 728 (2011).
- [7] D. J. Klionsky and S. D. Emr. *Science*, **290** 1717 (2000).
- [8] B. Levine and G. Kroemer. *Cell* **176** 11 (2019).
- [9] J. L. Jewell, R. C. Russell and K.-L. Guan. *Nat. Rev. Mol. Cell Biol.* **14** 133 (2013).
- [10] J. Liang, S. H. Shao, Z.-X. Xu, B. Hennessy, Z. Ding, M. Larrea, et al. *Nat. Cell Biol.* **9**, 218 (2007).
- [11] D. G. Hardie. *Genes Dev.* **25**, 1895 (2011).

- [12] K. Han, J. Kim and M.Y. Choi. *Heliyon* **1**, e00027 (2015).
- [13] F. M. Menzies, A. Fleming, A. Caricasole, C. F. Bento, S. P. Andrews, A. Ashkenazi, et al. *Neuron* **93**, 1015 (2017).
- [14] R. A. Nixon RA. *Nat. Med.* **19**, 983 (2013).
- [15] C. G. Towers and A. Thorburn A. *EBioMedicine* **14**, 15 (2016).
- [16] B. Boland, A. Kumar, S. Lee, F. M. Platt, J. Wegiel, W. H. Yu and R. A. Nixon. *J. Neurosci.* **28**, 6926 (2008).
- [17] S. Lee, Y. Sato and R. A. Nixon. *J. Neurosci.* **31**, 7817 (2011).
- [18] M. Komatsu, S. Waguri, T. Chiba, S. Murata, J.-I. Iwata, I. Tanida, et al. *Nature* **441**, 880 (2006).
- [19] T. Hara, K. Nakamura, M. Matsui, A. Yamamoto, Y. Nakahara, R. Suzuki-Migishima, et al. *Nature* **441**, 885 (2006).
- [20] H. Nam, L. E. Kim, Y. Jeon, H. Min, S. Ha, Y. Lee, et al. *Autophagy* **15**, 753 (2019).
- [21] M. P. Mattson, B. Cheng, D. Davis, K. Bryant, I. Lieberburg and R. E. Rydel. *J. Neurosci.* **12**, 376 (1992).
- [22] J. Hardy and D. J. Selkoe. *Science* **297**, 353 (2002).
- [23] D. J. Selkoe and J. Hardy. *EMBO Mol. Med.* **8**, 595 (2016).
- [24] M. Novo, S. Freire and W. Al-Soufi. *Sci. Rep.*, **8**, 1783 (2018).
- [25] S. Goh, H. W. Kwon, M.Y. Choi and J.-Y. Fortin. *Phys. Rev. E* **82**, 061115 (2010).
- [26] J. A. Mohawk, C. B. Green and J. S. Takahashi. *Annu. Rev. Neurosci.* **35**, 445 (2012).

- [27] M. Okawa and M. Uchiyama. *Sleep Med. Rev.* **11**, 485 (2007).
- [28] A. Germain and D. J. Kupfer. *Hum. Psychopharmacol.* **23**, 571 (2008).
- [29] G. Murray and A. Harvey. *Bipolar Disord.* **12**, 459 (2010).
- [30] Y.-H. Wu and D. F. Swaab. *Sleep Med.* **8**, 623 (2007).
- [31] M. Nocon, T. Hiemann, F. Muller-Riemenschneider, F. Thalau, S. Roll, S. Willich. *Eur. J. Cardiovasc. Prev. Rehabil.* **15**, 239 (2008).
- [32] C. Wen, J. Wai, M. Tsai, Y. C. Yang, T. Y. Cheng, M. Lee, et al. *The Lancet* **378**, 1244 (2011).
- [33] S. G. Trost, S. N. Blair and K. M. Khan. *Br. J. Sports Med.* **48**, 169 (2014).
- [34] R. Maddison, L. Gemming, J. Monedero, L. Bolger, S. Belton, J. Issartel, et al. *JMIR Mhealth Uhealth* **5**, e122 (2017).
- [35] H. J. Montoye, R. Washburn, S. Servais, A. Ertl, J. G. Webster, F. J. Nagle. *Med. Sci. Sports Exerc.* **15**, 403 (1983).
- [36] G. A. Meijer, K. R. Westerterp, H. Koper and F. ten Hoor. *Med. Sci. Sports Exerc.* **21**, 343 (1989).
- [37] K. Y. Chen and M. Sun. *J. Appl. Physiol.* **83**, 2112 (1997).
- [38] K. Han, S. H. Kim and M.Y. Choi. *In Submission* (2020).
- [39] OECD. *Road Infrastructure, Inclusive Development and Traffic Safety in Korea* (OECD Publishing, Paris, 2016).
- [40] M. M. Hamed. *Safety Sci.* **38** 63 (2001).
- [41] A. F. Te Velde, J. Van Der Kamp and G.J.P. Savelsbergh. Five- to twelve-year-olds' control of movement velocity in a dynamic collision avoidance task *Br. J. Dev. Psychol.* **26**, 33 (2008).

- [42] M. Azam, G.-J. Choi and Chung H. C. *Psychology* **8**, 1042 (2017).
- [43] A. Raju, B. B. Machta and J. P. Sethna. *Phys. Rev. E* **98**, 052112 (2018).
- [44] O. Conway, H. A. Akpınar, V. V. Rogov and V. Kirkin. *J. Mol. Biol.* **432**, 2483 (2020).
- [45] G. Zaffagnini and S. Martens. *J. Mol. Biol.* **428**, 1714 (2016).
- [46] F. Reggiori, M. Komatsu, K. Finley and A. Simonsen. *Int. J. Cell. Biol.* **2012**, 18 (2012).
- [47] C. Kraft, M. Peter and K. Hofmann. *Nat. Cell Biol.* **12**, 836 (2010).
- [48] T. Johansen and T. Lamark. *Autophagy* **7**, 279 (2011).
- [49] M. Fotuhi, V. Hachinski and P. J. Whitehouse. *Nat. Rev. Neurol.* **5**, 649 (2009).
- [50] *2018 Alzheimer's disease facts and figures*. *Alzheimer's & Dementia* **14**, 367 (2018).
- [51] F. J. Wippold, N. Cairns, K. Vo, D. M. Holtzman and J. C. Morris. *Am. J. Neuro-radiol.* **29**, 18 (2008).
- [52] J. Hardy, K. Duff, K. G. Hardy, J. Perez-Tur, M. Hutton. *Nat. Neurosci.* **1**, 355 (1998).
- [53] R. Kaye and C. A. Lasagna-Reeves. *J. Alzheimers Dis.* **33**, S67 (2013).
- [54] S. Oddo. *Front. Biosci.* **4**, 941 (2012).
- [55] P. Nilsson, K. Loganathan, M. Sekiguchi, Y. Matsuba, K. Hui, S. Tsubuki, et al. *Cell Rep.* **5**, 61 (2013).
- [56] P. Nilsson, M. Sekiguchi, T. Akagi, S. Izumi, T. Komori, K. Hui, et al. *Am. J. Pathol.* **185**, 305 (2015).

- [57] P. Nilsson and T. C. Saido. *BioEssays* **36**, 570 (2014).
- [58] E. Gibbs, J. M. Silverman, B. Zhao, X. Peng, J. Wang, C. L. Wellington, et al. *Sci. Rep.* **9**, 9870 (2019).
- [59] K. Bhaskar, M. Miller, A. Chludzinski, K. Herrup, M. Zagorski, B. T. Lamb. *Mol. Neurodegener.* **4**, 14 (2009).
- [60] C. Wang, J.-T. Yu, D. Miao, Z.-C. Wu, M.-S. Tan and L. Tan. *Mol. Neurobiol.* **49**, 120 (2014).
- [61] A. Caccamo, S. Majumder, A. Richardson, R. Strong and S. Oddo. *J. Biol. Chem.* **285**, 13107 (2010).
- [62] C. M. Yuede, H. Lee, J. L. Restivo, T. A. Davis, J. C. Hettinger, C. E. Wallace, et al. *J. Exp. Med.* **213**, 677 (2016).
- [63] K. G. Mawuenyega, W. Sigurdson, V. Ovod, L. Munsell, T. Kasten, J. C. Morris, et al. *Science* **330**, 1774 (2010).
- [64] U. Pfeifer. *J. Cell Biol.* **78**, 152 (1978).
- [65] C. M. Schworer, K. A. Shiffer and G. E. Mortimore. *J. Biol. Chem.* **256**, 7652 (1981).
- [66] J. Kovács, E. Fellingner, A. P. Kárpáti, A. L. Kovács, L. László and G. Réz. *Virchows Archiv. B* **53**, 183 (1987).
- [67] P. J. Plomp, P. B. Gordon, A. J. Meijer, H. Høyvik and P. O. Seglen. *J. Biol. Chem.* **264**, 6699 (1989).
- [68] P. J. Plomp, E. J. Wolvetang, A. K. Groen, A. J. Meijer, P. B. Gordon and P. O. Seglen. *Eur. J. Biochem.* **164**, 197 (1987).
- [69] P. O. Seglen and P. B. Gordon. *J. Cell Biol.* **99**, 435 (1984).

- [70] J.-Y. Lee and T.-P. Yao. *Autophagy* **6**, 555 (2010).
- [71] C. Behrends and S. Fulda. *Int. J. Cell Biol.* **2012**, 673290 (2012).
- [72] A. Kuma A and N. Mizushima. *Semin. Cell Dev. Biol.* **21**, 683 (2010).
- [73] G. E. Mortimore, A. R. Pösö. *Annu. Rev. Nutr.* **7**, 539 (1987).
- [74] T. Yoshimori. *Biochem. Biophys. Res. Commun.* **313**, 453 (2004).
- [75] N. Mizushima, A. Yamamoto, M. Matsui, T. Yoshimori and Y. Ohsumi. *Mol. Biol. Cell* **15**, 1101 (2004).
- [76] K. Han, H. W. Kwon, H. Kang, J. Kim, M.-S. Lee and M.Y. Choi. *Physica A* **391**, 686 (2012).
- [77] K. Han, J. Kim and M.Y. Choi. *J. Bio. Syst.* **22**, 659 (2014).
- [78] K. Han, J. Kim and M. Y. Choi. *Theor. Biol. Med. Model.* **11**, 31 (2014).
- [79] R. J. Bateman, L. Y. Munsell, J. C. Morris, R. Swarm R, K. E. Yarasheski and D. M. Holtzman. *Nat. Med.* **12**, 856 (2006).
- [80] P. O. Seglen and A. E. Solheim. *Biochim. Biophys. Acta.* **520**, 630 (1978).
- [81] P. O. Seglen and P. Bohley. *Experientia* **48**, 158 (1992).
- [82] D. J. Klionsky, A. M. Cuervo, J. W. A. Dunn, B. Levine, I. J. van der Klei and P. O. Seglen. *Autophagy* **3**, 413 (2007).
- [83] I. Tavassoly, J. Parmar, A. N. Shajahan-Haq, R. Clarke, W. T. Baumann and J. J. Tyson. *CPT Pharmacometrics Syst. Pharmacol.* **4**, 263 (2015).
- [84] I. Tavassoly. *Dynamics of Cell Fate Decision Mediated by the Interplay of Autophagy and Apoptosis in Cancer Cells: Mathematical Modeling and Experimental Observations* (Cham: Springer International Publishing, Switzerland, 2015).

- [85] O. Kapuy, P. K. Vinod, J. Mandl and G. Bánhegyi. *Mol. Biosyst.* **9**, 296 (2013).
- [86] H. Jin and J. Lei. *J. Theor. Biol.* **402**, 45 (2016).
- [87] B. Liu, Z. N. Oltvai, H. Bayır, G. A. Silverman, S. C. Pak, D. H. Perlmutter and I. Bahar. *Sci. Rep.* **7**, 17605 (2017).
- [88] D. Ma, S. Panda and J. D. Lin. *EMBO J.* **30**, 4642 (2011).
- [89] U. Pfeifer and H. Scheller. *J. Cell Biol.* **64**, 608 (1975).
- [90] U. Pfeifer and P. Strauss. *J. Mol. Cell Cardiol.* **13**, 37 (1981).
- [91] C. E. Remé and M. Sulser. *Graefes Arch. Klin. Exp. Ophthalmol.* **203**, 261 (1977).
- [92] U. Pfeifer. *Virchows Archiv. B* **12**, 195 (1972).
- [93] U. M. Sachdeva and C. B. Thompson. *Autophagy* **4**, 581 (2008).
- [94] U. Pfeifer U. *Virchows Archiv. B* **10** 1 (1972).
- [95] U. Pfeifer and J. Bertling. *Virchows Archiv. B* **24**, 109 (1977).
- [96] F. Nazio, M. Carinci, C. Valacca, P. Bielli, F. Strappazon, M. Antonioli, et al. *J. Cell Biol.* **215**, 841 (2016).
- [97] M. Ryzhikov, A. Ehlers, D. Steinberg, W. Xie, E. Oberlander, S. Brown, et al. *Cell Rep.* **26**, 1880 (2019).
- [98] M. Dorvash, M. Farahmandnia and I. Tavassoly. *Interdiscip. Sci.* **2019**, 1 (2019).
- [99] A. Yamamoto and A. Yue. *Annu. Rev. Neurosci.* **37**, 55 (2014).
- [100] S. E. Hickman, E. K. Allison, and J. El Khoury. *J. Neurosci.* **28**, 8354 (2008).
- [101] G. G. Glenner and W. W. Caine. *Biochem. Biophys. Res. Commun.* **120**, 885 (1984).

- [102] F. Chiti and C. M. Dobson. *Annu. Rev. of Biochem.* **75**, 333 (2006).
- [103] D. Scheuner, C. Eckman, M. Jensen, X. Song, M. Citron, N. Suzuki *et al.* *Nat. Med.* **2** 864 (1996).
- [104] B. De Strooper, P. Saftig, K. Craessaerts, H. Vanderstichele, G. Guhde, W. Annaert *et al.* *Nature*, **391**, 387 (1998).
- [105] M. S. Wolfe, W. Xia, B. L. Ostaszewski, T. S. Diehl, W. T. Kimberly and D. J. Selkoe. *Nature* **398**, 513 (1999).
- [106] E. H. Corder, A. M. Saunders, W. J. Strittmatter, D. E. Schmechel, P. C. Gaskell, G. Small *et al.* *Science*, **261**, 921 (1993).
- [107] G. W. Rebeck, J. S. Reiter, D. K. Strickland and B. T. Hyman. *Neuron*, **11**, 575 (1993).
- [108] D. M. Holtzman, K. R. Bales, T. Tenkova, A. M. Fagan, M. Parsadanian, L. J. Sartorius, *et al.* *Proc. Nat. Acad. Sci.* **97**, 2892 (2000).
- [109] J. M. Castellano, J. Kim, F. R. Stewart, H. Jiang, R. B. DeMattos, B. W. Patterson, *et al.* *Sci. Transl. Med.* **3**, 89ra57 (2011).
- [110] P. Hollingworth, D. Harold, R. Sims, A. Gerrish, J. C. Lambert, M. M. Carrasquillo, *et al.* *Nat. Genet.* **43**, 429 (2011).
- [111] W. S. Kim, H. Li, K. Ruberu, S. Chan, D. A. Elliott, J. K. Low, *et al.* *J. Neurosci.* **33**, 4387 (2013).
- [112] C. G. Glabe. *J. Biol. Chem.* **283**, 29639 (2008).
- [113] G. Bitan, M. D. Kirkitadze, A. Lomakin, S. S. Vollers, G. B. Benedek, and D. B. Teplow. *Proc. Nat. Acad. Sci.* **100**, 330 (2003).
- [114] S. Baglioni, F. Casamenti, M. Bucciantini, L. M. Luheshi, N. Taddei, F. Chiti, *et al.* *J. Neurosci.* **26**, 8160 (2006).

- [115] P. N. Lacor, M. C. Buniel, P. W. Furlow, A. S. Clemente, P. T. Velasco, M. Wood, *et al.* **27**, 796 (2007).
- [116] E. K. Pickett, R. M. Koffie, S. Wegmann, C. M. Henstridge, A. G. Herrmann, M. Colom-Cadena, *et al.* *J. Alzheimers Dis.* **53**, 787 (2016).
- [117] G. M. Shankar, S. Li, T. H. Mehta, A. Garcia-Munoz, N. E. Shepardson, I. Smith, *et al.* *Nat. Med.* **14**, 837 (2008).
- [118] R. M. Koffie, M. Meyer-Luehmann, T. Hashimoto, K. W. Adams, M. L. Mielke, M. Garcia-Alloza, *et al.* *Proc. Nat. Acad. Sci.* **106**, 4012 (2009).
- [119] A. Serrano-Pozo, M. L. Mielke, A. Muzitansky, T. Gómez-Isla, J. H. Growdon, B. J. Bacskai, *et al.* *J. Neuropathol. Exp. Neurol.* **71**, 694 (2012).
- [120] A. Serrano-Pozo, R. A. Betensky, M. P. Frosch and B. T. Hyman. *Am. J. Pathol.* **186**, 375 (2016).
- [121] M. Querol-Vilaseca, M. Colom-Cadena, J. Pegueroles, R. Nuñez-Llaves, J. Luque-Cabecerans, L. Muñoz-Llahuna and J. Clarimon. *Sci. Rep.* **9**, 1 (2019).
- [122] J. Jo, M. Y. Choi and D. S. Koh. *Biophys. J.* **93**, 2655 (2007).
- [123] B. T. Hyman, H. L. West, G. W. Rebeck, S. V. Buldyrev, R. N. Mantegna, M. Ukleja, *et al.* *Proc. Nat. Acad. Sci.* **92**, 3586 (1995).
- [124] S. Kumar-Singh, D. Pirici, E. McGowan, S. Serneels, C. Ceuterick and J. Hardy, *et al.* **167**, 527 (2005).
- [125] D. S. Eisenberg and M. R. Sawaya. *Annu. Rev. of Biochem.* **86**, 69 (2017).
- [126] A. Lomakin, D. S. Chung, G. B. Benedek, D. A. Kirschner and D. B. Teplow. *Proc. Nat. Acad. Sci.* **93**, 1125 (1997).
- [127] W. Zheng, M.-Y. Tsai, M. Chen, and P. G. Wolynes. *Proc. Nat. Acad. Sci.* **113**, 11835 (2016).

- [128] W. Zheng, M. Y. Tsai and P. G. Wolynes. *J. Am. Chem. Soc.* **139**, 16666 (2017).
- [129] F. Panza, M. Lozupone, G. Logroscino, and B. P. Imbimbo. *Nat. Rev. Neurol.* **15**, 73 (2019).
- [130] D. Bell-Pedersen, V. M. Cassone, D. J. Earnest, S. S. Golden, P. E. Hardin, T. L. Thomas and M. J. Zoran. *Nat. Rev. Genet.* **6**, 544 (2005).
- [131] C. B. Saper, G. Cano and T. E. Scammell. *J. Comp. Neurol.* **493**, 92 (2005).
- [132] B. Rusak, H. A. Robertson, W. Wisden and S. P. Hunt. *Science* **248**, 1237 (1990).
- [133] M. S. Freedman, R. J. Lucas, B. Soni, M. von Schantz, M. Munoz, Z. David-Gray, R. Foster. *Science* **284**, 502 (1999).
- [134] J. F. Duffy and K. P. Wright Jr. *J. Biol Rhythms* **20**, 326 (2005).
- [135] D.-J. Dijk and M. von Schantz. *J. Biol. Rhythms* **20**, 279 (2005).
- [136] M. G. Lee, O. K. Hassani and B. E. Jones. *J. Neurosci.* **25**, 6716 (2005).
- [137] T. Porkka-Heiskanen, R. E. Strecker, M. Thakkar, A. A. Bjorkum, R. W. Greene, R. W. McCarley. *Science.* **276**, 1265 (1997).
- [138] C. B. Saper, T. C. Chou and T. E. Scammell. *Trends Neurosci.* **24**, 726 (2001).
- [139] C. B. Saper, T. E. Scammell and J. Lu. *Nature* **437**, 1257 (2005).
- [140] A. Borbély. *Hum. Neurobiol.* **1**, 195 (1982).
- [141] M. J. Rempe, J. Best and D. Terman. *J. Math. Biol.* **60**, 615 (2010).
- [142] V. Booth, C. G. D. Behn. *Math. Biosci.* **54** 68 (2014).
- [143] A. J. K. Phillips and P. A. Robinson. *J. Biol. Rhythms.* **22**, 167 (2007).
- [144] A. J. K. Phillips and P. A. Robinson. *Phys. Rev. E.* **79**, 021913 (2009).

- [145] B. D. Fulcher, A. J. K. Phillips and P. A. Robinson. *Phys. Rev. E.* **78**, 051920 (2008).
- [146] D.-P. Yang, L. McKenzie-Sell, A. Karanjai and P. A. Robinson. *Phys. Rev. E.* **94**, 022412 (2016).
- [147] B. D. Fulcher, A. J. K. Phillips and P. A. Robinson. *J. Theor. Biol.* **264**, 407 (2010).
- [148] M. Puckeridge, B. D. Fulcher, A. J. K. Phillips and P. A. Robinson. *J. Theor. Biol.* **273**, 44 (2011).
- [149] B. D. Fulcher, A. J. K. Phillips, S. Postnova and P. A. Robinson. *PLoS ONE* **9**, e91982 (2014).
- [150] S. Postnova, P. A. Robinson and D. D. Postnov. *PLoS ONE.* **8**, e53379 (2013).
- [151] D. L. Rowe, P. A. Robinson and C. J. Rennie. *J. Theor. Biol.* **231**, 413 (2004).
- [152] P. A. Robinson, C. J. Rennie, D. L. Rowe and S. C. O’Conner. *Hum. Brain Mapp.* **23**, 53 (2004).
- [153] St. M. A. Hilaire, E. B. Klerman, S. B. Khalsa, K. P. Wright Jr., C. A. Czeisler and R. E. Kronauer. *J. Theor. Biol.* **247**, 583 (2007).
- [154] C. A. Czeisler, J. F. Duffy, T. L. Shanahan, E. N. Brown, J. F. Mitchell, D. W. Rimmer, et al. *Science.* **25**, 2177 (1999).
- [155] P. J. Schwartz, D. L. Murphy, T. A. Wehr, D. Garcia-Borreguero, D. A. Oren, D. E. Moul, et al. *Arch. Gen. Psychiatry.* **54**, 375 (1997).
- [156] A. J. K. Phillips, B. D. Fulcher, P. A. Robinson and E. B. Klerman. *PLoS Comput. Biol.* **9**, e1003213 (2013).
- [157] R. L. Sack, A. J. Lewy, M. L. Blood, L. D. Keith and H. Nakagawa. *J. Clin. Endocrinol. Metab.* **75**, 127 (1992).

- [158] S. W. Lockley, K. J. Skene, J. Arendt, H. Tabandeh, A. C. Bird and R. DeFrance. *J. Clin. Endocrinol. Metab.* **82**, 3763 (1997).
- [159] J. K. Wyatt. *Sleep*. **27** 1195 (2004).
- [160] N. E. Rosenthal, D. A. Sack and J. C. Gillin. *Arch. Gen. Psychiatry*. **41**, 72 (1984).
- [161] C. I. Eastman, M. A. Young and L. F. Fogg. *Arch. Gen. Psychiatry*. **55**, 883 (1998).
- [162] D. F. Kripke. *J. Affect. Disord.* **49**, 109 (1998).
- [163] F. Benedetti, C. Colombo, B. Barbini, E. Campori and E. Smeraldi. *J. Affect. Disord.* **62**, 221 (2001).
- [164] A. Joshi and K. Wong-Lin. *Orexin and sleep: functional and clinical aspects*. p. 299–322. T. Sakurai, S. R. Pandi-Perumal and J. M. Monti, editors (Cham: Springer International Publishing, Switzerland 2015).
- [165] D. H. Avery, A. Khan, S. R. Dager, G. B. Cox and D. L. Dunner. *Acta. Psychiatr. Scand.* **82**, 335 (1990).
- [166] R. Passmore and J.V.G.A. Durnin. *Physiol. Rev.* **35**, 801 (1955).
- [167] J. E. Cotes and F. Meade. *Ergonomics* **3**, 97 (1960).
- [168] D. B. Dill. *J. Appl. Physiol.* **20**, 19 (1965).
- [169] D. R. Menier and L.G.C.E. Pugh. *J. Physiol.* **197**, 717 (1968).
- [170] W. H. van der Walt and C. H. Wyndham. *J. Appl. Physiol.* **34**, 559 (1973).
- [171] K. G. Holt, J. Hamill and R. O. Andres. *Med. Sci. Sports Exerc.* **23**, 491 (1990).
- [172] R. Margaria, P. Cerretelli, P. Aghemo and G. Sassi. *J. Appl. Physiol.* **18**, 367 (1963).

- [173] M. Y. Zarrugh and C. W. Radcliffe. *Eur. J. Appl. Physiol.* **38**, 215 (1978).
- [174] P. R. Cavanagh and K. R. Williams. *Med. Sci. Sports Exerc.* **14**, 30 (1982).
- [175] K. Steudel. *Am. J. Phys. Anthropol.* **99**, 345 (1996).
- [176] A. E. Minetti and R. M. Alexander. *J. Theor. Biol.* **186**, 467 (1997).
- [177] R. M. Alexander. *Phil. Trans. R Soc. Lond. B* **338**, 189 (1992).
- [178] J. Doke, J. M. Donelan and A. D. Kuo. *J. Exp. Biol.* **208**, 439 (2005).
- [179] A. D. Kuo. *J. Biomech. Eng.* **124**, 113 (2002).
- [180] A. D. Kuo, J. M. Donelan and A. Ruina. *Exerc. Sport Sci. Rev.* **33**, 88 (2005).
- [181] A. Ruina, J.E.A. Bertram and M. Srinivasan. *J. Theor. Biol.* **237**, 170 (2005).
- [182] Y. Osaki, M. Kunin, B. Cohen and T. Raphan. Three-dimensional kinematics and dynamics of the foot during walking: a model of central control mechanisms. *Exp. Brain Res.* **176**, 476 (2007).
- [183] S. F. Donker, T. Mulder, B. Nienhuis and J. Duysens. *Exp. Brain Res.* **146**, 26 (2002).
- [184] E. P. Zehr and C. Haridas. *Exp. Brain Res.* **149**, 260 (2003).
- [185] E. Hirasaki, S. T. Moore, T. Raphan and B. Cohen. *Exp. Brain Res.* **127**, 117 (1998).
- [186] J. M. Hausdorff, G. Yogev, S. Springer, E. S. Simon and N. Giladi. *Exp. Brain Res.* **164**, 541 (2005).
- [187] O. Blin, A. M. Ferrandez and G. Serratrice. *Exp. Brain Res.* **98**, 91 (1990).
- [188] S. H. Collins, M. Wisse and A. Ruina. *Int. J. Robotics Res.* **20**, 607 (2001).

- [189] J. A. Noah, D. K. Spierer, J. Gu and S. Bronner. *J. Med. Eng. Tech.* **37**, 456 (2013).
- [190] J. V. Brugniaux, A. Niva, I. Pulkkinen, R.M.T. Laukkanen, J.-P. Richalet and A. P. Pichon. *Br. J. Sports Med.* **44**, 245 (2010).
- [191] S. Härtel, J.-P. Gnam, S. Löffler and K. Bös. *Eur. Rev. Aging Phys. Act.* **8**, 109 (2011).
- [192] J. Takacs, C. L. Pollock, J. R. Guenther, M. Bahar, C. Napier and M. A. Hunt. *J. Sci. Med. Sport* **17**, 496 (2014).
- [193] K. M. Diaz, D. J. Krupka, M. J. Chang, J. Peacock, Y. Ma, J. Goldsmith, J. E. Schwartz and K. W. Davidson. *Int. J. Cariol.* **185**, 138 (2015).
- [194] W. J. Tucker, D. M. Bhammar, B. J. Sawyer, M. P. Buman and G. A. Gaesser. *BMC Sports Sci. Med. Rehabil.* **7**, 14 (2015).
- [195] A. Shcherbina, C. M. Mattsson, D. Waggott, H. Salisbury, J. W. Christle, T. Hastie, et al. *Pers. Med.* **7**, 3 (2017).
- [196] P. N. Ainslie, T. Reilly and K. R. Westerterp. *Sports Med.* **33**, 683 (2003).
- [197] J. Levine. *Public Health Nutr.* **8**, 1123 (2005).
- [198] H. A. Haugen, L.-N. Chan and F. Li. *Nutr. Clin. Pract.* **22**, 377 (2007).
- [199] M. D. Mifflin, St. S. T. Jeor, L. A. Hill, B. J. Scott, S. A. Daugherty and Y. O. Koh. *Am. J. Clin. Nutr.* **51** 241 (1990).
- [200] S. Plagenhoef, F. G. Evans and T. Abdelnour. *Res. Q. Exerc. Sport* **54**, 169 (1983).
- [201] A. E. Minetti, C. Moia, G. S. Roi, D. Susta and G. Ferretti. *J. Appl. Physiol.* **93**, 1039 (2002).

- [202] A. E. Minetti, L. P. Ardigo and F. Saibene. *J. Physiol.* **472**, 725 (1993).
- [203] H. C. Chung, S. H. Kim, G. Choi, J. W. Kim and M.Y. Choi. *J. Vis. Exp.* **160**, e61116 (2020).
- [204] B. R. Fajen and W. H. Warren. *Brett. J. Exp. Psychol. Human* **29**, 343 (2003).
- [205] S. Chapman. *Am. J. Phys.* **36**, 868 (1968).
- [206] J. Bastin, C. Craig and G. Montagne. *Hum. Mov. Sci.* **25**, 718 (2006).
- [207] B. R. Fajen B. R. and W. H. Warren. *Exp. Brain Res.* **180**, 303 (2007).
- [208] W. H. Warren, B. A. Kay, W. D. Zosh, A. P. Duchon and S. Sahuc. *Nat. Neurosci.* **4**, 213 (2001).
- [209] B. R. Fajen and W. H. Warren. *Perception* **33**, 689 (2004).
- [210] J. J. Gibson. *The ecological approach to visual perception*. (Houghton Mifflin Harcourt, Boston, USA, 1979).
- [211] J. M. Plumert, J. K. Kearney and J. F. Cremer. *Child Dev.* **75**, 1243 (2004).
- [212] B. R. Fajen and J. S. Matthis. *J. Exp. Psychol. Hum. Percept. Perform.* **37**, 1442 (2011).
- [213] B. R. Fajen. *Front. Behav. Neurosci.* **7**, 1–15 (2013).
- [214] A. E. Patla. *Gait Posture*, **5**, 54 (1997).
- [215] G. Yannis, E. Papadimitriou, and A. Theofilatos. *Transport. Plan. Techn.* **36**, 450 (2013).
- [216] G. K. Zipf. *Human Behavior and the Principle of Least Effort*. (Addison-Wesley, Cambridge, 1949).
- [217] S. J. Guy, S. Curtis, M. C. Lin and D. Manocha. *Phys. Rev. E* **85**, 016110 (2012).

- [218] E. Patzelt, W. Kool, A. Millner, and S. Gershman. *Sci. Rep.* **9**, 1689 (2019).
- [219] D. F. Styer, M. S. Balkin, K. M. Becker, M. R. Burns, C. E. Dudley, C. E. Forth, et al. *Am. J. Phys.* **70**, 288 (2002).
- [220] C. W. Misner, K. S. Thorne and J. A. Wheeler. *Gravitation* (Freeman, San Francisco, 1973).
- [221] B. J. Chihak J. M. Plumert, C. J. Ziemer and J. K. Kearney. *J. Exp. Psychol. Hum. Percept. Perform* **36**, 1535.
- [222] M. Ostrogradsky. *Mem. Ac. St. Petersburg* **VI**, 385 (1850).
- [223] R. P. Woodard. *Lect. Notes Phys.* **720**, 403 (2007).
- [224] H. Motohashi and T. Suyama. *Phys. Rev. D* **91**, 085009 (2015).
- [225] F. C. Anderson and M. G. Pandy. *J. Biomech. Engineering* **123**, 381 (2001).
- [226] S. H. Creem-Regehr D. M. Gill G. D. Pointon, B. Bodenheimer and J. Stefanucci. *Frontiers Robotics AI* **6**, 96 (2019).
- [227] J. Yoon, S. H. Park and D. L. Damiano. *J. Neuroeng. Rehabil.* **9**, 62 (2012).

초 록

생물계는 자연의 대표적인 복잡계로, 여러 거리와 시간 눈금에서 떠오름 현상을 보인다. 생물계를 다루는 이론 물리학자에게는 하나의 이론적 틀로 이 복잡성을 이해하는 것이 궁극적인 목표가 되겠지만, 아직 각 눈금에서 떠오르는 현상을 하나씩 이해하기 위한 노력이 필요하다. 생물학의 많은 분야들은 각각의 대상 현상에 대한 방대한 실험 자료를 이해하기 위한 수학적 모형을 필요로 한다.

이 논문에서는 수리적 모형과 통계 물리적 방법일 이용하여 다섯 가지 생물계의 현상을 다루고 있다. 그 주제는 자가포식의 동역학과 아밀로이드-베타 농도에 주는 영향, 알차이머 병에서 아밀로이드-베타 단백질의 응집, 일주기의 환경과의 때맞음과 빛 치료, 기울어진 땅 위 걸음질할 때의 에너지 소비, 보행자의 행동 동역학이다. 각 주제에 대한 배경을 소개하고 그 현상을 연구하기 위한 수리적 모형을 소개한다. 그의 결과에 대한 논의가 잇따른다.

주요어: 수리적 모형, 복잡계, 생물계, 떠오름, 자가포식, 아밀로이드-베타, 알차이머 병, 크기 분포, 자라남 모형, 수면-각성 모형, 일주기 리듬, 오렉신, 때맞음, 에너지 소비, 걷기, 행동 동역학, 보행자, 라그랑주 동역학, 최소 노력의 법칙

학번: 2013-22982

감사의 글

학문의 길로 이끌어 주시고 학위 과정 동안 가르침을 주신 최무영 교수님께 깊은 감사의 말씀을 드립니다. 선생님께서는 대상과 상관 없이 물리학자로서 치밀하게 자연을 연구하는 방법을 알려주셨습니다. 그리고 학자로서 세상을 바라보는 법을 알려주셨습니다. 선생님께서 “지도 교수가 시시하게 느껴질 때 졸업할 준비가 된 것이다”라고 농담 삼아 말씀 하신 적이 있는데, 그럼 준비가 덜 된 것일까요. 학교를 떠나지만 앞으로도 선생님께 배우고 함께 연구하기를 바랍니다.

저의 첫 연구 주제를 소개해 주시고 4, 5, 6장 내용을 지도해주신 김종원 교수님께 감사를 드립니다. 교수님께서 연구자로서의 기본을 알려주시고 어려운 상황을 웃음으로 넘길 수 있는 해학과 지혜를 보여주셨습니다. 감사합니다.

자가포식과 아밀로이드-베타 주제를 소개시켜 주시고 지도해주신 한경림 박사님께 감사를 드립니다. 경림 형은 저에게 연구에 몰입한다는게 어떤건지 보여주시고, 학위 받은 이후 독립적인 학자의 길을 찾는 방법을 알려주셨습니다. 지금도 함께 연구를 할 수 있어 기쁘고 앞으로가 더 기대 됩니다.

박사학위 초기 동안 많은 도움을 주신 고세건 박사님께 감사합니다. 세건이 형의 아낌 없는 관심 덕분에 잘 적응했던 것 같습니다. 밥을 사주시며 위로해 주신 강혁 박사님, 늘 열심히 연구하는 모습을 보여주신 아람이 형, 많은 실질적인 조언을 주신 형준이 형, 항상 따뜻하게 대해주신 찬수형께 감사합니다. 항상 새로운 관점을 알려주시는 조정효 교수님, 항상 즐겁게 이야기를 나눌 수 있는 형님 임종수 박사님께 감사합니다. 상산수리과학관에서 늦게까지 연구하시며 저에게 영감을 주신 최인령 교수님께 감사합니다.

제가 선배님들께 도움 받은 만큼 해주지 못한 후배 지혜와 준혁이에게 미안하고, 그래도 잘 해주고 있어서 고맙습니다. 앞으로 훌륭하게 뜻을 펼칠 수 있을 것이라고 믿습니다.

보행행동 주제를 소개시켜 주시고 군산에 내려갔을때 따뜻한 마음으로 맞이해주신 정현채 교수님께 감사합니다.

박사과정 시작하기 전에 인턴으로서 받아주셔서 많은 것을 배우게 해주신 이주영 교수님께 이 자리를 빌려 감사의 말씀을 드립니다.

무한한 사랑과 지원을 주신 어머니 박신순 교수님과 아버지 김선욱 교수님께 감사와 사랑의 마음을 전합니다. 부모님께서 부족한 저를 항상 믿어주셔서 공부를 시작할 수 있었고 박사 과정을 무사히 끝낼 수 있었습니다. 인생에서 중요한게 무엇인지 일깨워주는 아우 순곤이에게도 사랑과 고마운 마음을 보냅니다.

Finally, thank you Soo Jin for picking me up whenever I was down. We did it!



저작자표시-비영리-변경금지 2.0 대한민국

이용자는 아래의 조건을 따르는 경우에 한하여 자유롭게

- 이 저작물을 복제, 배포, 전송, 전시, 공연 및 방송할 수 있습니다.

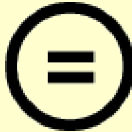
다음과 같은 조건을 따라야 합니다:



저작자표시. 귀하는 원저작자를 표시하여야 합니다.



비영리. 귀하는 이 저작물을 영리 목적으로 이용할 수 없습니다.



변경금지. 귀하는 이 저작물을 개작, 변형 또는 가공할 수 없습니다.

- 귀하는, 이 저작물의 재이용이나 배포의 경우, 이 저작물에 적용된 이용허락조건을 명확하게 나타내어야 합니다.
- 저작권자로부터 별도의 허가를 받으면 이러한 조건들은 적용되지 않습니다.

저작권법에 따른 이용자의 권리는 위의 내용에 의하여 영향을 받지 않습니다.

이것은 [이용허락규약\(Legal Code\)](#)을 이해하기 쉽게 요약한 것입니다.

[Disclaimer](#)

이학박사학위논문

Multi-scale modeling of biological systems

생물계의 여러 눈금 모형화

2020년 7월

서울대학교 대학원
물리천문학부
김 순 호

이학박사학위논문

Multi-scale modeling of biological systems

생물계의 여러 눈금 모형화

2020년 7월

서울대학교 대학원
물리천문학부
김 순 호

Abstract

Biological systems are the quintessential complex systems of nature, with emergent phenomena at multiple length scales. While the theoretical physicist's ultimate goal would be to understand the complexities of life under a unified framework, there is still much work to be done in understanding the rules that dictate the rich emergent phenomenon at each scale. Many fields of biology are in need of mathematical models that can explain the vast amount of experimental data regarding their specific target phenomena.

In this dissertation, five biological phenomena are studied with the aid of mathematical models and methods from statistical physics: autophagy dynamics and its effect on amyloid- β peptide levels; aggregation of amyloid- β in Alzheimer's disease; entrainment of the circadian system and recovery by light treatment; energy expenditure during gradient walking; and the behavioral dynamics of interceptive walking. For each topic, we provide background information on the topic at hand, discuss a model developed to understand the system, report the results of the model, and discuss the meaning of the results.

keywords: mathematical model, complex systems, biological systems, emergence, autophagy, amyloid-beta, Alzheimer's disease, size distribution, growth model, sleep-wake switch, circadian rhythm, orexin, entrainment, energy expenditure, gradient walking, behavioral dynamics, pedestrian, Lagrangian mechanics, principle of least effort

student number: 2013-22982

Contents

Abstract	i
Contents	ii
List of Tables	iv
List of Figures	v
1 Introduction	1
2 Autophagy and its effect on amyloid-β peptide levels	5
2.1 Background	5
2.2 Mathematical model	7
2.3 Model dynamics	15
2.4 Discussion of the autophagy model	23
3 Aggregation of amyloid-β peptides in Alzheimer's disease	28
3.1 Background	28
3.2 Merging model	30
3.3 Toxicity of aggregate size distributions	31
3.4 Size distribution of plaques	32
3.5 Discussion: Towards a multi-scale model of Alzheimer's disease	35

4	Disruption of the circadian rhythm and recovery via light treatment	36
4.1	Background	36
4.2	Model of the sleep-wake system coupled with the circadian oscillator	38
4.3	Period Locking Zone	45
4.4	Diseased States and Light Treatment	48
4.5	Discussion	54
5	Predicting expenditure during gradient walking	57
5.1	Background	57
5.2	Data collection	59
5.3	Model construction	62
5.4	Fitting results	67
5.5	Discussion	69
6	Behavioral dynamics of interceptive walking	71
6.1	Background	71
6.2	Model based on a least action principle	73
6.3	Recasting the model to describe bearing angle and affordance	85
6.4	Fitting results	89
6.5	Discussion	96
	국문 초록	117
	감사의 글	118

List of Tables

2.1	Nominal parameters for the autophagy model describing the essential autophagy dynamics of a neuron.	14
3.1	Table of $A\beta$ aggregation model parameters.	31
4.1	Nominal parameter values of the sleep-wake model.	43
5.1	Coefficients for the full model reported with the RMSD on comparison with data.	67
6.1	Fitting parameters v_m , t_a , and τ for the averaged data, together with Lagrangian constant a_m , using each model and fit to each age group. .	82
6.2	Table summarizing age groups and experimental parameters.	84
6.3	Proportion of successful crossings to all crossing attempts for several values of y_0 and l_g , when $v_c = 30$ km/h and vehicle type is sedan. . .	89
6.4	Proportion of two-step crossings to all successful crossings for several values of y_0 and l_g , when $v_c = 30$ km/h and vehicle type is sedan.. . .	90

List of Figures

2.1	Schematic diagram of the model system. The rounded rectangles with white borders illustrate the four compartments of the model: intracellular protein, autophagosome, autolysosome, and extracellular A β peptide.	7
2.2	The basal steady-state A β concentrations and fluxes.	16
2.3	Intracellular A β concentrations under normal and pathological conditions. The intracellular A β concentration C_{S3} displays oscillatory behaviors depending on the parameters.	17
2.4	Extracellular A β concentrations under normal and pathological conditions. The extracellular A β concentration C_{ES3} displays oscillatory behaviors depending on the parameters.	18
2.5	A β secretion and clearance fluxes in normal and pathological conditions. F_{sec} and F_{clr} denote the A β secretion flux (from the intracellular to the extracellular space) and A β clearance flux in the extracellular space, respectively. The results in the second column have been obtained under 20-fold increase in the autophagosome formation rate constant, with other parameters kept unchanged.	19

2.6	<p>$A\beta$ concentrations depending upon activities of three autophagy steps. The surfaces specify time-averaged intracellular $A\beta$ concentration $\langle C_{S3} \rangle$ (first row) and extracellular $A\beta$ concentration $\langle C_{ES3} \rangle$ (second row) for basal parameter values; regions above and below the surfaces correspond to $A\beta$ concentrations lower and higher than the basal values. The first and the second columns correspond to $\beta/\beta^{(0)} = 10$ and $\beta/\beta^{(0)} = 100$, respectively. Computations were performed with $r_{l3}/r_{l3}^{(0)}$ and $r_{h3}/r_{h3}^{(0)}$ varied in increments and the mixed cubic and quintic spline interpolation applied. On the surfaces in purple the $A\beta$ concentrations display oscillations while oscillations are absent on the green surfaces.</p>	22
2.7	<p>Log-normal relations between average $A\beta$ concentrations and $r_{g3}/r_{g3}^{(0)}$. Log-log plots of $\langle C_{S3} \rangle$ (top) and $\langle C_{ES3} \rangle$ (bottom) versus $r_{g3}/r_{g3}^{(0)}$ for $r_{l3}/r_{l3}^{(0)} = r_{h3}/r_{h3}^{(0)} = 1$ (left column) and 0.1 (right column). Data were obtained at $\beta/\beta^{(0)} = 10$. Squares indicate average values obtained via simulations and lines depict the least square fit of the log-normal relation.</p>	23
2.8	<p>Effects of r_{l3} and r_{h3} on $A\beta$ concentrations. Average intracellular $A\beta$ concentration $\langle C_{S3} \rangle$ (first and third rows) and extracellular $A\beta$ concentration $\langle C_{ES3} \rangle$ (second and fourth rows) at $\beta/\beta^{(0)} = 10$ (upper two rows) and $\beta/\beta^{(0)} = 100$ (lower two rows), depending upon changes of $r_{l3}/r_{l3}^{(0)}$ (first column), $r_{h3}/r_{h3}^{(0)}$ (second column), and $r_{l3}/r_{l3}^{(0)}$ and $r_{h3}/r_{h3}^{(0)}$ together (third column). At data points in purple, oscillations of $A\beta$ concentrations are observed; at green data points, concentrations are stationary.</p>	24
3.1	<p>Numerical solution of model in equations 1 and 2, along with Weibull and log-normal curve fits (left). Data curves of solutions at times $t = 10, 50, 100$ hs (right).</p>	32

3.2	Size distribution of a monomer population after ten years in basal, early AD, and late AD conditions.	33
3.3	Autophagy shifts the distribution away from the toxic species.	33
3.4	Effect of higher $A\beta$ production on size distribution of aggregates after ten years. Magenta indicates the normal rate, while green indicates AD. The size is in arbitrary units.	34
4.1	Schematic diagram of the connections between components of the model. Pointed-ends represent excitatory connections, while flat-ends represent inhibitory connections.	42
4.2	Limit-cycle dynamics of the model for nominal parameters, plotted for 48 h. Entrainment due to the light input I (in units of lux) is exhibited as seen in the period-locked oscillations of cell potentials V_v , V_m , and V_o (in units of mV) as well as the seven dynamical variables n , x , x_c , and H (unitless).	44
4.3	(a) Δ (average shift of the CBT minimum) obtained via simulations with $T_d = 11$ h, in the ν_{mo} - I_d parameter space. (b) Period-locking zone boundaries for $T_d = 9$ h and 11 h. Circle indicates the point representing normal conditions, square indicates seasonal disorder, and triangle indicates non-seasonal disorder. The arrows indicate shifts from the normal state to the disordered states. Note that in simulations the shift to seasonal disorder (leftward arrow) is accompanied by a change in T_d from 11 h to 9 h. The area enclosed in the the dotted box is enlarged in the inset.	47

4.4	Simulations of non-seasonal affective disorder: black lines indicate daily sleep times and colored dots indicate CBT minima. On day 7, ORX is increased, as indicated by an arrow, causing instability. Morning light treatment of 10,000 lux for 1.5 hour daily is administered starting on day 14, also indicated by an arrow. Periods of light treatment are labeled yellow. Note the gradual return to normal phase. . . .	48
4.5	(a) Recovery time t_r (in days) verses treatment timing t_0 . t_r indicates the number of days of treatment required for recovery from the circadian instability caused by orexinergic imbalance. Plotted for two values of ν_{mo} . Interpolation has been used to produce a smooth curve. (b) I_{tr} - ν_{mo} phase diagram for morning treatment ($t_0 = 7$ am) and afternoon treatment ($t_0 = 3$ pm). Recover occurs above the curves. . . .	51
4.6	(a) Core body temperature minimum time $t_{CBT,i}$ versus noise level D , obtained from simulations. The averages and standard deviations are plotted for the 90th, 110th, and 130th days (blue, green, orange) for $D = 0.01$ mV to 0.25 mV. (b) Light treatment simulations for $\nu_{mo} = 0.33$ mV s, treatment time $t_0 = 7:00$, and $I_{tr} = 10,000$ lux, in the presence of noise $D = 0.1$ mV. As in the case without noise, recovery to the normal phase is observed.	53
5.1	A sample of 4 seconds of raw data from the pressure sensors. The vertical position of each number of the array indicates the time, ordered from top to bottom at an increment of 0.1 seconds. Each column denotes a sensor, with left foot and right foot separated. The colored portions indicate when our algorithm decided the foot was off the ground.	61
5.2	Graph of total pressure from the left foot sole over an interval of 10 seconds obtained from the foot monitoring system from the same data as presented in Fig. 5.1. The two dashed lines indicate the upper and lower thresholds used to calculate the step frequency.	62

5.3	Three-dimensional scatterplot of data (dots) and model prediction (lines) of P versus P_U and P_K for (a) women and (b) men.	65
5.4	Boxplots of the percent errors of predictions made by the model and Fitbit Surge. Errors have been estimated via Eq. 5.9.	66
5.5	Step frequency f multiplied by height h plotted against average walking speed v . Least squares fit line $fh = 0.52v + 1.02$ (m/s) is also shown.	66
6.1	(a) Dependence of the Lagrangian L on the speed v (in the absence of acceleration, $a = 0$). (b) Dependence of L on a (for $v = 0$) for the quadratic form (blue) and the logarithmic form (red).	76
6.2	Top-down diagram of the crossing environment at time $t = 0$. The two boxes on the road depict two vehicles facing the right, which move forward at a constant speed. The circle depicts the pedestrian, who begins at rest and is facing in the direction the arrow. Labeled are experimental parameters l_g , y_0 , and the bearing angle to the crossing point θ_c	77
6.3	Fitting results and data for (a) adults and (b) children, displaying the position y (in meters) versus time t (in seconds). Circles and error bars indicate averages and standard deviations of positions, respectively. Blue and red lines correspond to the quadratic and logarithmic models fitted to the averaged data, respectively. The blue and red lines overlap significantly. Individual data time series are plotted in grey and rectangles represent vehicles.	81

6.4	Pedestrian position-time plots illustrating typical crossing patterns. Black traces indicate example data; red traces indicate the corresponding model fits. Left and right boxes indicate the temporal and spatial area that the leading and the trailing vehicles occupy, respectively. Intersecting one of the box lines would indicate a collision. In both examples, the conditions are described by $y_0 = -3.5$ m, $t_g = 3.0$ s, and $v_c = 30$ km/h, with the vehicle type set to be a sedan. (a) an example of the simple cross with a single acceleration event followed by constant speed walking; (b) an example of the two-step cross with two acceleration events.	87
6.5	Distributions of parameter t_a for varying y_0 and l_g . Here, $v_c = 30$ km/h and vehicle type is sedan. Columns indicate the average values of t_a in the data for given experimental conditions while error bars represent standard deviations. Pairs of samples, marked with asterisks, are presumed to belong to different distributions ($p < 0.05$) according to the Mann-Whitney U test. (Note here that not all such pairs are marked.)	92
6.6	Distributions of parameters t_a (left) and t_d (right) for varying vehicle speeds v_c and for two vehicle types. Other parameters are set to $t_g = 3$ s and $y_0 = -3.5$ m. Columns indicate the average values in the data for given experimental conditions while error bars represent standard deviations. Pairs of samples, marked with asterisks, are presumed to belong to different distributions ($p < 0.05$) according to the Mann-Whitney U test.	93

6.7 Data plotted with boundaries representing the affordance of the gap. (a) data plotted with surfaces in the three-dimensional parameter space (τ, v_{\max}, t_a) defined by Equation 6.20. Data points for $l_g = 25$ m and $y_0 = -3.5$ m are plotted for all age groups; dots represent simple crossings and crosses represent two-step crossings; (b) data plotted with boundaries on the two-dimensional plane (v_{\max}, t_a) defined by Equation 6.21. To illustrate the effects of a shift in affordance, data and boundaries for $l_g = 25$ m and $y_0 = -3.5$ m (black) are plotted with those for l_g changed to 33.3 m and for y_0 changed to -6.5 m are shown in red and in blue, respectively. Triangles indicate average parameter values. 95

6.8 Time evolution of the bearing angle θ_c , defined by Equation 6.23. The gap length is $l_g = 25$ m and the initial position is $y_0 = -3.5$ m and -6.5 m for red and cyan lines, respectively. Colored lines are computed from data, while black lines show the analytical results using average parameter values. The time axis is given in terms of time before crossing $t - t^*$, so that the zero point is equal to the intersection time of the run (i.e., the time at which $y(t) = 0$). 97

Chapter 1

Introduction

Biological systems are nature's quintessential complex systems. Complexity emerges at all length and time scales, from the scale of the molecular building blocks of life (e.g. the fractal nature of DNA packing) to the scale of organisms (e.g. language and movement) and further on into collective systems. More than any other type of system observed, countless emergent phenomena arise. To understand these systems with a unified framework may be one of the great tasks of theoretical physics. In order to reach this lofty goal, however, more work needs to be done to elucidate the workings of the large variety of systems within even a single organism.

This dissertation presents four chapters each detailing a modeling study of a specific biological phenomena. Chapters 2, 4, 5, and half of chapter 6 are reprints of publications by the author with a few modifications [1, 2, 3, 4]. These are all studies of human biology, although some of the results are general across a range of species. They are presented in terms of increasing length scale, ranging from the cellular scale to the behavioral scale.

We begin with a study of the effects of autophagy on amyloid- β ($A\beta$) monomer concentration and aggregation in the brain [1]. Autophagy (from the Greek, autos, or "self", and phagein, "to eat") is an evolutionarily conserved catabolic pathway whose primary function is to degrade cytoplasmic constituents such as proteins and organelles

in the lysosome and recycle them for energy [5, 6, 7]. However, it is becoming increasingly clear that autophagy interacts with various processes in complex ways, playing a roles in regulating protein quality, energy balance, metabolic homeostasis, and even cell death and survival [6, 7, 12, 8]. Adenosine triphosphate (ATP) and amino acids are produced by the recycling process, which in turn regulate the consecutive steps of the autophagy process, i.e., sequestration (or autophagosome formation), autophagosome maturation (autolysosome formation), and intralysosomal hydrolysis, via mammalian target of rapamycin (mTOR) (for amino acids) and AMP-activated protein kinase (AMPK) pathways (for ATP) [9, 10, 11, 76]. Neurons are especially vulnerable to autophagy dysfunction because they rely heavily upon autophagy for preventing the accumulation of toxic substances such as damaged proteins and protein aggregates [13, 14, 15]. For this, the brain is considered to be the most severely affected organ by the autophagy dysfunction [14, 15]: It is particularly related to the development of neurodegenerative disorders such as Alzheimer's disease (AD) and Parkinson's disease (PD) [13, 14, 16, 17, 18, 19, 20].

In chapter 3, we model the aggregation of $A\beta$ peptides into polymers, which is a key process implicated in Alzheimer's disease (AD). The amyloid hypothesis posits that amyloid aggregation plays a causal role in the disease [21, 22]. While the hypothesis is under debate, there is no doubt that understanding the mechanics behind the formation of $A\beta$ monomers into oligomers and fibrils and further into plaques is key to gaining a full understanding of the pathology of AD. We build a model for the aggregation of $A\beta$ by building a model based on key *in vitro* observations, in particular the existence of a critical aggregation concentration and a skewed size distribution [24]. Hence, we develop a model that pays special attention to the size distribution of the aggregates, based on the growth model from statistical physics [25].

In chapter 4, we move to a macroscopic description of the brain in order to study the entrainment of the circadian system, its disruption under abnormal circumstances, and its subsequent recovery via light treatment [2]. The suprachiasmatic nucleus (SCN),

located in the hypothalamus, plays the role of a central pacemaker in the brain [26]. Under normal circumstances, the SCN is entrained to the light-dark cycle of the environment via photic and non-photoc influences. However, under pathological conditions it may fail to be entrained to the environment. This often coincides with sleep disorders [27] as well as psychiatric disorders such as depression [28] and bipolar disorder [29], as well as neurodegenerative disorders such as Alzheimer's disease [30]. In all of these cases, the causal relation is not clear. Here, we study the potential effects of the neurotransmitter orexin on circadian treatment, and the prospect for recovery via light treatment.

In the chapter 5, we examine a whole-body phenomenon: the energy expenditure during walking on gradient surfaces [3]. Physical inactivity, despite its well-known health risks [31, 32], continues to be a serious public health issue [33]. Recently, various wearable devices, including wristbands and mobile phones, have offered a way to track physical activity throughout the day. Such devices can be used in ambulatory conditions by individuals or in clinical settings to monitor patients' physical activity. Many of these devices use an accelerometer-based method to predict energy expenditure [34, 35, 36]. However, these methods are limited in precision [37]. In order to begin addressing this, we propose a model based on simple physical arguments, and the model parameters are fit to data from a treadmill experiment.

Finally, we explore the behavioral dynamics of interceptive walking [4, 38]. In particular, we use the model to examine the behaviors of pedestrians crossing a road between moving vehicles. This problem is one of public health interest, as pedestrian accidents take up a large proportion of traffic-related accidents, particularly in areas of high population density [39, 40]. A quantitative study of the behavioral dynamics of road crossing may help develop strategies to prevent accidents [40, 41, 42]. A model for simple interceptive walking is proposed based on the principle of least action from Lagrangian mechanics. The model is used to extract statistical information from the data, and implications for pedestrian safety are discussed.

Biological systems are inherently unpredictable and contain a high degree of randomness. Order that does emerge can be described by mathematical models that ignore irrelevant details. Such models inherently have high uncertainty, but they are valuable in that they can capture the essential features of a phenomena.

The five topics under study all ask vastly different questions, and the models are tailored to describe specific phenomena at different scales. However, we observe some connections between the studies. The behavioral study of interceptive walking (chapter 6) assumes that effort is proportional to the metabolic energy consumption. The predictive model of energy consumption during walking in chapter 5 tells us that the metabolic energy consumption is proportional to v^2 , where v is the walking speed. This suggests that the effort function might change when the walking surface has a slope, and this connection can guide generalizations of the behavioral model. In chapter 4, we explore macroscopic oscillations of the brain that lead to the 24 hour sleep-wake cycle. The autophagy model of chapter 2 also exhibits intracellular oscillations modulated by up- and down-regulation of autophagy depending on stress levels. In real systems, these oscillations are linked and interacting. As both autophagy and sleep is linked to a myriad of diseases, a study of their interactions may provide hints towards understanding each. In particular, sleep disorders have also been linked to neurodegenerative disease such as AD.

The connections between the models studied reflect the flow of information between multiple scales in biological systems. When a renormalization group is applied to a model, information about relevant parameters is preserved while those about irrelevant parameters are lost [43]. A unified understanding of biology requires an understanding of how information flows not only from one component of the system to another, but also how it flows through a wide range of spatial and temporal scales.

Chapter 2

Autophagy and its effect on amyloid- β peptide levels

2.1 Background

In this chapter, we explore the effect of autophagy on amyloid- β ($A\beta$) levels in the extracellular fluid of the brain. Autophagy efficiently delivers toxic substances along the unusually large architectures of axons and dendrites to lysosomes, which are concentrated in the cell body, while old (deteriorated) neurons have reduced autophagic degradation efficacy. It is becoming increasingly evident that the autophagic degradations of aggregate-prone proteins in neurons are highly substrate-selective [44]. This specificity seems to rely on the specific interactions between substrates and autophagy receptors/adaptors to sequester certain substrates within autophagosomes, and then the substrates proceed to the same degradation machinery as non-selective (bulk) autophagy [45, 46, 47, 48]. The modulation of substrate–receptor/adaptor interactions has been suggested as a new therapeutic strategy for neurodegenerative disorders [44].

Alzheimer’s disease (AD) is the most common form of dementia, and it is expected to become for prevalent with the aging population [49, 50]. The neuropathological hallmarks include deposition of extracellular plaques and formation of intracellular neurofibrillary tangles (NFTs), which predominantly consist of amyloid- β peptides ($A\beta$) and tau proteins, respectively [51]. According to the amyloid hypothesis, an

accumulation of $A\beta$ is the primary factor for the onset and progression of AD and the rest of the process including the NFT formation is the secondary effects of the $A\beta$ toxicity [22, 52, 53]. Increased intracellular $A\beta$ level is observed prior to the onset of extracellular plaque formation.

$A\beta$ consists of 36 to 43 amino acids and is intracellularly generated by specific proteolytic cleavage of the amyloid precursor protein (APP), an integral membrane protein which is concentrated in the synapses of neurons. An altered balance between generation, degradation, secretion (from the intra to the extracellular space of a neuron), and clearance (from the extracellular space) of $A\beta$ is responsible for the intracellular accumulation and extracellular plaque formation. It has been reported that the $A\beta$ generation rate is abnormally high in the early and late stages of AD [54]. $A\beta$ is degraded preferentially via autophagy; yet during late stages of AD autophagosomes fail to fuse with lysosomes [54]. In addition, the $A\beta$ secretion rate depends on the autophagy activity [55, 56, 57]: the secretion rate is reduced in mice lacking autophagy-related gene 7 (Atg7) [56]. On the other hand, the autophagic activity is influenced by the intracellular $A\beta$ concentration [54, 59, 60, 61]. The $A\beta$ clearance rate in the extracellular space varies with the $A\beta$ concentration in a biphasic manner [62]. The AD patient is associated with a decrease in clearance by roughly 30%, which may lead to toxic levels of $A\beta$ accumulation in the extracellular space over about 10 years [63].

Although many individual mechanisms have been studied for decades, the association of $A\beta$ kinetics with autophagy activity and the roles of autophagy in the pathogenesis of AD remain elusive. In this study, we develop a mathematical model for autophagy with respect to $A\beta$ kinetics, integrating various individual molecular and cellular data sets, in hope of providing a unified framework for understanding the complex dynamics between autophagy and $A\beta$ pathways. Simulations are performed to identify the quantitative relationship between autophagy activity and $A\beta$ kinetics, including the intra and extracellular levels, secretion, clearance, and autophagic degradation. This may provide a starting point for understanding the effects of autophagy

on the pathogenesis of AD and implications of pharmacological autophagy modulation for AD therapy and prevention.

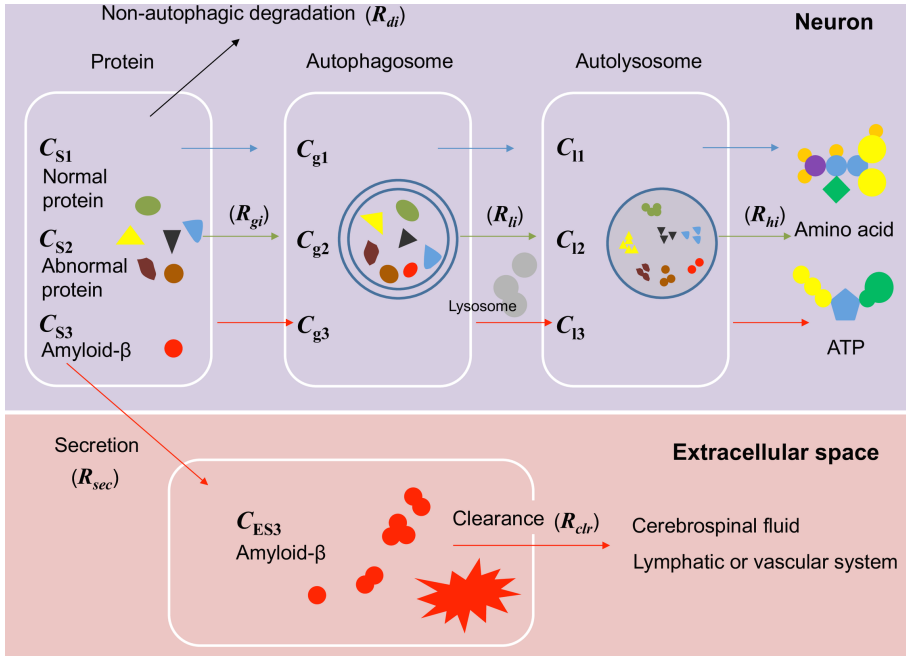


Figure 2.1: Schematic diagram of the model system. The rounded rectangles with white borders illustrate the four compartments of the model: intracellular protein, autophagosome, autolysosome, and extracellular A β peptide.

2.2 Mathematical model

The model assumes a four-compartment description of the autophagy process, including 1) intracellular protein (including normal/abnormal protein and intracellular A β), 2) autophagosome, 3) autolysosome, and 4) extracellular A β compartments (Fig. 2.1).

The model includes a nonlinear relationship between autophagy activity and intracellular and extracellular A β levels. Autophagy degrades intracellular A β and influences the A β secretion from the inside to the outside of the neuron (i.e., extracellu-

lar space) and the concentration-dependent biphasic $A\beta$ clearance in the extracellular space. Conversely, the intracellular $A\beta$ level regulates the autophagy induction step (i.e., autophagosome formation or protein sequestration). The dynamics of these relations are described by twelve coupled differential equations which are solved via the 5th order Runge-Kutta method for very high precision.

Dynamic equations Intracellular proteins are classified as resident proteins S_1 which conduct normal functions in a cell, abnormal proteins S_2 including damaged proteins and those abnormally transcribed or translated, and $A\beta$ peptide S_3 . We write the equations for the dynamics of their respective concentrations C_{S1} , C_{S2} , and C_{S3} as follows:

$$\frac{dC_{S1}}{dt} = (1 - \alpha)R_S - \sigma C_{S1} - R_{g1}C_{S1} - R_{d1} - \beta C_{S1}, \quad (2.1)$$

$$\frac{dC_{S2}}{dt} = \alpha R_S + \sigma C_{S1} - R_{g2}C_{S2} - R_{d2}, \quad (2.2)$$

$$\frac{dC_{S3}}{dt} = \beta C_{S1} - R_{g3}C_{S3} - R_{d3} - R_{sec}C_{S3}, \quad (2.3)$$

where R_S represents the (total) protein synthesis rate (from DNA) and α is the fraction of S_2 , namely, S_1 and S_2 are produced at the rates of $(1-\alpha)R_S$ and αR_S , respectively. σ is the rate constant for deterioration of S_1 (i.e., transformation from S_1 to S_2). R_{gi} and R_{di} represent the specific rates of autophagosome formation and the non-autophagic degradation of S_i (for $i = 1, 2$, and 3), respectively. β denotes the rate constant for $A\beta$ generation and R_{sec} is the $A\beta$ secretion specific rate from the intra to the extracellular space. The dynamics of the $A\beta$ concentration in the extracellular space C_{ES3} reads:

$$\frac{C_{ES3}}{dt} = R_{sec}C_{S3} - R_{clr}C_{ES3}, \quad (2.4)$$

where R_{clr} denotes the specific clearance rate for $A\beta$ in the extracellular space. Variations of the intracellular autophagosome concentration with time are determined by the difference between the autophagosome formation specific rate R_{gi} and the autolysosome formation specific rate R_{li} ($i = 1, 2$, and 3 for S_1, S_2 , and S_3 , respectively).

With C_{gi} denoting the concentration of autophagosome originating from S_i ($i = 1, 2$, and 3), the dynamics of the concentration is governed by the following equation:

$$\frac{dC_{gi}}{dt} = R_{gi}C_{Si} - R_{li}C_{gi}. \quad (2.5)$$

The intracellular concentration C_{li} of autolysosomes originating from S_i ($i = 1, 2$, and 3) is determined by the difference between R_{li} and the intralysosomal hydrolysis specific rate R_{hi} ($i = 1, 2$, and 3). The equation governing the dynamics takes the form:

$$\frac{dC_{li}}{dt} = R_{li}(t - \tau)C_{gi}(t - \tau) - R_{hi}C_{li}. \quad (2.6)$$

Note that the autolysosome concentration at time t is affected by the autophagosome concentration at time $t - \tau$, earlier by the delay time τ , which is taken to be eight minutes ($\tau = 480$ s) [64, 65, 66].

The dynamics of intracellular amino acids, the concentration of which is denoted by C_a reads:

$$\frac{dC_a}{dt} = \mu_a R_{hi} \sum_{i=1}^3 C_{li} + \mu_d \sum_{i=1}^3 R_{di} + R_a - \mu_s R_S. \quad (2.7)$$

The first and second terms on the right-hand side correspond to the supply of amino acids due to the autophagic intralysosomal hydrolysis and non-autophagic protein degradation, respectively, with appropriate constants μ_a and μ_d describing the average numbers of amino acids produced from autophagic and non-autophagic degradation, respectively. The third term represents the rate of amino acid supply from extracellular fluid into cells that is assumed to be proportional to the metabolic demand (i.e., protein synthesis rate R_S) and the loss of protein (i.e., secretion rate of $A\beta$, given by $R_{sec}C_{S3}$) such that $R_a = \mu_c R_S + \mu_\beta R_{sec}C_{S3}$ with appropriate constants μ_c and μ_β . The last term describes the reduction of amino acids due to protein synthesis with the constant μ_s , the average number of amino acids in a protein molecule.

The dynamic equation for intracellular ATP concentration C_A reads:

$$\frac{C_A}{dt} = \nu_a R_{hi} \sum_{i=1}^3 C_{li} + \nu_d \sum_{i=1}^3 R_{di} + R_A - \nu_s R_S. \quad (2.8)$$

where ν_a and ν_d are the average numbers of ATP molecules produced from autophagic degradation and from non-autophagic degradation, respectively. The net intracellular ATP generation rate R_A is assumed to be $R_A = \nu_c R_S + \nu_\beta R_{sec} C_{S3}$ that is associated with the metabolic demand and the loss of protein, with appropriate constants ν_c and ν_β . The last term corresponds to the reduction of ATP due to protein synthesis, where μ_s gives the average number of ATP molecules in a protein.

An average protein molecule in a cell is assumed to be composed of 500 amino acid residues; in other words, 500 amino acids are consumed in unit protein synthesis (i.e., $\mu_s = 500$). Considering that elongation of one amino acid during translation requires approximately four ATP molecules, we have assumed that 2000 ATP molecules are required for the synthesis of a protein ($\nu_s = 2000$). However, the numbers of amino acids and ATP molecules per degradation of one protein via autophagic or non-autophagic protein degradation have been set to be less than those required in the protein synthesis, because the efficacy of protein recycling is expected to be less than 100%; this yields $\mu_a = \mu_d = \mu_\beta = \nu_a = \nu_d = \nu_\beta = 300$, $\mu_c = 200$, and $\nu_c = 1700$.

Details of the autophagy-related rates in Eqs. (2.1) to (2.8) are given in the following subsections. The parameters are summarized in Table 1.

Autophagosome formation

We take the autophagosome formation specific rates R_{gi} from S_i (for $i = 1, 2$, and 3), which depend on the intracellular concentrations C_{S3} of A β [54, 59, 60, 61], C_A of

ATP [67, 62], and C_a of amino acids [69] as follows:

$$R_{g1}(C_{S3}, C_a, C_A) = r_{g1}(\omega_g C_{S3}^{\zeta_g} + \psi_g C_{S3} + 1) \frac{C_A^4}{C_a^4 + k_g^4} \frac{p_g^1 2}{C_A^1 2 + p_g^1 2} \frac{a_g^8}{C_a^8 + a_g^8} \left(1 + \gamma_g e^{-\xi C_a}\right), \quad (2.9)$$

$$R_{g2}(C_{S3}, C_a, C_A) = r_{g2}(\omega_g C_{S3}^{\zeta_g} + \psi_g C_{S3} + 1) \frac{C_A^4}{C_a^4 + k_g^4} \frac{p_g^1 2}{C_A^1 2 + p_g^1 2} \left(1 + \gamma_g e^{-\xi C_a}\right), \quad (2.10)$$

$$R_{g3}(C_{S3}, C_a, C_A) = r_{g3}(\omega_g C_{S3}^{\zeta_g} + \psi_g C_{S3} + 1) \frac{C_A^4}{C_a^4 + k_g^4} \frac{p_g^1 2}{C_A^1 2 + p_g^1 2} \left(1 + \gamma_g e^{-\xi C_a}\right), \quad (2.11)$$

where r_{gi} is the rate constant for autophagosome formation from S_i (for $i = 1, 2$, and 3), with appropriate constants $\omega_g, \zeta_g, \psi_g$ (for $A\beta$), k_g, p_g (ATP), a_g, γ_g , and ξ_g (amino acids). Intracellular $A\beta$ affects the mTOR signaling, which negatively regulates autophagy induction, exhibiting a nonlinear relationship: The mTOR activity increases (i.e., suppressing autophagosome formation) with the $A\beta$ level until reaching a certain threshold ($0.5 \mu M$) and then the activity gradually decreases (restoring autophagosome formation) above the threshold concentration [54, 59, 60, 61]. This nonlinear relationship has been included in Eqs. (2.9) to (2.11) as a simple algebraic equation in the form of $\omega_g C_{S3}^{\zeta_g} + \psi_g C_{S3} + 1$.

The remaining part of the right-hand side contains the ATP and amino acid dependency of the autophagosome formation step. Under normal conditions, it appears that S_2 and S_3 , abnormal proteins and $A\beta$, are preferentially degraded by autophagy. However, as the intracellular energy/nutrient reduces due to, e.g., starvation or increased metabolic demand, all the proteins (S_1, S_2 and S_3) are degraded non-selectively for the rapid supply of essential energy molecules (e.g., ATP) and metabolic building blocks (i.e., amino acids) [48, 47, 70, 71]. Therefore, it is assumed in this model that the autophagosome formation rate from resident proteins S_1 , which is lower than that from abnormal proteins and $A\beta$ (S_2 and S_3) under normal conditions, becomes gradually equal to those of S_2 and S_3 as the amino acid concentration is decreased [72, 73, 74,

75].

Autolysosome formation and intralysosomal hydrolysis

The autolysosome formation specific rate R_{li} reads ($i = 1, 2,$ and 3 for $S_1, S_2,$ and S_3)

$$R_{li}(C_A) = r_{li} \frac{C_A^4}{C_A^4 + k_l^4} \frac{p_l^2}{C_A^2 + p_l^2}, \quad (2.12)$$

where r_{li} denotes the rate constant for autolysosome formation from S_i with appropriate constants k_l and p_l for ATP, based on biological experiments [67, 68].

The intralysosomal hydrolysis specific rate R_{hi} is taken as a function of the intracellular ATP concentration ($i = 1, 2,$ and 3):

$$R_{hi}(C_A) = r_{hi} \frac{C_A^{\delta_h}}{C_A^{\delta_h} + k_l^{\delta_h}}, \quad (2.13)$$

with appropriate exponent δ_h and constant k_h for ATP, where r_{hi} is the rate constant for intralysosomal hydrolysis [67, 68]. Further details of the equations for autolysosome formation and intralysosomal hydrolysis can be found in literature [12, 76, 77, 78].

Secretion and clearance of amyloid- β

Considering that $A\beta$ secretion from the intra to extra cellular space of a neuron is positively correlated with the autophagy induction level [55, 56, 57], we assume the $A\beta$ secretion specific rate R_{sec} to be proportional to the degree of amino acid- and ATP-dependent autophagosome induction, as defined in Eqs. (9)-(11), with an appropriate constant r_{sec} :

$$R_{sec}(C_a, C_A) = r_{sec} \frac{C_A^4}{C_a^4 + k_g^4} \frac{p_g^2}{C_A^2 + p_g^2} \left(1 + \gamma_g e^{-\xi C_a}\right). \quad (2.14)$$

The concentration-dependent biphasic $A\beta$ clearance rate R_{clr} in the extracellular space is assumed, on the basis of biological experiments [62, 63, 79], to take the form:

$$R_{clr}(C_{ES3}) = r_{clr}(C_{ES3} + \omega_{ext}), \quad (2.15)$$

where r_{clr} denotes the rate constant for $A\beta$ clearance, with an appropriate constant ω_{ext} . The rate of $A\beta$ clearance varies with the concentration according to the measurement on Alzheimer's mouse model [62]: While the half-life is very short at high concentrations of extracellular $A\beta$, it grows longer as the concentration decreases. Equation (15) captures qualitatively this biphasic nature of $A\beta$ clearance and its value lies within a reasonable range consistent with the state-of-the-art measurements [63, 79].

Protein synthesis and non-autophagic degradation

The (total) protein synthesis rate R_S which depends on intracellular concentrations C_a of amino acids and C_A of ATP reads [80]

$$R_S(C_a, C_A) = \begin{cases} r_s \frac{C_a}{C_a + k_s} \frac{\exp[C_A] - 1}{\exp[C_A^{(m)}] - 1} & \text{for } C_A < C_A^{(m)} \\ r_s \frac{C_a}{C_a + k_s} & \text{for } C_A > C_A^{(m)} \end{cases} \quad (2.16)$$

with appropriate constant k_s for amino acid, where $C_A^{(m)}$ is the ATP concentration corresponding to the maximal protein synthesis rate and r_s denotes the rate constant for the protein synthesis. Further details of the protein synthesis can be found in literature [12, 76, 77, 78].

The non-autophagic protein degradation machinery such as the ubiquitin-proteasome system has been considered in the model. We assume that the amount of protein degradation by autophagy constitutes 80% of the total amount of protein degradation and the non-autophagic protein degradation machinery is responsible for the remaining 20% [81]. Accordingly, we take the rate of non-autophagic degradation R_{di} ($i = 1, 2,$ and 3) to be 25% of autophagic degradation:

$$R_{di} = \frac{1}{4} R_{hi} C_{li}. \quad (2.17)$$

Parameter	Value	Unit	Description
$r_{gi}^{(0)}$	1.12×10^{-5}	s^{-1}	Rate constant for autophagosome formation of Si ($i = 1, 2, 3$) (normal value)
α	1.00×10^{-2}	1	Fraction of S2 in protein synthesis rate R_S
$\beta^{(0)}$	5.56×10^{-10}	s^{-1}	Rate constant for A β generation (normal value)
σ	4.00×10^{-7}	s^{-1}	Rate constant for deterioration of S1
ω_g	-9.43×10^{-1}	$mM^{-0.1}$	Constant for autophagosome formation (A β dependency)
ζ_g	1.00×10^{-1}	1	Constant for autophagosome formation (A β dependency)
ψ_g	1.01×10^2	mM^{-1}	Constant for autophagosome formation (A β dependency)
k_g	2.83	mM	Constant for autophagosome formation (ATP dependency)
p_g	3.00	mM	Constant for autophagosome formation (ATP dependency)
a_g	4.50	mM	Constant for autophagosome formation (amino acids dependency)
a_g	4.50	mM	Constant for autophagosome formation (amino acids dependency)
ξ_g	7.49×10^{-2}	mM^{-1}	Constant for autophagosome formation (amino acids dependency)
$r_{li}^{(0)}$	2.47×10^{-5}	s^{-1}	Rate constant for autolysosome formation of Si ($i = 1, 2, 3$) (normal value)
k_l	2.43	mM	Constant for autolysosome formation (ATP dependency)
p_l	3.00	mM	Constant for autolysosome formation (ATP dependency)
$r_{hi}^{(0)}$	1.39×10^{-5}	s^{-1}	Rate constant for intralysosomal hydrolysis of Si ($i = 1, 2, 3$) (normal value)
δ	7.24×10^{-1}	1	Exponent for intralysosomal hydrolysis (ATP dependency)
k_h	2.99	mM	Constant for intralysosomal hydrolysis (ATP dependency)
r_s	1.48×10^{-5}	$mM \cdot s^{-1}$	Rate constant for protein/organelle synthesis
k_s	1.77×10^1	mM	Constant for protein/organelle synthesis (amino acids dependency)
$C_A^{(m)}$	2.00	mM	ATP concentration corresponding to maximal protein/organelle synthesis rate
r_{sec}	4.67×10^{-9}	s^{-1}	Rate constant for A β secretion
r_{clr}	2.23×10^{-1}	$mM^{-1} \cdot s^{-1}$	Rate constant for A β clearance
ω_{ext}	6.34×10^{-5}	mM	Rate constant for A β clearance

Table 2.1: Nominal parameters for the autophagy model describing the essential autophagy dynamics of a neuron.

2.3 Model dynamics

A β kinetics under normal and pathological conditions

In Fig. 2.2, the relation of intracellular (C_{S3}) and extracellular (C_{ES3}) A β levels with the respective A β fluxes under normal conditions (i.e., for basal parameter values) are shown, providing kinetic and dynamic insights into the A β regulation. As illustrated in Fig. 2.1, C_{S3} (the second row of the first column) is determined by the difference between influx (i.e., A β generation flux, denoted by F_{gen} , the concentration of A β generated per unit time given in units of mM/s) and efflux rates such as autophagic sequestration F_{seq} (the concentration of intracellular A β sequestered into autophagosomes per unit time, i.e., $F_{seq} = R_{g3}C_{S3}$), non-autophagic degradation F_{nap} (the concentration of intracellular A β degraded via the non-autophagic mechanism per unit time, i.e., $F_{nap} = R_{d3}$), and secretion F_{sec} (the concentration of intracellular A β secreted from the inside to outside of a neuron per unit time, i.e., $F_{sec} = R_{sec}C_{S3}$). C_{ES3} (the third row of the second column) is governed by F_{sec} and the clearance flux F_{clr} (the concentration of A β removed from the extracellular space per unit time, i.e., $F_{clr} = R_{clr}C_{ES3}$).

Figs. 2.3 and 2.4 compare values of C_{S3} and C_{ES3} , respectively, under the normal, early stage (i.e., abnormal increase in A β generation), and late stage AD (i.e., increased A β generation together with decreased autophagic lysosomal degradation) conditions [54]. The simulations have been performed with the basal value $\beta^{(0)}$ of the A β generation rate constant, i.e., $\beta = \beta^{(0)}$, for the normal condition, while data for the early and late stage AD conditions have been obtained at an extremely high A β generation rate, $\beta = 100 \times \beta^{(0)}$. Further, in the late stage case, the specific rate constants of autolysosome formation and intralysosomal hydrolysis have been set to be 10% of the basal values.

It is observed that C_{S3} and C_{ES3} are significantly higher in AD conditions than in the basal condition— C_{S3} is higher at the early stage than at the late stage AD (Fig.

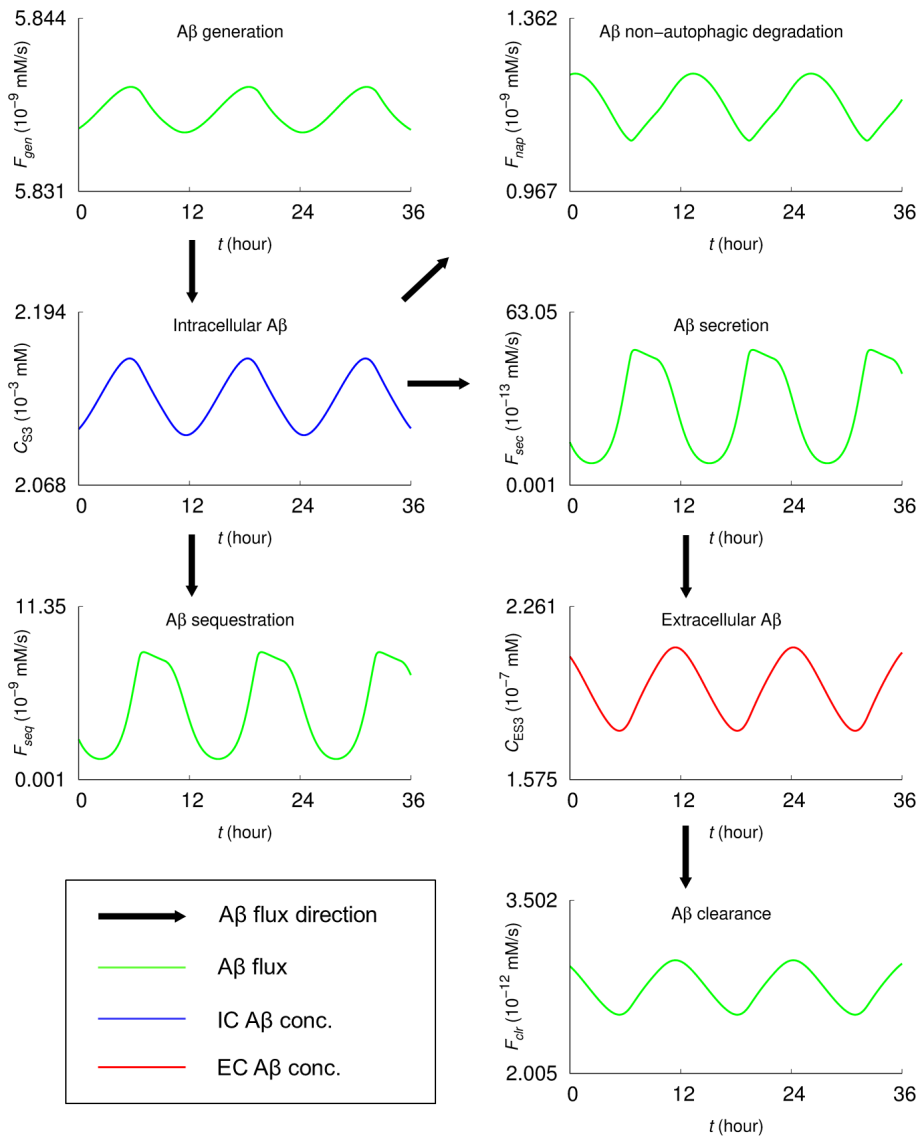


Figure 2.2: The basal steady-state A β concentrations and fluxes.

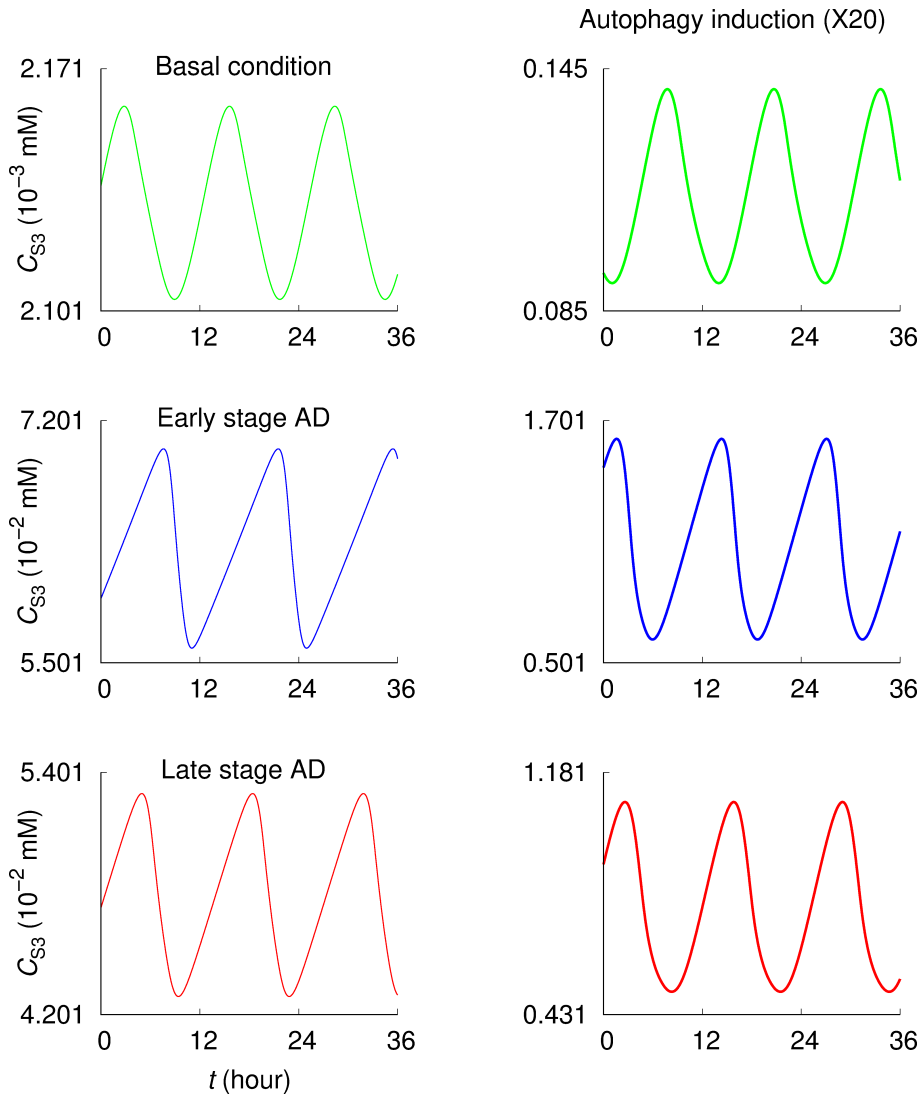


Figure 2.3: Intracellular $A\beta$ concentrations under normal and pathological conditions. The intracellular $A\beta$ concentration C_{S3} displays oscillatory behaviors depending on the parameters.

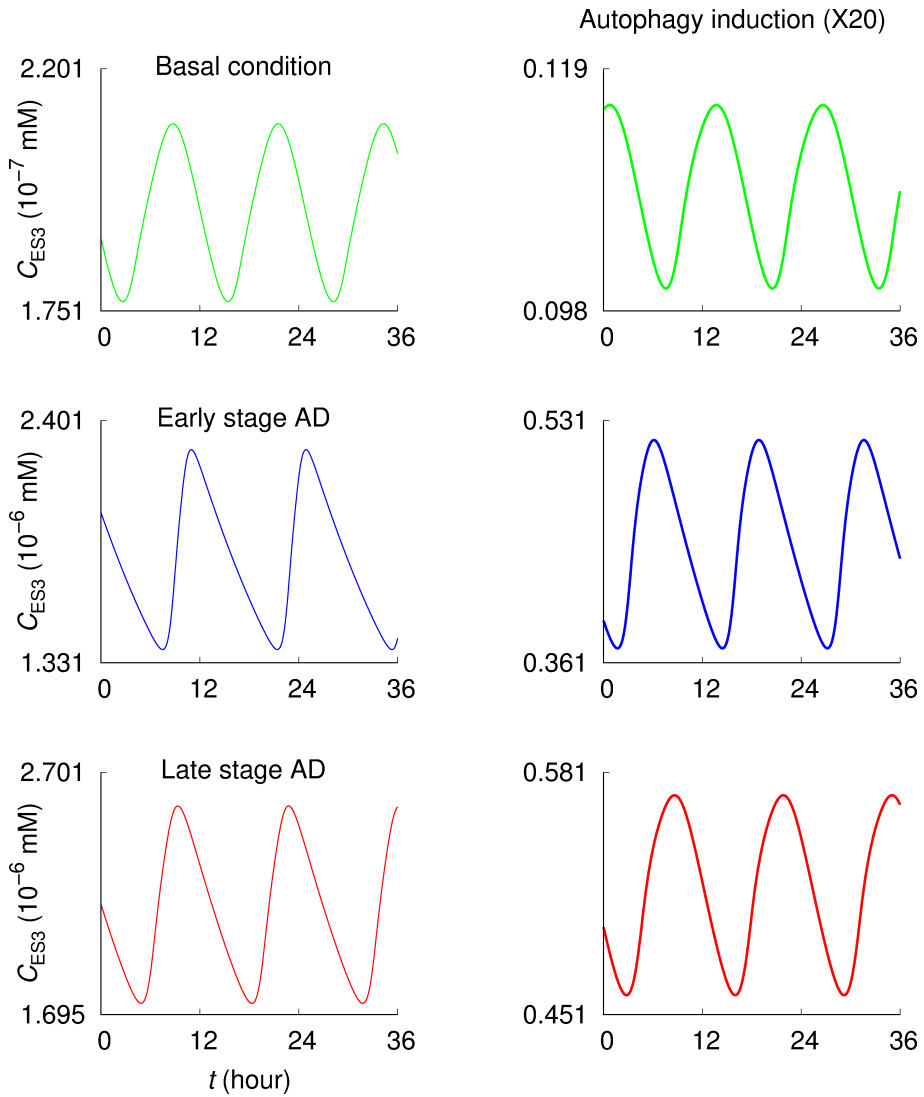


Figure 2.4: Extracellular $A\beta$ concentrations under normal and pathological conditions. The extracellular $A\beta$ concentration C_{ES3} displays oscillatory behaviors depending on the parameters.

2.3) while C_{ES3} is higher at the late stage AD (Fig. 2.4). In both pathological conditions, autophagy induction (i.e., a 20-fold increase in the autophagosome formation rate constant: $r_{g3} = 20 \times r_{g3}$) significantly reduces C_{S3} and C_{ES3} . In addition, the early and late stage AD exhibit asymmetric oscillating patterns. C_{S3} increases gradually and then drops rapidly; conversely, C_{ES3} increases rapidly and drops gradually. Under the basal condition they exhibit relatively symmetrical oscillation patterns.

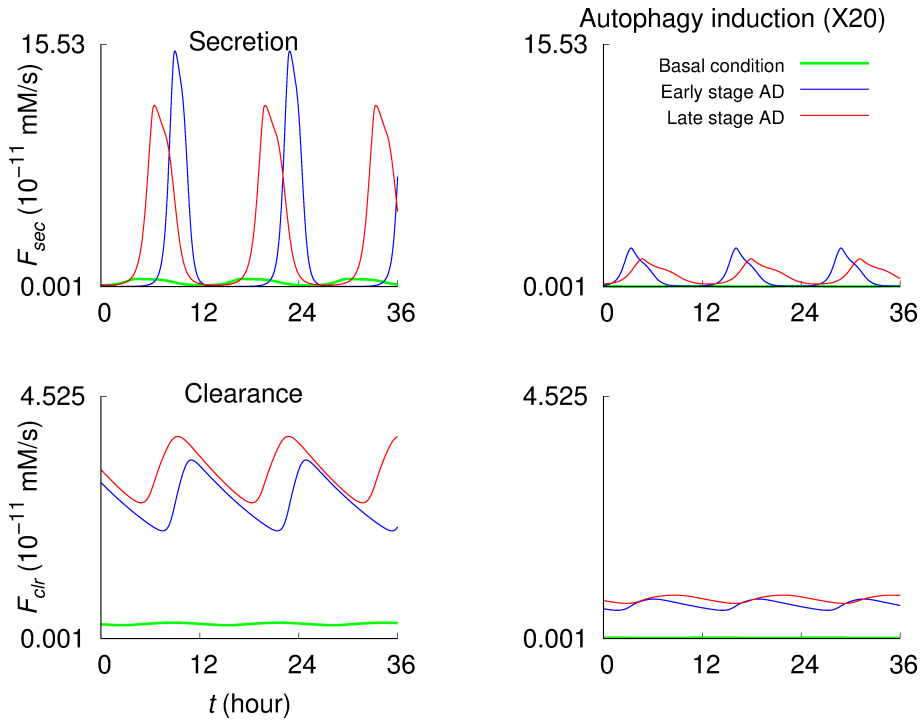


Figure 2.5: $A\beta$ secretion and clearance fluxes in normal and pathological conditions. F_{sec} and F_{clr} denote the $A\beta$ secretion flux (from the intracellular to the extracellular space) and $A\beta$ clearance flux in the extracellular space, respectively. The results in the second column have been obtained under 20-fold increase in the autophagosome formation rate constant, with other parameters kept unchanged.

Both $A\beta$ secretion flux F_{sec} and clearance flux F_{clr} are significantly promoted in the early and late stage AD cases compared to those in the basal condition (the first

column of Fig. 2.5). The peaks of F_{sec} in early AD are sharper and higher but stay at the near-zero rate for a longer period than in late AD. In contrast, F_{clr} exhibits higher peaks in late AD than in early AD. Autophagy induction (i.e., $r_{g3} = 20 \times r_{g3}$) significantly reduces those fluxes, close to the basal levels. In what follows, autophagy dynamics corresponding to the normal and AD conditions are presented, including steady-state concentrations of autophagosome, autolysosome, and autophagic fluxes.

Dynamics of autophagy and implications in the $A\beta$ regulations

Protein sequestration (i.e., autophagosome formation) flux F_{seq} , autophagosome maturation (i.e., autolysosome formation) flux F_{mat} , and intralysosomal hydrolysis flux F_{hyd} in both early and late stage AD are significantly increased compared with those on the basal condition (the first, third, and fifth rows of Fig. 2.6). The peaks of F_{seq} and F_{mat} in early stage AD are sharper and higher than those in the late stage. The steady-state concentrations of autophagosomes and autolysosomes, C_{g3} and C_{l3} , in the AD cases are greater than those in the basal condition case: the values at the late stage of AD are about ten times greater than those at the early stage (the second and fourth rows of Fig. 2.6).

In the cases of early and late stage AD, autophagy induction significantly decreases F_{seq} and F_{mat} , while it increases F_{hyd} (Fig. 2.6). The steady-state autophagosome concentration C_{g3} is decreased while the autolysosome concentration C_{l3} is increased upon autophagy induction (the second and fourth rows of the second and third columns of Fig. 2.6). Under the basal condition, the oscillatory patterns of autophagic fluxes and steady-state concentrations of autophagosomes and autolysosomes are not significantly affected by the autophagy induction, compared to the AD cases.

As shown above, autophagy induction (i.e., $r_{g3} = 20 \times r_{g3}$) significantly reduces C_{S3} and C_{ES3} . Increasing r_{g3} beyond this rate further reduces the $A\beta$ levels until they reach basal levels. However, the required value of r_{g3} to bring the basal levels may vary depending on the stage of AD and the activities of the other autophagic steps.

Fig. 2.7 presents a three-dimensional surface plot, exhibiting step-specific and combined effects of the autophagy pathway on $A\beta$ levels for a moderately high $A\beta$ formation rate $\beta/\beta^{(0)} = 10$ (first column) and an extremely high formation rate $\beta/\beta^{(0)} = 100$ (the second column). The vertical axis measures the autophagosome formation rate relative to its normal value (i.e., $r_{g3}/r_{g3}^{(0)}$) and the two horizontally placed axes represent the autolysosome formation and the intralysosomal hydrolysis rates relative to the normal values, spanning the range from highly induced activity ($r_{l3}/r_{l3}^{(0)} = r_{h3}/r_{h3}^{(0)} = 30$) to normal ($r_{l3}/r_{l3}^{(0)} = r_{h3}/r_{h3}^{(0)} = 1$) and extremely reduced activity ($r_{l3}/r_{l3}^{(0)} = r_{h3}/r_{h3}^{(0)} = 0.1$). The surfaces designate time-averaged intracellular $A\beta$ concentration $\langle C_{S3} \rangle$ (top) and extracellular $A\beta$ concentration $\langle C_{ES3} \rangle$ (bottom) for basal parameter values (i.e., under normal conditions); regions above and below the surface correspond to $A\beta$ concentrations lower and higher than the basal values, respectively.

For both $A\beta$ synthesis rates ($\beta/\beta^{(0)} = 10$ and 100), $\langle C_{S3} \rangle$ and $\langle C_{ES3} \rangle$ decrease with r_{g3} in a log-normal manner,

$$\langle C \rangle (r_{g3}/r_{g3}^{(0)} = x) = (\gamma / (x\sigma\sqrt{2\pi})) \exp a[-(\log x\mu)^2 / 2\sigma^2], \quad (2.18)$$

where $\langle C \rangle$ denotes $\langle C_{ES3} \rangle$ or $\langle C_{S3} \rangle$ and γ , σ , and μ are adjustable parameters (Fig. 2.8). When r_{l3} is decreased from 1 to 0.1, $\langle C_{S3} \rangle$ decreases while $\langle C_{ES3} \rangle$ increases. In contrast, when $r_{l3} > 1$, the concentrations are relatively independent of r_{l3} . The effects of r_{h3} generally follow the trend.

The surface shape of Fig. 2.7 reflects the combined effects of the three-autophagy steps. A greater value of r_{g3} is required to return to basal values in the case $\beta/\beta^{(0)} = 100$ compared with the case $\beta/\beta^{(0)} = 10$. At $r_{l3}/r_{l3}^{(0)} < 1$ and $r_{h3}/r_{h3}^{(0)} < 1$ both concentrations change greatly compared with the case $r_{l3}/r_{l3}^{(0)} > 1$ and $r_{h3}/r_{h3}^{(0)} > 1$, indicating that reduction of autolysosome formation and/or intralysosomal hydrolysis has greater impact on the $A\beta$ concentrations than promotion of these steps. Above $r_{h3}/r_{h3}^{(0)} = 45.21$ (for $\beta/\beta^{(0)} = 10$) and $r_{h3}/r_{h3}^{(0)} = 11.1$ (for $\beta/\beta^{(0)} = 100$), the oscillations of proteins (C_{S1} , C_{S2} , C_{S3} , C_{ES3}), ATP (C_A), and amino acids (C_a)

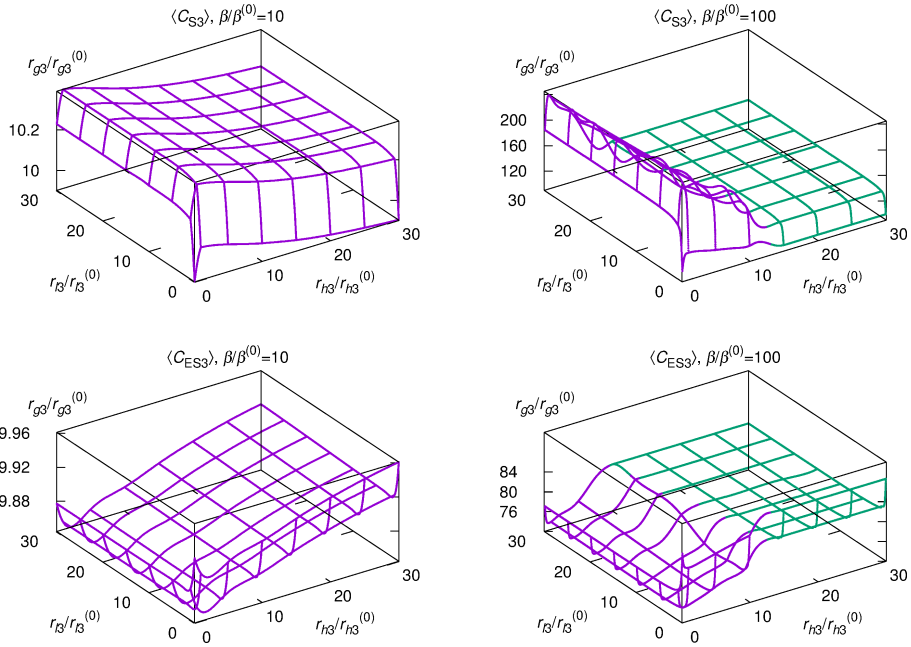


Figure 2.6: $A\beta$ concentrations depending upon activities of three autophagy steps. The surfaces specify time-averaged intracellular $A\beta$ concentration $\langle C_{S3} \rangle$ (first row) and extracellular $A\beta$ concentration $\langle C_{ES3} \rangle$ (second row) for basal parameter values; regions above and below the surfaces correspond to $A\beta$ concentrations lower and higher than the basal values. The first and the second columns correspond to $\beta/\beta^{(0)} = 10$ and $\beta/\beta^{(0)} = 100$, respectively. Computations were performed with $r_{l3}/r_{l3}^{(0)}$ and $r_{h3}/r_{h3}^{(0)}$ varied in increments and the mixed cubic and quintic spline interpolation applied. On the surfaces in purple the $A\beta$ concentrations display oscillations while oscillations are absent on the green surfaces.

disappear, converging to stationary values (green surfaces in Figs. 2.7 and 2.9). In the stationary region, the effects of $r_{l3}/r_{l3}^{(0)}$ and $r_{h3}/r_{h3}^{(0)}$ are minimal, as manifested by the flatness of the green surface.

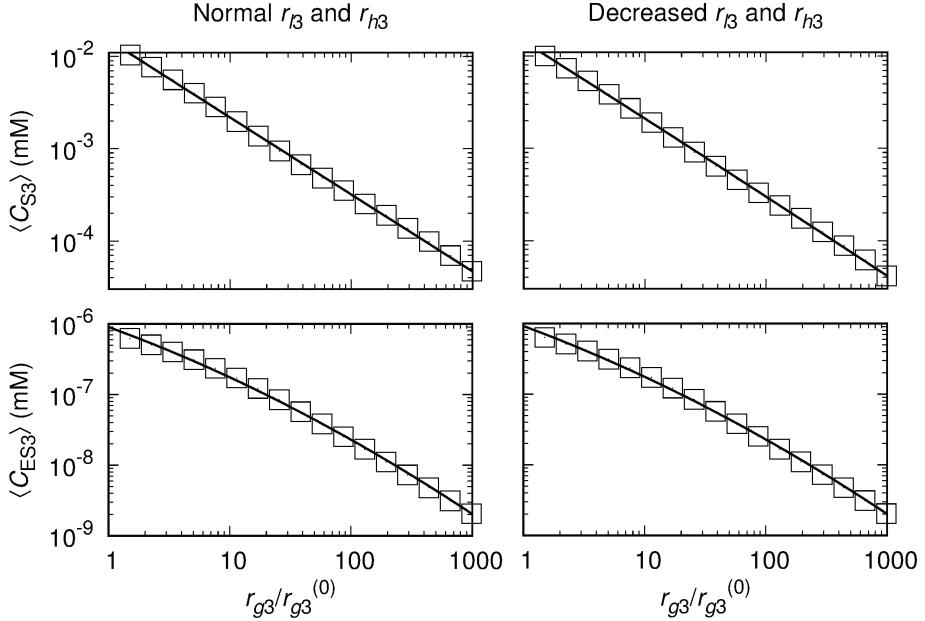


Figure 2.7: Log-normal relations between average A β concentrations and $r_{g3}/r_{g3}^{(0)}$. Log-log plots of $\langle C_{S3} \rangle$ (top) and $\langle C_{ES3} \rangle$ (bottom) versus $r_{g3}/r_{g3}^{(0)}$ for $r_{l3}/r_{l3}^{(0)} = r_{h3}/r_{h3}^{(0)} = 1$ (left column) and 0.1 (right column). Data were obtained at $\beta/\beta^{(0)} = 10$. Squares indicate average values obtained via simulations and lines depict the least square fit of the log-normal relation.

2.4 Discussion of the autophagy model

In this chapter we have investigated via modeling and simulations how autophagy activity affects A β kinetics such as the intra and extracellular levels, secretion, clearance, and autophagic degradation. The mathematical model is extended from the multi-compartment autophagy model originally developed by Han and Choi [12, 76, 77, 78]

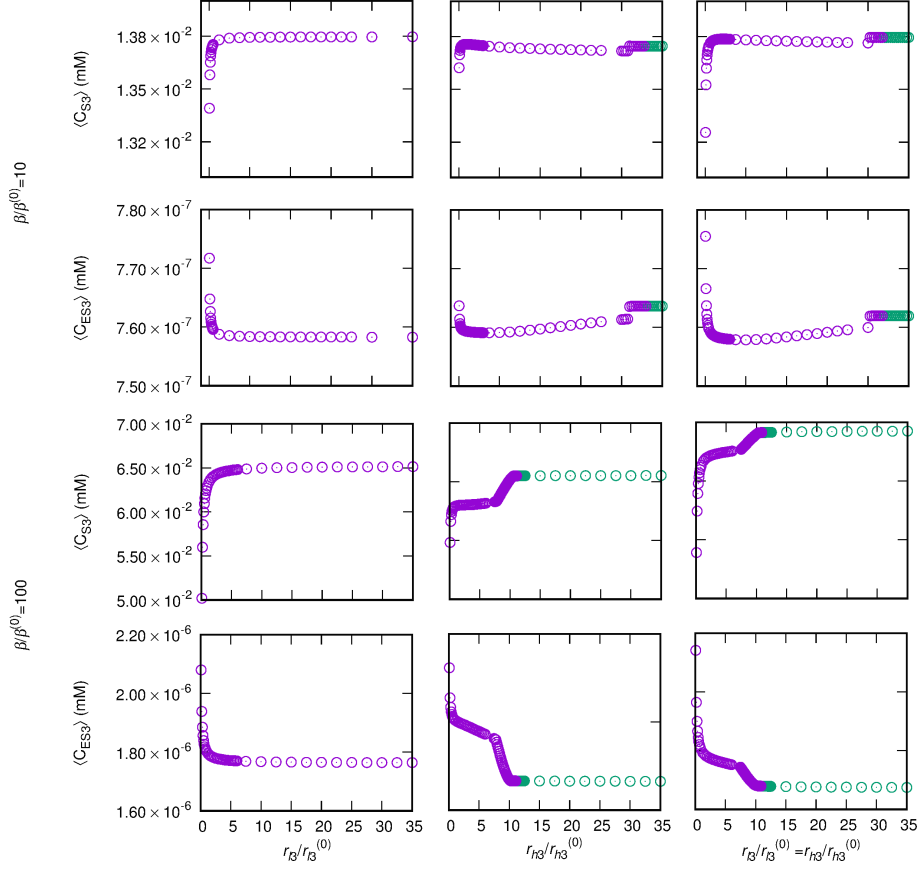


Figure 2.8: Effects of r_{l3} and r_{h3} on $A\beta$ concentrations. Average intracellular $A\beta$ concentration $\langle C_{S3} \rangle$ (first and third rows) and extracellular $A\beta$ concentration $\langle C_{ES3} \rangle$ (second and fourth rows) at $\beta/\beta^{(0)} = 10$ (upper two rows) and $\beta/\beta^{(0)} = 100$ (lower two rows), depending upon changes of $r_{l3}/r_{l3}^{(0)}$ (first column), $r_{h3}/r_{h3}^{(0)}$ (second column), and $r_{l3}/r_{l3}^{(0)}$ and $r_{h3}/r_{h3}^{(0)}$ together (third column). At data points in purple, oscillations of $A\beta$ concentrations are observed; at green data points, concentrations are stationary.

to incorporate $A\beta$ kinetics, accommodating the current working hypothesis and the experimental mechanistic studies on the relationship between autophagy activity and $A\beta$ kinetics. Such multi-compartment frameworks are especially useful for testing biological hypotheses regarding the selective autophagy including Aggrephagy (i.e., autophagic degradation of protein aggregates), Mitophagy (for mitochondria), and Xenophagy (for microbes) [82] because the model can be easily modified to incorporate new substrates for selective degradation in each compartment. This approach can be further improved by including detailed mathematical descriptions of autophagy-related cellular signaling pathways, which have been extensively explored in recent years [84, 84, 85, 86, 87].

In the examination of autophagy dynamics under normal and pathological conditions (Fig. 2.6), the autophagic fluxes and the concentrations of autophagosome and autolysosome in both early and late stage AD are significantly increased than in the basal condition. C_{g3} and C_{l3} are about ten times greater in late stage AD than in early stage AD. This implies that at the late stage AD the increased concentrations due to reduced maturation and intralysosomal hydrolysis may clog neurons, which would further reduce the autophagic $A\beta$ degradation efficacy. Under normal conditions the basal autophagy level is sufficient for removing intracellular $A\beta$ as the mTOR activity is tightly regulated. However, during early and late stage of AD, an increase in soluble $A\beta$ levels leads to mTOR hyperactivity, which should in turn suppress autophagosome formation (i.e., reduced $A\beta$ sequestration) (for details see Autophagosome formation in Mathematical model). Reduced autophagosome formation would increase further the $A\beta$ levels, creating a vicious cycle.

The influence of each autophagic step on the intracellular and the extracellular $A\beta$ concentrations (C_{S3} and C_{ES3}) was examined, providing insight into disease and potential effects of drugs targeting specific steps in the autophagic pathway. The autophagosome formation activity plays a significant role in regulating average values of C_{S3} and C_{ES3} via a log-normal relation: promoting the autophagosome formation

step decreases both $A\beta$ levels. As the autolysosome formation and intralysosomal hydrolysis rates are decreased, as expected in late stage AD, C_{S3} decreases but C_{ES3} increases. It is thus disclosed that the progress from early to late stage AD leads to higher C_{ES3} levels, which could contribute to the deposition of extracellular plaques. On the other hand, C_{S3} decreases along the pathway to late stage AD (i.e., autophagic $A\beta$ degradation is defective in addition to the increased $A\beta$ generation).

The model successfully reproduced the oscillatory behavior of autophagy activity concerning the autophagy-related fluxes and the concentrations of $A\beta$, autophagosome, and autolysosome (Figs. 2.2-6). Such simulated “autophagy oscillations” are qualitatively similar to those observed via biological experiments [88, 89, 90, 91, 94, 93, 94, 95, 96, 97]. However, mechanisms underlying the phenomena have only begun to be explored [96, 97, 98]; the oscillations may be tightly controlled via the autophagy-related signaling pathways to keep the autophagy activity within physiological levels that is important for cellular homeostasis. The simulations presented here exhibit two interesting features: 1) In the early and late-stage AD asymmetric oscillating patterns of C_{S3} and C_{ES3} are exhibited, while symmetrical patterns were seen under the basal condition. 2) Above certain activity levels of autolysosome formation (r_{l3}) and intralysosomal hydrolysis (r_{h3}) for $A\beta$, the oscillations of proteins (C_{S1} , C_{S2} , C_{S3} , and C_{ES3}), ATP (C_A), and amino acids (C_a) disappear.

These findings are expected to be useful for the design of future studies and may give insight to maintaining physiological regulation of the $A\beta$ levels. Defects arising in different steps of the autophagy process would influence in a different way the $A\beta$ kinetics, which will give rise to distinct AD pathology. This suggests that pharmacological modulations of the different autophagy steps may have different implications for AD therapy and prevention.

There is much room for refinement of the model. While the current model describes autophagy in the general neuron, for a more complete picture of the role of autophagy in neurodegenerative disorders, cell type-specific modeling must be done.

Different types of neurons may respond differently to stress. Moreover, non-neuronal cells such as microglia cells and astrocytes may have drastically different autophagic responses to stress compared to neurons, and they may play a crucial role in pathology [99]. Microglia in particular can contribute to $A\beta$ clearance by digesting extracellular $A\beta$ via endocytosis, and an impaired microglial response may be a factor in AD [100]. A complete picture of the effects of autophagy on $A\beta$ levels will thus include such factors. We leave this to a future study.

Chapter 3

Aggregation of amyloid- β peptides in Alzheimer's disease

3.1 Background

Although Alzheimer's disease (AD) has many contributing factors, the amyloid hypothesis currently stands as the dominant model of AD pathogenesis [101, 102, 21, 22, 23]. According to this model, the key initiating event in AD is the aggregation of the amyloid- β peptide ($A\beta$), a naturally occurring peptide consisting of 36 to 43 amino acids generated from proteolytic cleavage of the amyloid precursor protein (APP). AD-causing mutations in APP and in presenilins 1 and 2 alter the active cleavage sites of APP, elevating the relative levels of the more aggregate-prone species $A\beta_{42}$ [103, 104, 105]. The apolipoprotein E (ApoE) $\epsilon 4$ allele, the strongest known genetic risk factor for AD [106], exhibits an increase in amyloid plaques and deposits [107, 108], likely due to chronically impaired $A\beta$ clearance [109]. ABCA7, a more recently found risk factor [110], has also been shown to be involved in $A\beta$ clearance [111]. $A\beta$ dyshomeostasis and its subsequent aggregation is thus a central process in AD, and understanding the precise aggregation features of $A\beta$ is important in identifying therapeutic targets.

A large part of the difficulty in studying the precise pathological mechanisms of $A\beta$ is its diverse structure [112]. The AD-relevant $A\beta_{42}$ is more hydrophobic and aggregate prone compared to $A\beta_{40}$ and forms soluble oligomers through a distinct pathway [113]. While the highly ordered fibrillar structures were thought to be necessary for amyloid toxicity, mounting evidence points towards soluble oligomers as the primary toxic species [114, 53]. $A\beta_{42}$ oligomers can lead to a decrease in synapse density and cause memory loss [115, 116]. Plaque cores isolated from AD brains and washed do not impair long term potentiation, but the diffusible $A\beta_{42}$ oligomers that are released from them do [117]. A separate study has also shown that plaques have a penumbra of soluble $A\beta$ oligomers in which the synaptic density is low [118]. While the plaque sizes do not seem to change over time [119], plaque-associated toxicity has also been shown to increase over time [120]. A recent study of the nanoscale structure of amyloid plaques also found a higher concentration of soluble oligomers around plaques of autosomal dominant AD patients [121].

In systems containing elements across multiple length scales, size distributions contain information about the underlying formation process [122, 25]. *In vitro* studies of oligomer size distributions have reported skewed distributions, sometimes fit to log-normal curves [113, 24]. Interestingly, skewed size distributions in large plaques in post mortem brains also exhibit a skewed distribution [123, 119]. Mouse models also exhibit skewed plaque size distributions [124].

The previous chapter examined the relation between the autophagy process of a generic neuron and the secretion of $A\beta$ into the extracellular space. This chapter seeks to characterize the aggregation of $A\beta$ into oligomers by modeling the size distribution of aggregates.

3.2 Merging model

We define the size distribution function $f(x, t)$, defined as the concentration of oligomers of size x at time t . The time evolution of $f(x, t)$ is given by

$$\begin{aligned} \frac{df(x; t)}{dt} = & [R_{sec}(g(t))g(t) - R_{clr}(f(1; t))f(1; t)]\delta(x - 1) \\ & + \sum_{\alpha} \left[-\lambda(\alpha, x)f(x; t) - \frac{\lambda(\alpha, x)}{\alpha - 1} f\left(\frac{x}{\alpha - 1}; t\right) + \frac{\lambda(\alpha, x/\alpha)}{\alpha} f\left(\frac{x}{\alpha}; t\right) \right] \\ & + \sum_{\beta} \left[-r(\beta, x)f(x; t) + \frac{r(\beta, x/(\beta - 1))}{\beta - 1} f\left(\frac{x}{\beta - 1}; t\right) + \frac{r(\beta, x/\beta)}{\beta} f\left(\frac{x}{\beta}; t\right) \right] \end{aligned} \quad (3.1)$$

Here R_{sec} is the secretion rate of $A\beta$ into the extracellular space, R_{clr} is the clearance from the extracellular space, $\lambda(\alpha, x)$ is the merging rate of polymers of size x with those of size $(\alpha - 1)x$. The summation is over all α such that αx spans all positive integers (in numerical integrations, up to some maximum size N_{max}). $r(\beta, x)$ is the disassociation rate from polymers of sizes x to sizes of βx and $(1 - \beta)x$.

$$\begin{aligned} \lambda(\alpha, x) &= \lambda_0 e^{-(\alpha-1)x/A} \\ r &= r_0 e^{B(\beta-1)} \end{aligned} \quad (3.2)$$

We first consider the case in which we begin with a solution of only monomers, and observe their aggregation. We assume negligible disassociation rate $r(\beta, x) = 0$ and no secretion or clearance, hence having

$$\frac{df(x; t)}{dt} = \sum_{\alpha} \left[-\lambda(\alpha, x)f(x; t) - \frac{\lambda(\alpha, x)}{\alpha - 1} f\left(\frac{x}{\alpha - 1}; t\right) + \frac{\lambda(\alpha, x/\alpha)}{\alpha} f\left(\frac{x}{\alpha}; t\right) \right]$$

With initial condition $f(x, t = 0) = c\delta(x - 1)$. The rate constants are set to $\lambda_0 = 0.01$ mM/h, $r_0 = 0.1$ mM/h, $A = 20.0$ mM, $B = 20.0$ (Table 3.1). This results in the distribution described in Figure 1.

The figure also shows fits of the Weibull and lognormal distributions to the numerical solution. The log-normal fit parameters are $\mu = 4.4662 \pm 0.0002$, $\sigma =$

Parameter	Description	Value
λ_0	rate of association	0.01 nM/h
A	exponential factor of association	0.01 nM/h
r_0	rate of disassociation	0.0 nM/h
B	exponential factor of disassociation	0.0 nM/h
x_n	fibril nucleus size	6
c_n	”critical concentration”	90nM

Table 3.1: Table of A β aggregation model parameters.

0.5026 ± 0.0002 . The log-normal distribution is given by

$$f(x) = \frac{A}{x\sigma\sqrt{2\pi}} e^{-(\log x - \mu)^2/\sigma^2} \quad (3.3)$$

We find that the merging/disassociation model gives rise to a distribution very close to a log-normal distribution, as found in [24]. This model is structurally similar to the binary fission model [25], which in the simplest case results in a Weibull distribution. Interestingly, the addition of multiple ratios b and β , along with the exponential forms in Eq. 3.2, result in a distribution closer to the log-normal distribution. The log-normal distribution also emerges from a self-replicating growth process.

3.3 Toxicity of aggregate size distributions

Recent studies suggest that the toxic amyloid species are middle-sized oligomers. Figure 3.2 shows the resulting distribution after 10 years of monomers secreted by a neuronal cell as established in chapter 2. The magenta points indicate basal autophagy rates. The red points indicate early AD, while the blue indicate late AD. We observe a slight shift towards larger oligomers in late AD compared to early AD, and a significant shift towards larger species for both early and late AD when compared with the basal levels.

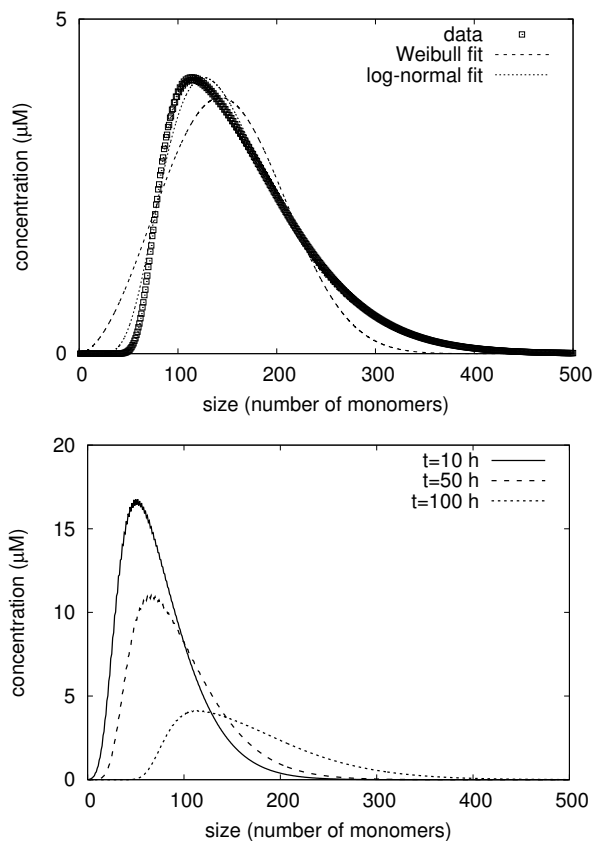


Figure 3.1: Numerical solution of model in equations 1 and 2, along with Weibull and log-normal curve fits (left). Data curves of solutions at times $t = 10, 50, 100$ hs (right).

When autophagy is induced during this time, we have the distribution plotted in green Figure 3.3. This exhibits a significant shift towards small, non-toxic oligomeric species. This indicates the potential clinical effects of autophagy induction in reducing $A\beta_{42}$ buildup.

3.4 Size distribution of plaques

The merging model was fit to *in vitro* data and describes oligomer formation. This resulted in a log-normal distribution, as found in experiments. $A\beta$ oligomers and fibrils

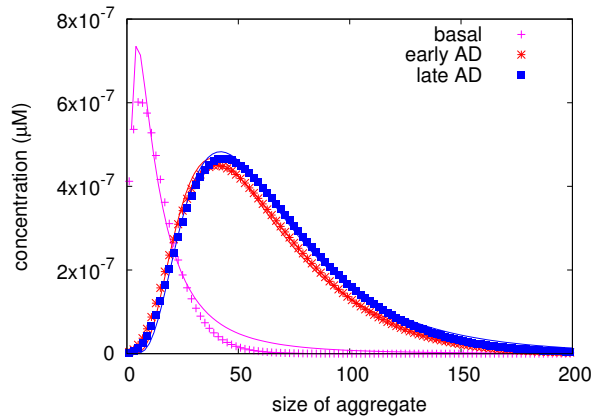


Figure 3.2: Size distribution of a monomer population after ten years in basal, early AD, and late AD conditions.

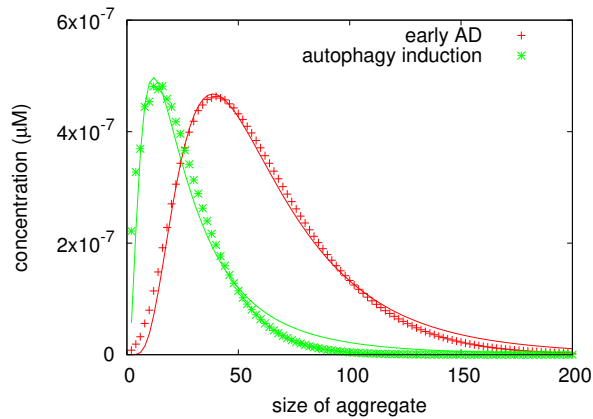


Figure 3.3: Autophagy shifts the distribution away from the toxic species.

further aggregate into plaques, dense macroscopic structures composed of entangled fibrils and oligomers.

Here we use Equation (3.1) to mimic an *in vivo* situation in which there is $A\beta$ secretion and clearance. The delta function in the first line of Eq. (3.1) indicates that only monomers are subject to secretion and clearance. It should be noted that in reality, oligomers up to a certain size can be subject to clearance by proteolysis or microglial

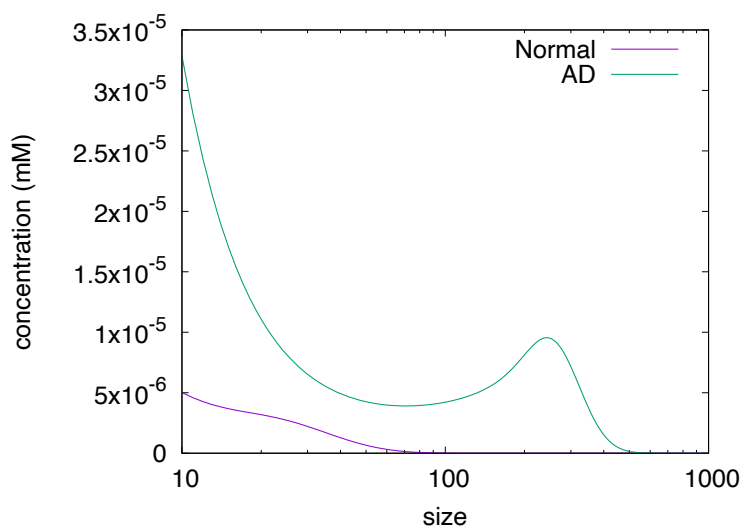


Figure 3.4: Effect of higher $A\beta$ production on size distribution of aggregates after ten years. Magenta indicates the normal rate, while green indicates AD. The size is in arbitrary units.

endocytosis. However, aggregates beyond a certain size are no longer able to be removed. The current model serves as a first approximation of such a situation.

We assume that $A\beta$ secretion and clearance levels are such that $f(1, t)$ is constant, with the value 0.00019 mM in the basal case and 0.0022 mM in AD with higher $A\beta$ production, according to the results of the previous chapter. The results are shown in Figure (3.4). Here we see a log-normal-like peak in the higher sizes superposed with decaying curve starting from the monomer population.

3.5 Discussion: Towards a multi-scale model of Alzheimer's disease

Despite great efforts to treat Alzheimer's disease by targeting $A\beta$ aggregation, such therapeutic methods have seen limited efficacy [129]. This has led to some researchers to turn to other targets. While it is important to explore other avenues treatment, our understanding of the effects of $A\beta$ is incomplete, and gaining a better understanding of $A\beta$ aggregation could lead to new ways to target aggregation.

While preliminary, the results of this chapter provides a starting point to quantitatively model the aggregation of $A\beta$ into oligomers and further on into plaques. The form of Figure (3.4) represents a complete size distribution including oligomers and larger aggregates, albeit with a simplified model. Future studies should used data from *in vivo* samples that analyze the size distribution more completely than found in previous studies, which focus either on oligomers or plaques and rarely both.

Future work will also seek to perform Monte Carlo simulations of aggregation. While the current merging model can compute size distributions, it does not contain information about aggregate morphology. Simulations can reveal how microscopic aggregation mechanics lead to the range of structures seen in postmortem histology data (e.g. diffuse plaques, dense core plaques, etc.).

Chapter 4

Disruption of the circadian rhythm and recovery via light treatment

4.1 Background

As a result of the 24 hour light-dark cycle of the earth, organisms have evolved to have biological oscillations that are collectively termed circadian rhythms [130]. In the case of mammals, the suprachiasmatic nucleus (SCN), located in the hypothalamus, orchestrates these circadian rhythms, playing the role of a central pacemaker [26]. The SCN has an intrinsic cycle of near-24 hours with some individual variation. It gives various cues throughout the brain, acting as a master clock.

The evolutionary advantage of the circadian pacemaker is its ability to allow the body to anticipate periodic events of the environment. While period of the SCN is not exactly 24 hours, it adjusts its phase in response to the environment, becoming entrained to the daily cycle in normal circumstances. While entrainment can be due to multiple environmental cues, one of the most significant ones is the light-dark cycle. Information on light intensity is transmitted via the retinohypothalamic tract to the SCN [132, 133]. With a strong enough light-dark cycle, the SCN is locked to the 24-h cycle of the environment, ensuring that we are active during the day and at rest during

the night [134, 135]. One of the most significant ways in which the SCN regulates the body is surely its influence on the sleep-wake cycle. The SCN applies increasing sleep pressure as the clock approaches subjective night [131]. The monoamine nucleus (MA), ventrolateral preoptic nucleus (VLPO), homeostatic (H) regulators including adenosine, and orexergic (ORX) neurons along with the SCN interact to consolidate a stable 24-hour sleep-wake cycle [136, 137, 138, 139, 131].

The SCN may, however, fail to be entrained to the environment. This often coincides with sleep disorders [27]. When the SCN is desynchronized with the environment, one may experience drowsiness during the day and sleeplessness during the night. These sleep disorders are associated with psychiatric disorders such as depression [28] and bipolar disorder [29], as well as neurodegenerative disorders such as Alzheimer's disease [30]. In all of these cases, the causal relation is not clear. In order to model the phenomenon of circadian entrainment and how it may fail, we model the brain at a macroscopic scale. We consider the essential regions of the brain involved in the regulation of the sleep-wake cycle and circadian rhythm, and quantitatively model their interactions with physiological evidence. Indeed, for centuries such mathematical models for sleep-wake dynamics have accompanied experimental discoveries [140, 141, 142]. For our purposes, we borrow the framework of the Phillips-Robinson (PR) model [143, 144], which models the sleep-wake system as a flip-flop switch between mutually inhibiting neuronal populations [138]. The PR model has been used to successfully describe the main features of sleep, and can be fit to quantitative observations. Previous studies have examined responses of the model to external impulses [145] and noise [146]. The model has been extended to study specific phenomena including sleep deprivation [147], caffeine [148], narcolepsy [149], and shift work [150].

In this chapter, we extend the PR model to incorporate the effects of both orexin and a circadian oscillator. We show the interdependent effects of both an imbalanced orexin level and insufficient light on the stability of the 24-h period lock. This pro-

vides a way to examine the effects of orexin and light on the circadian system together, whereas previous research has focused on the effects of just one or the other. The effects of orexin on sleep stability was examined by a previous study [149] but did not explore the question of entrainment. A circadian oscillator model was developed to study circadian dysregulation in a shift work setting, but physiological factors such as orexin were not considered [150]. This combined model allows us to examine the effects of orexin, a neurotransmitter implicated in many of the aforementioned disorders, together in and conjunction with light. We also simulate light treatment, and seek to offer a more complete picture of the efficacy of such procedures, providing insight into optimal treatment.

4.2 Model of the sleep-wake system coupled with the circadian oscillator

We base our model on the PR model [143]. At the center of the model is the flip-flop switch consisting of two mutually inhibiting neuronal populations, the VLPO and the MA. The dynamical variables V_v and V_m of the model represent the average cell body potentials of the VLPO and MA, respectively. In addition, ORX neurons are incorporated with cell potential V_o , following the previous model of narcolepsy [149]. The MA represents the ascending arousal system; when it is activated, it sustains the wake state. The VLPO's role is to measure sleep pressure and, when it is high enough, inhibit the MA, thereby causing sleep. The ORX plays a role in stabilizing the wake state by exciting the MA neurons during wake, preventing random fluctuations causing a transition into sleep. The following coupled differential equations describe their time

evolution:

$$\begin{aligned}
\tau_v \frac{dV_v}{dt} &= -V_v + \nu_{vm}Q_m + \nu_{vh}H + \nu_{vc}C + A_v \\
\tau_m \frac{dV_m}{dt} &= -V_m + \nu_{mv}Q_v + \nu_{mo}Q_o + A_m \\
\tau_o \frac{dV_o}{dt} &= -V_o + \nu_{ov}Q_v + \nu_{oc}C + A_o
\end{aligned} \tag{4.1}$$

Here, τ_j is the characteristic time of population j ($= v, m, o$) and ν_{ij} (for $i, j = v, m, o, c, h$) total strength of the connection between j to i , with its sign indicating whether it is an excitatory or inhibitory connection [151]. ν_{ij} is hence proportional to the average number of synapses from neurons of region j to neurons of region i [152]. In particular, ν_{mo} is positive; this reflects the stabilizing effect of orexin by exciting the MA, thus promoting wake. ν_{mo} , dubbed the orexin level, is interpreted to be the amount of orexin neurotransmitters in the brain.

The firing rate Q_j of population j has the form

$$Q_j = \frac{Q_{\max}}{1 + \exp[(\Theta - V_j)/\sigma]}, \tag{4.2}$$

where Q_{\max} is the maximum firing rate, Θ the mean firing threshold, and $(\pi/\sqrt{3})\sigma$ the standard deviation of the firing threshold. In Eq. (4.1), A_v , A_m , and A_o are constants while H and C denote the homeostatic sleep drive and the circadian sleep drive, respectively.

The homeostatic sleep drive H is described by

$$\chi \frac{dH}{dt} = -H + \mu_m \frac{Q_m^2}{\eta_h + Q_m^2} \tag{4.3}$$

where χ is the characteristic time of its decay. Hence, H increases during wake (when Q_m large) and decreases during sleep (when Q_m is close to zero). The second term on the right-hand side describes the saturation behavior of H for larger values of Q_m , with appropriate constants μ_m and η_h [149].

The sleep-wake switch is coupled with the SCN, which has previously been modeled with a modified van der Pol oscillator subject to photic and non-photoc influences [153]. A previous work combined this with the PR model to study adaptation to

shift work [150]. The equations for the circadian oscillator are

$$\begin{aligned}\frac{1}{\Omega} \frac{dx}{dt} &= x_c + \gamma \left(\frac{1}{3}x + \frac{4}{3}x^3 - \frac{256}{105}x^7 \right) + B + N_s \\ \frac{1}{\Omega} \frac{dx_c}{dt} &= qBx_c - x (\delta^2 + kB),\end{aligned}\tag{4.4}$$

which can be derived via the Liénard transformation of the Van der Pol equation [153]. Here x is the component directly related to the circadian sleep drive while x_c is a complementary variable. Their ratio gives the circadian phase ϕ_x according to the formula $\tan \phi_x = x/x_c$. Ω , the characteristic frequency, scales the equation to the 24-hour period. γ is the oscillator's stiffness constant while q and k are constants modulating the strength of the effect of light via B . Finally, δ represents the intrinsic period of the oscillator relative to 24 hours. We here set the intrinsic circadian period to 24.2 h [154], or $\delta = (24 \times 3600)/(24.2 \times 3600 \times 0.997) = 0.994$, where the correction factor 0.997 accounts for the nonlinearity of the oscillator.

The sleep drive C is defined simply to be $C = x$ while the photic and non-photoc influences B and N_s on the circadian oscillator are

$$\begin{aligned}B &= G\alpha(1-n)(1-\epsilon x)(1-\epsilon x_c) \\ N_s &= \rho \left(\frac{1}{3} - s \right) [1 - \tanh(rx)].\end{aligned}\tag{4.5}$$

Here G , ϵ , and r are constants and dynamical variable n is the fraction of photoreceptor cells that are activated. The first equation in Eq. 4.5 characterizes the varying sensitivity of the circadian oscillator to light throughout a day. Here ρ is the rate constant while s is a binary state variable indicating wake ($s = 1$) or sleep ($s = 0$). Hence $s = \theta(V_m - V_m^{th})$, where θ is the Heavyside step function and $V_m^{th} = -2$ mV is the threshold mean potential above which the system is defined to be in the waking state.

The rate of conversion of the photoreceptors from the ready to the activated state is given by

$$\frac{dn}{dt} = \alpha(1-n) - \beta n\tag{4.6}$$

where I is the light intensity and

$$\alpha = \alpha_0 \left(\frac{I}{I_0} \right)^p \frac{I}{I + I_1}, \quad (4.7)$$

where β is the rate of conversion from the activated state to the ready state. The form of α and constants α_0 , I_0 , I_1 , and p are borrowed from [153], in which they were calibrated to fit the intensity response curve in a wide range of intensities. At low intensities, α increases with the light intensity in proportion to $I^{3/2}$, and at intensities much higher than I_1 it does in proportion to $I^{1/2}$. The light intensity $I(t)$ affecting the photoreceptor cells is a function of the environmental light $\tilde{I}(t)$ along with the gating effect:

$$I(t) = s\tilde{I}(t). \quad (4.8)$$

The photic driving force is thus gated by the sleep-wake state. The tilde sign on \tilde{I} will henceforth be omitted for simplicity.

It should be noted that Eqs. (4.4) to (4.8) are not present in Ref. [149], which assumed a fixed sinusoidal sleep drive C . This is reasonable when modeling narcolepsy, a state of unstable sleep-wake patterns. The purpose of the current model is to probe the effects of orexin on a different kind of instability, circadian disruption, and hence the addition of a circadian oscillator is necessary. The oscillator model adopted accurately describes the human phase-response curve to light [153], and we have found that the phase-response curve remains nearly unchanged in the integrated model. The above model is illustrated schematically in Fig. 4.1, which exhibits the components of the model and interconnections between them.

Nominal Parameters and Light Input

Table 1 displays the nominal parameters of the model. We have taken parameters involving the sleep-wake switch and homeostatic sleep drive from Ref. [149] and those involving the circadian oscillator from Ref. [150], with a few adjustments, e.g. $\chi = 40$ h to produce a stable 8-hour daily sleep bout with the 24-hour period.

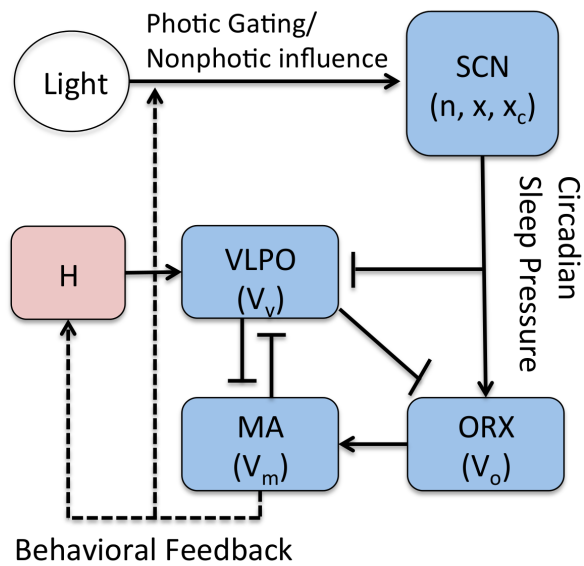


Figure 4.1: Schematic diagram of the connections between components of the model. Pointed-ends represent excitatory connections, while flat-ends represent inhibitory connections.

Sleep-Wake Switch			Circadian Pacemaker		
Parameters	Values	Units	Parameters	Values	Units
Q_{max}	100.00	s^{-1}	Ω	7.2722×10^{-5}	s^{-1}
Θ	10.000	mV	γ	0.13000	—
σ	3.000	mV	q	0.60000	—
ν_{vm}	-2.1000	mVs	k	0.51000	—
ν_{mv}	-1.8000	mVs	δ	0.9944	—
ν_{vc}	-0.3000	mV	β	0.0070000	s^{-1}
ν_{vh}	1.0000	mV	α_0	0.100000	s^{-1}
ν_{oc}	1.0000	mV	p	0.5	—
ν_{mo}	0.30000	mVs	I_0	9500	lux
ν_{ov}	-1.0000	mVs	I_1	100	lux
τ_v, τ_m	10	s	G	2220.0	s
τ_o	120	s	ρ	0.032000	—
χ	40.000	h	ϵ	0.40000	—
μ_m	17.000	—	r	10.000	—
η_h	2.3000	s^{-2}	I_d	600	lux
A_v	-8.5000	mV	I_n	150	lux
A_m	0.52000	mV	T_d	11.000	h
A_o	1.0000	mV			

Table 4.1: Nominal parameter values of the sleep-wake model.

The environmental light is described by a simple square wave,

$$I(t) = \begin{cases} I_d & \text{for } 12 \text{ h} - T_d/2 \leq t^* < 12 \text{ h} + T_d/2 \\ I_n & \text{otherwise,} \end{cases} \quad (4.9)$$

where t^* is defined to be t modulo 24 h and corresponds to the day time. $I(t)$ is given by a 24-h-periodic square function with T_d hours of daylight of intensity I_d and $24 - T_d$ hours of dim light of intensity I_n . The dynamical equations then exhibit periodic oscillations, corresponding to the 24-hour day-night cycle. For our nominal parameter set, we select $I_d = 600$ lux, $I_n = 150$ lux, and $T_d = 11$ h (see Table 4.1).

Figure 4.2 exhibits the resulting oscillations of the seven dynamical variables: the fraction n of activated photoreceptor cells, circadian oscillator variables x and x_c ,

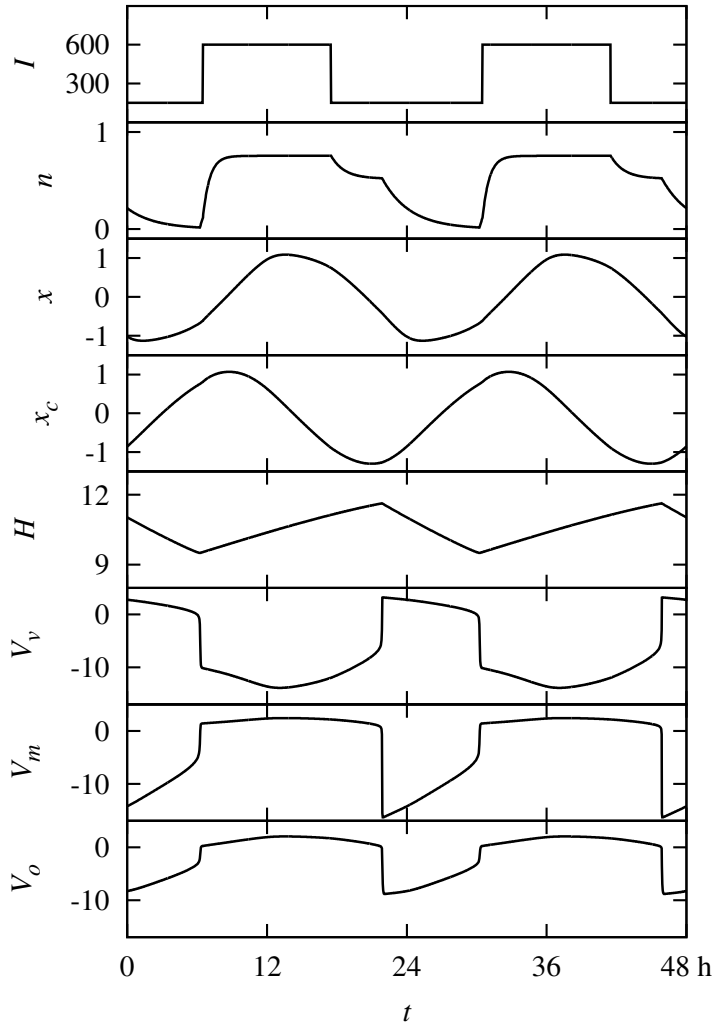


Figure 4.2: Limit-cycle dynamics of the model for nominal parameters, plotted for 48 h. Entrainment due to the light input I (in units of lux) is exhibited as seen in the period-locked oscillations of cell potentials V_v , V_m , and V_o (in units of mV) as well as the seven dynamical variables n , x , x_c , and H (unitless).

sleep drive H , and cell potentials V_v , V_m , and V_o of VLPO, MA, and ORX neurons, respectively, are plotted, together with the input light intensity I .

The circadian phase is related to the core body temperature (CBT) minimum via [153]

$$t_{\text{CBT},i} = t_{\phi,i} + t_d, \quad (4.10)$$

where $t_{\text{CBT},i}$ is the time of the CBT minimum on the i th day and $t_{\phi,i}$ is the time at which the circadian phase takes the value $\phi_x = -170.7^\circ$ on the same day i . The time lag between the two is given by $t_d = 0.97$ h. We then define the average phase shift between CBT minima of successive days to be

$$\Delta \equiv \frac{1}{N-1} \sum_{i=1}^{N-1} [t_{\text{CBT},i+1} - t_{\text{CBT},i}], \quad (4.11)$$

where N is the number of days under calculation.

4.3 Period Locking Zone

We now study the dynamics of the model by means of simulations, employing the 4th-order Runge-Kutta method. Numerical integration of the equations describing the model with the nominal parameters in Table 1 results in a stable 24-hour limit cycle, which is interpreted as successful light entrainment: The circadian oscillator is coupled well to the light Zeitgeber, via the term B in Eq. (4.4), and the circadian oscillator in turn fixes the sleep-wake cycle [Eq. (1)], so that sleep occurs during the dark phase and wake occurs during the light phase.

Performing simulations in the absence of light ($I_d = I_n = 0$), we find that the system exhibits a limit cycle with a period of 24 hours and 22 minutes. Hence if the strength of light is weakened, the intrinsic period of the system will overcome the effects of light and there will be a constant phase delay. The critical daylight intensity at which the stable state disappears corresponds to the period-locking bifurcation point.

On the other hand, when the orexin level ν_{mo} is varied, this intrinsic period is altered by the change in the phase and length of the non-photoc influence N_s : A higher

values of ν_{mo} leads to a longer period. This is an alternate way in which stability can disappear.

We carry out simulations of the model using a range of values of ν_{mo} and I_d . To be specific, we sweep the ν_{mo} - I_d parameter space, and take values of ν_{mo} ranging from 0.2 mV s to 0.35 mV s with increments of 0.0002 mV s and of I_d from 150 to 16,000 lux with increments of 10 lux. For each pair of parameters, simulations have been performed for the duration of 60 weeks, of which the data for the first 20 weeks are discarded for equilibration. Accordingly, the average phase shift Δ in Eq. (4.11) is obtained via averaging over the last 40 weeks (i.e., $N = 280$ days). The resulting heatmap plot of the phase shift Δ is given in Fig. 4.3a. The red region indicates the period-locked zone, where no phase shift arises ($\Delta = 0$).

The boundaries of this zone are depicted in Fig. 4.3(b) for two different values of daytime duration T_d . When the total exposure to bright light is low as in winter ($T_d = 9$ h), the stability region is observed to be reduced appreciably. On the other hand, extended duration of daytime ($T_d = 11$ h) tends to widen the stable region.

Figure 4.3 manifests that there are three routes to the loss of the 24-h period: (1) by decreasing the daytime duration T_d , which shrinks the area of the period-locked zone; (2) by lowering the daylight intensity I_d , which amounts to moving left on the ν_{mo} - I_d parameter plane; and (3) by changing ν_{mo} , which corresponds to moving up or down on the parameter plane.

The sleep-wake system maintains a stable 24-hour cycle by means of its phase-resetting response to light. When daylight is insufficient, the photic driving force is not enough for entrainment to occur. This is the case in routes (1) and (2) above. However, route (3) shows that an imbalance in orexinergic neurons can cause circadian disruption even when daylight is typically sufficient. The mechanism by which this occurs is due to the wake-promoting nature of ORX. When ν_{mo} is increased, sleep and wake onset times are delayed with respect to the phase of the circadian oscillator. Due to the gating effects present in the photic drive B , this causes more light to enter

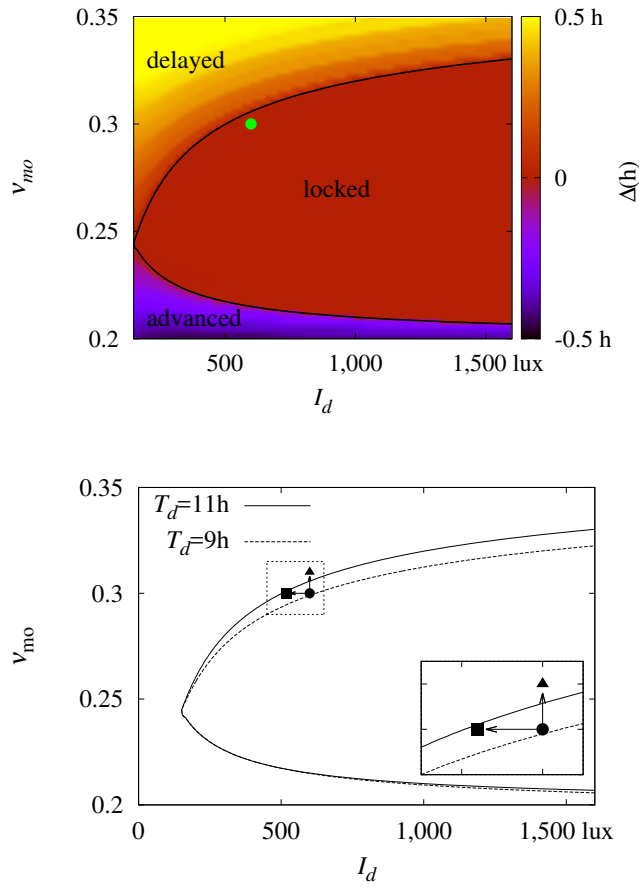


Figure 4.3: (a) Δ (average shift of the CBT minimum) obtained via simulations with $T_d = 11$ h, in the ν_{mo} - I_d parameter space. (b) Period-locking zone boundaries for $T_d = 9$ h and 11 h. Circle indicates the point representing normal conditions, square indicates seasonal disorder, and triangle indicates non-seasonal disorder. The arrows indicate shifts from the normal state to the disordered states. Note that in simulations the shift to seasonal disorder (leftward arrow) is accompanied by a change in T_d from 11 h to 9 h. The area enclosed in the the dotted box is enlarged in the inset.

the system at subjective night and less to enter in the subjective morning. The human phase response curve is such that morning light causes phase advance and evening light causes delay. In consequence the increase in ORX causes phase delay. Similar effects are observed when a constant excitatory stimulation term is added to ORX; this may be achieved simply by increasing the constant A_o .

4.4 Diseased States and Light Treatment

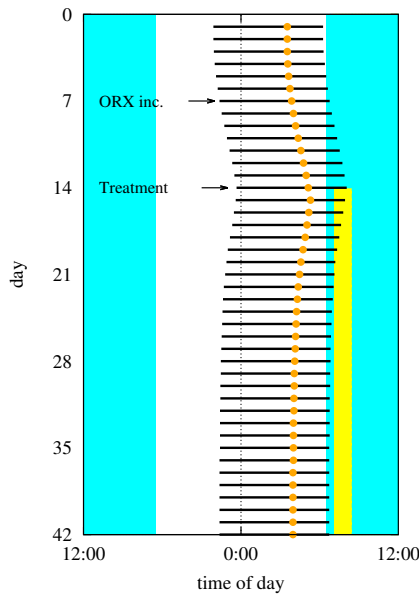


Figure 4.4: Simulations of non-seasonal affective disorder: black lines indicate daily sleep times and colored dots indicate CBT minima. On day 7, ORX is increased, as indicated by an arrow, causing instability. Morning light treatment of 10,000 lux for 1.5 hour daily is administered starting on day 14, also indicated by an arrow. Periods of light treatment are labeled yellow. Note the gradual return to normal phase.

The above results show that both lack of daylight and high orexin levels can cause destabilization in the timing of the onset of sleep. The former is thought to be the case

in seasonal affective disorder while the latter is regarded as a possible mechanism for non-seasonal affective disorder. Here we examine the effects of light treatment on such diseased states.

We first simulate bright light treatment in the case of insufficient light, which consists in artificial exposure to strong white light for a short time (e.g., 1.5 h). Simulations begin in the limit cycle of the model with nominal parameters; then the daylight length T_d and intensity I_d are reduced linearly, from 11 to 9 hours and from 600 to 520 lux, respectively. This is intended to simulate a rapid change into winter light conditions, inducing circadian phase shifts to become increasingly misaligned with the light input.

We then consider the treatment by applying light of intensity I_{tr} in addition to the underlying (environmental) light in Eq. (4.9). During four days into full winter, light treatment is applied daily by taking $I_{tr} = 10,000$ lux for an hour and half each day. Light treatment protocols vary across studies; here the intensity and duration of light has been adopted from the study of light treatment as an antidepressant [155]. Treatment begins at time t_0 of each day, which we set to 7 am unless stated otherwise. If the time t_{CBT} of the CBT minimum drifts towards a stable time within an hour from its initial value, we consider the system to be recovered.

In winter simulations, the wake onset time is retarded under the winter conditions and becomes desynchronized with light in the absence of light treatment. When light treatment is applied, the wake onset is advanced from the delayed phase and settles into the value near its initial phase of 10 pm, indicating recovery.

Next, we simulate a diseased state under normal light circumstances, where the instability is caused by an abnormal value of ν_{mo} . We see in Fig. 4.3 that there are two ways in which this can happen: one by a large value of ν_{mo} , where sleep timing is constantly delayed, and the other by a low value of ν_{mo} , where sleep is advanced. Here we illustrate the former case only.

Figure 4.4 presents the result of the non-seasonal case. Starting on day 10, we raise ν_{mo} from 0.3 to 0.31 mV s, which lies above the stable zone in Fig. 4.3(a), while keep-

ing I_d and T_d in their nominal values. As in the seasonal case, stability is restored when light treatment is applied and the system returns to a normal sleep-wake cycle. Thus the model shows that light treatment has stabilizing effects even when the instability does not arise from the lack of environmental light.

Optimal Light Treatment Times

We now explore how the efficacy of bright light treatment depends on the timing of treatment. Figure 4.5(a) demonstrates the sensitive dependence of the recovery time t_r , i.e., the time duration of treatment required for a return to the initial phase, on the beginning time t_0 of light treatment in the case of non-seasonal depression, for two values of ν_{mo} . Note that in the case of $\nu_{mo} = 0.31$ mV s, recovery occurs in the two limits of the treatment timing: one in the morning and the other in the afternoon. When $\nu_{mo} = 0.315$ mV s, the recovery time for morning recovery is increased while afternoon recovery ceases to work.

It is suggested in Fig. 4.5(a) that in the case of phase-delay instability, both morning and evening bright light treatments are effective although morning treatment will be efficacious in a larger range of parameters. To make clear the difference in the efficacy between morning and afternoon treatments, we select two representative values of t_0 corresponding to morning ($t_0 = 7:00$) and afternoon ($t_0 = 15:00$) treatments. For each treatment time, we calculate the light treatment intensity I_{tr} at which recovery occurs for varying orexin levels.

This leads to a phase diagram on the I_{tr} - ν_{mo} plane, which is shown in Fig. 4.5(b). It is observed that for all values of ν_{mo} , the required treatment intensity is much larger for afternoon treatment. It is also observed that the required treatment intensity I_{tr} grows rapidly with ν_{mo} . Specifically, at $\nu_{mo} = 0.32$ mV s, the intensity I_{tr} becomes unrealistically large, indicating that only morning treatment is feasible. As ν_{mo} is increased further, e.g., to $\nu_{mo} = 0.34$ mV s, this light treatment scheme becomes unfeasible at any intensity.

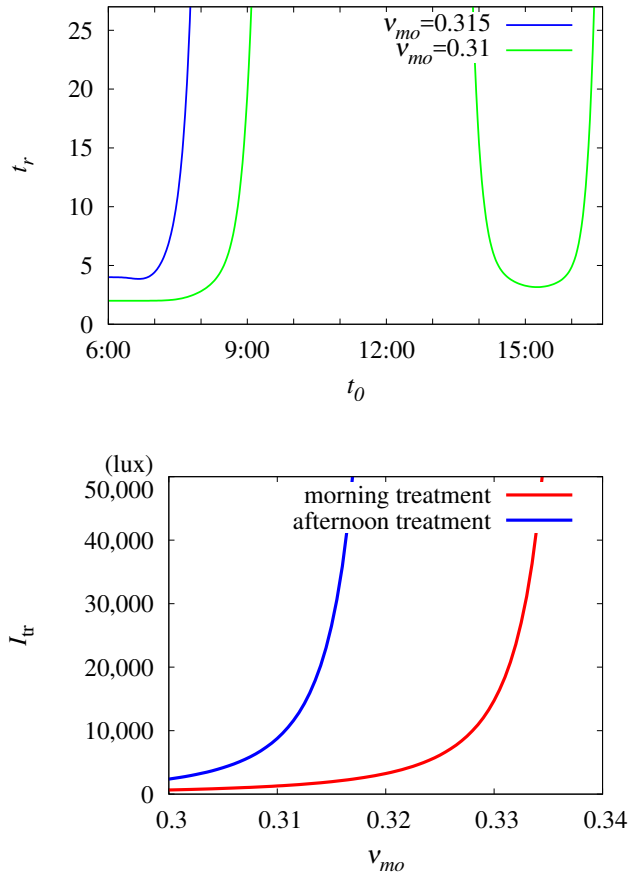


Figure 4.5: (a) Recovery time t_r (in days) versus treatment timing t_0 . t_r indicates the number of days of treatment required for recovery from the circadian instability caused by orexinergic imbalance. Plotted for two values of ν_{mo} . Interpolation has been used to produce a smooth curve. (b) I_{tr} - ν_{mo} phase diagram for morning treatment ($t_0 = 7$ am) and afternoon treatment ($t_0 = 3$ pm). Recover occurs above the curves.

Effects of Noise

Noise is an important aspect of a realistic biological system. Here we consider the effects of noise by modifying the VLPO and MA equations of Eq. (4.1) in the following way:

$$\begin{aligned}\tau_v \frac{dV_v}{dt} &= -V_v + \nu_{vm}Q_m + \nu_{vh}H + \nu_{vc}C + A_v + D\xi_v(t), \\ \tau_m \frac{dV_m}{dt} &= -V_m + \nu_{mv}Q_v + \nu_{mo}Q_o + A_m + D\xi_m(t),\end{aligned}\quad (4.12)$$

where the added terms ξ_j ($j = v, m$) are Gaussian white noise characterized by $\langle \xi_j(t) \rangle = 0$ and $\langle \xi_j(t)\xi_j(t') \rangle = \delta(t - t')$ with noise strength D . Following existing studies [149, 156], we choose not to add noise to the ORX equation; we expect that doing so would bring additional noise in the MA neurons and not affect significantly the results.

Starting from the periodic solution, we perform simulations for 90 days, so as for the circadian system to settle possibly into its new equilibrium. We then simulate additional 40 days and observe whether circadian phase shifts occur. This process is repeated 50 times with new random seeds. Initially, the noise level is taken to be $D = 0.01$ mV, and the entire process is repeated with D increased in increments of 0.01 mV.

Figure 4.6(a) shows the distribution of the CBT minimum time $t_{\text{CBT},i}$ over the last 40 days of simulations for the range of D considered. It is observed that the circadian phase shifts to earlier timings as the noise level is increased. Moreover, noise tends to provoke the CBT timing (specified by $t_{\text{CBT},i}$) to spread: For instance, the standard deviation of $t_{\text{CBT},i}$ takes the value of about 7 minutes at $D = 0.1$ mV. When the noise level is low ($D < 0.21$ mV), the system settles into a new equilibrium within 90 days and the distribution of $t_{\text{CBT},i}$ does not change significantly over the next 40 days. In other words, periodicity, albeit fluctuating, is preserved. At $D = 0.21$ mV, however, there appears a slight advance, which, for $D > 0.21$ mV, increases substantially; this indicates that circadian disruption occurs at $D = 0.21 \pm 0.01$ mV. When D is increased

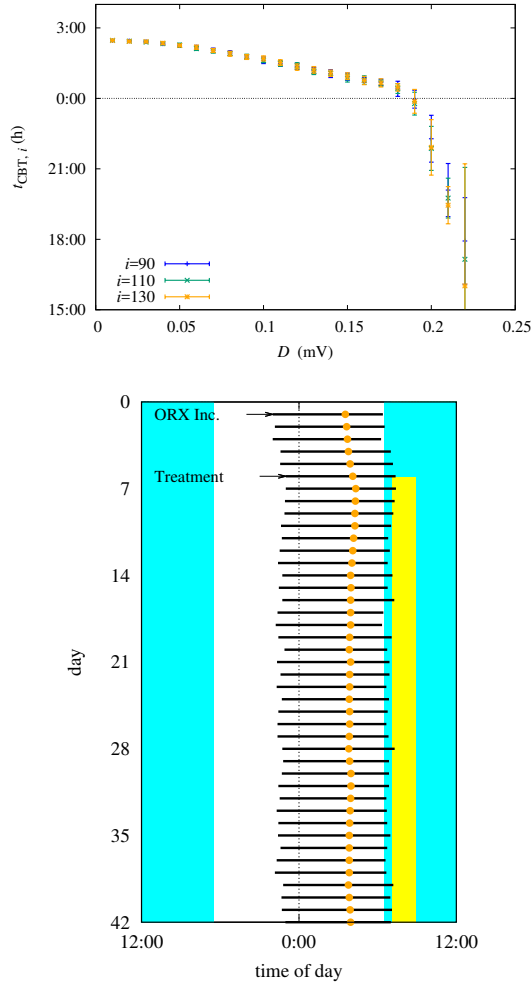


Figure 4.6: (a) Core body temperature minimum time $t_{CBT,i}$ versus noise level D , obtained from simulations. The averages and standard deviations are plotted for the 90th, 110th, and 130th days (blue, green, orange) for $D = 0.01$ mV to 0.25 mV. (b) Light treatment simulations for $\nu_{mo} = 0.33$ mV s, treatment time $t_0 = 7:00$, and $I_{tr} = 10,000$ lux, in the presence of noise $D = 0.1$ mV. As in the case without noise, recovery to the normal phase is observed.

further to the order of 1 mV, noise dominates the sleep-wake switch and drives the system to switch erratically between sleep and wake.

Due to the phase advance effect described above, we expect the stability landscape of Fig. 4.6(a) to change with the introduction of noise. Setting $D = 0.1$ mV, we perform simulations with ν_{mo} varied about its nominal value in increments of 0.001 mV s, and find that circadian entrainment occurs in the range $0.244 \text{ mV s} \leq \nu_{mo} \leq 0.321 \text{ mV s}$, below/above which continuous phase advance/delay is observed. This range is to be compared with that in the absence of noise ($D = 0$ mV), namely, $0.229 \text{ mV s} \leq \nu_{mo} \leq 0.305 \text{ mV s}$. Such a shift of the stability region toward higher orexin levels indicates that the addition of noise offsets some of the phase-delaying effects of orexin. Finally, we simulate morning bright light treatment with $D = 0.1$ mV, $\nu_{mo} = 0.33 \text{ mV s}$, $t_0 = 7:00$, and $I_{tr} = 10,000$ lux, to find that the system undergoes recovery to the normal phase [see Fig. 4.6(b)].

4.5 Discussion

The results of the integrated sleep-wake model provides a mathematical basis for many results established as to circadian entrainment. For example, many blind individuals experience a cyclic sleep disorder: They experience normal sleep-wake behavior for days to weeks at one time, followed by difficulty in sleeping at night and staying awake during the day for a period of time. Observation of such patients discloses that they experience continuous phase delay [157, 158]. Such patients are not entrained to light because they lack stimulation via the retinohypothalamic tract. Assuming nominal parameters otherwise, we should expect behavior corresponding to the upper left-most region in Fig. 4.3(a), which does indicate continuous phase delay.

In sighted individuals, failure of entrainment results in non-24-h sleep-wake syndrome, similar to the above case. On the other hand, there are cases where the circadian phase is period-locked but at an abnormal time. This is the case in delayed sleep

phase syndrome or advanced sleep phase syndrome, where the patient has a 24-hour circadian rhythm but with a phase significantly late or early relative to the socially acceptable time. Namely, the system locates on the right of the curves in Fig. 4.3, but has a late or early phase due to an abnormal orexin level or inadequate exposure to light. Previous studies reported that delayed sleep phase syndrome arises in both circadian and sleep homeostatic systems [159]; our model offers a way to examine the interplay of those contributions, and although this issue is not explicitly explored in this study, it should be explored in the future.

Circadian rhythm disruption is known to be important in seasonal affective disorder, where change in the intensity and duration of light exposure is involved [160, 28]. In our model, we have seen that this corresponds to moving to the left on the parameter plane of Fig. 4.3(b) and shrinking the period-locking curve. The restoration of entrainment via bright light treatment as seen in our model is a possible mechanism behind the reported efficacy of bright light treatment as an antidepressant in seasonal affective disorder [160, 161]. Note here that lack of light exposure is not the only cause of circadian instability and that there is also evidence for the effectiveness of the bright light therapy in treatment of nonseasonal mood disorders [162, 163]. Relatedly, ORX neurons are implicated both in sleep disorders and in mood disorders [164]; our model study has shown that circadian disruption is a channel through which these effects may occur.

Our results thus demonstrate two different channels through which circadian disruption can occur: lack of light and orexin imbalance. Moreover, it shows that bright light treatment can be effective in restoring a normal circadian rhythm in both cases. In the case of orexin imbalance, Fig. 4.4 shows that there are two time windows during which bright light treatment is effective, with morning treatment being effective for a wider range of circumstances. This result is consistent with the fact that morning bright light treatment is generally more effective than evening treatment in clinical studies. For example, Ref. [165] studied changes in the Hamilton Rating Scale for De-

pression (HRSD) scores after bright light treatment in winter depression, and found that morning treatment resulted in significantly higher remission rates compared with evening treatment. With refinement, our approach can be used to predict the efficacy of bright light treatment in specific circumstances and to guide practical applications. In that regard, it would be desirable to have more rigorous fitting to experimental results, based on, e.g., systematic investigation of the noise effects on entrainment conditions and the efficacy of bright light treatment.

Chapter 5

Predicting expenditure during gradient walking

5.1 Background

Physical inactivity, despite its well-known health risks [31, 32], continues to be a serious public health issue [33]. Recently, various wearable devices, including wristbands and mobile phones, have offered a way to track physical activity throughout the day. Such devices can be used in ambulatory conditions by individuals or in clinical settings to monitor patients' physical activity. Many of these devices use an accelerometer-based method to predict energy expenditure [34, 35, 36]. However, these methods are limited in precision [37]. A basic, common assumption used is that the calorie consumption rate is proportional to the walking velocity. A GPS tracker can then be used to measure the walking distance and then compute the total energy consumption. However, this method is limited in accuracy and may not be feasible indoors.

The energetics of human locomotion has been closely studied for decades. Early studies focused on energy expenditure during walking [166, 167, 168, 169, 170] and running [171, 172, 173, 174], and made comparisons with the energy expenditures of other animals [175]. Most relevantly, studies on walking energetics found a proportional relationship between energy expenditure and the square of the velocity. These early studies showed that reasonable accuracy can be attained with simple relations,

despite the complexity of the act of walking. More recently, detailed models of walking dynamics have been presented that examine more closely the mechanics of walking [18-24][176, 177, 178, 179, 180, ?, 182]. These biomechanical models aim to explain human gait patterns via energy minimization. Also studied have been movements of the arm [183, 184] and the head and trunk [185], as well as gait patterns in special groups of interest [186, 187]. Such models have also been used in the field of robotics in developing walking robots [188]. Previous studies were primarily of academic interest, although inexpensive commercial devices have recently been made available for personal or clinical use. Such devices offer noninvasive ways to measure daily caloric consumption, and they have been assessed by numerous validation studies in the literature [189, 190, 191, 192, 193, 194]. The most common types of commercially available products include the wrist-worn accelerometer and devices based on heart rate monitors. Although these devices are good predictors of the number of steps and heart rate, accurate prediction of energy expenditure is yet to be achieved [195]. These validation studies test for various settings; however, they usually lack a discussion of the model or algorithm used in their predictions.

This study proposes a model of walking energetics applicable to a range of slopes. The model is based on a simple equation and uses data from a wearable device. The method uses a foot monitoring system that can sense footsteps, which allows for direct measurement of step frequency. We found that a high-accuracy model can be developed for a range of upward and downward slopes. The fact that it is based on a direct measurement of footsteps allows the device to be versatile and applicable to diverse walking situations. The ability to track expenditure while walking on sloped surfaces is helpful for sloped outdoor ground and also indoor use of stairs or sloped treadmills.

5.2 Data collection

For model development and validation, an experiment was devised in which 73 healthy participants (34 female, 39 male) walked on a treadmill. The participants had a mean age of 43.6 (SD 15.0) years, mean height of 168.3 (SD 10.5) cm, and mean weight of 68.1 (SD 12.1) kg. Participants were selected from healthy volunteers (age 20 to 60 years) who registered in the department of Sport Science, Pusan National University, Busan, Korea. We excluded participants who had cardiovascular, musculoskeletal, or neurological disorders to avoid any confounding factors or biases. The participants were asked to walk on a treadmill at various values of the incline angle, θ , and speed, v . Specifically, the angle was taken to be 0° (indicating no incline); 4° , 9° , and 14° (uphill); and -4° , -9° , and -14° (downhill). It was observed that calorie consumption took approximately 30 seconds to stabilize to a linear rate while walking. Each walking measurement lasted approximately 5 minutes to ensure a sufficiently long sample.

Calorie consumption was measured with a COSMED K4b2 portable gas analyzer system. This indirect calorimetry, based on the gas analyzer system, measures oxygen consumption, from which energy expenditure is computed. This method has been validated as an accurate measure through numerous comparative studies [196, 197, 198] and is used as a criterion measure in many validation studies [189, 190, 191, 193, 194, 195]. The gas analyzer was worn during the treadmill experiment, and it recorded a time series of cumulative calorie consumption. To eliminate noise associated with the beginning and end of the experiment, we discarded data for the first 50 seconds and the final 10 seconds before computing the energy consumption rate. Then the basal metabolic rate [199] was subtracted to obtain the energy expenditure associated with walking, which is denoted by P .

Each participant also wore a foot monitoring system, consisting of shoe insoles equipped with eight pressure sensors. The insole used was a prototype developed by 3L Labs (Seoul, Korea), and provided to us for research purposes. A Fitbit Surge, a wrist-worn accelerometer device, was also worn by each participant to compare the accuracy

of its caloric consumption prediction. This study was approved by the Institutional Review Board of Pusan National University, Busan, Korea. All participants provided written informed consent (PNU IRB/2015_33_HR).

A value of 0, 1, or 2 indicated the pressure on each of the pressure sensors and was recorded with a frequency of 10 Hz, which resulted in an array of 16 integers for each time step of 0.1 s. A snippet from example data is shown in Fig. 5.1. From the pressure sensor data, we were able to extract the step frequency, f . We performed this by examining the sum of the pressure sensor values at each time step. An example is shown in Fig. 5.2.

Although it is natural to consider the foot to be off the ground when this sum is 0, this can result in erroneous results if one or more of the pressure sensors remain at a value above 0 throughout the entire step cycle, either due to a faulty sensor or residual pressure. We found that better accuracy was achieved when high and low thresholds were used. This was done by first assigning the on-ground status to the first-time step, and then sequentially assigning either the on-ground or off-ground status to each following time step. If the previous time step was on-ground and the pressure sum was below the lower threshold, we assigned the off-ground status to that time step; if the threshold was not crossed, the time step was left in on-ground status. If the previous status was off-ground, the on-ground status was assigned if the pressure sum was above the upper threshold, and the off-ground status was assigned otherwise. Threshold values between 1 and 10 were tested and compared with manually assigned steps. Lower and upper threshold values of 2 and 5, shown in Fig. 2., were found to produce accurate results.

After assigning a status to each time step, we counted the number of transitions from the on-ground to off-ground status and divided it by the time interval to obtain the frequency. As with the gas analyzer data, we omitted data for the first 50 s and the final 10 s. Only one shoe insole is required to calculate the step frequency; however, we used the average of both sides in this study.

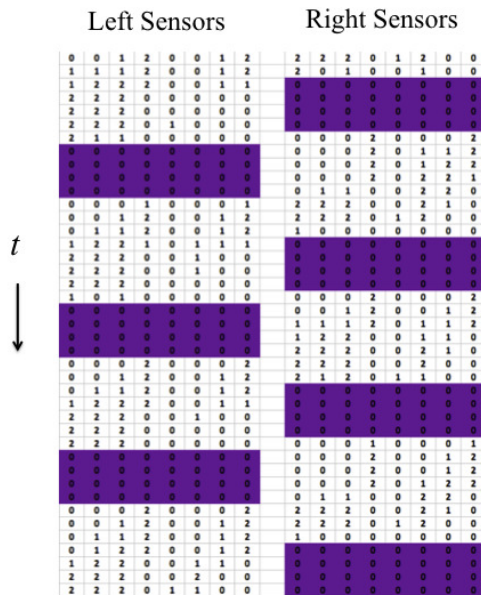


Figure 5.1: A sample of 4 seconds of raw data from the pressure sensors. The vertical position of each number of the array indicates the time, ordered from top to bottom at an increment of 0.1 seconds. Each column denotes a sensor, with left foot and right foot separated. The colored portions indicate when our algorithm decided the foot was off the ground.

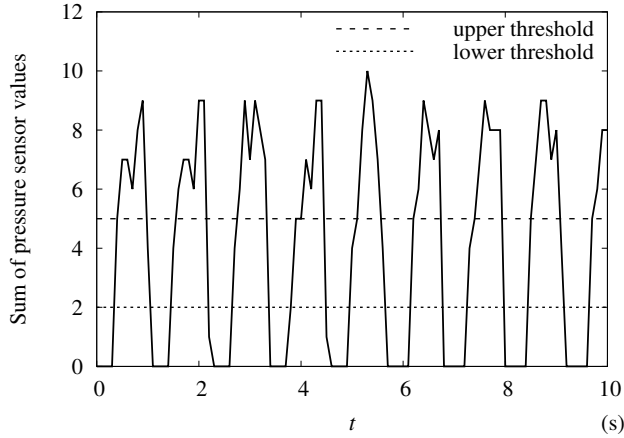


Figure 5.2: Graph of total pressure from the left foot sole over an interval of 10 seconds obtained from the foot monitoring system from the same data as presented in Fig. 5.1. The two dashed lines indicate the upper and lower thresholds used to calculate the step frequency.

5.3 Model construction

Our model was constructed from considering the energy changes involved in walking. Suppose a participant with body mass M is walking with average speed v on a surface inclined by θ from the horizontal. The participant is swinging their legs with frequency f . The energy consumption rate, P , is given by

$$P = \begin{cases} \gamma P_K + b_0 P_U + P_0 & \text{if } \theta \geq 0 \\ \gamma P_K + b_0 P_U + b_1 P_0^{-1} P_U^2 + P_0 & \text{if } \theta < 0 \end{cases} \quad (5.1)$$

Here positive and negative values of the slope, θ , of the walking surface correspond to walking uphill and downhill, respectively. P_K and P_U are rates of changes in the kinetic energy and in the potential energy, respectively, whereas coefficients γ , b_0 , b_1 , and P_0 are parameters to be determined empirically from the data. The energy change

rates for P_K and P_U are given by

$$P_K = 2Mv^2f, \quad (5.2)$$

$$P_U = Mgv \sin \theta \quad (5.3)$$

In the following, we give an explanation of each term in consideration of energy.

Kinetic energy component

We first consider walking on a horizontal surface (ie, $\theta = 0$). When walking on a treadmill, the upper body moves in a relatively constant velocity, with the moving legs supporting this movement. The legs swing back and forth relative to the upper body's position, undergoing an acceleration-deceleration cycle. We postulated that the energy expenditure was proportional to the kinetic energy change of the legs. The work done on the legs during each walking cycle is given by

$$W = 4 \times \frac{1}{2}mv_0^2 \quad (5.4)$$

Here m is the mass of each leg, v_0 is the maximum speed of each leg's center of mass, and the factor of 4 accounts for the two legs each undergoing acceleration and then deceleration. This differs from the assumption that the legs swing like a pendulum, in which case gravity would do the work.

Since we usually have no way to easily measure leg mass or leg velocity, we defined two ratios: (1) the ratio α of the leg mass, m , to the body mass, M ; and (2) the ratio β of the maximum velocity, v_0 , of the leg to the average walking speed, v , as follows:

$$\alpha \equiv \frac{m}{M}, \beta \equiv \frac{v_0}{v} \quad (5.5)$$

This allowed us to rewrite Eq. 5.3 as $W = 2\alpha\beta M^2v^2$, giving an expression for the work done per cycle. Assuming that the human body converts chemical energy into kinetic energy with efficiency η_K , the energy consumption rate due to the kinetic

energy is given by

$$\frac{1}{\eta_K} W f = 2\gamma M v^2 f = \gamma P_K. \quad (5.6)$$

In writing the right-hand side of Eq. 5.5, the measurable terms are grouped into P_K as in Eq. 5.2, whereas the rest are grouped into dimensionless coefficient γ , given by

$$\gamma \equiv \frac{\alpha\beta^2}{\eta_K} \quad (5.7)$$

Potential energy component

When walking on a horizontal surface perpendicular to the direction of gravity, there is no net change in potential energy. It changes when the subject is walking up or down a slope. We first considered upward inclines. When one walks up a slope of angle θ at speed v parallel to the surface, their potential energy, U , changes at a rate $\frac{dU}{dt} = P_U$, given by Eq. 5.2. For simplicity, we further assumed that when walking up a slope, additional energy proportional to this term is required. Accordingly, the energy expenditure rate associated with the changing potential energy is given by $b_0 P_U$, where b_0 is the inverse of the efficiency, η_U , (Eq. 5.7) with which the body converts stored energy to potential energy.

One might consider simply using the same formula for downhill inclines, in which case the term $b_0 P_U = b_0 M g v \sin \theta$ becomes negative. This would imply that when walking downslope, the change in potential energy can be converted into kinetic energy, thereby subtracting from the total energy cost. However, this leads to a nonsensical result for higher slopes, as it can lead to negative energy consumption. When a downhill slope is steeper than a certain angle, the subject would need to exert a frictional force to prevent from falling forward or walking too fast. Therefore, $b_0 P_U$ does not provide an adequate description of the energy expenditure in this case.

Figs. 5.3 present scatterplots of the data in the three-dimensional space (P_K , P_U , P) for women and men, respectively. This visualization shows that P first decreases then increases as P_U is decreased from zero. Such a parabolic shape indicates the

presence of a quadratic term; thus, we added to P a term proportional to P_U^2 . The energy expenditure associated with potential energy in the case of downhill walking is given by Eq. 5.8. The second term is multiplied by P_0^{-1} so that the coefficient b_1 is kept dimensionless. In other words, b_1 is the coefficient of the quadratic term in the case of downhill walking in units of P_0 . This leads to the full model, described by Eq. 5.1.

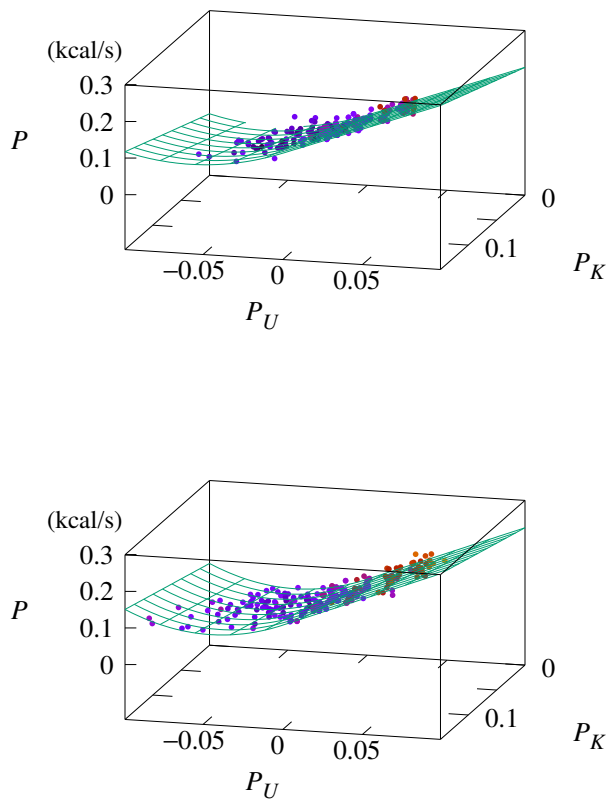


Figure 5.3: Three-dimensional scatterplot of data (dots) and model prediction (lines) of P versus P_U and P_K for (a) women and (b) men.

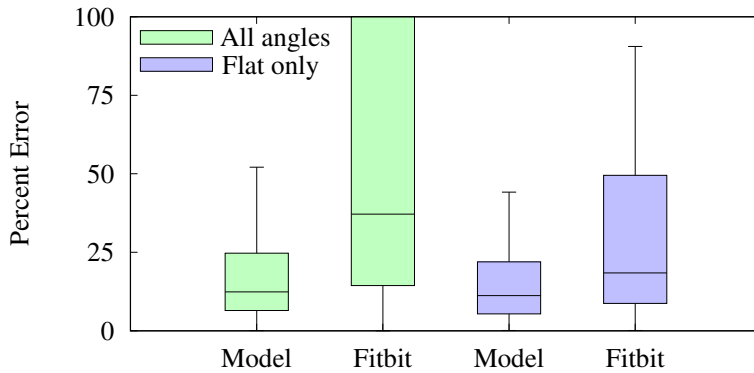


Figure 5.4: Boxplots of the percent errors of predictions made by the model and Fitbit Surge. Errors have been estimated via Eq. 5.9.

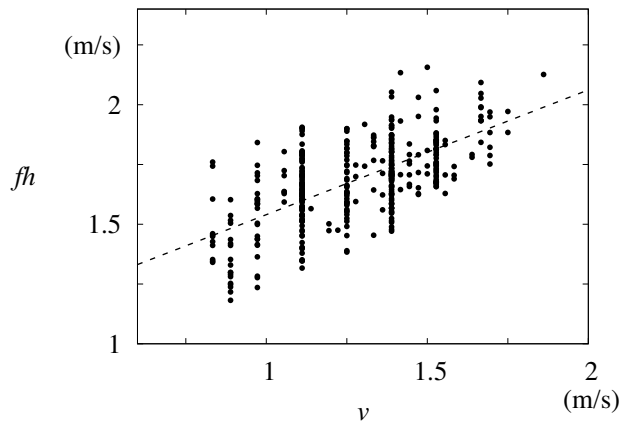


Figure 5.5: Step frequency f multiplied by height h plotted against average walking speed v . Least squares fit line $fh = 0.52v + 1.02$ (m/s) is also shown.

Coefficient	Units	Women	Men
γ	1	0.662	0.517
b_0	1	1.591	1.694
b_1	1	0.575	1.086
P_0	kcal/s	0.0042	0.058
RMSD	kcal/s (kcal/min)	0.016 (0.96)	0.016 (0.96)

Table 5.1: Coefficients for the full model reported with the RMSD on comparison with data.

Linear Regression

The preceding model described leaves parameters γ , b_0 , b_1 , and P_0 to be determined. We obtained these parameters by first taking data for flat and uphill surfaces ($\theta \geq 0$) and performing multiple linear regression through the use of the first equation in Eq. 5.1 with γ , b_0 , and P_0 as fitting parameters. The adjusted R^2 value for the fits of both women and men was .83. Then b_1 was obtained via fitting the second equation of Eq. 5.1 to flat and downslope data ($\theta \leq 0$). During this secondary fit, γ , b_0 , and P_0 were set constant at the values obtained earlier.

5.4 Fitting results

The full set of coefficients, obtained through linear regression, is given in Table 5.1. The dependency of P on P_K and P_U is represented by the surfaces in Fig. 5.3. Due to the piecewise functional form of the model (Eq. 5.1), the prediction plane has no curvature for $P_U > 0$ but does in the region $P_U < 0$.

in a root-mean-square deviation (RMSD) of 0.96 kcal/min for both women and men. A boxplot of the percentage errors of all trials is given in Fig. 5.4, in which the errors have been calculated according to Eq. 5.9. Here P is the prediction by the

method whereas P' is the standard given by the gas analyzer. The median errors were 16.9% for women, 11.2% for men, and 12.4% for both groups. These errors are substantially lower than those found in a validation study for multiple commercial devices, which yielded median accuracies of 28.6% to 35.0% across devices for walking [195].

The predictions made by Fitbit Surge had an RMSD of 2.58 kcal/min (2.7 times that of the model) and a median percent error of 37.3% (3 times that of the model). However, this high error was mostly due to inaccuracies in sloped walking. When restricted to flat surfaces, the Fitbit Surge's accuracy increased dramatically, whereas the model's accuracy increased moderately. The Fitbit Surge's RMSD on flat surfaces was 1.82 kcal/min (2.3 times that of the model, 0.79 kcal/min), and the median percent error was 18.4% (1.6 times that of the model, 11.2%). Distributions of percent errors are portrayed with boxplots in Fig. 5.4.

Before discussing the implications of these results, we note that the variables v and f are not independent. If l is the average length of a step, then $v = fl$. Assuming the approximate relation $h \approx l$, where h is the subject's height, we obtain

$$v \sim fh. \quad (5.8)$$

This relation was observed in the data, as shown in Fig. 5.5.

Equation 5.7 implies that $\eta_U = 0.547$ for women and 0.596 for men. In principle, γ depends on α , β , and η_K . We assumed the average value of $\alpha = 0.185$ for women and 0.165 for men, obtained from an anatomical reference [200], and that $\eta_K = \eta_U$. Taking these values and the fitting result for γ , we obtained from Eq. 5.6 the ratio β with values 1.47 for women and 1.36 for men. This difference in the average may reflect the difference in the average height between women and men. Specifically, Eqs. 5.4 and 5.10 imply $\beta = v_0/v \sim v_0/fh$. The ratio of the value of β for women to that for men equaled 1.08, whereas the ratio of the average height of men to that of women equaled 1.11.

5.5 Discussion

We developed a model based on rates of change in kinetic and potential energies. In general, it predicts linear dependence of the energy consumption on these rates; in particular, it predicts quadratic dependence of the energy consumption on the potential energy change in the case of downhill walking. The method, used in conjunction with a foot monitoring system, predicts energy expenditure with an RMSD of 0.98 kcal/min and a median percent error of 12.4%, lower than those of wrist-worn commercial devices in predicting energy expenditure for walking. With one simple piecewise function, the model adequately predicts energy expenditure for walking in a wide range of the gradient. Notice the differences in parameter values between women and men. The appreciable difference in the value of b_1 between men and women may result from the difference in walking posture; this is beyond the scope of this work and left for future study. In principle, the parameters are fit for each individual and should vary by subject. Thus, Table 1 presents average values of the coefficients within each gender. Even so, it is remarkable that a high degree of accuracy is observed.

Although the model accounts for varying body mass and step frequency (cadence), this does not account for additional individual variations in parameter values due to walking gait and body dimensions. There may be ways to account for such variations without complicating the model. In addition, because the treadmill incline lies between 14° uphill and 14° downhill, we are not able to validate the model for more extreme slopes [201]. In addition, the method has not been tested and calibrated for outdoor walking or variable temperatures and altitudes. However, we believe that our pilot study provides a groundwork for follow-up studies under more ambulatory conditions.

Prior studies have noted the strong correlations between P and v^2 for level walking [168]. The authors have also similarly considered additional energy expenditure when walking uphill, attributing it to vertical lift work. In contrast, our study proposes a simple formula that predicts energy consumption reasonably well for horizontal, uphill, and downhill surfaces within a unified framework. In addition, Ref. [167] made

use of individual measurements, including resting metabolic rate and leg length. Our model shows that high accuracy can be achieved via reasonable assumptions used in conjunction with a wearable, mobile device.

Other existing studies have studied energy expenditure during uphill and downhill walking [201, 202]. The authors reported a minimum energy cost when walking 10° downhill, which is consistent with our results. These studies did not incorporate varying walking speed and body weight, and relied on regression analysis with those variables kept constant. Our study offers a simple formula that applies to various walking speeds and subjects, while also accounting for the surface gradient.

Our method fits separately for women and men. Prior validation studies have found differences in the accuracy of devices between the two genders. A comparative validation study found that gender was one of the strongest predictors for accuracy, with a rate significantly higher for men than for women [195]. Our results suggest that similar error rates for both genders can be achieved.

In conclusion, we have developed a model that predicts energy expenditure during walking on a gradient surface between 14° uphill and 14° downhill, with an RMSD of 0.98 kcal/min. The model has been used in conjunction with a wearable device, the foot monitoring system, which directly measures footsteps. Thus, it offers an accessible method of measuring energy expenditure in realistic walking settings, where gradient walking is common. Future work may test Eq. 5.1 in a wider range of values in the P_K – P_U space. Testing the method on outdoor walking is also desirable for further validation. Although not yet explored, the device could also be used in conjunction with other activity monitoring devices, such as wrist-worn ones, to produce more accurate measures of energy expenditure.

Chapter 6

Behavioral dynamics of interceptive walking

6.1 Background

In this chapter, we explore the walking trajectories of pedestrians crossing a road between vehicles. When pedestrians cross a road with moving vehicles, a situation that can commonly arise in countries where traffic laws are not strictly obeyed, they are intercepting a gap between the cars. Thus we may formulate the problem as one of interceptive walking. This problem is one of public health interest, as pedestrian accidents take up a large proportion of traffic-related accidents, particularly in areas of high population density [39, 40]. A quantitative study of the behavioral dynamics of road crossing may help develop strategies to prevent accidents [40, 41, 42].

The crossing task involved an act of avoidance [41, 204] as well as interception [205, 206, 207]. One possible strategy that people employ to intercept moving objects is the constant bearing angle strategy [205, 206, 207], connected to how walking is visually controlled [214, 208, 209, 210]. In addition, the concept of affordance has also been utilized in the study of such tasks, where affordance is the range of possibilities for action constrained by the environment and physical conditions of the actor [211, 212, 213]. Other studies have provided statistical analyses of pedestrian inter-vehicle gap acceptance rates, which were shown to be related with the pedestri-

ans' perception of affordance [215]. However, these studies do not provide a dynamic model of interceptive walking. We thus need an approach that describes the essential components of walking. To do this, we look for inspiration in the principle of least effort, a widely used idea in studies of human activity. It was first used to explain the rank-frequency distributions of words in the English language[216], and subsequently a diverse range of phenomena such as crowd behavior [217], and even mental effort [218]. These studies have found predictable patterns within the unpredictability of human behavior. The principle of least effort has precedence in the principle of least action in classical mechanics, and other such principles in theories of physics (e.g. in quantum mechanics [219] and general relativity [220]). The interceptive walking task considered here, while not without variability, is simple enough to reveal regularly chosen crossing trajectories that can be modeled quantitatively. We may thus take the approach of Lagrangian mechanics and perhaps model the individual trajectories of pedestrians.

In the following section, we develop such a model by following the procedure of Lagrangian mechanics. We define a Lagrangian and solve the resulting Euler-Lagrange equation, which yields the path of stationary action. We postulate that the Lagrangian is a function of effort (taking inspiration from the principle of least effort) as well as a quantity we call security. Two specific forms of the Lagrangian are proposed and their equations of motion are derived. We verify the model by fitting them to positional time series data from a virtual reality crossing experiment. The experiment simulates a road crossing situation in which a pedestrian crosses a road between two moving vehicles [221, 42, 203]. We find that both forms of the model describe the data accurately.

In the next section, we take one of the models and apply it to data from a wide range of experimental parameters. The best fit parameters contain information about the essential characteristics of each crossing event. We examine the dependence of the average value of each parameter on the crossing conditions. We examine the effects

of the gap size and the initial distance as well as the pedestrian's age, vehicle speed, and vehicle type. We also derive an inequality among the parameters that must be satisfied for successful crossing to occur, hence describing the affordance [212, 213], and also discuss the bearing angle hypothesis within the context of the model.

6.2 Model based on a least action principle

We take inspiration from Lagrangian mechanics, where the Lagrangian is defined as $L = T - U$ with kinetic energy T and potential energy U . Here, we consider a Lagrangian of the form

$$L = E - S, \quad (6.1)$$

where E denotes the *effort* and S the *security*. It is well established that the energy expenditure during walking is proportional to the square of the walking speed [167, 217, 3]. We thus assume that the effort for walking is proportional to v^2 , and write, up to multiplicative and additive constants,

$$E = \left(\frac{v}{v_m} \right)^2, \quad (6.2)$$

where v_m is a scaling constant, making E dimensionless. It will be seen that it is the maximum walking speed.

We reason that security is related to the motivation of the pedestrian to reach a goal while avoiding danger, depends on the walking speed and acceleration. The pedestrian should feel safe when she or he can quickly crosses the gap. Measuring the speed in units of v_m , we thus assume that the drive to move forward is described by $v/v_m (< 1)$, neglecting higher-order terms. We also assume a biomechanically preferred degree of acceleration. The pedestrian thus feels unsafe at low accelerations and prefers either to keep a constant speed or to accelerate quickly. This effect is taken into account by a function $g(a)$ (again up to multiplicative and additive constants), which we presume to be a function with zeros at $a = 0$ and a_m which is convex in between so that $g(a) < 0$

when $0 < a < a_m$, thus preferring either zero or high accelerations. This results in

$$S = \frac{v}{v_m} + g(a). \quad (6.3)$$

We discuss two different forms of $g(a)$ below. The Lagrangian is then given by the difference between Eq. (6.2) and Eq. (6.3).

The Lagrangian is naturally independent of the position y and depends only on the speed $\dot{y} \equiv v$, and of the acceleration $\ddot{y} \equiv a$. We may assume $v > 0$ without loss of generality by choosing a reference frame in which the pedestrian is moving forward. Further, we suppose that the pedestrian does not decelerate until crossing, which implies $a \geq 0$.

We now derive a form of the Euler-Lagrange equation that will simplify the calculations of each specific Lagrangian form. The stationary path for a Lagrangian of the form $L = L(y, v, a)$ obeys the Euler-Lagrange equation

$$\frac{\partial L}{\partial y} - \frac{d}{dt} \frac{\partial L}{\partial v} + \frac{d^2}{dt^2} \frac{\partial L}{\partial a} = 0. \quad (6.4)$$

We use the fact that $\partial L / \partial y = 0$ and integrate with respect to time t , reducing Eq. (6.4) to

$$\frac{\partial L}{\partial v} - \frac{d}{dt} \frac{\partial L}{\partial a} + c_1 = 0 \quad (6.5)$$

with an integration constant c_1 . The chain rule, together with the fact $\partial L / \partial t = \partial L / \partial y = 0$, yields $dL / dt = \partial L / \partial t + v \partial L / \partial y + a \partial L / \partial v + \dot{a} \partial L / \partial a = a \partial L / \partial v + \dot{a} \partial L / \partial a$, which we substitute into Eq. (6.5) to obtain

$$\frac{dL}{dt} - \dot{a} \frac{\partial L}{\partial a} - a \frac{d}{dt} \frac{\partial L}{\partial a} + c_1 a = \frac{d}{dt} \left[L - \left(a \frac{\partial L}{\partial a} \right) + c_1 v \right] = 0 \quad (6.6)$$

Integrating Eq. (6.6), we have

$$L - a \frac{\partial L}{\partial a} + c_1 v - c_2 = 0, \quad (6.7)$$

where integration constants c_2 and c_1 may respectively be absorbed into L as an overall additive constant and as a multiplicative coefficient of the linear velocity term in

Eq. (6.3). We may therefore set $c_1 = c_2 = 0$, which gives us

$$L - a \frac{\partial L}{\partial a} = 0. \quad (6.8)$$

We next discuss two forms of $g(a)$ and solve the resulting Euler-Lagrange equations.

Case 1: Quadratic form

We first consider a quadratic equation $g(a) = (a/a_m)(1 - a/a_m)$, resulting in the Lagrangian

$$L = \left(\frac{v}{v_m}\right)^2 - \frac{v}{v_m} + \frac{a}{4a_m} \left(1 - \frac{a}{a_m}\right), \quad (6.9)$$

where we have included a factor $1/4$ on the second term. Substituting Eq. (6.9) into Eq. (6.8) results in

$$\frac{dv}{dt} = 2a_m \sqrt{\frac{v}{v_m} \left(1 - \frac{v}{v_m}\right)}. \quad (6.10)$$

Eq. (6.10) has fixed points at $v = 0$ and v_m which are unstable. In the range $0 \leq v \leq v_m$, we have the solution

$$v(t) = v_m \cos^2 \left(\frac{t}{4\tau} - \frac{\pi}{4} \right), \quad (6.11)$$

where $\tau \equiv v_m/4a_m$. Eq. (6.11) oscillates between the fixed points and τ corresponds to the duration of each acceleration and deceleration region. With boundary conditions such that the pedestrian begins at rest and intercepts a target at constant speed, the least action path can be constructed as a piecewise functions with the two fixed points and Eq. (6.11) during a time interval centered at time $t = t_a$, resulting in:

$$v(t) = \begin{cases} 0, & t - t_a \leq -\pi\tau \\ v_m \cos^2((t - t_a)/4\tau - \pi/4), & -\pi\tau < t - t_a < \pi\tau \\ v_m, & t - t_a \geq \pi\tau \end{cases} \quad (6.12)$$

Integrating Eq. (6.12) gives us

$$y(t) = \begin{cases} y_0, & t - t_a \leq -\pi\tau \\ y_0 + \frac{\tau v_m}{2} \left(\pi + \frac{t-t_a}{\tau} - 2 \cos \left[\frac{t-t_a}{2\tau} \right] \right), & -\pi\tau < t - t_a < \pi\tau \\ y_0 + v_m(t - t_a), & t - t_a \geq \pi\tau \end{cases} \quad (6.13)$$

Eq. (6.12) and Eq. (6.13) obey the Euler-Lagrange equation at all points. However, they exhibit singularities in the higher derivatives at times $t = t_a \pm \pi\tau$.

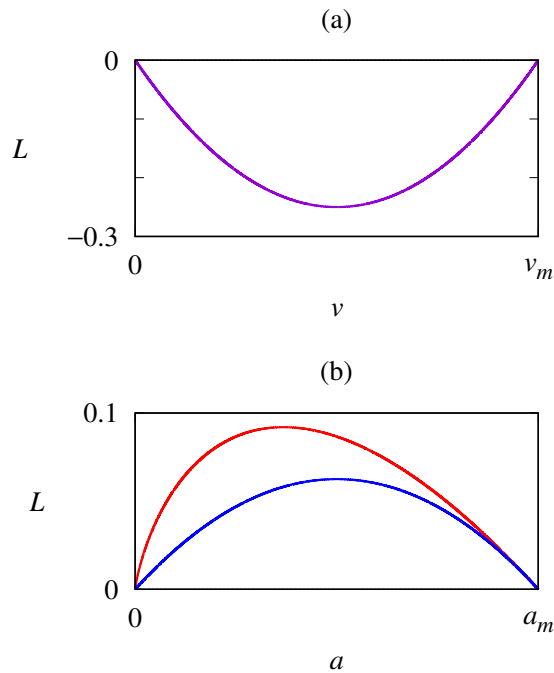


Figure 6.1: (a) Dependence of the Lagrangian L on the speed v (in the absence of acceleration, $a = 0$). (b) Dependence of L on a (for $v = 0$) for the quadratic form (blue) and the logarithmic form (red).

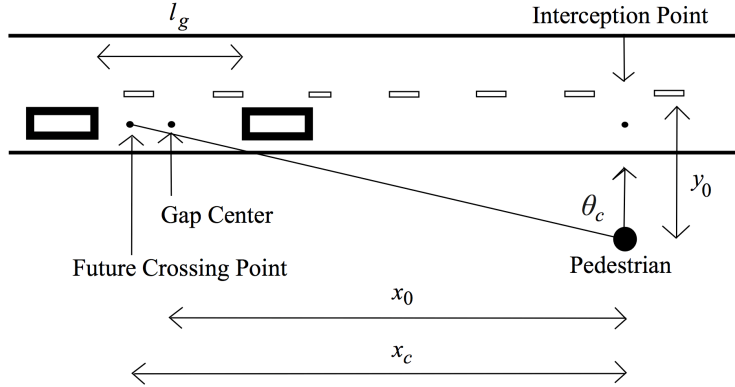


Figure 6.2: Top-down diagram of the crossing environment at time $t = 0$. The two boxes on the road depict two vehicles facing the right, which move forward at a constant speed. The circle depicts the pedestrian, who begins at rest and is facing in the direction the arrow. Labeled are experimental parameters l_g , y_0 , and the bearing angle to the crossing point θ_c .

Case 2: Logarithmic form

As a second case, we take $g(a) = (a/a_m) \log(a/a_m)$, giving us

$$L = \left(\frac{v}{v_m}\right)^2 - \frac{v}{v_m} - \frac{a}{4a_m} \log\left(\frac{a}{a_m}\right), \quad (6.14)$$

again with a factor of $1/4$. Unlike the quadratic equation, this form of $g(a)$ is asymmetrical and steeper on the left side. Plugging into Eq. (6.8) results in the logistic equation

$$\frac{dv}{dt} = \frac{4a_m v}{v_m} \left(1 - \frac{v}{v_m}\right), \quad (6.15)$$

which carries the solution for the speed:

$$v(t) = \frac{v_m}{2} \left[\tanh\left(\frac{t - t_a}{2\tau}\right) + 1 \right], \quad (6.16)$$

where τ is defined the same way as above and again measures the duration of acceleration, and the integration constant t_a determines the timing of acceleration. Note in

Eq. (6.16) that v_m indeed corresponds to the maximum walking speed; further, differentiation of Eq. (6.16) with respect to t manifests that the maximum acceleration is given by a_m . Integrating Eq. (6.16) also gives the position as a function of time:

$$y(t) = y_0 + v_m \tau \log \left[1 + \exp \left(\frac{t - t_a}{\tau} \right) \right]. \quad (6.17)$$

Unlike Eq. (6.13), Eq. (6.17) is free singularities. But the velocity never reaches exactly 0 or v_m , and so has the disadvantage of being an approximation (albeit with an error that decays exponentially).

Hamiltonian formulation

The definition of a Lagrangian immediately suggests that a Hamiltonian can also be constructed. The proposed Lagrangian differs from those typical in classical mechanics in that it contains a derivative of order higher than one. Lagrangians of such form have been studied, and instabilities that arise from unavoidable linear terms in their Hamiltonian functions have been cited as reasons that nature is not described by higher-order Lagrangians in fundamental theory[223, 224]. We appeal to the phenomenological nature of the model and ignore these instabilities here. We construct a Hamiltonian by using Ostrogradsky's construction for third order Lagrangians:[222]

$$\begin{aligned} Q_1 &\equiv x \\ Q_2 &\equiv \dot{x} \\ P_1 &\equiv \frac{\partial L}{\partial \dot{x}} - \frac{d}{dt} \frac{\partial L}{\partial \ddot{x}} \\ P_2 &\equiv \frac{\partial L}{\partial \ddot{x}}. \end{aligned} \quad (A1)$$

Then the Hamiltonian is obtained by performing the Legendre transform,

$$H(Q_1, Q_2, P_1, P_2) = P_1 Q_2 + P_2 A(Q_1, Q_2, P_2) - L(Q_1, Q_2, A), \quad (A2)$$

where A is the acceleration function written in terms of the canonical coordinates.

In the quadratic case, this results in a Hamiltonian of the form

$$H = \frac{Q_2}{v_m} - \frac{Q_2^2}{v_m^2} + Q_2 P_1 - \frac{a_m}{2} P_2 - a_m^2 P_2^2 + \frac{3}{16}, \quad (\text{A3})$$

while in the logarithmic case, we have

$$H = \frac{Q_2^2}{v_m^2} - \frac{1}{4} e^{-4a_m P_2 - 1} + Q_2 P_1 - \frac{2Q_2^2}{v_m^2} - \frac{1}{v_m}. \quad (\text{A5})$$

The Hamiltonians obtained are indeed conserved quantities.

Data Collection

To verify the validity of each case of the model, we make a comparison with the data obtained from a virtual reality road-crossing experiment. In this experiment, human participants walked on a customized treadmill (of dimensions 0.67 m wide, 1.26 m long, and 1.10 m high) with four magnetic counters that track movements. A Velcro belt connected to the treadmill was worn for suppression of vertical and lateral movements, and a handrail was placed for safety. Each participant wore a commercial virtual reality headset connected to a standard desktop PC. The headset portrayed a realistic view of a typical crosswalk in Korea in 1280×800 resolution stereoscopic visual images which shift in real time according to the participant's steps and head turns. Sixteen children (of age 12.2 ± 0.8 yrs, i.e., mean age 12.2 years and standard deviation 0.8 years) and sixteen adults (of age 22.8 ± 2.6 yrs) with normal or corrected-to-normal vision were recruited for this experiment. Informed written consent was obtained from every individual participant. The protocol was approved by the Kunsan National University Research Board. Details of the experiment can be found in Chung *et al.* [203]

Fig. 6.2 presents a schematic diagram of the crossing simulations viewed from above. While the two parallel vehicles are moving at equal constant speed $v_c = 30$ km/h, the pedestrian attempts to cross the road in the perpendicular direction. The paths of the pedestrian and of vehicles intersect at the crossing point. The pedestrian is instructed to cross between the two vehicles if possible. The empty space between

the two vehicles, called the gap, is set to be $l_g = 25$ m in length. The distance between the midpoint of the gap and the intersection point, denoted by x_g , has the initial value 33.3 m, so that the gap center reaches the crossing point in 4 s. The position of the pedestrian is measured by the distance y from the crossing point taken as the origin, and is recorded to generate positional time series. The initial position y_0 is set to be -4.5 m.

Fitting Results

Eq. (6.13) and Eq. (6.17) were fit to the data, making use of v_m , τ , and t_a as fitting parameters. When Eq. (6.13) was fit to the data, the root-mean-square deviation (RMSD) turned out to be 0.052 m on average, with the standard deviation 0.022 m and the maximum RMSD of 0.10 m. Meanwhile, when Eq. (6.17) was fit to the data, the RMSD was 0.056 m on average, with the standard deviation 0.024 m and the maximum RMSD of 0.12 m. It was thus concluded that each model function makes a description of each individual crossing with high accuracy, and no significant difference between the two was found. All time series are plotted in Fig. 6.4, which manifests that overall, data (thin gray lines) fit closely to the model.

There were individual variations in the slope v_m and the acceleration timing t_a , resulting in a spread of the data as seen in Fig. 6.4. Taking the average of the position data in 0.25 s increments, we obtain the average behavior of each collective group, and plot the averages and standard deviations also in Fig. 6.4. The thick red and blue lines depict Eq. (6.13) and (6.17) fitted to the averaged position data, with the fitting parameters given in Table 6.3. Note first that the averaged data also display a good fit to both cases of the model. By plotting the two age groups separately, we observe a difference in the slope. Accordingly, v_m takes different fitting values: The adult group has a higher value by 0.24 m/s (see Table 6.3). Other parameters do not differ significantly.

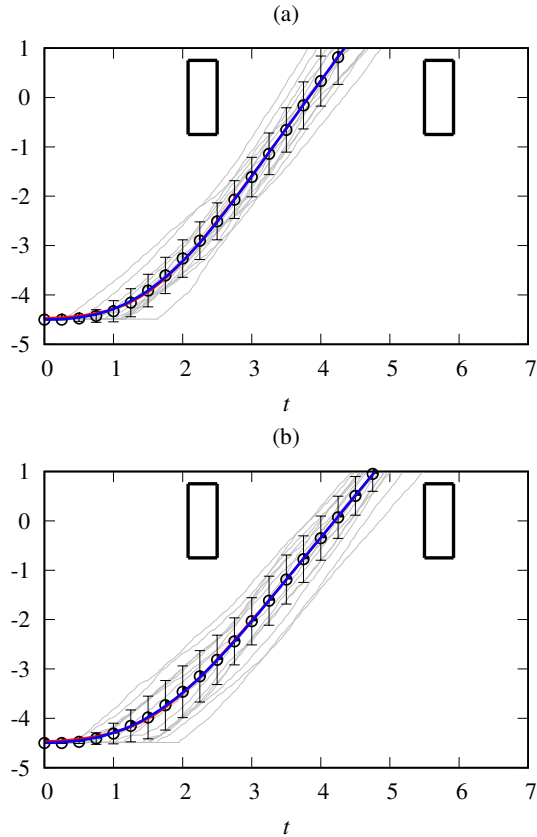


Figure 6.3: Fitting results and data for (a) adults and (b) children, displaying the position y (in meters) versus time t (in seconds). Circles and error bars indicate averages and standard deviations of positions, respectively. Blue and red lines correspond to the quadratic and logarithmic models fitted to the averaged data, respectively. The blue and red lines overlap significantly. Individual data time series are plotted in grey and rectangles represent vehicles.

Model	Age group	v_m (m/s)	τ (s)	t_a (s)	a_m (m/s ²)
quadratic	adults	1.94	0.54	1.50	0.90
	children	1.70	0.59	1.55	0.72
logarithmic	adults	1.94	0.43	1.51	0.32
	children	1.70	0.47	1.57	0.27

Table 6.1: Fitting parameters v_m , t_a , and τ for the averaged data, together with Lagrangian constant a_m , using each model and fit to each age group.

Discussion of the model

We have presented a model for goal-directed human walking behavior, based on a principle of least action. The approach can be considered as generalization of the principle of least effort, incorporating another term called security. Walking behavior results from the assumption of three simple terms making up effort and security. The resulting equations have been found to fit experimental data from a virtual reality road-crossing experiments.

It is not conceivable that our simple model captures the full complexity of the complex biomechanics and psychology involved in walking. The model treats the walker as a self-propelling particle and thus provides rather a coarse approach compared with biomechanical studies [225]. However, we presume that the form of Eq. (6.1) should contain all the essential features of goal-directed walking, including psychological factors. This approach may thus be useful in the study of pedestrian trajectories.

In validating the model, an experimental setup was employed which imposed a gap interception task on the participant. The results show that the participant choose the path of least action as defined by the model. However, while the initial conditions are constrained, the experiments force the participants not into a single point but into a spatiotemporal range (the gap). Accordingly, there are individual variations in the

end point the participant chooses. In addition, we expect that physiological differences lead to differences in constants v_m and a_m , which could result in variations in the least-action path even with the same boundaries. This is made apparent in the difference in v_m between the age groups, which is manifested by different values of v_m and a_m in the Lagrangian.

One may note the limitations of using a treadmill, which may change walking behavior and also constrains the participant to walk in a straight line. Additional walking simulations have been done in which the participants walk freely in a room, with sensors used to detect their positions. The results were again consistent with the model (data not shown). However, an additional dimension is added due to the freedom in the walking direction. There were no interesting features in the dynamics of the angle, which was generally held constant. The choice of the angle exhibits also individual variations; this is beyond the scope of the current model.

The model has been also limited to the case of positive acceleration ($a > 0$). The quadratic Lagrangian (Eq. (6.9)) can already describe negative accelerations, as a piecewise function can be constructed with a deceleration event from velocity v_m to 0 due to the oscillatory form of Eq. (6.11). For the logarithmic Lagrangian of Eq. (6.14), if negative acceleration ($a < 0$) is allowed, we may assume that the security feeling of the pedestrian should depend only on the magnitude (regardless of the sign), and put the absolute value $|a|$ in place of a in equation (6.3). This time-reverses the solution: The speed begins at v_m , then decreases to zero. These solutions describe the deceleration event after the pedestrian has reached a destination. Under some experimental conditions not shown here, the participant walked forward, stopped, and then accelerated again to cross the gap. The stopping behavior between walking can be seen as a deceleration event described by the model with $a < 0$. For simplicity, this is treated in a later section.

We note that the present model has similarity with other models of pedestrian behavior, e.g., in Guy *et al.*, [217], which also defines effort as the metabolic energy

Participant group	Number of participant
Children	16
Young adults	16
Elderly	14
Experimental parameter	Values used
y_0 (initial distance)	-3.5, -4.5, -5.5, -6.5 m
t_g (gap time)	2.5, 3, 4 s
v_c (vehicle speed)	30, 60 km/h
vehicle type	sedan, bus
total configurations	48

Table 6.2: Table summarizing age groups and experimental parameters.

consumption. Our model differs from those previous models in that it includes additional terms (security) affecting the trajectory and also in that it produces an analytical solution for the entire walking trajectory, which is possible due to the simplicity of the walking task. Guy *et al* instead simulate collision avoidance in crowds by restricting the direction of movement based on the environment at each simulation step.

There is much room for refinement of the present model. For instance, the model may be extended further to include a second dimension and/or interactions with other pedestrians. This is left for future study. A detailed examination of the effects of various other crossing conditions (e.g. the initial position of the pedestrian, the gap length, and the vehicle speed) on fitting parameters using one of the models developed here is given next.

6.3 Recasting the model to describe bearing angle and affordance

The position and velocity data from the logarithmic form are here called the simple crossing model. We use this to analyze the crossing data. The velocity is reproduced below,

$$v(t) = v_{\max} \frac{\exp[(t - t_a)/\tau]}{1 + \exp[(t - t_a)/\tau]}, \quad (6.18)$$

which, upon integration, results in the position as a function of time:

$$y(t) = y_0 + v_{\max} \tau \log\{1 + \exp[(t - t_a)/\tau]\}. \quad (6.19)$$

Equation (6.19) is plotted in Figure 6.4a (red line). Constants t_a , τ , v_{\max} are fitting parameters whose meanings can be understood as follows: The measurement begins at time $t = 0$. Assuming $t_a - 2\tau > 0$, we have the initial position and velocity of the pedestrian, $y(t=0) \approx y_0 (< 0)$ and $v(t=0) \approx 0$, respectively. Then, the pedestrian accelerates smoothly until the maximum velocity v_{\max} is reached. The parameter τ then serves as a measure for the duration of this acceleration, the midpoint between which is given by t_a . Note that, at time $t = t_a - 2\tau$, the velocity in Equation (6.18) becomes $v(t = t_a - 2\tau) = v_{\max} e^{-2}/(1 + e^{-2}) \approx 0.1 v_{\max}$. While Equation (6.18) never gives $v = 0$ exactly, in practice, we may define $t_d \equiv t_a - 2\tau$ to be the time at which the pedestrian begins to accelerate forward. If preferable, one may take alternatively $t_d \equiv t_a - 3\tau$, which corresponds to $v(t = t_d) \approx 0.01 v_{\max}$.

A second model, called the two-step crossing model, is used to analyze crossings that have more than one acceleration event and thus do not fit the simple crossing model (Figure 6.4b). The two-step crossing model is discussed in the Appendix.

Each piece of data classified as a simple crossing is fit to Equation (6.19) by minimizing RMSD with respect to the fitting parameters. We probe the effects of gap characteristics by examining how the distributions of parameters change with the variation of certain features of the gap, and discuss the results in Section 6.4. Those data

displaying the two-step pattern are fitted separately to the extended model, and the results are discussed in the Appendix.

Affordance

Affordance stands for the range of possible actions that the environment offers to the acting agent. In the crossing task, the affordance is determined by how long the gap overlaps with the participant's walking trajectory. Assuming the simple crossing model (i.e., Equations (6.18) and 6.19), the affordance of the gap is described by the inequality

$$\begin{aligned} t_f - \tau \log[e^{(-y_0 - w/2)/v_{\max}\tau} - 1] &< t_a \\ &< t_b - \tau \log[e^{(-y_0 + w/2)/v_{\max}\tau} - 1]. \end{aligned} \quad (6.20)$$

Here, $t_f \equiv |x_0 + l_g/2|v_c^{-1}$ corresponds to the time at which the back bumper of the leading vehicle passes the intersection point and $t_b \equiv |x_0 - l_g/2|v_c^{-1}$ corresponds to the time at which the front bumper of the trailing vehicle passes the point, while w denotes the width of the vehicles and equals 1.5 m in our experiment. t_f is hence manifested in Figure 6.4a by the time coordinate of the right side of the box to the left (2.5 s), while t_b is by that of the left side of the box to the right (5.5 s). Equation (6.20) thus describes the condition under which the pedestrian's trajectory passes between the two boxes in Figure 6.4a.

In general typical values of τ are smaller than the time scale of crossing, e.g., compared with $(-y_0 \pm w/2)/v_{\max}$. (Note that $y_0 < 0$ in our coordinate system.) Accordingly, we may take the limit $\tau \rightarrow 0$, and reduce Equation (6.20) to

$$t_f - \frac{1}{v_{\max}} \left(-y_0 - \frac{w}{2} \right) < t_a < t_b - \frac{1}{v_{\max}} \left(-y_0 + \frac{w}{2} \right). \quad (6.21)$$

This provides a simpler inequality involving two fitting parameters.

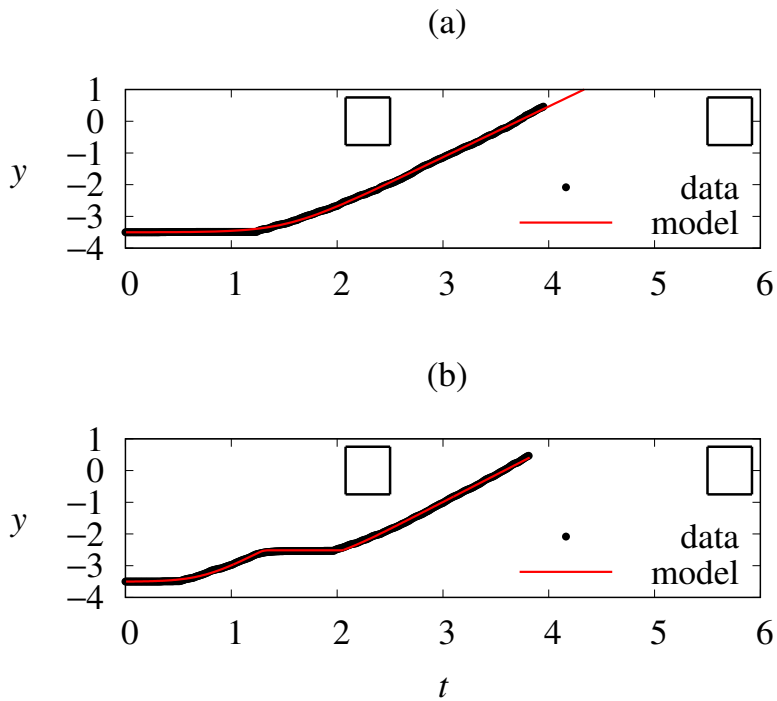


Figure 6.4: Pedestrian position-time plots illustrating typical crossing patterns. Black traces indicate example data; red traces indicate the corresponding model fits. Left and right boxes indicate the temporal and spatial area that the leading and the trailing vehicles occupy, respectively. Intersecting one of the box lines would indicate a collision. In both examples, the conditions are described by $y_0 = -3.5$ m, $t_g = 3.0$ s, and $v_c = 30$ km/h, with the vehicle type set to be a sedan. **(a)** an example of the simple cross with a single acceleration event followed by constant speed walking; **(b)** an example of the two-step cross with two acceleration events.

Bearing Angle

Dynamics of interceptive movement are often described in terms of the bearing angle [206, 207], which refers to the angle between the velocity vector of the human subject and the line of sight between the subject and the object she/he hopes to intercept. In brief, this model asserts that people intercept a moving object by choosing such a trajectory that the bearing angle is kept constant.

Our case of crossing a road may be cast into an interception task: The pedestrian must “intercept” the empty gap between the vehicles [221]. We may hence apply the bearing angle approach to our crossing experiment and model. One difficulty with this approach is that the gap is not a point but a moving area. As an obvious choice, we may simply use the gap center $x_g(t)$, with respect to which the bearing angle is $\theta_g(t) = \arctan [x_g(t)/y(t)]$. However, the pedestrian may not cross the gap center; it is thus more appropriate to examine the bearing angle with respect to the point within the moving gap that the pedestrian actually crosses. With t^* denoting the crossing time, we have $y(t^*) = 0$ and let the position of the gap center at the crossing time be Δx , i.e., $x_g(t^*) = \Delta x$. We then define the crossing point,

$$x_c(t) = x_g(t) - \Delta x = x_0 - \Delta x + v_c t = v_c(t - t^*), \quad (6.22)$$

and consider the angle with respect to x_c :

$$\theta_c(t) = \arctan \left[\frac{x_c(t)}{y(t)} \right]. \quad (6.23)$$

Taking the time derivative of Equation (6.23) results in

$$\dot{\theta}_c = \frac{x_c y}{x_c^2 + y^2} \left(\frac{\dot{x}_c}{x_c} - \frac{\dot{y}}{y} \right). \quad (6.24)$$

Assuming that y follows the simple crossing model (i.e., Equation (6.19)), $|y|$ is small when $t < t_a$. Considering the signs of variables (especially, $x_c < 0$ and $\dot{x}_c > 0$), we thus have that $\dot{\theta}_c < 0$, indicating a decreasing bearing angle. When $t > t_a + 2\tau$, the speed approaches the maximum: $\dot{y} \approx v_{\max}$, so that we have

$$\frac{\dot{x}_c}{x_c} - \frac{\dot{y}}{y} \approx \frac{v_c}{v_c(t - t^*)} - \frac{v_{\max}}{v_{\max}(t - t^*)} = 0, \quad (6.25)$$

which, upon substituting into Equation (6.24), yields $\dot{\theta}_c = 0$ or a constant bearing angle. The model thus predicts that the bearing angle should decrease at the first stage of crossing and remain constant thereafter. The constant value θ_c^* that the bearing angle approaches can be estimated by

$$\begin{aligned} \lim_{\Delta t \rightarrow 0} \theta_c(t^* - \Delta t) &= \lim_{\Delta t \rightarrow 0} \arctan \left(\frac{v_c \Delta t}{v_{\max} \Delta t} \right) \\ &= \arctan \left(\frac{v_c}{v_{\max}} \right). \end{aligned} \quad (6.26)$$

6.4 Fitting results

Data Analysis

Tables 6.3 and 6.4 show the percentage of successful crossings in this group and the proportions of two-step crossings to the total successful crossings. The success rate drops significantly when the gap length is made small at 20.8 m but still stays above 80%. The highest proportion of two-step crossings occurs when the gap is the shortest and the walking distance is the furthest.

Successful Crossings			
l_g (m) \diagdown y_0 (m)	20.8	25	33.3
-3.5	88 %	100 %	100 %
-4.5	100 %	100 %	100 %
-5.5	100 %	94 %	100 %
-6.5	82 %	94 %	100 %

Table 6.3: Proportion of successful crossings to all crossing attempts for several values of y_0 and l_g , when $v_c = 30$ km/h and vehicle type is sedan.

Equation (6.19) was fit to simple crossings with an average RMSD of 0.068 m.

Two-Step Crossings			
l_g (m) \ y_0 (m)	20.8	25	33.3
-3.5	42 %	25 %	6 %
-4.5	31 %	0 %	0 %
-5.5	0 %	26 %	0 %
-6.5	15 %	6 %	0 %

Table 6.4: Proportion of two-step crossings to all successful crossings for several values of y_0 and l_g , when $v_c = 30$ km/h and vehicle type is sedan..

The low RMSD values indicate that the model accurately describes the majority of crossings. Two-step crossings were also found to be accurate, and are discussed in the Appendix. Examples of the model equations fit to simple and two-step crossing time series are given in Figure 6.4a,b, respectively.

Behavioral Response to Gap Features

Restricting the analysis to simple crossings, we consider the variations of the parameters to changing crossing conditions. Experimental parameters y_0 and l_g affect directly the affordance of the gap by changing the temporal window of the gap or the distance the pedestrian needs to traverse to reach the gap. Effects of the experimental parameters on the three fitting parameters v_{\max} , t_a , and τ have been examined; only t_a has turned out to respond significantly. Figure 6.5 shows the distribution of t_a obtained for several values of y_0 and l_g . It is observed that t_a generally increases as y_0 approaches zero. This can be understood intuitively as follows: Recall that y_0 denotes the distance the pedestrian must traverse to reach the gap. The larger the distance, the earlier they must begin walking. However, when the initial position is farther, namely, when y_0

is made larger, this trend disappears and t_a tends to stay at slightly over one second ($t_a \gtrsim 1$ s). This is likely to result from the minimum response time. Namely, the pedestrian may not cross earlier than the earliest timing at which they can reasonably begin to walk. On the other hand, an increase in the gap size appears to lower t_a . This indicates that, when the gap is accessible earlier, the pedestrian tends to cross earlier. The distributions of the other two parameters v_{\max} and τ have also been examined. While the average value of v_{\max} tends generally to increase with y_0 , the trend is not statistically significant. No significant trends have been observed for τ .

Contrary to y_0 and l_g , the vehicle speed v_c and the vehicle type are manipulated without changing the gap affordance. These experimental parameters affect the visual perception of the gap without changing its temporal window of availability. Figure 6.6 displays the effects of the vehicle speed and type on t_a when the gap time t_g is set to be 3 s and y_0 to be -3.5 m. Doubling the vehicle speed results in a significant increase in t_a . Moreover, in several cases, buses resulted in a greater value of t_a than sedans did.

On the other hand, when the same comparison is made for data with $y_0 < -3.5$ m, there arises no significant shift in t_a or t_d upon changing the vehicle type. For $y_0 < -4.5$ m, no significant shift is observed upon changing the vehicle speed as well. This suggests that, when the initial distance is sufficiently far, pedestrian's judgement of the gap is hardly affected by the vehicle type or speed.

Finally, we examine differences among age groups. According to the Mann–Whitney U test, the difference in the distribution of v_{\max} is found to be significant ($p < 0.05$) when either the young adult group or the elderly group is compared with the child group. Both the young adult and elderly groups consistently have higher average values of v_{\max} across all crossing conditions, by about 0.3 m/s. While children have generally slightly lower values of t_a , perhaps a sign of earlier start up times to compensate for their lower speeds, the differences are not found to be statistically significant. The young adult and elderly groups do not show significant differences.

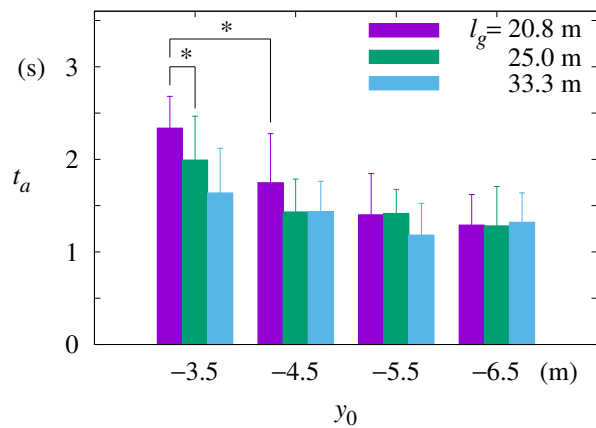


Figure 6.5: Distributions of parameter t_a for varying y_0 and l_g . Here, $v_c = 30$ km/h and vehicle type is sedan. Columns indicate the average values of t_a in the data for given experimental conditions while error bars represent standard deviations. Pairs of samples, marked with asterisks, are presumed to belong to different distributions ($p < 0.05$) according to the Mann-Whitney U test. (Note here that not all such pairs are marked.)

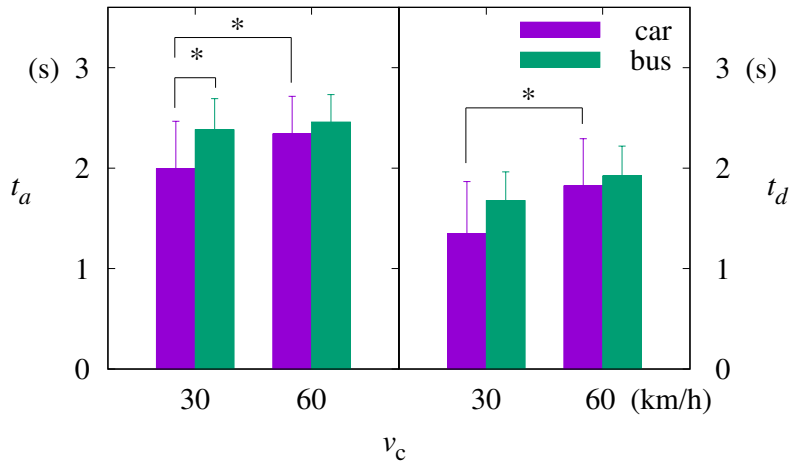


Figure 6.6: Distributions of parameters t_a (left) and t_d (right) for varying vehicle speeds v_c and for two vehicle types. Other parameters are set to $t_g = 3$ s and $y_0 = -3.5$ m. Columns indicate the average values in the data for given experimental conditions while error bars represent standard deviations. Pairs of samples, marked with asterisks, are presumed to belong to different distributions ($p < 0.05$) according to the Mann–Whitney U test.

Parameters Fall within Affordance

Due to the accuracy of the simple crossing model, we expect Equations (6.20) and (6.21) to hold for the fitting parameters derived from the data. Figure 6.7a presents the affordance boundaries in the 3D parameter space. The curved surfaces depict the boundaries specified by Equation (6.20), and each data point plots the parameters corresponding to a single crossing. For comparison, data for two-step crossings (crosses) as well as simple crossings (circles) are displayed. It is observed that the circles, corresponding to simple crossings indeed lie within the volume between the boundaries. In contrast, most of the crosses are located outside, above the higher surface. This indicates that the subject is on route to collide with the leading vehicle and therefore deceleration is necessary.

Plotting Equation (6.21) on the 2D parameter plane (v_{\max}, t_a) corresponds to the projection of the 3D plot in Figure 6.7a onto the plane defined by $\tau = 0$. This results in Figure 6.7b, where two more cases have been included in addition to the case of the gap length $l_g = 25$ m and the initial position $y_0 = -3.5$ m presented in Figure 6.7a. Namely, to probe how the distribution of parameter values shifts with l_g and y_0 , we consider the data for a larger gap $l_g = 33.3$ m and for a farther initial position $y_0 = -6.5$ m. Accordingly, Figure 6.7b presents data for three sets of the gap length and initial position together with the corresponding boundaries (lines instead of surfaces in Figure 6.7a) determined by Equation (6.21). Specifically, the cases of $(l_g = 33.3$ m, $y_0 = -3.5$ m) and $(l_g = 25$ m, $y_0 = -6.5$ m) are plotted in red and in blue, respectively, as well as the case of $(l_g = 25$ m, $y_0 = -3.5$ m) plotted in black. It is observed that, as the gap is widened, the average behavior (designated by red triangles) shifts toward smaller t_a and larger v_{\max} . This reflects the tendency of the pedestrian to cross early before the gap center when possible. On the other hand, in the case that the initial position becomes farther from the intersection point, the pedestrian must compensate by either beginning to walk earlier or walking faster. Data in blue indeed exhibit on average a decrease in t_a and a slight increase in v_{\max} (which is,

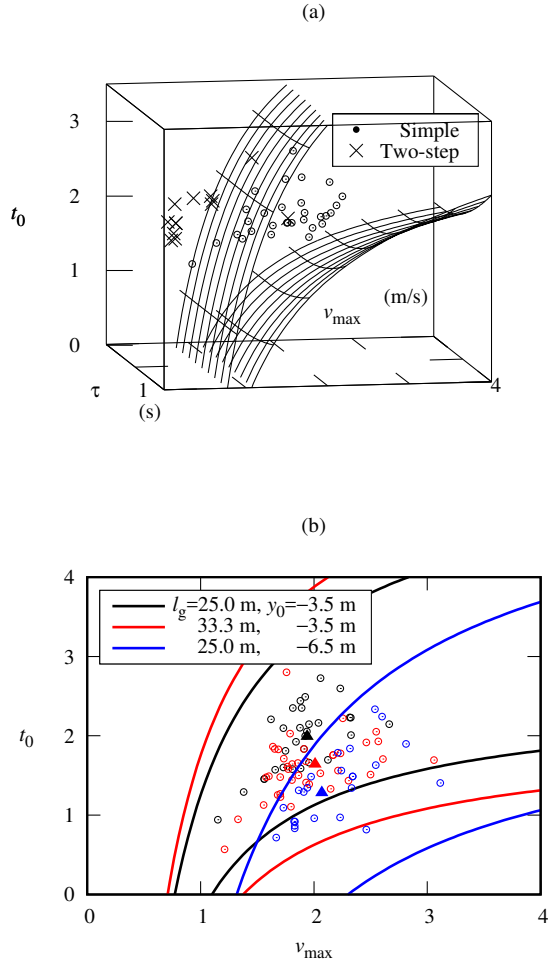


Figure 6.7: Data plotted with boundaries representing the affordance of the gap. **(a)** data plotted with surfaces in the three-dimensional parameter space (τ, v_{\max}, t_a) defined by Equation 6.20. Data points for $l_g = 25$ m and $y_0 = -3.5$ m are plotted for all age groups; dots represent simple crossings and crosses represent two-step crossings; **(b)** data plotted with boundaries on the two-dimensional plane (v_{\max}, t_a) defined by Equation 6.21. To illustrate the effects of a shift in affordance, data and boundaries for $l_g = 25$ m and $y_0 = -3.5$ m (black) are plotted with those for l_g changed to 33.3 m and for y_0 changed to -6.5 m are shown in red and in blue, respectively. Triangles indicate average parameter values.

however, not statistically significant). We remark that Figure 6.7b corresponds directly to Figures 3C and 3D of [213] while Figure 6.7a is a generalization.

Bearing Angle Analysis

Finally, we examine the bearing angle of the data and compare it with the model predictions. Figure 6.8 shows the bearing angle as a function of time for two sets of data (colored lines). The bearing angle tends to decrease in the first few seconds of crossing and to remain constant thereafter, as predicted by Equation (6.26). In addition, the analytical results given by Equation (6.23) are plotted with the average parameter values (black line). Both the theory (analytical result from the model) and the experiment (result computed from data) show that a constant bearing angle is held once the pedestrian starts moving at a nearly constant speed. It is shown in Figure 6.8 that the time interval during which the constant angle is observed is significantly shorter for $y_0 = -3.5$ m (red) than for $y_0 = -6.5$ m (cyan). This reflects the smaller value of t_a in the latter case, when the initial position is farther from the interception point.

We note that the fluctuations of the data in Figure 6.8 are due to measurement error, which is magnified immediately before the pedestrian meets the crossing point. This can be seen in Equation (6.22) by considering that $y(t) \rightarrow 0$ as $t \rightarrow t^*$, causing the error in the argument of the arctan function to become magnified.

6.5 Discussion

In this study, we have proposed a model for pedestrian crossing and utilized it to extract information from experimental data. The model fit the data with high accuracy, allowing for applications of different methods. In particular, the model allows us to visualize the affordance of each gap and see whether the data lies within it. The model also predicts a constant bearing angle, which has been observed in the data.

The fitting parameters of the model, t_a , v_{\max} and τ , provide a physically intuitive

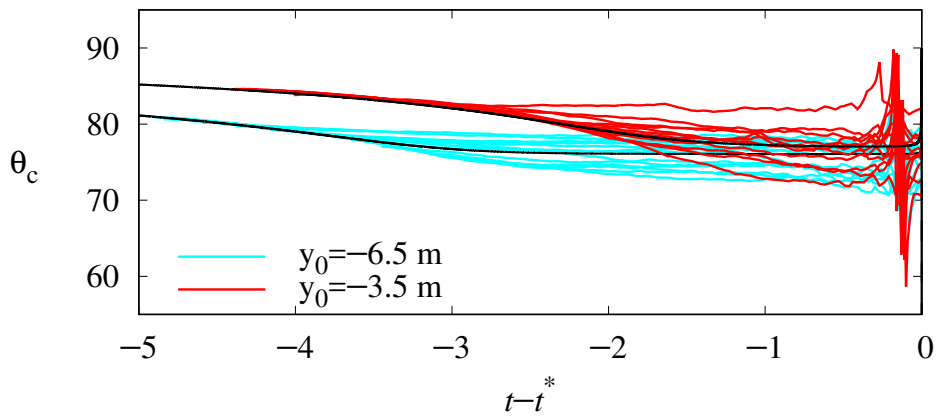


Figure 6.8: Time evolution of the bearing angle θ_c , defined by Equation 6.23. The gap length is $l_g = 25$ m and the initial position is $y_0 = -3.5$ m and -6.5 m for red and cyan lines, respectively. Colored lines are computed from data, while black lines show the analytical results using average parameter values. The time axis is given in terms of time before crossing $t - t^*$, so that the zero point is equal to the intersection time of the run (i.e., the time at which $y(t) = 0$).

interpretation of the data. Analysis has revealed that pedestrians respond to shifting gap affordances primarily by timing their accelerations, rather than changing their walking speeds, as shown by the distributions of t_a . Moreover, shifts in t_a have been observed in response to the speed of the gap and the size of the surrounding vehicles, even if the gap affordance remains the same, indicating that these environmental factors can change the visual perception of the gap. However, this trend disappeared when the initial distance was greater, suggesting that a greater distance from the road tends to offer a more accurate visual perception of the gap. It has also been observed that children's lower walking velocities indirectly shrank the affordances of the gaps and in certain situations failed to compensate.

Due to the simplicity of the equations, this methodology offers a versatile method to analyze pedestrian behavior. While the velocity equation does not necessarily need to follow a logistic function in particular, the high accuracy with which the equation fits the data and its ease of manipulation makes it an ideal tool for such an analysis.

It should be noted that the accuracy of affordance judgments in virtual environments has been questioned in previous studies [226]. In addition, it is not straightforward to measure walking speeds on treadmills, and a different method was proposed [227]. These factors should be considered when interpreting the results, but we expect them to affect neither qualitative results nor the efficacy of the model. Moreover, it would be desirable to include more general walking scenarios where the pedestrian is not constrained to walk in a straight line. This is left for future study.

Analysis of two-step crossings

In order to model two-step crossings in which there are two acceleration events (Figure 6.4b), we extend the model in the following way: We first take the acceleration equation

$$\ddot{y} = \frac{\dot{y}}{\tau} \left(1 - \frac{\dot{y}}{v_{\max}} \right), \quad (\text{A1})$$

which is equivalent to Equations 1 and 2 with appropriate initial conditions. In the two-step crossing, after acceleration (i.e., at time $t > t_a + 2\tau$), the pedestrian will decelerate at a point y_s and stop until she/he accelerates again at time t_s . This behavior may be described by adding two terms in Equation A1, which leads to

$$\ddot{y} = \frac{\dot{y}}{\tau} \left(1 - \frac{\dot{y}}{v_{\max}} \right) - r_s \dot{y} \exp \left[-\frac{(y - y_s)^2}{\sigma_s^2} \right] \theta(t_s - t) + v_s \delta(t - t_s), \quad (\text{A2})$$

where the second and the third terms of the right-hand side represent repulsion and impulse force, respectively. The repulsion is centered at position y_s with range σ_s ; y_s may be interpreted as the point beyond which the pedestrian perceives to be unsafe, due to the incoming traffic. Accordingly, y_s is the position of the flat region of the curve in Figure 6.4b, i.e., $y_s = -2.3$ m in this example. The Heaviside step function $\theta(t_s - t)$ effectively "turns off" the repulsion force at time t_s , thus removing the potential for collision after the vehicle has passed. The parameter r_s adjusts the overall strength of the repulsion. The impulse term is necessary for the model to undergo sharp acceleration from rest, so that the pedestrian starts to walk again at time t_s . In the example of Figure 6.4b, the time at which the subject begins the second acceleration is given by $t_s = 2.0$ s. The magnitude v_s of the impulse is a fraction of v_{\max} , and determines how quickly the model regains the maximum velocity.

We fit Equation A2 to the data for the case $y_0 = -3.5$ m and $l_g = 25$ m, yielding $y_s = -2.29 \pm 0.22$ m. This implies that participants who performed two-step crossings walked forward about 1.2 m before stopping, which amounts to about 1.5 m from the path of the vehicles. We also have the impulse magnitude $v_s/v_{\max} = 0.67 \pm 0.22$ and time $t_s = 2.41 \pm 0.26$ s, which corresponds to the time for the pedestrian to start walking again. This range includes the time (about 2.5 s) at which the leading vehicle passes the interception point. Other parameters, repulsion strength r_s and range σ_s , which suffer from large fluctuations due to the very limited sample number, are obtained as $r_s = 520 \pm 480 \text{ s}^{-1}$ and $\sigma_s = 0.26 \pm 0.24$ m. However, the sample size of

two-step crossings was insufficient to derive statistically meaningful results. A possible behavioral interpretation of this type of crossing is as exchanging the additional energy required for deceleration and acceleration in favor of more safety or security.

Bibliography

- [1] K. Han, S. H. Kim and M.Y. Choi. *Theor. Biol. Med. Model*, **17**, 2 (2020).
- [2] S. H. Kim, S. Goh, K. Han, J. W. Kim and M.Y. Choi. *Theor. Biol. Med. Model*. **15**, 5 (2018).
- [3] S. H. Kim, J. W. Kim, J. J. Park, M. J. Shin and M. Y. Choi. *JMIR MHealth UHealth* **7**, e12335 (2019).
- [4] S. H. Kim, J. W. Kim, H. C. Chung, G. Choi and M. Y. Choi. *Appl. Sci.* **10**, 859 (2020).
- [5] A.V.S. De Reuck and M. P. Cameron, eds. *Ciba Foundation Symposium on Lysosomes* (London: J.A. Churchill Ltd; 1963).
- [6] N. Mizushima and M. Komatsu. *Cell* **147**, 728 (2011).
- [7] D. J. Klionsky and S. D. Emr. *Science*, **290** 1717 (2000).
- [8] B. Levine and G. Kroemer. *Cell* **176** 11 (2019).
- [9] J. L. Jewell, R. C. Russell and K.-L. Guan. *Nat. Rev. Mol. Cell Biol.* **14** 133 (2013).
- [10] J. Liang, S. H. Shao, Z.-X. Xu, B. Hennessy, Z. Ding, M. Larrea, et al. *Nat. Cell Biol.* **9**, 218 (2007).
- [11] D. G. Hardie. *Genes Dev.* **25**, 1895 (2011).

- [12] K. Han, J. Kim and M.Y. Choi. *Heliyon* **1**, e00027 (2015).
- [13] F. M. Menzies, A. Fleming, A. Caricasole, C. F. Bento, S. P. Andrews, A. Ashkenazi, et al. *Neuron* **93**, 1015 (2017).
- [14] R. A. Nixon RA. *Nat. Med.* **19**, 983 (2013).
- [15] C. G. Towers and A. Thorburn A. *EBioMedicine* **14**, 15 (2016).
- [16] B. Boland, A. Kumar, S. Lee, F. M. Platt, J. Wegiel, W. H. Yu and R. A. Nixon. *J. Neurosci.* **28**, 6926 (2008).
- [17] S. Lee, Y. Sato and R. A. Nixon. *J. Neurosci.* **31**, 7817 (2011).
- [18] M. Komatsu, S. Waguri, T. Chiba, S. Murata, J.-I. Iwata, I. Tanida, et al. *Nature* **441**, 880 (2006).
- [19] T. Hara, K. Nakamura, M. Matsui, A. Yamamoto, Y. Nakahara, R. Suzuki-Migishima, et al. *Nature* **441**, 885 (2006).
- [20] H. Nam, L. E. Kim, Y. Jeon, H. Min, S. Ha, Y. Lee, et al. *Autophagy* **15**, 753 (2019).
- [21] M. P. Mattson, B. Cheng, D. Davis, K. Bryant, I. Lieberburg and R. E. Rydel. *J. Neurosci.* **12**, 376 (1992).
- [22] J. Hardy and D. J. Selkoe. *Science* **297**, 353 (2002).
- [23] D. J. Selkoe and J. Hardy. *EMBO Mol. Med.* **8**, 595 (2016).
- [24] M. Novo, S. Freire and W. Al-Soufi. *Sci. Rep.*, **8**, 1783 (2018).
- [25] S. Goh, H. W. Kwon, M.Y. Choi and J.-Y. Fortin. *Phys. Rev. E* **82**, 061115 (2010).
- [26] J. A. Mohawk, C. B. Green and J. S. Takahashi. *Annu. Rev. Neurosci.* **35**, 445 (2012).

- [27] M. Okawa and M. Uchiyama. *Sleep Med. Rev.* **11**, 485 (2007).
- [28] A. Germain and D. J. Kupfer. *Hum. Psychopharmacol.* **23**, 571 (2008).
- [29] G. Murray and A. Harvey. *Bipolar Disord.* **12**, 459 (2010).
- [30] Y.-H. Wu and D. F. Swaab. *Sleep Med.* **8**, 623 (2007).
- [31] M. Nocon, T. Hiemann, F. Muller-Riemenschneider, F. Thalau, S. Roll, S. Willich. *Eur. J. Cardiovasc. Prev. Rehabil.* **15**, 239 (2008).
- [32] C. Wen, J. Wai, M. Tsai, Y. C. Yang, T. Y. Cheng, M. Lee, et al. *The Lancet* **378**, 1244 (2011).
- [33] S. G. Trost, S. N. Blair and K. M. Khan. *Br. J. Sports Med.* **48**, 169 (2014).
- [34] R. Maddison, L. Gemming, J. Monedero, L. Bolger, S. Belton, J. Issartel, et al. *JMIR Mhealth Uhealth* **5**, e122 (2017).
- [35] H. J. Montoye, R. Washburn, S. Servais, A. Ertl, J. G. Webster, F. J. Nagle. *Med. Sci. Sports Exerc.* **15**, 403 (1983).
- [36] G. A. Meijer, K. R. Westerterp, H. Koper and F. ten Hoor. *Med. Sci. Sports Exerc.* **21**, 343 (1989).
- [37] K. Y. Chen and M. Sun. *J. Appl. Physiol.* **83**, 2112 (1997).
- [38] K. Han, S. H. Kim and M.Y. Choi. *In Submission* (2020).
- [39] OECD. *Road Infrastructure, Inclusive Development and Traffic Safety in Korea* (OECD Publishing, Paris, 2016).
- [40] M. M. Hamed. *Safety Sci.* **38** 63 (2001).
- [41] A. F. Te Velde, J. Van Der Kamp and G.J.P. Savelsbergh. Five- to twelve-year-olds' control of movement velocity in a dynamic collision avoidance task *Br. J. Dev. Psychol.* **26**, 33 (2008).

- [42] M. Azam, G.-J. Choi and Chung H. C. *Psychology* **8**, 1042 (2017).
- [43] A. Raju, B. B. Machta and J. P. Sethna. *Phys. Rev. E* **98**, 052112 (2018).
- [44] O. Conway, H. A. Akpınar, V. V. Rogov and V. Kirkin. *J. Mol. Biol.* **432**, 2483 (2020).
- [45] G. Zaffagnini and S. Martens. *J. Mol. Biol.* **428**, 1714 (2016).
- [46] F. Reggiori, M. Komatsu, K. Finley and A. Simonsen. *Int. J. Cell. Biol.* **2012**, 18 (2012).
- [47] C. Kraft, M. Peter and K. Hofmann. *Nat. Cell Biol.* **12**, 836 (2010).
- [48] T. Johansen and T. Lamark. *Autophagy* **7**, 279 (2011).
- [49] M. Fotuhi, V. Hachinski and P. J. Whitehouse. *Nat. Rev. Neurol.* **5**, 649 (2009).
- [50] *2018 Alzheimer's disease facts and figures. Alzheimer's & Dementia* **14**, 367 (2018).
- [51] F. J. Wippold, N. Cairns, K. Vo, D. M. Holtzman and J. C. Morris. *Am. J. Neuro-radiol.* **29**, 18 (2008).
- [52] J. Hardy, K. Duff, K. G. Hardy, J. Perez-Tur, M. Hutton. *Nat. Neurosci.* **1**, 355 (1998).
- [53] R. Kaye and C. A. Lasagna-Reeves. *J. Alzheimers Dis.* **33**, S67 (2013).
- [54] S. Oddo. *Front. Biosci.* **4**, 941 (2012).
- [55] P. Nilsson, K. Loganathan, M. Sekiguchi, Y. Matsuba, K. Hui, S. Tsubuki, et al. *Cell Rep.* **5**, 61 (2013).
- [56] P. Nilsson, M. Sekiguchi, T. Akagi, S. Izumi, T. Komori, K. Hui, et al. *Am. J. Pathol.* **185**, 305 (2015).

- [57] P. Nilsson and T. C. Saido. *BioEssays* **36**, 570 (2014).
- [58] E. Gibbs, J. M. Silverman, B. Zhao, X. Peng, J. Wang, C. L. Wellington, et al. *Sci. Rep.* **9**, 9870 (2019).
- [59] K. Bhaskar, M. Miller, A. Chludzinski, K. Herrup, M. Zagorski, B. T. Lamb. *Mol. Neurodegener.* **4**, 14 (2009).
- [60] C. Wang, J.-T. Yu, D. Miao, Z.-C. Wu, M.-S. Tan and L. Tan. *Mol. Neurobiol.* **49**, 120 (2014).
- [61] A. Caccamo, S. Majumder, A. Richardson, R. Strong and S. Oddo. *J. Biol. Chem.* **285**, 13107 (2010).
- [62] C. M. Yuede, H. Lee, J. L. Restivo, T. A. Davis, J. C. Hettinger, C. E. Wallace, et al. *J. Exp. Med.* **213**, 677 (2016).
- [63] K. G. Mawuenyega, W. Sigurdson, V. Ovod, L. Munsell, T. Kasten, J. C. Morris, et al. *Science* **330**, 1774 (2010).
- [64] U. Pfeifer. *J. Cell Biol.* **78**, 152 (1978).
- [65] C. M. Schworer, K. A. Shiffer and G. E. Mortimore. *J. Biol. Chem.* **256**, 7652 (1981).
- [66] J. Kovács, E. Fellingner, A. P. Kárpáti, A. L. Kovács, L. László and G. Réz. *Virchows Archiv. B* **53**, 183 (1987).
- [67] P. J. Plomp, P. B. Gordon, A. J. Meijer, H. Høyvik and P. O. Seglen. *J. Biol. Chem.* **264**, 6699 (1989).
- [68] P. J. Plomp, E. J. Wolvetang, A. K. Groen, A. J. Meijer, P. B. Gordon and P. O. Seglen. *Eur. J. Biochem.* **164**, 197 (1987).
- [69] P. O. Seglen and P. B. Gordon. *J. Cell Biol.* **99**, 435 (1984).

- [70] J.-Y. Lee and T.-P. Yao. *Autophagy* **6**, 555 (2010).
- [71] C. Behrends and S. Fulda. *Int. J. Cell Biol.* **2012**, 673290 (2012).
- [72] A. Kuma A and N. Mizushima. *Semin. Cell Dev. Biol.* **21**, 683 (2010).
- [73] G. E. Mortimore, A. R. Pösö. *Annu. Rev. Nutr.* **7**, 539 (1987).
- [74] T. Yoshimori. *Biochem. Biophys. Res. Commun.* **313**, 453 (2004).
- [75] N. Mizushima, A. Yamamoto, M. Matsui, T. Yoshimori and Y. Ohsumi. *Mol. Biol. Cell* **15**, 1101 (2004).
- [76] K. Han, H. W. Kwon, H. Kang, J. Kim, M.-S. Lee and M.Y. Choi. *Physica A* **391**, 686 (2012).
- [77] K. Han, J. Kim and M.Y. Choi. *J. Bio. Syst.* **22**, 659 (2014).
- [78] K. Han, J. Kim and M. Y. Choi. *Theor. Biol. Med. Model.* **11**, 31 (2014).
- [79] R. J. Bateman, L. Y. Munsell, J. C. Morris, R. Swarm R, K. E. Yarasheski and D. M. Holtzman. *Nat. Med.* **12**, 856 (2006).
- [80] P. O. Seglen and A. E. Solheim. *Biochim. Biophys. Acta.* **520**, 630 (1978).
- [81] P. O. Seglen and P. Bohley. *Experientia* **48**, 158 (1992).
- [82] D. J. Klionsky, A. M. Cuervo, J. W. A. Dunn, B. Levine, I. J. van der Klei and P. O. Seglen. *Autophagy* **3**, 413 (2007).
- [83] I. Tavassoly, J. Parmar, A. N. Shajahan-Haq, R. Clarke, W. T. Baumann and J. J. Tyson. *CPT Pharmacometrics Syst. Pharmacol.* **4**, 263 (2015).
- [84] I. Tavassoly. *Dynamics of Cell Fate Decision Mediated by the Interplay of Autophagy and Apoptosis in Cancer Cells: Mathematical Modeling and Experimental Observations* (Cham: Springer International Publishing, Switzerland, 2015).

- [85] O. Kapuy, P. K. Vinod, J. Mandl and G. Bánhegyi. *Mol. Biosyst.* **9**, 296 (2013).
- [86] H. Jin and J. Lei. *J. Theor. Biol.* **402**, 45 (2016).
- [87] B. Liu, Z. N. Oltvai, H. Bayır, G. A. Silverman, S. C. Pak, D. H. Perlmutter and I. Bahar. *Sci. Rep.* **7**, 17605 (2017).
- [88] D. Ma, S. Panda and J. D. Lin. *EMBO J.* **30**, 4642 (2011).
- [89] U. Pfeifer and H. Scheller. *J. Cell Biol.* **64**, 608 (1975).
- [90] U. Pfeifer and P. Strauss. *J. Mol. Cell Cardiol.* **13**, 37 (1981).
- [91] C. E. Remé and M. Sulser. *Graefes Arch. Klin. Exp. Ophthalmol.* **203**, 261 (1977).
- [92] U. Pfeifer. *Virchows Archiv. B* **12**, 195 (1972).
- [93] U. M. Sachdeva and C. B. Thompson. *Autophagy* **4**, 581 (2008).
- [94] U. Pfeifer U. *Virchows Archiv. B* **10** 1 (1972).
- [95] U. Pfeifer and J. Bertling. *Virchows Archiv. B* **24**, 109 (1977).
- [96] F. Nazio, M. Carinci, C. Valacca, P. Bielli, F. Strappazon, M. Antonioli, et al. *J. Cell Biol.* **215**, 841 (2016).
- [97] M. Ryzhikov, A. Ehlers, D. Steinberg, W. Xie, E. Oberlander, S. Brown, et al. *Cell Rep.* **26**, 1880 (2019).
- [98] M. Dorvash, M. Farahmandnia and I. Tavassoly. *Interdiscip. Sci.* **2019**, 1 (2019).
- [99] A. Yamamoto and A. Yue. *Annu. Rev. Neurosci.* **37**, 55 (2014).
- [100] S. E. Hickman, E. K. Allison, and J. El Khoury. *J. Neurosci.* **28**, 8354 (2008).
- [101] G. G. Glenner and W. W. Caine. *Biochem. Biophys. Res. Commun.* **120**, 885 (1984).

- [102] F. Chiti and C. M. Dobson. *Annu. Rev. of Biochem.* **75**, 333 (2006).
- [103] D. Scheuner, C. Eckman, M. Jensen, X. Song, M. Citron, N. Suzuki *et al.* *Nat. Med.* **2** 864 (1996).
- [104] B. De Strooper, P. Saftig, K. Craessaerts, H. Vanderstichele, G. Guhde, W. Annaert *et al.* *Nature*, **391**, 387 (1998).
- [105] M. S. Wolfe, W. Xia, B. L. Ostaszewski, T. S. Diehl, W. T. Kimberly and D. J. Selkoe. *Nature* **398**, 513 (1999).
- [106] E. H. Corder, A. M. Saunders, W. J. Strittmatter, D. E. Schmechel, P. C. Gaskell, G. Small *et al.* *Science*, **261**, 921 (1993).
- [107] G. W. Rebeck, J. S. Reiter, D. K. Strickland and B. T. Hyman. *Neuron*, **11**, 575 (1993).
- [108] D. M. Holtzman, K. R. Bales, T. Tenkova, A. M. Fagan, M. Parsadanian, L. J. Sartorius, *et al.* *Proc. Nat. Acad. Sci.* **97**, 2892 (2000).
- [109] J. M. Castellano, J. Kim, F. R. Stewart, H. Jiang, R. B. DeMattos, B. W. Patterson, *et al.* *Sci. Transl. Med.* **3**, 89ra57 (2011).
- [110] P. Hollingworth, D. Harold, R. Sims, A. Gerrish, J. C. Lambert, M. M. Carrasquillo, *et al.* *Nat. Genet.* **43**, 429 (2011).
- [111] W. S. Kim, H. Li, K. Ruberu, S. Chan, D. A. Elliott, J. K. Low, *et al.* *J. Neurosci.* **33**, 4387 (2013).
- [112] C. G. Glabe. *J. Biol. Chem.* **283**, 29639 (2008).
- [113] G. Bitan, M. D. Kirkitadze, A. Lomakin, S. S. Vollers, G. B. Benedek, and D. B. Teplow. *Proc. Nat. Acad. Sci.* **100**, 330 (2003).
- [114] S. Baglioni, F. Casamenti, M. Bucciantini, L. M. Luheshi, N. Taddei, F. Chiti, *et al.* *J. Neurosci.* **26**, 8160 (2006).

- [115] P. N. Lacor, M. C. Buniel, P. W. Furlow, A. S. Clemente, P. T. Velasco, M. Wood, *et al.* **27**, 796 (2007).
- [116] E. K. Pickett, R. M. Koffie, S. Wegmann, C. M. Henstridge, A. G. Herrmann, M. Colom-Cadena, *et al.* *J. Alzheimers Dis.* **53**, 787 (2016).
- [117] G. M. Shankar, S. Li, T. H. Mehta, A. Garcia-Munoz, N. E. Shepardson, I. Smith, *et al.* *Nat. Med.* **14**, 837 (2008).
- [118] R. M. Koffie, M. Meyer-Luehmann, T. Hashimoto, K. W. Adams, M. L. Mielke, M. Garcia-Alloza, *et al.* *Proc. Nat. Acad. Sci.* **106**, 4012 (2009).
- [119] A. Serrano-Pozo, M. L. Mielke, A. Muzitansky, T. Gómez-Isla, J. H. Growdon, B. J. Bacskai, *et al.* *J. Neuropathol. Exp. Neurol.* **71**, 694 (2012).
- [120] A. Serrano-Pozo, R. A. Betensky, M. P. Frosch and B. T. Hyman. *Am. J. Pathol.* **186**, 375 (2016).
- [121] M. Querol-Vilaseca, M. Colom-Cadena, J. Pegueroles, R. Nuñez-Llaves, J. Luque-Cabecerans, L. Muñoz-Llahuna and J. Clarimon. *Sci. Rep.* **9**, 1 (2019).
- [122] J. Jo, M. Y. Choi and D. S. Koh. *Biophys. J.* **93**, 2655 (2007).
- [123] B. T. Hyman, H. L. West, G. W. Rebeck, S. V. Buldyrev, R. N. Mantegna, M. Ukleja, *et al.* *Proc. Nat. Acad. Sci.* **92**, 3586 (1995).
- [124] S. Kumar-Singh, D. Pirici, E. McGowan, S. Serneels, C. Ceuterick and J. Hardy, *et al.* **167**, 527 (2005).
- [125] D. S. Eisenberg and M. R. Sawaya. *Annu. Rev. of Biochem.* **86**, 69 (2017).
- [126] A. Lomakin, D. S. Chung, G. B. Benedek, D. A. Kirschner and D. B. Teplow. *Proc. Nat. Acad. Sci.* **93**, 1125 (1997).
- [127] W. Zheng, M.-Y. Tsai, M. Chen, and P. G. Wolynes. *Proc. Nat. Acad. Sci.* **113**, 11835 (2016).

- [128] W. Zheng, M. Y. Tsai and P. G. Wolynes. *J. Am. Chem. Soc.* **139**, 16666 (2017).
- [129] F. Panza, M. Lozupone, G. Logroscino, and B. P. Imbimbo. *Nat. Rev. Neurol.* **15**, 73 (2019).
- [130] D. Bell-Pedersen, V. M. Cassone, D. J. Earnest, S. S. Golden, P. E. Hardin, T. L. Thomas and M. J. Zoran. *Nat. Rev. Genet.* **6**, 544 (2005).
- [131] C. B. Saper, G. Cano and T. E. Scammell. *J. Comp. Neurol.* **493**, 92 (2005).
- [132] B. Rusak, H. A. Robertson, W. Wisden and S. P. Hunt. *Science* **248**, 1237 (1990).
- [133] M. S. Freedman, R. J. Lucas, B. Soni, M. von Schantz, M. Munoz, Z. David-Gray, R. Foster. *Science* **284**, 502 (1999).
- [134] J. F. Duffy and K. P. Wright Jr. *J. Biol Rhythms* **20**, 326 (2005).
- [135] D.-J. Dijk and M. von Schantz. *J. Biol. Rhythms* **20**, 279 (2005).
- [136] M. G. Lee, O. K. Hassani and B. E. Jones. *J. Neurosci.* **25**, 6716 (2005).
- [137] T. Porkka-Heiskanen, R. E. Strecker, M. Thakkar, A. A. Bjorkum, R. W. Greene, R. W. McCarley. *Science.* **276**, 1265 (1997).
- [138] C. B. Saper, T. C. Chou and T. E. Scammell. *Trends Neurosci.* **24**, 726 (2001).
- [139] C. B. Saper, T. E. Scammell and J. Lu. *Nature* **437**, 1257 (2005).
- [140] A. Borbély. *Hum. Neurobiol.* **1**, 195 (1982).
- [141] M. J. Rempe, J. Best and D. Terman. *J. Math. Biol.* **60**, 615 (2010).
- [142] V. Booth, C. G. D. Behn. *Math. Biosci.* **54** 68 (2014).
- [143] A. J. K. Phillips and P. A. Robinson. *J. Biol. Rhythms.* **22**, 167 (2007).
- [144] A. J. K. Phillips and P. A. Robinson. *Phys. Rev. E.* **79**, 021913 (2009).

- [145] B. D. Fulcher, A. J. K. Phillips and P. A. Robinson. *Phys. Rev. E.* **78**, 051920 (2008).
- [146] D.-P. Yang, L. McKenzie-Sell, A. Karanjai and P. A. Robinson. *Phys. Rev. E.* **94**, 022412 (2016).
- [147] B. D. Fulcher, A. J. K. Phillips and P. A. Robinson. *J. Theor. Biol.* **264**, 407 (2010).
- [148] M. Puckeridge, B. D. Fulcher, A. J. K. Phillips and P. A. Robinson. *J. Theor. Biol.* **273**, 44 (2011).
- [149] B. D. Fulcher, A. J. K. Phillips, S. Postnova and P. A. Robinson. *PLoS ONE* **9**, e91982 (2014).
- [150] S. Postnova, P. A. Robinson and D. D. Postnov. *PLoS ONE.* **8**, e53379 (2013).
- [151] D. L. Rowe, P. A. Robinson and C. J. Rennie. *J. Theor. Biol.* **231**, 413 (2004).
- [152] P. A. Robinson, C. J. Rennie, D. L. Rowe and S. C. O’Conner. *Hum. Brain Mapp.* **23**, 53 (2004).
- [153] St. M. A. Hilaire, E. B. Klerman, S. B. Khalsa, K. P. Wright Jr., C. A. Czeisler and R. E. Kronauer. *J. Theor. Biol.* **247**, 583 (2007).
- [154] C. A. Czeisler, J. F. Duffy, T. L. Shanahan, E. N. Brown, J. F. Mitchell, D. W. Rimmer, et al. *Science.* **25**, 2177 (1999).
- [155] P. J. Schwartz, D. L. Murphy, T. A. Wehr, D. Garcia-Borreguero, D. A. Oren, D. E. Moul, et al. *Arch. Gen. Psychiatry.* **54**, 375 (1997).
- [156] A. J. K. Phillips, B. D. Fulcher, P. A. Robinson and E. B. Klerman. *PLoS Comput. Biol.* **9**, e1003213 (2013).
- [157] R. L. Sack, A. J. Lewy, M. L. Blood, L. D. Keith and H. Nakagawa. *J. Clin. Endocrinol. Metab.* **75**, 127 (1992).

- [158] S. W. Lockley, K. J. Skene, J. Arendt, H. Tabandeh, A. C. Bird and R. DeFrance. *J. Clin. Endocrinol. Metab.* **82**, 3763 (1997).
- [159] J. K. Wyatt. *Sleep*. **27** 1195 (2004).
- [160] N. E. Rosenthal, D. A. Sack and J. C. Gillin. *Arch. Gen. Psychiatry*. **41**, 72 (1984).
- [161] C. I. Eastman, M. A. Young and L. F. Fogg. *Arch. Gen. Psychiatry*. **55**, 883 (1998).
- [162] D. F. Kripke. *J. Affect. Disord.* **49**, 109 (1998).
- [163] F. Benedetti, C. Colombo, B. Barbini, E. Campori and E. Smeraldi. *J. Affect. Disord.* **62**, 221 (2001).
- [164] A. Joshi and K. Wong-Lin. *Orexin and sleep: functional and clinical aspects*. p. 299–322. T. Sakurai, S. R. Pandi-Perumal and J. M. Monti, editors (Cham: Springer International Publishing, Switzerland 2015).
- [165] D. H. Avery, A. Khan, S. R. Dager, G. B. Cox and D. L. Dunner. *Acta. Psychiatr. Scand.* **82**, 335 (1990).
- [166] R. Passmore and J.V.G.A. Durnin. *Physiol. Rev.* **35**, 801 (1955).
- [167] J. E. Cotes and F. Meade. *Ergonomics* **3**, 97 (1960).
- [168] D. B. Dill. *J. Appl. Physiol.* **20**, 19 (1965).
- [169] D. R. Menier and L.G.C.E. Pugh. *J. Physiol.* **197**, 717 (1968).
- [170] W. H. van der Walt and C. H. Wyndham. *J. Appl. Physiol.* **34**, 559 (1973).
- [171] K. G. Holt, J. Hamill and R. O. Andres. *Med. Sci. Sports Exerc.* **23**, 491 (1990).
- [172] R. Margaria, P. Cerretelli, P. Aghemo and G. Sassi. *J. Appl. Physiol.* **18**, 367 (1963).

- [173] M. Y. Zarrugh and C. W. Radcliffe. *Eur. J. Appl. Physiol.* **38**, 215 (1978).
- [174] P. R. Cavanagh and K. R. Williams. *Med. Sci. Sports Exerc.* **14**, 30 (1982).
- [175] K. Steudel. *Am. J. Phys. Anthropol.* **99**, 345 (1996).
- [176] A. E. Minetti and R. M. Alexander. *J. Theor. Biol.* **186**, 467 (1997).
- [177] R. M. Alexander. *Phil. Trans. R Soc. Lond. B* **338**, 189 (1992).
- [178] J. Doke, J. M. Donelan and A. D. Kuo. *J. Exp. Biol.* **208**, 439 (2005).
- [179] A. D. Kuo. *J. Biomech. Eng.* **124**, 113 (2002).
- [180] A. D. Kuo, J. M. Donelan and A. Ruina. *Exerc. Sport Sci. Rev.* **33**, 88 (2005).
- [181] A. Ruina, J.E.A. Bertram and M. Srinivasan. *J. Theor. Biol.* **237**, 170 (2005).
- [182] Y. Osaki, M. Kunin, B. Cohen and T. Raphan. Three-dimensional kinematics and dynamics of the foot during walking: a model of central control mechanisms. *Exp. Brain Res.* **176**, 476 (2007).
- [183] S. F. Donker, T. Mulder, B. Nienhuis and J. Duysens. *Exp. Brain Res.* **146**, 26 (2002).
- [184] E. P. Zehr and C. Haridas. *Exp. Brain Res.* **149**, 260 (2003).
- [185] E. Hirasaki, S. T. Moore, T. Raphan and B. Cohen. *Exp. Brain Res.* **127**, 117 (1998).
- [186] J. M. Hausdorff, G. Yogev, S. Springer, E. S. Simon and N. Giladi. *Exp. Brain Res.* **164**, 541 (2005).
- [187] O. Blin, A. M. Ferrandez and G. Serratrice. *Exp. Brain Res.* **98**, 91 (1990).
- [188] S. H. Collins, M. Wisse and A. Ruina. *Int. J. Robotics Res.* **20**, 607 (2001).

- [189] J. A. Noah, D. K. Spierer, J. Gu and S. Bronner. *J. Med. Eng. Tech.* **37**, 456 (2013).
- [190] J. V. Brugniaux, A. Niva, I. Pulkkinen, R.M.T. Laukkanen, J.-P. Richalet and A. P. Pichon. *Br. J. Sports Med.* **44**, 245 (2010).
- [191] S. Härtel, J.-P. Gnam, S. Löffler and K. Bös. *Eur. Rev. Aging Phys. Act.* **8**, 109 (2011).
- [192] J. Takacs, C. L. Pollock, J. R. Guenther, M. Bahar, C. Napier and M. A. Hunt. *J. Sci. Med. Sport* **17**, 496 (2014).
- [193] K. M. Diaz, D. J. Krupka, M. J. Chang, J. Peacock, Y. Ma, J. Goldsmith, J. E. Schwartz and K. W. Davidson. *Int. J. Cariol.* **185**, 138 (2015).
- [194] W. J. Tucker, D. M. Bhammar, B. J. Sawyer, M. P. Buman and G. A. Gaesser. *BMC Sports Sci. Med. Rehabil.* **7**, 14 (2015).
- [195] A. Shcherbina, C. M. Mattsson, D. Waggott, H. Salisbury, J. W. Christle, T. Hastie, et al. *Pers. Med.* **7**, 3 (2017).
- [196] P. N. Ainslie, T. Reilly and K. R. Westerterp. *Sports Med.* **33**, 683 (2003).
- [197] J. Levine. *Public Health Nutr.* **8**, 1123 (2005).
- [198] H. A. Haugen, L.-N. Chan and F. Li. *Nutr. Clin. Pract.* **22**, 377 (2007).
- [199] M. D. Mifflin, St. S. T. Jeor, L. A. Hill, B. J. Scott, S. A. Daugherty and Y. O. Koh. *Am. J. Clin. Nutr.* **51** 241 (1990).
- [200] S. Plagenhoef, F. G. Evans and T. Abdelnour. *Res. Q. Exerc. Sport* **54**, 169 (1983).
- [201] A. E. Minetti, C. Moia, G. S. Roi, D. Susta and G. Ferretti. *J. Appl. Physiol.* **93**, 1039 (2002).

- [202] A. E. Minetti, L. P. Ardigo and F. Saibene. *J. Physiol.* **472**, 725 (1993).
- [203] H. C. Chung, S. H. Kim, G. Choi, J. W. Kim and M.Y. Choi. *J. Vis. Exp.* **160**, e61116 (2020).
- [204] B. R. Fajen and W. H. Warren. *Brett. J. Exp. Psychol. Human* **29**, 343 (2003).
- [205] S. Chapman. *Am. J. Phys.* **36**, 868 (1968).
- [206] J. Bastin, C. Craig and G. Montagne. *Hum. Mov. Sci.* **25**, 718 (2006).
- [207] B. R. Fajen B. R. and W. H. Warren. *Exp. Brain Res.* **180**, 303 (2007).
- [208] W. H. Warren, B. A. Kay, W. D. Zosh, A. P. Duchon and S. Sahuc. *Nat. Neurosci.* **4**, 213 (2001).
- [209] B. R. Fajen and W. H. Warren. *Perception* **33**, 689 (2004).
- [210] J. J. Gibson. *The ecological approach to visual perception*. (Houghton Mifflin Harcourt, Boston, USA, 1979).
- [211] J. M. Plumert, J. K. Kearney and J. F. Cremer. *Child Dev.* **75**, 1243 (2004).
- [212] B. R. Fajen and J. S. Matthis. *J. Exp. Psychol. Hum. Percept. Perform.* **37**, 1442 (2011).
- [213] B. R. Fajen. *Front. Behav. Neurosci.* **7**, 1–15 (2013).
- [214] A. E. Patla. *Gait Posture*, **5**, 54 (1997).
- [215] G. Yannis, E. Papadimitriou, and A. Theofilatos. *Transport. Plan. Techn.* **36**, 450 (2013).
- [216] G. K. Zipf. *Human Behavior and the Principle of Least Effort*. (Addison-Wesley, Cambridge, 1949).
- [217] S. J. Guy, S. Curtis, M. C. Lin and D. Manocha. *Phys. Rev. E* **85**, 016110 (2012).

- [218] E. Patzelt, W. Kool, A. Millner, and S. Gershman. *Sci. Rep.* **9**, 1689 (2019).
- [219] D. F. Styer, M. S. Balkin, K. M. Becker, M. R. Burns, C. E. Dudley, C. E. Forth, et al. *Am. J. Phys.* **70**, 288 (2002).
- [220] C. W. Misner, K. S. Thorne and J. A. Wheeler. *Gravitation* (Freeman, San Francisco, 1973).
- [221] B. J. Chihak J. M. Plumert, C. J. Ziemer and J. K. Kearney. *J. Exp. Psychol. Hum. Percept. Perform* **36**, 1535.
- [222] M. Ostrogradsky. *Mem. Ac. St. Petersburg* **VI**, 385 (1850).
- [223] R. P. Woodard. *Lect. Notes Phys.* **720**, 403 (2007).
- [224] H. Motohashi and T. Suyama. *Phys. Rev. D* **91**, 085009 (2015).
- [225] F. C. Anderson and M. G. Pandy. *J. Biomech. Engineering* **123**, 381 (2001).
- [226] S. H. Creem-Regehr D. M. Gill G. D. Pointon, B. Bodenheimer and J. Stefanucci. *Frontiers Robotics AI* **6**, 96 (2019).
- [227] J. Yoon, S. H. Park and D. L. Damiano. *J. Neuroeng. Rehabil.* **9**, 62 (2012).

초 록

생물계는 자연의 대표적인 복잡계로, 여러 거리와 시간 눈금에서 떠오름 현상을 보인다. 생물계를 다루는 이론 물리학자에게는 하나의 이론적 틀로 이 복잡성을 이해하는 것이 궁극적인 목표가 되겠지만, 아직 각 눈금에서 떠오르는 현상을 하나씩 이해하기 위한 노력이 필요하다. 생물학의 많은 분야들은 각각의 대상 현상에 대한 방대한 실험 자료를 이해하기 위한 수학적 모형을 필요로 한다.

이 논문에서는 수리적 모형과 통계 물리적 방법일 이용하여 다섯 가지 생물계의 현상을 다루고 있다. 그 주제는 자가포식의 동역학과 아밀로이드-베타 농도에 주는 영향, 알차이머 병에서 아밀로이드-베타 단백질의 응집, 일주기의 환경과의 때맞음과 빛 치료, 기울어진 땅 위 걸음질할 때의 에너지 소비, 보행자의 행동 동역학이다. 각 주제에 대한 배경을 소개하고 그 현상을 연구하기 위한 수리적 모형을 소개한다. 그의 결과에 대한 논의가 잇따른다.

주요어: 수리적 모형, 복잡계, 생물계, 떠오름, 자가포식, 아밀로이드-베타, 알차이머 병, 크기 분포, 자라남 모형, 수면-각성 모형, 일주기 리듬, 오렉신, 때맞음, 에너지 소비, 걷기, 행동 동역학, 보행자, 라그랑주 동역학, 최소 노력의 법칙

학번: 2013-22982

감사의 글

학문의 길로 이끌어 주시고 학위 과정 동안 가르침을 주신 최무영 교수님께 깊은 감사의 말씀을 드립니다. 선생님께서는 대상과 상관 없이 물리학자로서 치밀하게 자연을 연구하는 방법을 알려주셨습니다. 그리고 학자로서 세상을 바라보는 법을 알려주셨습니다. 선생님께서 “지도 교수가 시시하게 느껴질 때 졸업할 준비가 된 것이다”라고 농담 삼아 말씀 하신 적이 있는데, 그럼 준비가 덜 된 것일까요. 학교를 떠나지만 앞으로도 선생님께 배우고 함께 연구하기를 바랍니다.

저의 첫 연구 주제를 소개해 주시고 4, 5, 6장 내용을 지도해주신 김종원 교수님께 감사를 드립니다. 교수님께서 연구자로서의 기본을 알려주시고 어려운 상황을 웃음으로 넘길 수 있는 해학과 지혜를 보여주셨습니다. 감사합니다.

자가포식과 아밀로이드-베타 주제를 소개시켜 주시고 지도해주신 한경림 박사님께 감사를 드립니다. 경림 형은 저에게 연구에 몰입한다는게 어떤건지 보여주시고, 학위 받은 이후 독립적인 학자의 길을 찾는 방법을 알려주셨습니다. 지금도 함께 연구를 할 수 있어 기쁘고 앞으로가 더 기대 됩니다.

박사학위 초기 동안 많은 도움을 주신 고세건 박사님께 감사합니다. 세건이 형의 아낌 없는 관심 덕분에 잘 적응했던 것 같습니다. 밥을 사주시며 위로해 주신 강혁 박사님, 늘 열심히 연구하는 모습을 보여주신 아람이 형, 많은 실질적인 조언을 주신 형준이 형, 항상 따뜻하게 대해주신 찬수형께 감사합니다. 항상 새로운 관점을 알려주시는 조정효 교수님, 항상 즐겁게 이야기를 나눌 수 있는 형님 임종수 박사님께 감사합니다. 상산수리과학관에서 늦게까지 연구하시며 저에게 영감을 주신 최인령 교수님께 감사합니다.

제가 선배님들께 도움 받은 만큼 해주지 못한 후배 지혜와 준혁이에게 미안하고, 그래도 잘 해주고 있어서 고맙습니다. 앞으로 훌륭하게 뜻을 펼칠 수 있을 것이라고 믿습니다.

보행행동 주제를 소개시켜 주시고 군산에 내려갔을때 따뜻한 마음으로 맞이해주신 정현채 교수님께 감사합니다.

박사과정 시작하기 전에 인턴으로서 받아주셔서 많은 것을 배우게 해주신 이주영 교수님께 이 자리를 빌려 감사의 말씀을 드립니다.

무한한 사랑과 지원을 주신 어머니 박신순 교수님과 아버지 김선욱 교수님께 감사와 사랑의 마음을 전합니다. 부모님께서 부족한 저를 항상 믿어주셔서 공부를 시작할 수 있었고 박사 과정을 무사히 끝낼 수 있었습니다. 인생에서 중요한게 무엇인지 일깨워주는 아우 순곤이에게도 사랑과 고마운 마음을 보냅니다.

Finally, thank you Soo Jin for picking me up whenever I was down. We did it!